Effect of H$_2$S on the Thermodynamic Stability and Electrochemical Performance of Ni Cermet-type of Anodes for Solid Oxide Fuel Cells

Manga Venkateswara Rao

Dissertation
an der
Universität Stuttgart

Effect of H$_2$S on the Thermodynamic Stability and Electrochemical Performance of Ni Cermet-type of Anodes for Solid Oxide Fuel Cells

Von der Fakultät Chemie der Universität Stuttgart
zur Erlangung der Würde eines Doktors der
Naturwissenschaften (Dr. rer. nat.) genehmigte Abhandlung

Vorgelegt von
Manga Venkateswara Rao
aus Visakhapatnam, India

Hauptberichter: Prof. Dr. rer. nat. F. Aldinger
Mitberichter: Prof. Dr. rer. nat. J. Maier
Vorsitz: Prof. Dr. Ir. E.J. Mittemeijer

Tag der mündlichen Prüfung: 20.12.2006

Institut für Nichtmetallische Anorganische Materialien der Universität Stuttgart
Max-Planck-Institut für Metallforschung, Stuttgart
Pulvermetallurgisches Laboratorium

Stuttgart 2006

Dedicated to
my mother
Alamelu Manga

Acknowledgements

Contents

Abstract

For SOFCs to be main means of power generation, they should be able to exploit wide variety of fuels. Among Ni-cermets, Ni-YSZ is the state-of-the-art materials for the anode in SOFC which is the fuel electrode. But sulphur impurity present in different gaseous fuels (e.g Biogas), depending on its concentration, is highly poisonous to the stability and electrochemical performance of the Ni catalyst in the cermet anodes. Thus in this study the microstructural stability of Ni-YSZ, Ni-CGO and Ni-LSGM cermets in H_2S-containing hydrogen gas is studied in the intermediate temperature range of SOFC operation. Thermodynamic modelling of Ni-S-O-H quaternary system was performed for the calculation of the thermodynamic stability and sulphur-tolerance limit of Ni in the gaseous atmosphere made up of H, O and S. The effect of the presence of H_2S in fuel gas, in the concentrations well below the thermodynamic tolerance limit, on the electrochemical performance of the anodes is studied by using model Ni-patterned electrodes on YSZ and LSGM.

Ni-YSZ and Ni-CGO cermets were studied in H_2 + H_2S (1 vol%) gas in the intermediate temperature range (500-750°C). At temperatures above 901 K (calculated eutectic temperature), Ni upon its reaction with sulphur forms a eutectic melt as given on the Ni-S binary phase diagram where as at 773 K, it forms Ni_3S_2. YSZ in the cermets was found to be stable against H_2 + H_2S (1 vol%) gas in the temperature range of the study. CGO also remained stable at 500°C but was found to react with H_2S to form $(Ce,Gd)_2O_2S$ at 750°C.

Ni-LSGM cermets were studied as a novel anode material for SOFCs. It is known from the literature that NiO and LSGM react with each other during the fabrication of the fuel cell. In this study a LaNiO3-type phase was found to form during sintering in air and in inert atmosphere. The TEM investigation of NiO-LSGM interface after sintering in air at 1350°C has revealed that the LaNiO3-type phase formed was similar to the cubic LSGM phase with a relatively high amount of Ni. During the sintering interdiffusion across the NiO-LSGM led to incorporation of Ni into LSGM. The compositional analysis across the NiO-LSGM interface revealed the interface chemistry to be $Ni(Mg,Ga)O - (La,Sr)(Ga,Mg,Ni)O_{3-x}$.

A further reactivity of NiO/Ni with LSGM during the reduction of the sintered NiO-LSGM samples in H_2 was observed. The LaNiO$_3$-type phase (i.e LSGM(Ni)) decomposed into La_2O_3 and $SrLaGaO_4$ accompanied by diffusion of excess amount Ga into FCC-Nickel. So after

reduction Ni in the cermet showed about 9 at% of dissolved Ga. Ni-LSGM cermets without any reactivity, for their investigation as a SOFC anode could not be made.

The as-obtained Ni-LSGM cermets were studied for their stability in H_2+H_2S (1 vol%) gas. Interestingly the FCC solid solution of Ni-Ga alloy formed at 750°C was found to be stable against the H_2S at 750°C while it was known that pure Ni forms $Ni+Ni_3S_2$ eutectic melt under the same condition. The increase in sulphur tolerance limit of Ni by alloying with Ga at 750°C is further supported by the phase diagram calculations of Ni-Ga-S ternary.

Since Ni-LSGM cermets could not be made successfully, Ni-patterned LSGM cells were made by photolithography for the study of electrochemical performance. The interfacial stability of these Ni-patterned LSGM cells in hydrogen gaseous atmosphere was investigated further in the intermediate range of temperature. From the Auger depth profile analysis of these cells, it was identified that at temperatures below 650°C the interface was stable without any reactivity/interdiffusion. However at 750°C interdiffusion across the interface led to the diffusion of Ni into LSGM with simultaneous diffusion of Ga into Ni. Hence the electrochemical performance of the symmetrical cells of Ni-patterned LSGM could be investigated in the temperature regime below 650°C, where there is no reactivity between Ni and LSGM.

For the Ni-patterned LSGM cells which were annealed in H_2 at 750°C, the chemistry across the interface can be represented as (Ni, Ga) | $(La_{0.8}, Sr_{0.2})(Ga^{+3}, Mg^{+2} Ni^{+3}, Ni^{+2}) O_{3-x}$. So these annealed samples were also used to check the stability of Ni-Ga alloy patterns in H_2+H_2S (1 vol%) gas at 750°C and 500°C. It was found that this Ni-Ga alloy is stable against H_2+H_2S (1 vol%) gas at 750°C, but formed Ni_3S_2 at 500°C.

Thermodynamic modelling of the Ni-S-O-H quaternary was performed to understand the stability of Ni in the gaseous atmosphere comprising the species of S, O and H. CALPHAD methodology was employed to model the quaternary system. The modelling of the Ni-S binary phase diagram was performed employing sublattice models for the non-stoichiometric phases. The optimised binaries of systems Ni-O, and Ni-H were taken from the literature. The Ni-O-S and Ni-O-H ternaries were extrapolated from the lower order binary systems. In the Ni-O-S system, $NiSO_4$ is the only ternary compound present. The ternary compounds, $Ni(OH)_2$ and $NiOOH$ in the system Ni-O-H were considered as stoichiometric line

compounds. The model parameters of the ternary compounds were optimised using the experimental data. The quaternary Ni-S-O-H system was calculated by the extrapolation method as employed in the CALPHAD methodology.

The predominance area diagrams with different potentials (variables) as axes were calculated. The stability of Ni in H_2, H_2O and H_2S gaseous atmosphere can be predicted from the calculated stability diagrams with the required independent variables ($P(H_2S)/P(H_2)$ vs $P(H_2O)/P(H_2)$)) as axes. Similar potential phase diagrams for stability of Ni in the gaseous atmospheres made up of the species of S, O and H, can be calculated using the Ni-S-O-H quaternary.

The Ni-Ga-S ternary phase diagram was calculated in order to explain the relatively higher H_2S-tolerance of FCC solid solution of Ni-Ga alloy in comparison to pure Ni. The predominance area diagrams calculated for 750°C, supported the increase in sulphur-tolerance with increasing activity of Ga in the FCC Ni-Ga alloy. However at 500°C the sulphur tolerance of the Ni-Ga alloy remains almost the same as that of pure Ni. This is completely in agreement with the experimental findings of the stability of Ni-Ga alloy in H_2+H_2S (1 vol%) gaseous atmosphere.

Investigation of the effect of H_2S on the electrochemical reaction mechanism of H_2- oxidation at Ni-patterned anodes on YSZ and LSGM was carried out.

In order to understand the H_2-oxidation mechanism and the role played by the electrolyte in the reaction mechanism, symmetrical cells of Ni-patterned YSZ single crystals with different crystallographic orientations were studied in H_2+H_2O gas in the intermediate temperature range. In the entire range of experimental conditions Ni-patterned single crystal YSZ cells were found to be limited by a single electrode process. A single impedance arc very close to a perfect semicircle was measured.

The total polarisation resistance (R_p) which is inversely related to the rate of the elementary process responsible for the impedance arc appears to depend on the face of the YSZ single crystals. But solely from the above measurements it is not possible to unambiguously interpret the variation of R_p and its dependence on the face of the YSZ crystal. Further experiments are

necessary to clearly establish the dependence of Rp and its relationship to the surface structure of YSZ.

The impedance analysis of the symmetrical cells of Ni-patterned YSZ single crystals of different orientations also revealed that the capacitance calculated from impedance arc was dependent on the face of the YSZ single crystal. The capacitance values are found in the order of $C_{<100>} < C_{<111>} < C_{<110>}$. The obtained values of capacitance were found to be independent of temperature, but can not be exclusively due to the double layer.

In the case of Ni-patterned YSZ (Polycrystalline) symmetrical cells also a single process was found to be responsible for the impedance arc. The capacitance exhibited by these polycrystalline samples are similar to that of the cells of YSZ single crystals and appears to be average of the capacitance values measured with single crystal cells of different orientations. Also as in the case of YSZ single crystal cells, the capacitance was found to be independent of temperature. So the obtained capacitance values can not be *exclusively* due to the double layer but could be due to a double layer capacitance and/or pseudo-capacitance associated with adsorption of species accompanied by partial charge transfer.

Based on the results a possible reaction mechanism was assumed at the Ni-patterned YSZ single and polycrystalline cells. The elementary charge transfer reaction $H_{Ni} + O^{-2}_{YSZ} \leftrightarrow OH^-_{Ni}$ + e is thought to be the rate determining step responsible for the impedance arc. The process of formation and adsorption of OH^- on Ni from the reaction between O^{-2}_{YSZ} and H_{Ni} at Ni-YSZ interface (two phase boundary) can be taken as the process responsible for the observed capacitance. At the two phase boundary it is thought to be a capacitive process, but not to be a DC process.

Effect of 5 ppm of H_2S on the H_2 oxidation kinetics at Ni-patterned electrodes was studied. It was found that even 5 ppm of H_2S, in H_2+H_2O gas, is poisonous to the Ni-electrodes on YSZ. The addition of 5ppm of H_2S doubled the total polarisation resistance of symmetrical cell. But there was no change in the shape of the impedance arc and a single arc was recorded also with the 5 ppm of H_2S impurity. The activation energy obtained from the impedance arc measured with and without 5 ppm of H_2S was also the same. Hence it can be said that the addition of 5 ppm of H_2S does not lead to change of the rate limiting step, but leads to a decrease in the rate of the reaction.

An interesting feature of an initial drop in the impedance spectrum immediately after the addition of H_2S was observed. The drop may be due to the reaction between OH^- intermediates and the H_2S during the initial stages of dissociative adsorption of H_2S on the Ni surface. The poisonous effect of H_2S is reversible upon its withdrawal from H_2+H_2O gaseous atmosphere. But at 823 K the reversibility is very slow.

The electrochemistry of Ni-patterned LSGM is studied for the first time in the temperature range where there is no Ni-LSGM interfacial reactivity. The results are very encouraging and if Ni-LSGM cermets can be made without any reactivity, then this will be a better candidate for anode material for its operation in the safe identified temperature regime. The measured conductivity of LSGM from these symmetrical cells is in good agreement with the conductivity data reported in literature, but measured with Pt electrodes.

The reaction mechanism and rate determining step of H_2 oxidation at Ni-patterned electrodes on LSGM may not be same as that of Ni-patterned YSZ. In the case of Ni-patterned LSGM cells also, a single arc was measured in the entire range of experimental conditions and a single electrode process was assumed to be responsible for the arc. The equivalent circuit fit results revealed that the capacitance is dependent on temperature unlike in Ni-patterned YSZ cells. The rate determining step responsible for the impedance arc is not clearly understood. However the magnitude of the capacitance obtained and its dependence on temperature indicates that an adsorption reaction (on Ni or LSGM) involving O^{-2} ions could be responsible for the arc.

The presence of 5 ppm of H_2S in H_2+H_2O gas was found to decrease the electrode conductivity as in the case of Ni-patterned YSZ. The decrease in the electrode conductivity is dependent on the partial pressure of water in the gas. In dry gas the effect of 5 ppm of H_2S is much more poisonous. However the poisonous effect of the H_2S impurity, for the same gas composition and experimental conditions, was found to be relatively more for Ni-patterned YSZ than Ni-patterned LSGM cells.

An initial drop in the impedance spectrum immediately after the release of H_2S was also observed with Ni-Patterned LSGM cells. As discussed in the case of Ni-patterned YSZ cells, this initial enhancement in the reaction rate could be due to the reaction of H_2S with the charged intermediates on the Ni surface during the initial stages of its dissociative adsorption.

It appears that also in the case of Ni-patterned LSGM cells, the reaction mechanism remains unaltered with the addition of 5 ppm of H_2S except for the decrease in the rate of the elementary process responsible for the impedance arc. This assumption is supported by the fact that the shape of the impedance arc and the activation energy obtained from the arc remains same with and without 5 ppm of H_2S.

The poisonous effect of the H_2S impurity was reversible. The reversal of the poisonous effect in the case of Ni-patterned LSGM cells is relatively faster when compared with the Ni-patterned YSZ cells, at the same gas composition and operating temperatures. The partial pressure of water in the gas was found to effect the time taken for the reversibility, with higher partial pressures of water causing relatively fast reversal.

1.0 Introduction

1.1 General introduction

Solid oxide fuel cells (SOFCs) offer the advantages of clean environment and high fuel efficiency [1]. But the high operating temperatures lead to material degradation and high operating costs. For SOFC to be the main means of power generation it is required to reduce the operating temperatures. So the development of SOFC for operation at intermediate temperatures is necessary. Another important factor which determines the success of the SOFCs is their ability to work with wide variety of fuels e.g., natural gas, biogas etc., beside hydrogen fuel. So a lot of research is aimed at developing new materials for SOFC which can work at lower or intermediate temperatures with wide variety of fuels.

Ni-cermets are widely used as the material for anode which is the fuel electrode. However, H_2S which is a constituent of fuel gases like natural gas and biogas is very poisonous to the electrochemical performance of Ni in the cermet anode. It is known from the available thermodynamic data that the tolerance limit of Ni for H_2S in gas mixtures with H_2 is ~195ppm at 773 K. But the electrochemical performance of Ni is adversely affected by even few ppms of H_2S, well below the thermodynamic tolerance, in the gas mixture. Sulphur chemisorption on the surface of Ni can modify the surface structure of Ni significantly. The strong adsorbate-metal bonding causes the rearrangement of the surface structure according to the environment. It is known that the energetics of the electrochemical reactions and their rates are significantly dependent on the surface composition and structure. Thus, the stability and performance of the anode materials of SOFCs in the presence of H_2S require further studies.

1.2 Motivation and objectives
1.2.1 Microstructural stability of Ni-Cermets in H_2 and H_2+H_2S

Ni-YSZ (Y_2O_3-doped ZrO_2) and Ni-CGO (Gd_2O_3-doped CeO_2) cermets are widely used as the SOFC anode materials. Ni in these two cermets is stable and doesn't show any reactivity with either YSZ or CGO. Nothing is known about the stability of cermets of Ni-CGO and Ni-YSZ in H_2+H_2S (1vol%) in literature and therefore was investigated in this work.

Recently in 1994 Ishihara et al [2] reported Sr- and Mg-doped $LaGaO_3$ (LSGM) as a new oxide ionic conductor. Later Goodenough and et al in their detailed investigation of LSGM

reported that it is a promising electrolyte for operation of SOFCs in the intermediate temperature range 600-800°C [3-5]. It is reported that it is a pure ionic conductor over a wide range of oxygen partial pressure (10^{-22} to 1 atm). They also reported LSGM20-17 ($La_{0.8}Sr_{0.2}Ga_{0.83}Mg_{0.17}O_{2.815}$), as the optimised composition which exhibits the highest ionic conductivity at 700 to 800°C. So this attracted researchers to try for novel Ni-LSGM cermet as anode for intermediate temperature SOFCs (IT-SOFCs). Ni-patterned LSGM electrodes which are prepared by photolithography can be used for this purpose. When producing Ni-LSGM cermets the reactivity of LSGM with NiO/Ni in the anode during fabrication and operation of the cell leads to poor performance [5-11]. It is interesting to know whether there is a safe temperature range of production and operation of Ni-LSGM and its performance as SOFC anode. Therefore in this work, the microstructural stability of NiO-LSGM during sintering and reduction was investigated. Then the as-produced Ni-LSGM cermets were studied in H_2+H_2S(1vol%) gaseous atmosphere. In addition, the stability of the Ni-LSGM interface of the photolithographically prepared sample was investigated in reducing atmosphere (H_2). Further on the electrode performance Ni-patterned YSZ and Ni-patterned LSGM electrodes was studied.

1.2.2 Thermodynamic modelling of Ni-S-O-H quaternary system

The operating temperature of the intermediate temperature SOFC is in the range of 500-800°C. With hydrogen as fuel, the gas at the anode comprises of H_2 and H_2O and H_2S depending on the type of fuel. In order to understand the thermodynamic stability of Ni in such an atmosphere under the operating conditions of SOFCs, a complete thermodynamic description of the Ni-S-O-H quartenary is necessary. The CALPHAD approach has been employed for this purpose.

1.2.3 Effect of H₂S on Electrochemistry of Ni-patterned model electrodes in H₂+H₂O

The reaction mechanism of hydrogen oxidation at the anode is not well understood [12]. There have been a lot of studies aiming at understanding of the electrode reaction kinetics by various methods, but there is no clear understanding about how the charge transfer reaction takes place. Similarly, it has been shown that water has a catalytic effect on the reaction kinetics of Ni-patterned YSZ electrodes. However, there is a wide disagreement in understanding of the possible reaction path(s) and rate determining step(s).

The electrode reactions occurring on the surface are sensitive to the surface structure and composition. The binding energies of various surface species vary depending on the surface structure and chemistry. So the reaction rates and the reaction paths are significantly influenced by these aspects. Hence the effect of surface structure of YSZ on the reaction kinetics and a possible derivation of understanding of the reaction mechanism would be interesting to investigate. YSZ single crystal with different orientations, i.e, with different faces may lead to a better understanding of the role played by the surface of the electrolyte in the reaction mechanism. So this prompted to prepare symmetrical cells of Ni-patterned YSZ single crystals with different orientations. Furthermore Ni-pattern electrodes with defined length of the triple phase boundary were studied. These simplified model Ni-patterns allow to avoid the complex microstructure of the Ni-cermets and thus leading to a better understanding of the reaction mechanism avoiding the microstructural effects.

In this work, electrochemical impedance spectroscopy (EIS) investigation of symmetrical cells of Ni-patterned YSZ single crystals of different orientations, Ni-patterned YSZ (polycrystalline) and Ni-patterned LSGM in H_2+H_2O atmosphere was carried out. Since investigations of Ni-patterned LSGM cells have not yet been reported in literature it will be possible for the first time to compare the electrode performance of Ni-patterned YSZ and Ni-patterned LSGM cells in H_2+H_2O gaseous atmosphere and to understand the effect of H_2S on the reaction kinetics.

2.0 Fundamentals and state-of-the-art

2.1 Solid oxide fuel cell

2.1.1 Working principle

Solid oxide fuel cells are electrochemical devices which convert chemical energy into electrical energy from a reaction between a fuel and an oxidant. Figure 2.1 depicts the working principle and the basic components of a SOFC. The fuel and oxygen gases flow along surface of the porous anode and cathode respectively. On the cathode side the oxidant is electrochemically reduced and the thus produced oxygen ions migrate through the electrolyte to the anode. The driving force for the migration of oxygen ions from the cathode side to anode side is the difference in partial pressure of oxygen (oxygen activity) between cathode and anode sides. On the anode side the oxygen ions react with hydrogen to form water and release electrons.
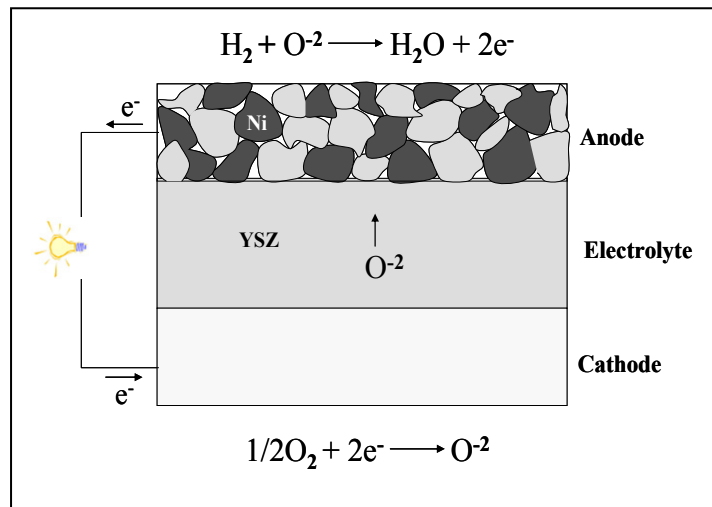
Figure 2.1 Working principle of solid oxide fuel cells.

2.1.2 Materials

Electrolyte
YSZ is the most widely used electrolyte. ZrO_2 is doped with Y_2O_3 (8-10 mole%) which leads to the stabilisation of cubic fluorite structure with high concentration of oxygen vacancies. The recently reported LSGM has been demonstrated as an electrolyte material suitable for low

and intermediate temperature solid oxide fuel cells [13-14]. Gd- doped CeO_2 has also been studied as an electrolyte [15] although it is a mixed ionic and electronic conducting material.

Cathode

Sr-doped $LaMnO_3$ perovskite (LSM) is the commonly used cathode material. LSM is a poor ionic conductor and it is assumed that the electrode surface path dominates the reaction rate of the cathodic reaction [16-19]. LSM-YSZ composites have also been studied as cathodes [20-21]

Anode

The performance of the fuel cell is mainly dependent on the performance of its fuel electrode i.e., the anode. The required properties of an anode are, a) a high catalytic activity for oxidation of the fuel b) a high electrical conductivity under wide range of operating conditions, c) it should be chemically, mechanically and thermally compatible with the other components of the fuel cell, and d) it should have optimum porosity for easy transportation of the gas phase.

Ni-YSZ cermets are most widely used and studied anode materials for SOFCs. This is because even though Ni has several limitations, it has excellent catalytic properties, does not react with other components of SOFC and it is relatively low in cost. Ni can also withstand high operating temperatures and reducing conditions and it plays the role of catalytically active and electronic conductor. YSZ in the cermet supports the Ni network avoiding the coarsening of Ni in the cermet. Furthermore YSZ also makes the thermal expansion coefficient of the anode similar to the electrolyte. However the role played by the YSZ in electrode reactions is not completely understood. It is thought that YSZ enhances the active sites for electrode reaction by providing the conductive path for oxygen transport within the cermet.

As mentioned before Ni in the Ni-YSZ cermets has several limitations also. Ni-cermet anodes are not suitable for operation with different kinds of gaseous fuels, for example natural gas and biogas. With natural gas there is a strong tendency for carbon deposition which can cause physical disintegration of the Ni-structure and fragmentation of the cermet anode, while gases containing H_2S impurity even in several ppms, are poisonous to Ni leading to high polarisation resistance. H_2S can cause the degradation of the electrode performance depending on its concentration. At higher concentrations depending on the temperature it can either lead to the formation of nickel sulphide or eutectic melting. Another limitation of Ni is the

formation of volatile $Ni(OH)_2$, at higher partial pressures of $P(H_2O)$ and high temperatures (at 950°C).

Ni-LSGM cermets were also studied as a SOFC anode. It was reported that the reactivity of LSGM with NiO/Ni in the anode during fabrication and operation of the cell leads to poor performance [5-11]. Huang et al. investigated the reactivity of LSGM with NiO after sintering at 1400 °C and 1200 °C. They reported $LaNiO_3$ as a reaction product, after sintering at 1400 °C, which does not conduct oxide ions under anodic conditions [5]. Zhang et.al [9] in their studies of the NiO–SDC–LSGM system reported the formation of an hexagonal $LaNiO_3$-based compound after sintering NiO–LSGM mixtures at three different temperatures 1150 °C, 1250 °C and 1350 °C. They found a drastic decrease in the measured conductivities of LSGM and attributed it to a low-conductivity layer of a $LaNiO_3$-based phase between the Ni anode and LSGM electrolyte. It was also indicated that this $LaNiO_3$-based phase probably contains other elements. However, the composition of the interfacial layer due to the reaction of NiO with LSGM is not known exactly. The thickness of the interlayer formed, for instance, after 2 hours of sintering is also not known. However the reactivity of Ni-LSGM in reducing conditions was not investigated.

In recent times several other materials have been investigated in the search of better alternative anode materials. Instead of composite materials several compounds have been studied as the potential anode candidates. One such anode material is ceria. Ceria exhibits both ionic and some electronic conduction. By doping ceria with gadolinia, the mixed electronic ionic conduction (MIEC) is enhanced. Such anodes can attain a performance comparable to that of Ni/YSZ anodes in hydrogen and can work in methane atmosphere without showing any carbon formation [22]. Chromite and titanate based perovskites compounds have also been investigated as anode material [23].

2.2 SOFC anode reaction mechanism

2.2.1 H_2 oxidation reaction kinetics at Ni-based anodes

Both Ni-YSZ cermets and model Ni-patterned YSZ materials have been studied to understand the reaction kinetics [24-30]. Using model Ni-patterned electrodes on YSZ it is possible to avoid the complex microstructure of the commercially used Ni-YSZ cermets. The complex microstructure may lead to variable conditions of partial pressures of fuel and water vapour at

different locations, and so may lead to different reaction mechanisms to operate at different locations. Simple Ni-patterned electrodes avoid the complex microstructure and any possible polarisation due to concentration.

Mogensen et. al reported the study of oxidation kinetics of hydrogen on Ni-YSZ cermet anode by impedance spectroscopy in the high temperature regime 850°C to 1000°C [24]. The operating conditions such as P_{H2O}, P_{H2}, temperature, and anodic over-potential have been varied. At least three rate-limiting processes have been reported. The high frequency relaxation process has been attributed to charge transfer. The two low-frequency processes have not been clearly understood. The dependence of the performance of the Ni-YSZ cermet on the microstructure has been demonstrated.

Holtappels et al. [25-26] reported the investigation of hydrogen/water reaction on Ni-YSZ cermet electrode. They studied in a temperature range of 725°C–950°C and reported that at temperatures below 845°C the real part of the faradaic impedance was charge transefer controlled. At temperatures above 890°C two reaction steps, charge transfer and adsorption, determined the rate of the overall reaction

Jiang et al. [27] studied the reaction mechanism in dry and moist H_2 atmosphere. In dry H_2 (with ~0.07% H_2O) the rate controlling step was supposed to be dissociative adsorption/diffusion of hydrogen on the surface of the metal electrode.

They proposed a reaction mechanism for H_2 oxidation in moist H_2. It was indicated that both Ni and Y-TZP(electrolyte) surfaces contribute to the H_2 oxidation reaction.

In moist hydrogen

$$H_2O(gas) + S_M \Leftrightarrow (O\text{-}S_M) + H_2 \qquad (2.1)$$
$$H_2(gas) + 2S_M \Leftrightarrow 2(H_{ads}\text{-}S_M) \qquad (2.2)$$

$$H_{ads}\text{-}S_M + O\text{-}S_M \rightarrow H_{ads}\text{-}O\text{-}S_M + S_M \qquad (2.3)$$

$$H_{ads}\text{-}O\text{-}S_M \rightarrow H_{ads}\text{-}O\text{-}S_M (tpb) \qquad (2.4)$$
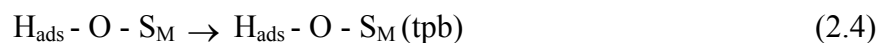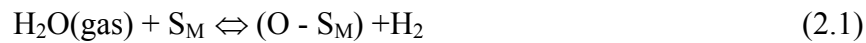
charge transfer and H_2O formation on Y-TZP electrolyte surface near TPB,

$$H_{ads}\text{-}S_M \text{ and/or } H_{ads}\text{-}O\text{-}S_M \rightarrow H_{ads,\ Y\text{-}TZP} \qquad (2.5)$$
$$O^{-2}_{Y\text{-}TZP} + 2\,H_{ads,\ Y\text{-}TZP} \rightarrow H_2O + 2\,e_{Y\text{-}TZP} + V_O^{\bullet\bullet} \qquad (2.6)$$

$$2\,e_{Y\text{-}TZP} \rightarrow 2\,e_M \qquad (2.7)$$
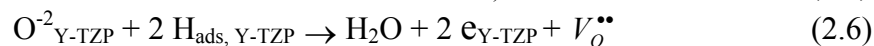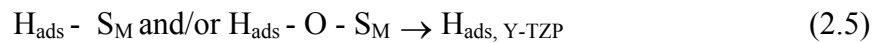
where S_M is an active metal surface site for adsorption and $O - S_M$ is an active metal surface site adjacent to an O_{ads} or a suboxide.

Investigations of the kinetics with well defined Ni-patterned anodes, have also been reported [28-30].

In earlier studies with Ni-patterned electrodes in H_2-H_2O atmospheres Mizusaki et al [28] reported either the dissociative adsorption of reactants or the surface diffusion of the adsorbed species on the nickel surface, as the rate determining step. Mizusaki et al thought exclusively the Ni surface to be electrochemically active. They assumed the presence of O_{ad}, H_{ad}, OH_{ad}, and H_2O_{ad} as adsorbed species on the Ni surface. A vacant site on the Ni surface is indicated by V_{ad}. The elementary relationships which hold under equilibrium conditions were assumed to be

$$H_2O + V_{ad} \leftrightarrow H_2O_{ad} \qquad (2.8)$$

$$H_2O_{ad} + V_{ad} \leftrightarrow H_{ad} + OH_{ad} \qquad (2.9)$$

$$OH_{ad} + V_{ad} \leftrightarrow H_{ad} + O_{ad} \qquad (2.10)$$

$$H_2 + 2 V_{ad} \leftrightarrow 2 H_{ad} \qquad (2.11)$$

$$O \text{ (YSZ bulk)} + V_{ad} \leftrightarrow O_{ad}. \qquad (2.12)$$

The reaction (2.12) is believed to occur as result of the assumed charge transfer process across the TPB with a local electronic equilibrium which holds between Ni and YSZ close to the nickel/YSZ interface as follows,

$$2 e^- \text{(Ni)} + O_{ad} \leftrightarrow O^{2-} \text{(YSZ bulk)} + V_{ad} \leftrightarrow O\text{(YSZ bulk)} + 2e^- \text{(YSZ bulk)} + V_{ad} \quad (2.13)$$

$$\text{and} \quad e\text{-(Ni)} \leftrightarrow e\text{- (YSZ bulk)} \qquad (2.14)$$
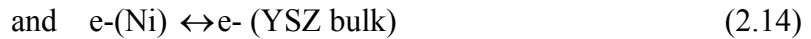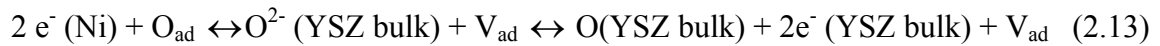
where (YSZ bulk) means the bulk of YSZ close to TPB.

Boer et al. [29] also studied the H_2 oxidation reaction mechanism at Ni-patterned electrodes on YSZ by EIS. However they fitted the impedance spectra of Ni-patterned electrodes with three arcs while the dominating process is ascribed to charge transfer step. But the exact nature of the different processes is not clearly understood.

Boer et al assumed the reaction mechanism as

8

$$H_2 + 2\ S_{Ni} \rightarrow 2\ H_{Ni} \tag{2.15}$$

$$H_{Ni} + O_O^X \rightarrow OH_O^{\bullet} + S_{Ni} + e^- \tag{2.16}$$
$$OH_O^{\bullet} + S_{electrolyte} \rightarrow OH_{ads}^- + V_O^{\bullet\bullet} \tag{2.17}$$

$$H_{Ni} + OH_{ads}^- \rightarrow H_2O_{ads} + S_{Ni} + e^- \tag{2.18}$$
$$H_2O_{ads} \rightarrow H_2O_{gas} + S_{electrolyte} \tag{2.19}$$
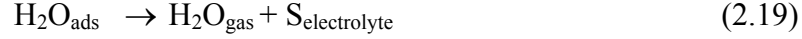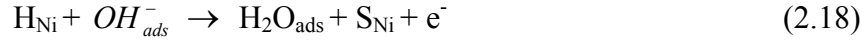
where S_{Ni} and $S_{electrolyte}$ indicate the vacant sites for the adsorption on Ni and YSZ surfaces, respectively. The OH_{ads}^- and H_2O_{ads} are adsorbed species present on YSZ surface, and $OH_O^{\bullet}$ indicates the interstitial hydroxyl.

It can be seen from the reaction mechanism that the presence of interstitial protons is assumed. They observed that, although the impedance measurements at equilibrium indicated that the electrode reaction was governed by one dominating process, the assumption of one rate determining step with the other steps in virtual equilibrium did not hold. However the dominating electrode process was attributed to a charge transfer process.

Gauckler et al [30] reported the impedance analysis of the Ni-patterned electrodes. In their measurements a single elementary process was thought to be responsible for the impedance arc. The rate determining elementary process was attributed either adsorption/desoprtion reaction of H_2 on Ni or removal of O^{-2} from the electrolyte.

Many other studies have also been reported to understand the anodic reaction mechanism at Ni/YSZ interface. However there are diversified opinions and no clear understanding of the reaction mechanism because of the difficulties in interpretation of the experimental electrochemical data. Understanding of the surface chemistry and surface structure at equilibrium and steady state conditions is crucial and its knowledge is very little at present.

2.2.2 Effect of H_2S on H_2-oxidation kinetics

It is known that sulphur, even in amounts as low as 5 ppms, is highly poisonous to the electrochemical performance of Ni in the cermet anodes. However the exact mechanism by which it interferes into oxidation kinetics of H_2 is not known.

Mogensen et al [24] studied the poisoning of Ni by 35ppm of H_2S impurity in H_2+H_2O gas mixture in the temperature range of 850°C-1000°C. They found out a 60% increase in polarisation resistance irrespective of the temperature.

Matsuzaki et al [31] studied the poisoning effect of H_2S on Ni-YSZ cermet electrode as a function of time, H_2S concentration and temperature in the range of 1023-1273K. The degree of poisoning caused by sulphur was found to have large dependence on the operating temperature. The minimum concentration of H_2S to cause the performance loss is smaller at lower operating temperatures. An increase in polarisation resistance was noticed when the H_2S concentration exceeded 0.05, 0.5, and 2ppm at 1023, 1173, and 1273 K respectively. The reversibility of the complex impedance spectra upon the withdrawal of H_2S from the fuel was reported. The time for recovery at lower temperatures was found to be longer than at higher temperatures.

2.3 CALPHAD methodology

The CALPHAD methodology is used to estimate phase diagrams from a variety of experimental data relevant to phase equilibria. Figure 2.5 depicts the Flow sheet of the CALPHAD methodology [32]. Actually it is a computational optimization process.
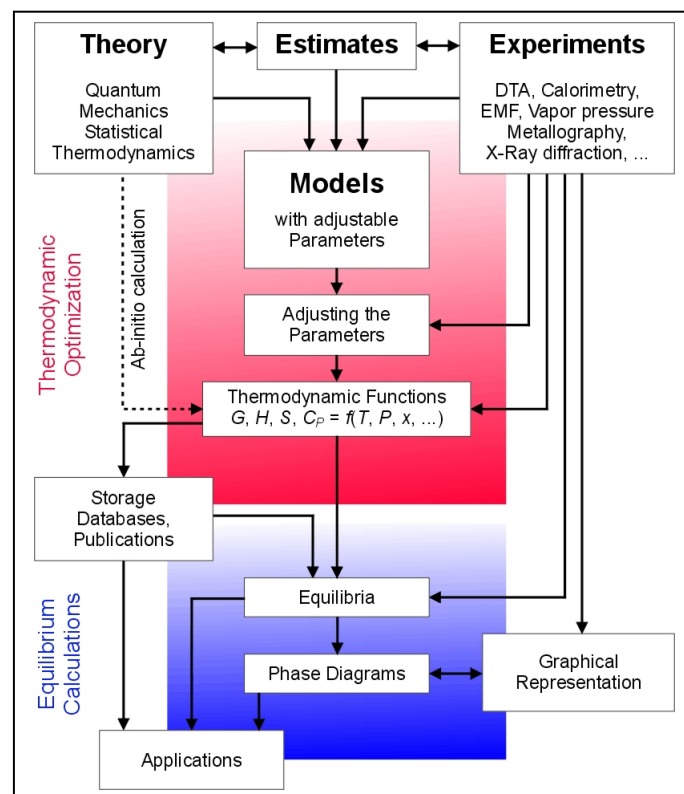
Figure 2.5 CALPHAD methodology [32]

10

The description of Gibbs energy of a phase as a function of temperature, pressure and composition is at the core of the CALPHAD methodology. From such functions the phase relationships can be calculated based on the criterion of the global minimum of the free energy [33, 34].

The Gibbs energy function of a phase is obtained by using a suitable model and calculating the model parameters using any experimental data of the phase. The model selected is based on the crystallographic data of the phase.

Experimental phase equilibria data and the thermodynamic data like enthalpies of mixing, partial molar properties, heat capacity data etc., from experiments, ab initio data from the quantum mechanical calculations and experimental phase diagram data are critically judged and used for the optimisation of the model parameters of the phase. The Gibbs energy functions of the phases so calculated can then be used to calculate various thermodynamic properties and phase diagrams.

Calculation of the ternary or quaternary or any higher order systems begin with the assessment of binary systems. As a first step the model parameters of the binary phases are optimised. These obtained binary model parameters are then used and kept fixed in the Gibbs energy description of the ternary phase while optimising the ternary parameters using the experimental data of that phase. Consider a ternary hypothetical system A-B-C. If all the binaries A-B, B-C and A-C are modelled, then along with the known ternary experimental data, the ternary A-B-C system is calculated by the extrapolation from the lower order binaries. This strategy is more useful when calculating a quaternary or a higher order system. A reasonable prediction of phase stabilities in complex higher order systems can be made. However it has to be noted here that the CALPHAD has no ability to predict a new phase. But the possibility of appearance of new phases becomes less with going towards higher order systems. The extrapolation strategy is depicted as a flow sheet in the figure 2.6.
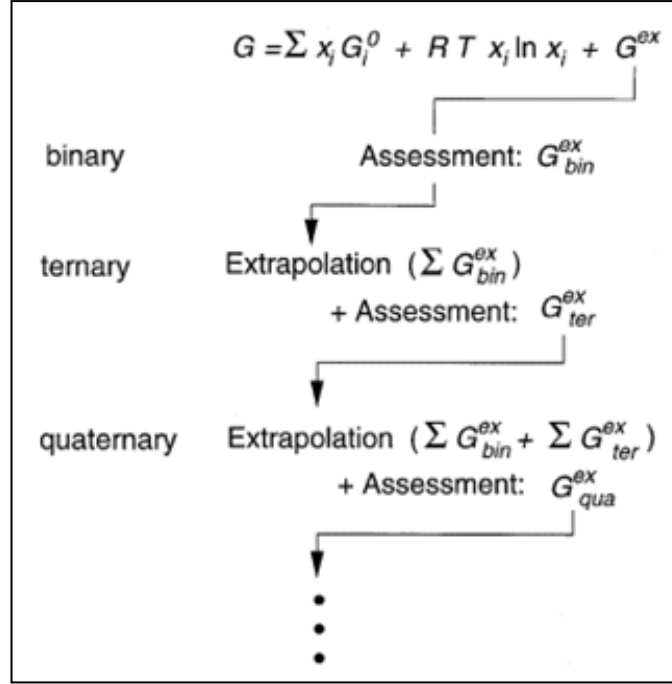
Figure 2.6 Extrapolation strategy of lower-order model parameters to higher orders as followed in CALPHAD methodology [35].

2.3.1 Gibbs energy of phases as a function of temperature and composition [34]

Only those models which have been utilised in the present work are explained.

2.3.1.1 Elements

Thermodynamic data of elements as a function of temperature are given using a polynomial function for the Gibbs energy according to the SGTE (Scientific Group thermodata Europe) database

$$G_{m[T]} - H_m^{SER} = a + bT + cTln(T) + \sum_{2}^{n} d_n T^n \qquad (2.20)$$

where

$G_{m[T]} - H_m^{SER}$ is the Gibbs energy relative to a standard element reference (SER),

H^{SER} is the enthalpy of an element in its defined reference state at 298.15 K,

a, b, c and d_n are coefficients, and

n is an integer taking the values 2,3 and -1.

2.3.1.2 Stoichiometric compounds

Gibbs energy of a stoichiometric compound relative to the standard element reference (SER) is given by

$$°G_m(\phi) - H^{REF} = \Delta G_m(\phi) + \sum X_i(°G_i^{(\alpha)} - H_i^{REF}) \qquad (2.21)$$

12

where $\Delta G_m(\phi)$ is the Gibbs energy of formation of the compound and X_i is the mole fraction.

2.3.1.3 Solution phases

Regular and sub-regular solution model

For regular solutions the Gibbs energy is given by

$$G_m = \sum_i x_i G_i^o + RT \sum_i x_i \ln x_i + \sum_i \sum_{j>i} x_i x_j \sum_v {}^v L_{ij} (x_i - x_j)^v \qquad (2.22)$$

where, the first term on the right hand side is the Gibbs energy of the element i, the second term is ideal Gibbs energy of mixing and the third term is the excess Gibbs energy of mixing in which ${}^v L_{ij}$ is a binary interaction parameter. This term is known as the Redlich-Kister expansion. Depending on $v=0$ or 1 the excess Gibbs energy term becomes regular or sub-regular. A ternary interaction parameter may also be added to account for the higher-order interactions.

Sublattice model

For a three sublattice phase $(A,B)_1(C,D)_1(E)_1$ the Gibbs energy is given as

$$\begin{aligned}
G_m &= y_A^1 y_C^2 G_{A:C:E}^0 + y_B^1 y_C^2 G_{B:C:E}^0 + y_A^1 y_D^2 G_{A:D:E}^0 + y_B^1 y_D^2 G_{B:D:E}^0 \\
&+ RT((y_A^1 \ln y_A^1 + y_B^1 \ln y_B^1) + (y_C^1 \ln y_C^1 + y_D^1 \ln y_D^1)) \\
&+ y_A^1 y_B^1 y_C^2 (\sum_v {}^v L_{A,B:C:E} (y_A^1 - y_B^1)^v) \\
&+ y_A^1 y_B^1 y_D^2 (\sum_v {}^v L_{A,B:D:E} (y_A^1 - y_B^1)^v) \qquad (2.23) \\
&+ y_A^1 y_C^2 y_D^2 (\sum_v {}^v L_{A:C,D:E} (y_C^2 - y_D^2)^v) \\
&+ y_B^1 y_C^2 y_D^2 (\sum_v {}^v L_{B:C,D:E} (y_C^2 - y_D^2)^v)
\end{aligned}$$

where
y_A^1, is the site fraction of component A (subscript) on sublattice 1(superscript), and

$G_{A:C:E}^0$, is the Gibbs energy of the compound $A_1C_1E_1$ when all of the sites on sublattice one and sublattice two are filled with A and C, respectively.

${}^v L_{A,B:C:E}$, denote the regular solution parameter for mixing on the sublattice 1 when the second sublattice is fully occupied by C. $A_1C_1E_1$ is called the end-member. Those end-members may be real or hypothetical. If the end-members are hypothetical then the estimation of Gibbs energies of such compounds needs a physical basis.

Associated solution model

In liquid phases described by this model it is assumed that associate is formed from the constituent elements of the system. In the liquid phase of a binary system A-B e.g. if an associate of the formula A_iB_j is formed, then the liquid phase is assumed to contain free A, B and A_iB_j. The mole fractions of A, B and A_iB_j, in a binary alloy containing 1 mole of A and B atoms are then given by the formula

$$X_A = n_A + i.n_{A_iB_j} \tag{2.24}$$

$$X_B = n_B + j.n_{A_iB_j} \tag{2.25}$$

$$\text{and} \qquad X_{A_iB_j} = n_{A_iB_j} \tag{2.26}$$

Then the excess Gibbs energy of mixing is then given by the general formula

$$G^{xs} = G^{ass} + G^{reg} \tag{2.27}$$

$$G^{ass} = n_{A_iB_j} G^0_{A_iB_j} \tag{2.28}$$

$$G^{reg} = G^{reg}_{A,B} \frac{n_A n_B}{n} + G^{reg}_{A,A_iB_j} \frac{n_A n_{A_iB_j}}{n} + G^{reg}_{B,A_iB_j} \frac{n_B n_{A_iB_j}}{n} \tag{2.29}$$

The configurational entropy is given by

$$S^{conf}_{mix} = -R(n_A \ln x_A + n_B \ln x_B + n_{A_iB_j} \ln x_{A_iB_j}) \tag{2.30}$$

Gas phase

For the gas phases the ideal gas solution model is considered. The Gibbs energy of an ideal gaseous mixture of various constituent species is given by

$$G = \sum_{i \geq 1} X_i G_i^{gas} + RT \sum_{i \geq 1} (X_i \ln X_i) \tag{2.31}$$

$$\text{and} \quad G_i^{gas}(P) = {}^0G_i^{gas} + RT \ln(P/P_0) \tag{2.32}$$

2.3.2 Calculations and Optimisation

Thermodynamic modelling of a phase begins with choosing a correct model based on the type of phase and on crystallographic data. The experimental data includes experimental phase diagram data like phase relations, composition of the phases, various invariant reactions etc., and thermodynamic data. When thermodynamic data of the same kind, measured by different researchers are available in literature and if the published data is not consistent with each other, it is necessary to critically evaluate them. In fact, one of the important objectives of the

CALPHAD is to couple computational methods with all the available thermo-chemical data and thus providing a self-consistent description of all the thermodynamic information.

A general rule for selection of adjustable parameters is that only those coefficients that are determined by the experimental values should be adjusted [36]. The calculation of the model parameters using the experimental thermodynamic data is done within the PARROT module of the Thermo-Calc software [37].

3.0 Experimental Procedures

3.1. Sample Preparation

3.1.1 Electrolytes

3.1.1.1 Preparation of LSGM

Powders of LSGM ($La_{0.8}Sr_{0.2}Ga_{0.83}Mg_{0.17}O_{2.815}$), are prepared by the mixed oxide route. La_2O_3, Ga_2O_3, $SrCO_3$ and MgO are taken as the starting materials. MgO is calcined at 1000°C for 6 h before mixing the starting materials in ball mill for 12 h. Then the mixture is calcined twice at 1000°C with intermediate ball milling step. The calcined powder is compacted in a cold isostatic press. The compacts achieved are annealed twice at 1500°C for 6 h with intermediate grinding and ball milling step. Otherwise single annealing step at 1500 °C for 10 h is also enough to produce the single phase LSGM measured by XRD. But SEM examination of the produced LSGM samples shows a very little quantity of $SrLaGa_3O_7$ impurity (<3vol %).

3.1.1.2 Preparation of CGO

CGO ($Ce_{0.8}Gd_{0.2}O_{1.9}$) powder is also prepared by mixed oxide route. The starting powders CeO_2 and Gd_2O_3 are mixed in a ball mill and calcined twice at 1350°C for 20 h with intermediate ball milling. The calcined powder is then compacted in a cold isostatic press at a pressure of 650 MPa. The obtained compacts are then annealed at 1585 °C for 15 h [38] and subsequently ground to powder.

3.1.1.3 Preparation of YSZ

YSZ (ZrO_2+ 8 mol% Y_2O_3) powder is also prepared by mixed oxide route. The starting powder are mixed in a ball mill, compacted and then annealed at 1600°C for 15 h. A single phase YSZ is obtained after annealing.

3.1.2 Ni-Cermets

3.1.2.1 Preparation of Ni-LSGM cermets

NiO-LSGM compacts were made by cold isostatic pressing of the ball milled powder mixture of NiO (50 wt %) and LSGM. The compacts were subsequently sintered in air at three different temperatures 1200, 1300 and 1350°C. Sintering of the compacts was also done in argon and nitrogen atmospheres. The NiO-LSGM pellets were sintered in air and then

reduced in hydrogen atmosphere for 2 h. The reduction was carried out at 750°C which is the operating temperature for IT-SOFCs and also at a higher temperature of 1000°C.

The nickel cermet anode prepared was then exposed to a gas mixture of H_2 and H_2S (1 vol%) at 500 or 750 °C for 3 h. Beside the cermet samples, LSGM without NiO was produced and exposed to the gas mixture to understand the reactivity of the electrolyte material to sulphur.

3.1.2.2 Preparation of Ni-CGO cermets

NiO-CGO compacts were prepared by wet mixing of powders of NiO and CGO in a ratio of 65:35 by weight percent. Wet mixing of the powders in ethanol was performed for 20 h in a ball with subsequent drying. NiO-CGO samples were prepared by cold isostatic pressing of such powder mixture followed by sintering at 1350°C for 2 h.

After sintering the obtained NiO-CGO samples were reduced in H_2 atmosphere for 2 h to produce Ni-CGO cermets. Ni-CGO cermets were then exposed to H_2+H_2S (1vol%) gas mixture at two different temperatures 500°C and 750°C for 3 h. CGO pellets alone were also exposed to H_2+H_2S (1vol%) gas mixture at two different temperatures 500°C and 750°C but for 12 h.

3.1.2.3 Preparation of Ni-YSZ cermets

NiO and YSZ powder were mixed in a proportion of 56 wt% and 44 wt% respectively, in a ball mill. Mixing was performed in a ball mill using ethanol. Subsequently the powder was dried before NiO-YSZ compacts were prepared from it by cold isostatic pressing. These compacts were then sintered at 1400°C for 2 h followed by reduction in hydrogen at 1000°C for 2 h. The Ni-YSZ cermets obtained after reduction were then exposed to H_2+H_2S (1 vol%) gas mixture.

3.1.3 Photolithographic preparation of Ni pattern electrodes

3.1.3.1 Preparation of the mask

A mask with a mesh size of 70 μm X 70 μm was prepared for patterning. The triple phase boundary length of 1.43 m/cm^2 is obtained from the design. The mask is used to selectively expose the applied photoresist to UV light. The Ni-pattern obtained by this mask can be seen in the Figure 3.1

Figure 3.1 Ni patterns made by photolithography (the small squares are the surface of the electrolyte where there is no Ni and their size is 70 μm x 70 μm)

3.1.3.2 Ni-patterns by photolithography

The ceramic samples of YSZ, LSGM and CGO of ~11.5 mm diameter and 1.4 mm thickness were fine polished with ¼ diamond paste. YSZ single crystals were of 10x10x1 mm^3 size. For the preparation of Ni patterns, firstly photoresist was applied onto the clean surface of the single crystals and subjected to prebaking. Subsequently with the help of the mask the prebaked photoresist over the sample surface was selectively exposed to the UV light, followed by removal of those portions by the developer. Then the so prepared sample surface was cleaned by the Reactive Ion Etching (RIE) to remove any impurities from those portions of sample surface from where the photoresist was selectively removed. Nickel was deposited onto the sample by two different techniques, physical vapour deposition and magnetron sputtering. Ni patterns on polycrystalline samples of YSZ and LSGM were prepared by vapour deposition. In the case of YSZ single crystals, Ni patterns were made by sputtering. Vapour deposition of Ni was done by an electron-gun with 10 KV and 100-125 mA. The deposition rate under these conditions was 0.8 °A/sec.

Figure 3.2 shows the Ni-patterned YSZ sample. The thickness of the Ni patterns is 200nm. The stability of the Ni patterns at high temperatures was studied. It is found that the patterns are stable at temperatures at and below 823 K. Figure 3.3 shows a Ni-patterned YSZ sample which was measured at 1073 K. It can be seen from the figure that the Ni patterns were disintegrated and formed islands at this temperature. In order to have the same length of the triple phase boundary during the entire course of the measurements, EIS measurements were performed in the temperature range 823 – 673 K.
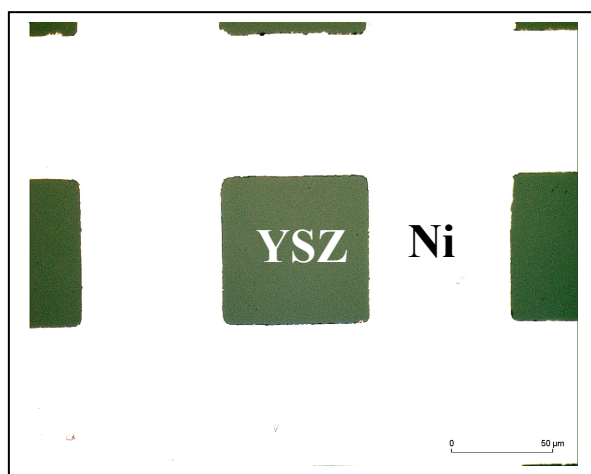
Figure 3.2 Ni-patterned YSZ<111> single crystal sample (bright Ni patterns and dark YSZ areas can be seen. The width of the pattern is 70 μm)
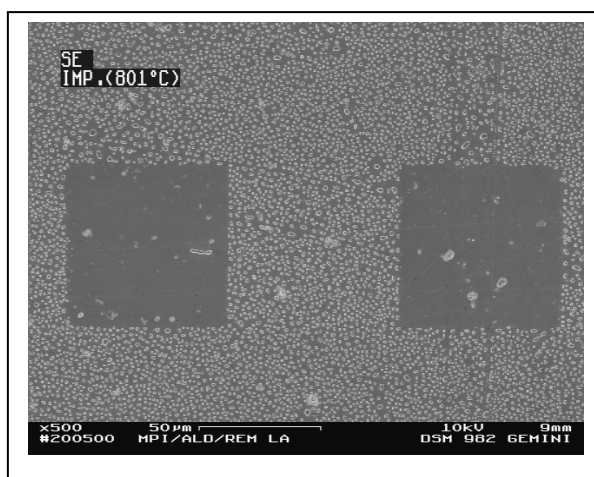
Figure 3.3 Ni-patterned YSZ sample which was measured at 1073 K

3.2 Sample characterisation

3.2.1 X-ray diffraction (XRD)

The identification of crystalline phases was performed by XRD using a Siemens diffractometer (D5000 Kristalloflex) with Ni-filter and Cu K_α radiation (λ=1.5405 Å). The X-ray tube was operated at 40 kV and 20 mA. The XRD patterns were measured in a 2θ range of 10-100° using a position sensitive detector with 8° acceptance angle. The usual scan rate was 2°/min. A slower scan of 0.2°/min was also used to identify very small fractions of impurity phases. The data analysis was performed by using EVA software(EVA 5.0).

For the lattice parameter determination of the crystalline phases in NiO-LSGM samples, X-ray spectra were recorded by using STOE diffractometer with bent Ge monochromator and Mo Kα radiation (λ = 0.70930 Å). The refinement of the XRD patterns to determine the crystal structure and cell parameters of all the phases was done by the public domain software "FullProf" [39].

3.2.2 Scanning electron microscopy (SEM)

Scanning Electron Microscopic investigation is carried out by field emission SEM (model DSM 982 Gemini) with thermal Schottky-field emitter for high resolution and low-KV operation. Compositional analysis is obtained from the integrated EDX (INCA-ENERGY from Oxford instrument) with a new highly resolving Germanium detector.

3.2.3 Transmission electron microscopy (TEM)

Study of the NiO-LSGM interface was carried out in VG HB 501 UX scanning transmission electron microscope (STEM) with 100 keV accelerating voltage. The spot size was around 0.6nm. For exact quantification of LSGM(Ni) in the NiO–LSGM sample, an LSGM standard of known composition (LSGM20-17) was used. Cliff-Lorimer factors (k_{AB}) for various elements [40] were determined by using the LSGM standard. The quantitative energy dispersive X-ray (EDX) analysis in the VG microscope was carried out by using the Cliff-Lorimer equation.

$$C_A/C_B = k_{AB} (I_A/I_B),$$

where C_A and C_B are the weight fractions , I_A and I_B are the characteristic X-ray intensities of the elements A and B, respectively, and k_{AB} is a constant at a given operating voltage [40]. Absorption correction was done by plotting the measured k_{AB} factors as a function of the measured relative thickness of the sample t/λ, where λ is the inelastic mean free path. The

relative thickness is taken as a logarithm of the ratio of energy loss intensity integrated over a wide range of energy and the zero loss peak intensity.

$$t/\lambda = \ln (I_t/I_0) \tag{3.1}$$

k_{AB} is linearly related to the relative thickness through the expression

$$\log k_{AB} = \log (k_{AB})_0 + \Delta_{AB} t \tag{3.2}$$

where $\Delta_{AB} = 1/t (\log CF)$

and CF is the correction factor for absorption

Extrapolation to t = 0 zero gives $(k_{AB})_0$ which is the *k*-factor at zero foil thickness. These obtained k_{AB} factors were then used to quantify the composition of the LSGM(Ni) sample under study.

3.2.4 Auger spectroscopy

Ni-patterned LSGM specimens were annealed in reducing atmosphere (in hydrogen gas) at different temperatures for 24-30 h. Auger examination of these samples was done to study the interfacial reactivity as a function of temperature. It has to be noted here that the design and thickness (500 nm) of the Ni patterns used for Auger studies are different from the samples used for electrochemical studies.

A field emission Auger microprobe (JAMP-7830F of JEOL) with 3 keV primary beam energy was used for the examination. A tilt angle of 54° was employed to avoid the charging effects with the examination of LSGM surface. The depth profile is recorded from the surface of Ni into LSGM across the interface. The sputtering was done by Ar^+ ions of energy of 1 keV.

Quantitative analysis of the Auger spectrum was performed by measuring the relative Auger intensities of the elements present in the specimen. For accurate quantitative analysis a standards of known composition similar to the specimen under study can be used. In this way the chemical effects, back scatter factors and electron depths are same. The Auger spectrum of the as prepared Ni-LSGM sample was also used as a standard to determine the sensitivity factors of all the elements in LSGM. These sensitivity factors were used for quantifying the composition of the treated Ni-LSGM samples.

3.2.5 Electrochemical impedance spectroscopy

The impedance measurements of the symmetrical cells were carried out at various temperatures and H_2+H_2O gas compositions.

An alternating ac amplitude of v(ω,t) is applied and the resulting current i(ω,t) is measured [41].

21

$$V(\omega,t) = V_0 \, e^{-i\omega t} \tag{3.3}$$

$$I(\omega,t) = I_0 \, e^{-i(\omega t+\theta)} \tag{3.4}$$

where t is the time, ω is the angular frequency, V_0 and I_0 are amplitudes, θ is the phase difference between voltage and current

Then the impedance is given by

$$Z(\omega) = \frac{V(\omega,t)}{I(\omega,t)} = \frac{V_0}{I_0} e^{i\theta} \tag{3.5}$$

From Euler's equation

$$e^{i\theta} = \cos(\theta) + i\sin(\theta) \tag{3.6}$$

Now the impedance $Z(\omega) = Z'(\omega) + i\, Z''(\omega)$ is such a vector quantity and may be plotted in the plane with either rectangular or polar coordinates. The two rectangular coordinate values are

$$\text{Real}(Z) = Z'(\omega) = |Z| \cos(\theta) \tag{3.7}$$

$$\text{and} \quad \text{Imag}(Z) = Z''(\omega) = |Z| \sin(\theta) \tag{3.8}$$

where

$$\theta = \tan^{-1}(Z''/Z') \tag{3.9}$$

$$|Z| = [(Z')^2 + (Z'')^2]^{1/2} \tag{3.10}$$

Impedance of an Re(RpCp) circuit [42]:
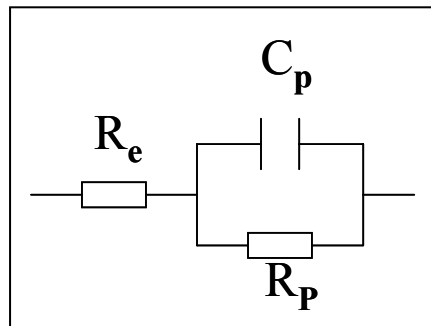
Figure 3.4 the Re(RpCp) circuit

The impedance of the Re(RpCp) circuit is given by

$$Z = Z_p + R_e = \frac{1}{1/R_P + i\omega C_P} + R_e \tag{3.11}$$

22

which can be written as

$$Z = R_e + \frac{R_P - i\omega R_P^2 C_P}{1 + \omega^2 R_P^2 C_P^2} \tag{3.12}$$

from equation (3.12) it is clear that

$$\text{Real}(Z) = R_e + \frac{R_P}{1 + \omega^2 R_P^2 C_P^2} \tag{3.13}$$

and $\quad |\text{Imag}(Z)| = \dfrac{\omega R_P^2 C_P}{1 + \omega^2 R_P^2 C_P^2} \tag{3.14}$

from the above equations, when

$$\omega \to 0: \quad \text{Real}(Z) \to R_e + R_P; \quad \text{Imag}(Z) \to 0$$
$$\omega \to \infty: \quad \text{Real}(Z) \to R_e; \quad \text{Imag}(Z) \to 0$$
$$\omega = \frac{1}{R_P C_P}: \text{Real}(Z) \to R_e + \frac{R_P}{2}; \quad \text{Imag}(Z) \to \frac{R_P}{2}$$

Nyquist and Bode plots for the circuit given in the figure 3.4 are shown in the figures 3.5 and figure 3.6, respectively.
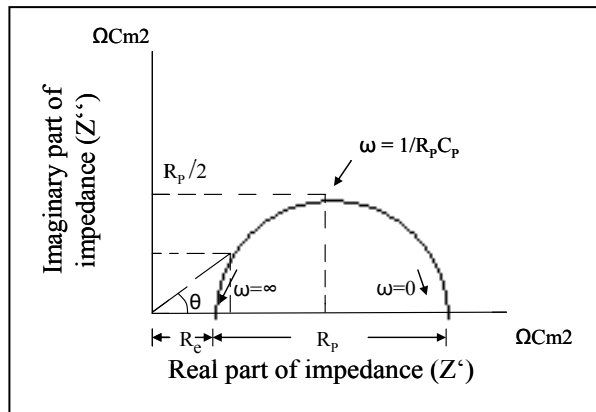
Figure 3.5 Nyquist plot for the equivalent circuit shown in the figure 3.4

23
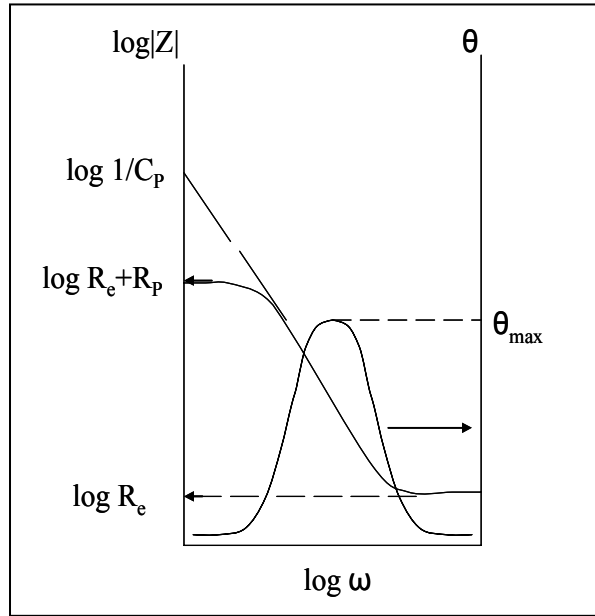
Figure 3.6 Bode plot for the equivalent circuit as shown in the Figure 3.4

In the case of constant phase element (CPE) instead of an Ideal capacitance:

The impedance of a CPE is given by

$$Z = \frac{1}{(i\omega)^n Q_P} \qquad (3.15)$$

when n=1, the equation becomes same as that of a capacitor, i.e., $Q_P = C_p$

So for a CPE (Q_p) instead of a capacitor (C_p) in the circuit as given in the figure 3.4, the impedance is given by

$$Z = Z_P + R_e = \frac{1}{1/R_P + (i\omega)^n Q_P} + R_e \qquad (3.16)$$

However the CPE, Q is given in units of F by normalisation to the Ideal capacitance. This is done in the case of ZAHNER impedance analyzer. The equation for the impedance of constant phase element after normalisation with "ω_0" is

$$Z = Z_P + R_e = \frac{1}{1/R_P + (i\omega)^n Q_P \omega_0^{1-n}} + R_e \qquad (3.17)$$

The experimental parameters are listed in Table 3.1. The schematic of the experimental set-up is shown in the figure 3.7. Impedance measurements were carried out in the gaseous atmosphere of $H_2 + H_2O$ with and without 5 ppm of H_2S. Hydrogen gas was bubbled through a

water bottle which was maintained at a certain temperature to get the required composition of H_2+H_2O gas mixture in the furnace. For measurements with 5 ppm of H_2S in H_2+H_2O (3 vol%) the gases H_2+H_2O (6 vol%) and H_2+H_2S (10 ppm) are mixed in equal proportions. The total flow rate is always maintained at the same level. To study the reversal of poisonous effect after the measurements in 5 ppm of H_2S in H_2+H_2O (3vol%), the H_2+H_2S (10 ppm) supply was stopped and only the H_2+H_2O (6 vol%) gas was allowed. So the reversal is recorded in H_2+H_2O (6 vol%) gas. In the study of the poisonous effect of 5 ppm of H_2S at other partial pressures of H_2O similar procedure was followed.
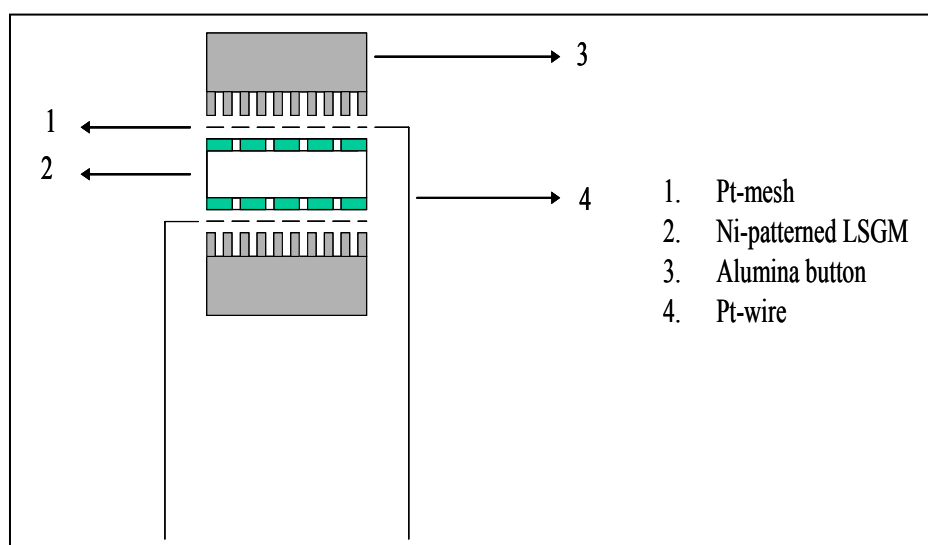
Figure 3.7 Schematic of the symmetrical cell set-up

Table 3.1 Experimental conditions for EIS measurements

Parameter	Value
Temperature	400-550°C
H_2+H_2O Gas flow rate	50 mL/min
Partial pressure of H_2O (P(H_2O))	0.01-0.4 atm
Frequency range	500 KHz – 5mHz
AC-Amplitude	10 mV

The impedance measurements and the equivalent circuit fitting were carried out with ZAHNER, IM6 impedance analyser. The equivalent circuit used for the analysis of the measured impedance data is shown in the Figure 3.8.
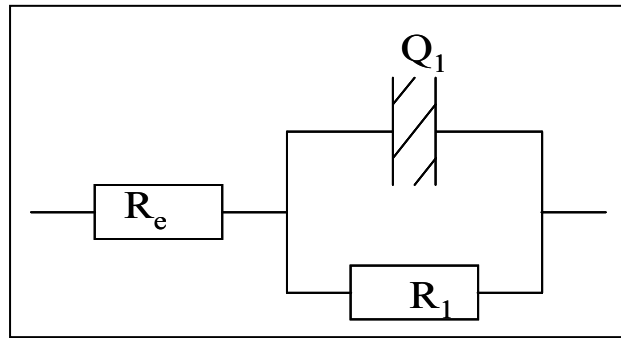
Figure 3.8 The equivalent circuit used for the analysis of the impedance arc.(R_e – electrolyte resistance and the resistance of the leads, R_1 – Total electrode resistance and Q_1 – constant phase element)

4.0 Results

4.1. Microstructural stability in H_2+H_2S (1 vol%) atmosphere

4.1.1. Ni-YSZ cermet anodes

Figure 4.1 shows the photograph of a Ni-YSZ cermet anode after exposing to H_2+H_2S (1 vol%) gas mixture at 750 °C for 3 h. Tiny spherical particles are seen on the surface of the cermet sample.

Figure 4.1 Nickel cermet after exposure to $H_2 + H_2S$ (1 vol%) at 750°C for 3 h.

The chemical composition of the spheres corresponds exactly to the eutectic composition (21 wt% S and 79 wt% Ni) between Ni and Ni_3S_2 [43].
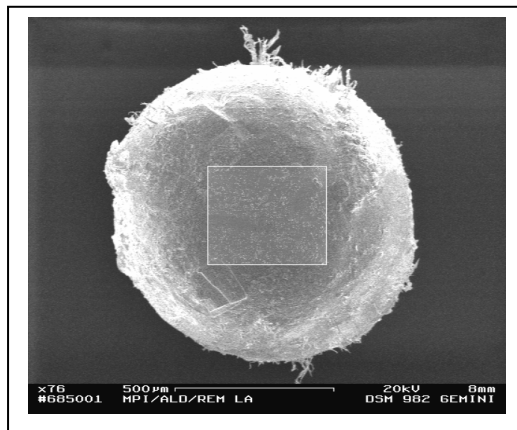
Figure 4.2. SEM micrograph of the eutectic spheres formed over the surface of the Ni-YSZ cermet during its exposure to H_2+H_2S (1 vol%) gas at 750 °C for 3 h.
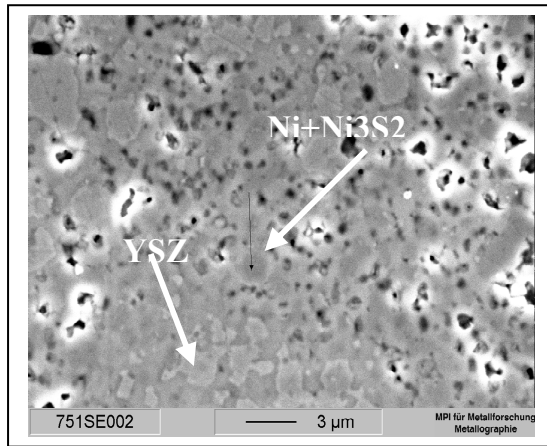
Figure 4.3 SEM micrograph of Ni-YSZ cermet after exposure to H_2 + H_2S (1 vol%) at 750 °C for 3 h.

Figure 4.2 shows the micrograph of one of such spheres of eutectic composition. The SEM micrograph of the cermet is shown in Figure 4.3. The dark phase is a mixture of nickel and nickel sulphide (Ni + Ni_3S_2), while the bright phase is YSZ. Figure 4.4 shows the XRD pattern of the specimen and of the spheres which show only Ni and Ni_3S_2 peaks.
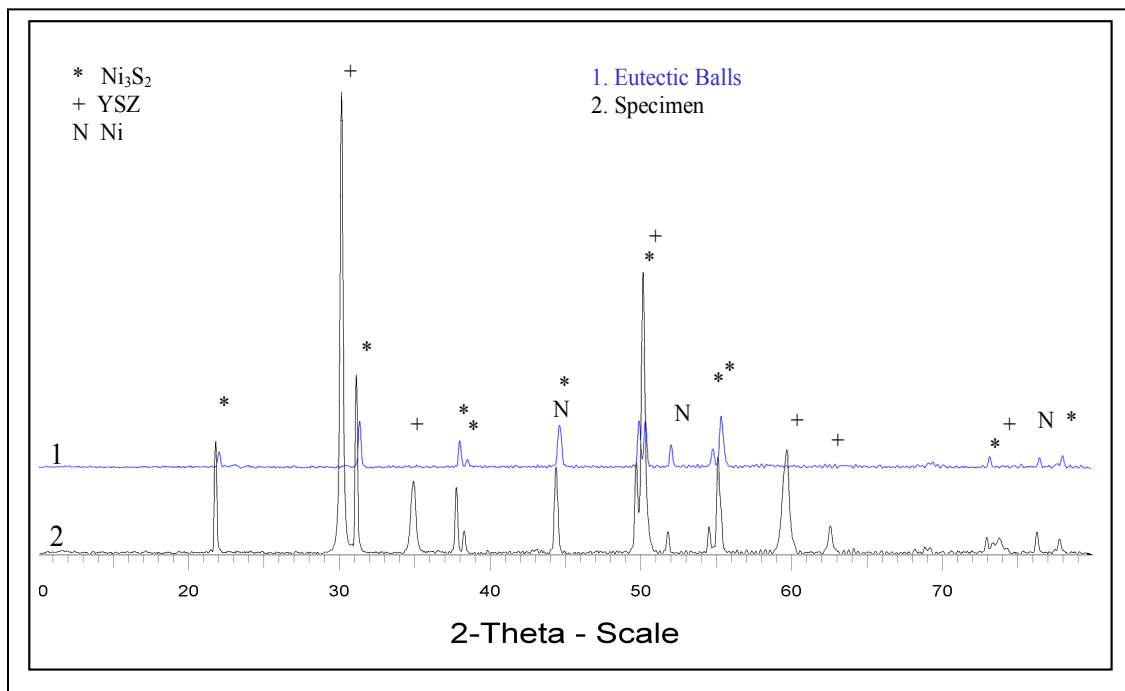
Figure 4.4. XRD patterns of the spherical particles formed over the bulk specimen surface and of the specimen after exposure to H_2+H_2S (1 vol%) at 750 °C for 3 h.
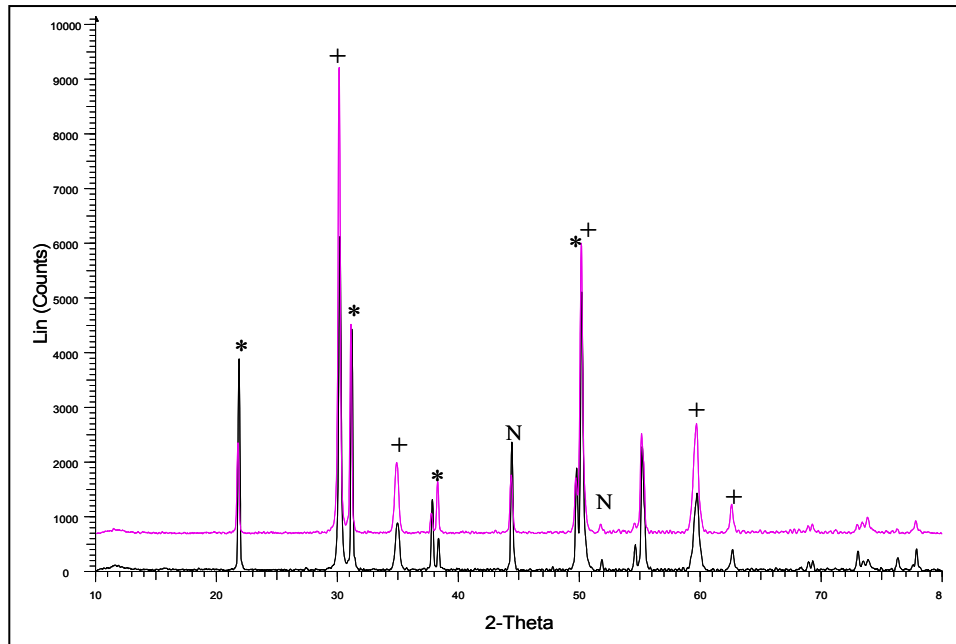
Figure 4.5 XRD patterns of the Ni-YSZ samples exposed to H_2+H_2S (1 vol%) at two different temperatures 500 °C and 600 °C for 3 h (+ – YSZ, * – Ni_3S_2, N – Ni).

From figure 4.5 it is evident that Ni in the cermet reacts with H_2S to form Ni_3S_2 even at 500°C. A thin film of Ni and Ni_3S_2 is found on the surface of the cermet after exposure.

Figure 4.6 shows the microstructure of Ni-YSZ cermet after exposure to H_2+H_2S (1 vol%) at 600°C for 3 h. The compositional analysis by SEM/EDX analysis showed only Ni_3S_2 and YSZ in the exposed sample. The latter is not reactive to the sulphur in the gas.
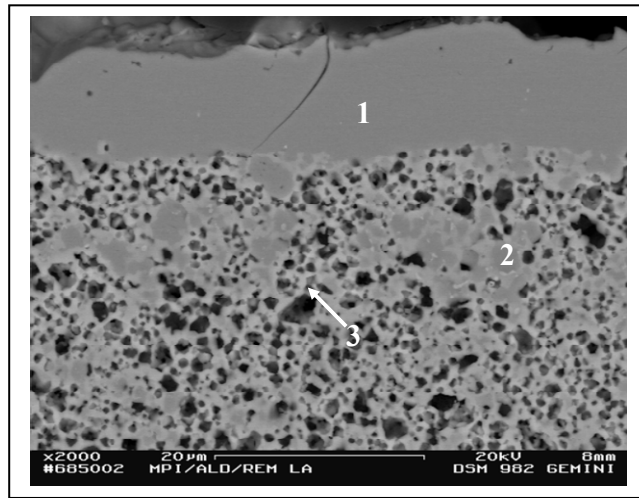
Figure 4.6 SEM micrograph of the Ni-YSZ cermet after exposure to H_2+H_2S (1 vol%) at 600°C for 3 h (EDX from point 1- corresponds to Ni_3S_2, point 2- corresponds to Ni_3S_2, point 3-YSZ. see Table 4.1)

Table 4.1 EDX data of the phases as shown in the figure 4.6 (all elements in at%)

	Zr	Y	O	S	Ni
Bright phase(3)	21.34	3.54	63.42	4.53	7.17
Grey phase(2)	0.81	0.29	7.46	38.66	52.78
Grey phase-film(1)	0.15	0.01	5.15	40.35	54.35

4.1.2 Ni-CGO cermet anodes

Figure 4.7 depicts the microstructure of as prepared Ni-CGO samples. There is no interaction between Ni and CGO. Figure 4.8 shows the X-ray diffraction pattern of the Ni-CGO cermet after being exposed to $H_2 + H_2S$ (1 vol%) for 3 h at 500 °C and 750 °C, respectively. The diffraction patterns show the formation of Ce_2O_2S in the sample exposed at 750 °C, whereas no Ce_2O_2S peaks are visible in the sample exposed at 500 °C. Ni_3S_2 can be seen in both the XRD patterns of the cermets exposed at 500°C and 750°C.
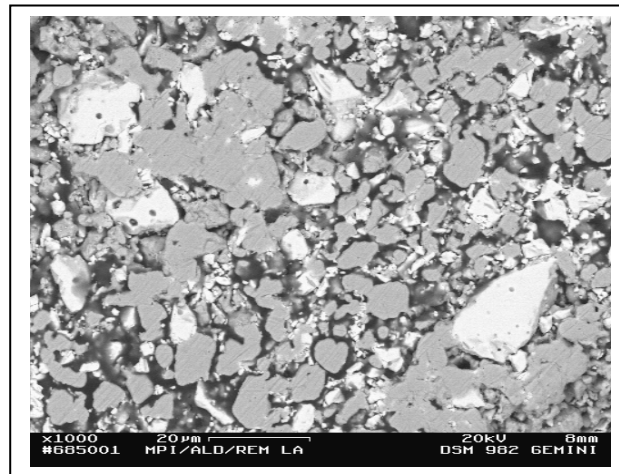
Figure 4.7 SEM micrograph of the as-prepared Ni-CGO cermet (the bright phase is CGO and the grey phase is Ni)
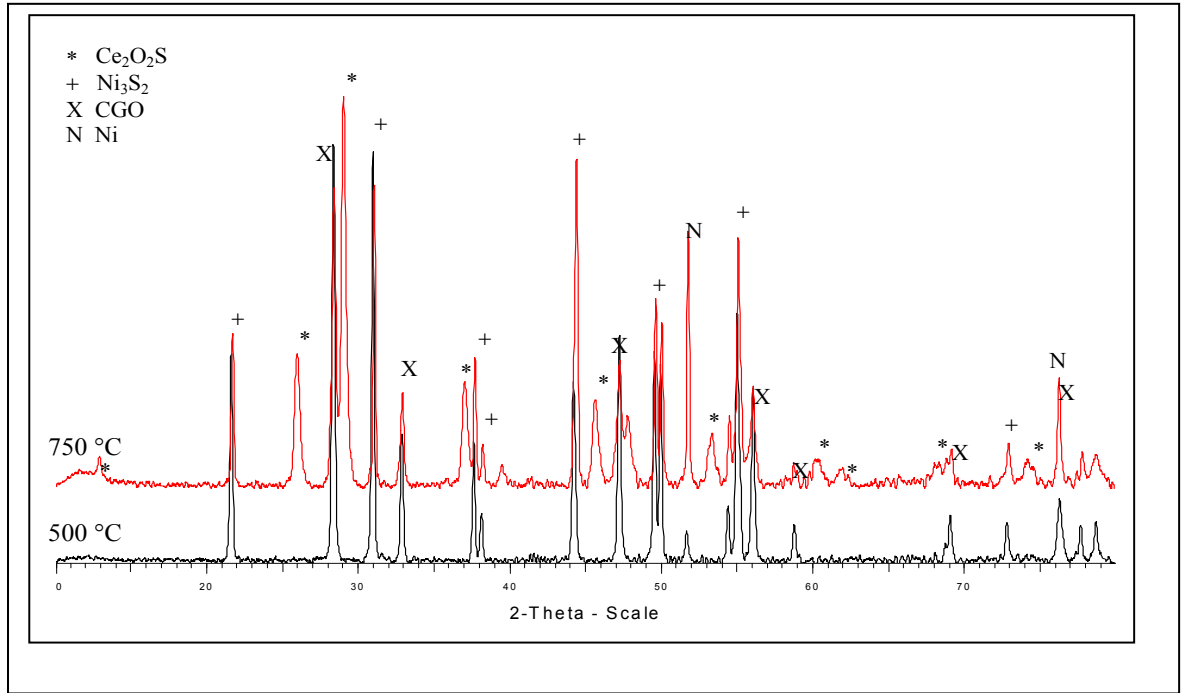
Figure 4.8 XRD patterns of Ni-CGO cermets exposed to H_2+H_2S (1 vol%) gas for 3 h at two different temperatures 500°C and 750°C.

Figure 4.9a and 4.9b show the microstructure of Ni-CGO cermets after being exposed to $H_2 + H_2S$ (1 vol%) for 3 h at 500 °C and 750 °C, respectively.

Figure 4.9(a) Ni-CGO cermet after exposure to H_2+H_2S (1 vol%) gas at 500°C for 3 h (the bright phase marked by 1 is CGO, grey region marked by 2 is Ni and the dark region marked by 3 is Ni_3S_2)

Figure 4.9a illustrates the microstructure of Ni-CGO cermet treated at 500 °C. The sample shows some porosity unlike the sample treated at 750 °C (figure 4.9b). The SEM/EDX analysis of the dark phase reveals around 32.57 at% S and 66.61 at% Ni. EDX obtained from the dark phase (marked by 3 on figure Figure 4.9(a)) may contain some Ni from the adjacent grey phase. The grey phase is pure Ni and the bright phase is CGO. The CGO phase does not show any variation of composition within the grain.

The microstructure of the Ni-CGO cermet exposed to H_2+H_2S (1 vol%) gas at 750°C (in the Figure 4.9b) shows the continuous, matrix-like dark phase. The composition obtained from EDX of the dark phase (point 3 in the figure) shows around 59.77 at % Ni, 35.29 at% S and 4.49 at% O. This is most likely the eutectic mixture of Ni and Ni_3S_2. The eutectic melting might have resulted in the continuous matrix of the dark phase. The grey phase (point marked by 2 in the figure) is Ni and the bright phase (marked by 1 in the figure) is CGO.

A closer view of the CGO grain in the sample exposed at 750°C is shown in the Figure 4.10. Point 1 marked on the grain gives the composition of CGO. However the EDX spectrum obtained from the light grey area as shown by point 2 gives a mixture of phases. Analysis of the composition obtained from the point two revealed that it can be a mixture of Ni_3S_2 and $(Ce,Gd)_2O_2S$ phases. This also leads to the understanding that Ce_2O_2S phase detected in XRD may not be pure Ce_2O_2S, but contains some Gd in it.
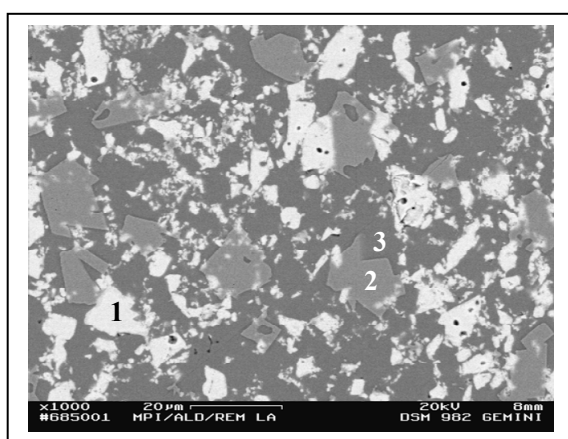
Figure 4.9b Ni-CGO cermet after exposure to H_2+H_2S (1 vol%) gas at 750°C for 3 h (1-CGO, 2-Ni, 3- Ni_3S_2 or Ni+Ni_3S_2)
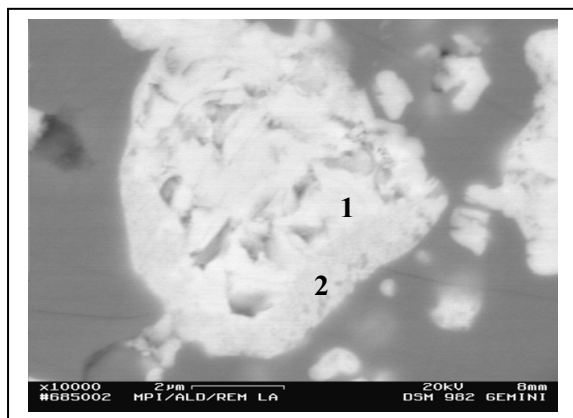
Figure 4.10 CGO particle in Ni-CGO cermet after exposure to H_2+H_2S (1 vol%) gas at 750°C for 3 h (1- CGO grain, 2- rim of the CGO grain. For EDX results see Table 4.2)

Table 4.2 EDX results of the phase at different points as marked in the Figure 4.10 (elements in at%)

	Ce	Gd	O	S	Ni
surface(point marked by 2)	24.79	7.44	26.85	22.06	18.86
Centre(point marked by 1)	28.07	6.87	61.17	1.46	2.42

In order to understand the reactivity of cermet component to sulphur the electrolyte material CGO alone was also exposed to H_2+H_2S (1 vol%) gas mixture at 750°C for 12 h. A Ce_2O_2S-based phase as shown in the figure 4.11, is formed.

Figure 4.12(a) and (b) shows the SEM micrographs of CGO exposed to H_2+H_2S (1 vol%) gas at 750°C for 12 h. In Figure 4.12(a) protruding spheres-like particles with cracks are shown. These grains contain relatively high amounts of sulphur (Table 4.3). The composition of these regions correspond to $(Ce,Gd)_2O_2S$ type compound.

34
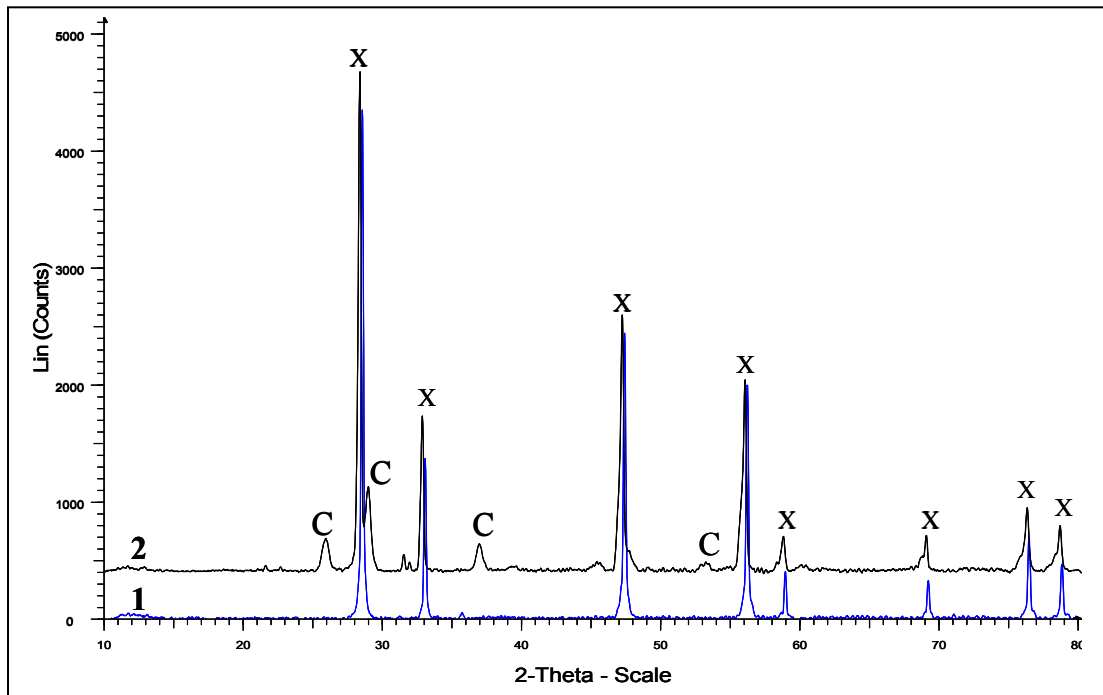
Figure 4.11 CGO before and after exposure to H_2+H_2S (1 vol%) gas at 750°C for 12 h.
(**1**- before exposure and **2**-after exposure. C-Ce_2O_2S and X- CGO)

The other grain as marked in Figure 4.12(b) contains relatively less sulphur (Table 4.3). However it is quite likely that the EDX taken from the spot covers the sulphide and CGO beneath.
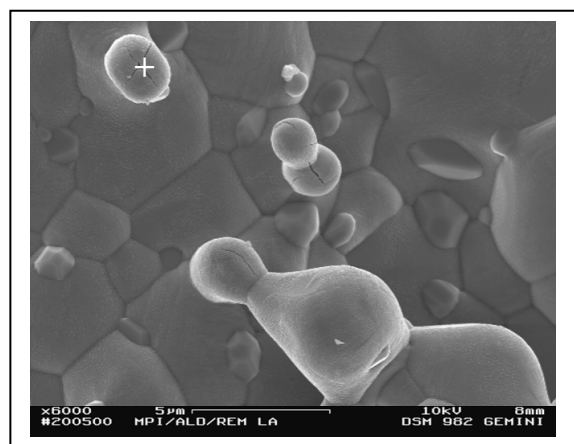
Figure 4.12(a) CGO exposed to H_2+H_2S (1 vol%) gas at 750 °C for 12 h.
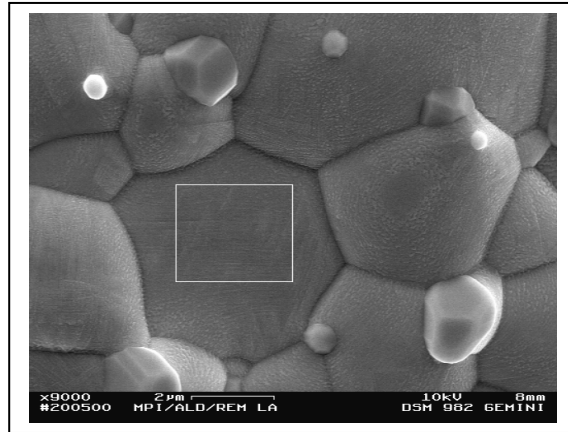
Figure 4.12(b) CGO exposed to H_2+H_2S (1 vol%) gas at 750 °C for 12 h.

Table 4.3 EDX results of the phases shown in Figure 4.12a and b (all elements in at%)

	Ce	Gd	O	S
Particle (marked by +)	34.70	9.80	39.35	15.27
Grain (marked by square)	34.96	12.66	38.38	12.17

4.1.3 Ni-LSGM cermet anodes

4.1.3.1 NiO-LSGM reactivity

4.1.3.1.1 Sintering in air

Figures 4.13 a,b show the microstructure of the LSGM pellets sintered in air at 1500°C for 6 h. In figure 4.13b a small fraction of the impurity phase $SrLaGa_3O_7$ can be seen. Figure 4.14 shows the corresponding XRD pattern. XRD shows only the peaks of LSGM but no lines of any impurity phases such as $SrLaGa_3O_7$ or $SrLaGaO_4$. Since a small quantity of $SrLaGa_3O_7$ can be seen under SEM but not in XRD, this impurity phase can be approximated to be less than 5 vol %.

(a) (b)
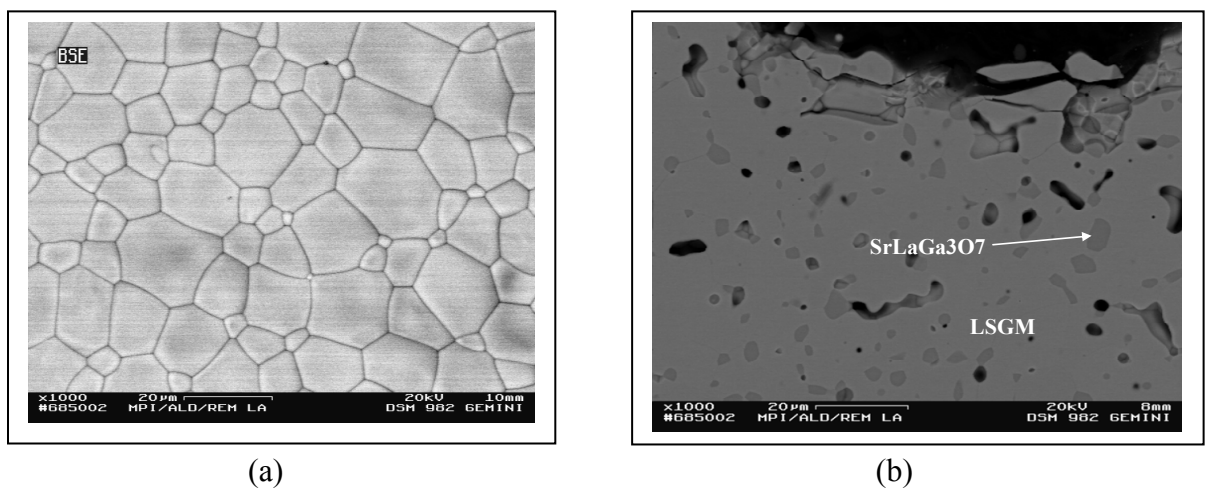
Figure 4.13 a,b SEM image of LSGM
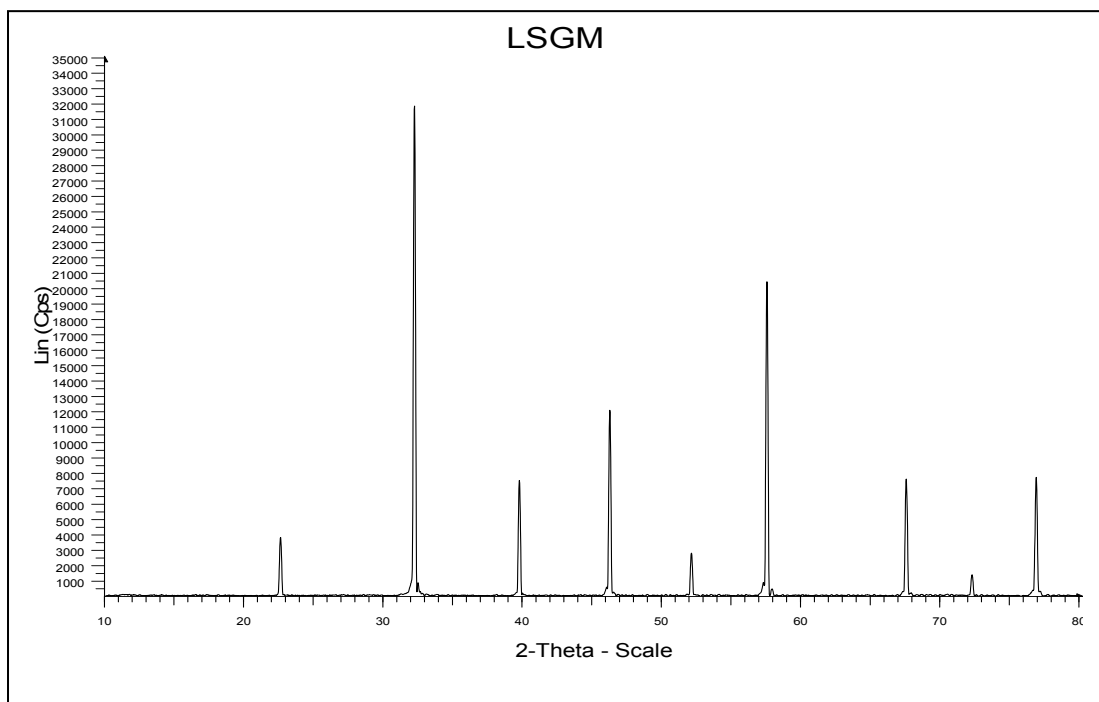
Figure 4.14 X-ray diffraction pattern of single phase LSGM
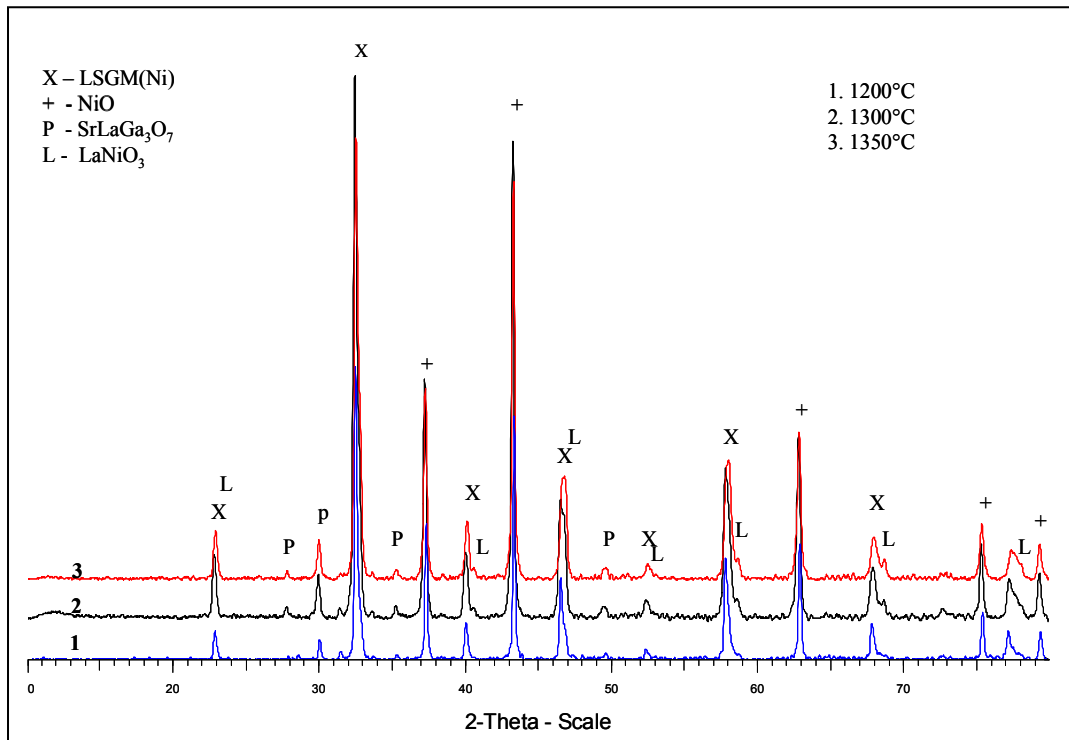
Figure 4.15 XRD of the NiO-LSGM sintered in air at three different temperatures.
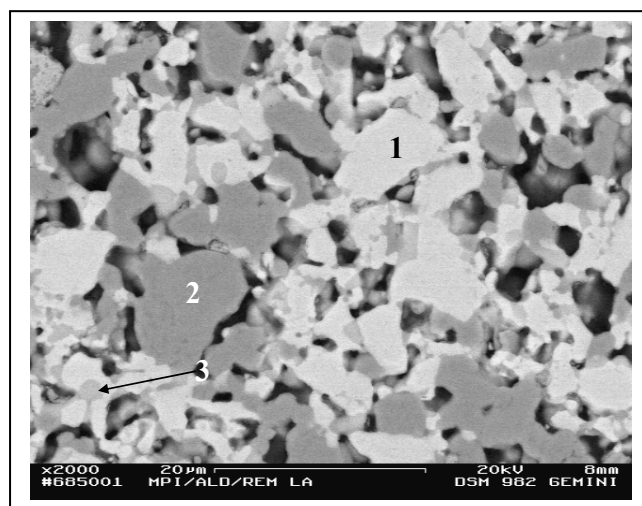
Figure 4.16 SEM micrograph of NiO-LSGM sintered in air at 1300°C(1- LSGM, 2-NiO, 3-SrLaGa$_3$O$_7$)

Figure 4.15 shows the XRD patterns of NiO-LSGM samples sintered in air at three different temperatures 1200, 1300, and 1350°C for 2h. Beside those of LSGM and NiO, the X-ray peaks of LaNiO$_3$-type phase (L- LaNiO$_3$ in Figure 4.15) and SrLa(Ga,Ni)$_3$O$_{7-x}$ (P- SrLaGa$_3$O$_7$

in Figure 4.15) can be seen in the samples sintered at all three temperatures. However, in the sample sintered at 1200 °C the peaks of $LaNiO_3$-type phase (in XRD) are not as evident as in the case of other two temperatures. So, temperatures less than 1200°C are necessary to avoid the formation of $LaNiO_3$-type phase. But even the temperature 1200 °C was not high enough for obtaining a good sintered body.

The SEM micrograph of the NiO-LSGM sample sintered at 1300°C is shown in Figure 4.16. Besides NiO (dark phase) and LSGM (bright phase), $SrLaGa_3O_7$-type impurity phase can also be seen. Its exact composition obtained from EDX corresponds to the formula $Sr_{1-x} La_{1+x}$ $(Ga,Ni)_3O_{7-\delta}$ $(Sr_{0.79}La_{1.0162}(Ga_{0.9396}Ni_{0.1087})_3O_{7-1.0134})$. The EDX result for different phases in Figure 4.16, are given in Table 4.4. The EDX analysis of the LSGM phase showed a Ni content of ~2.2 at%. Ni sits on B–sites in LSGM. The EDX analysis of the NiO phase showed that it does not dissolve any elements from LSGM.

Table 4.4 EDX results of various phases as shown in the figure 4.16

Bright phase (1)		Grey phase (3)		Dark phase (2)	
Element	Atomic%	Element	Atomic%	Element	Atomic%
O	56.62	O	54.49	O	48.51
Mg	1.62	Mg	0.42	Mg	0.08
Ni	2.19	Ni	2.97	Ni	50.90
Ga	18.53	Ga	25.66	Ga	0.39
Sr	3.84	Sr	7.20	Sr	0.03
La	17.19	La	9.25	La	0.09

$Sr_{1-x}La_{1+x}Ga_3O_{7-\delta}$ is a non-stoichiometric phase with x varying from 0 to 0.5 [44]. From the EDX analysis of this phase in the sample sintered at 1300°C, it is evident that the phase contains ~2.97 at % Ni. The $SrLaG_3O_7$ phase (<3 vol%) comes from the LSGM and it appears to increase slightly during the sintering of NiO-LSGM in air at 1300°C.

Figure 4.17 shows the refined XRD pattern of the NiO–LSGM sample sintered in air at 1350 °C for 2 h. The $LaNiO_3$-type phase can be seen from the diffraction pattern. Table 4.5 lists all the phases identified in the XRD pattern, their crystal structures and cell parameters obtained from the refinement. The $LaNiO_3$-type phase formed during sintering was found to be cubic with the cell parameter of 3.8561 Å, whereas pure $LaNiO_3$ is rhombohedral in structure with the cell parameters of a=5.4535 Å and c=13.1369 Å (JCPDF 79-2450). The impurity phases, $SrLaGa_3O_7$ and $SrLaGaO_4$ can also be seen in the table.

Diffusion of Ni into LSGM occurs during sintering at 1350 °C [11]. It is likely that the bulk LSGM contains variable fractions of Ni after sintering. Zhang et al [7] reported a $LaNiO_3$-based compound with a hexagonal structure, identified from the XRD patterns (JCPDF 34-1028). However LSGM in their study was of different composition, $La_{0.9}Sr_{0.1}Ga_{0.8}Mg_{0.2}O_{3-x}$.
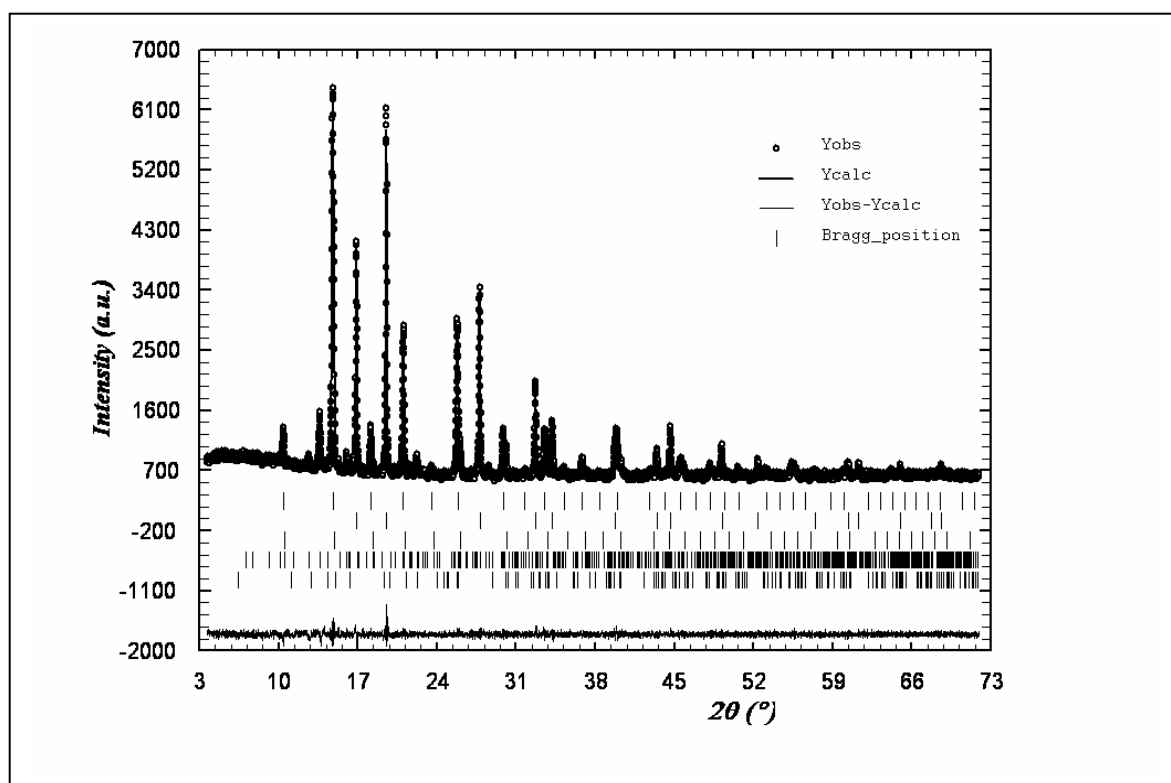
Figure 4.17 Refined XRD pattern of the NiO-LSGM sample after sintering at 1350 °C for 2 h. Open circles (Yobs) corresponds to the observed spectrum, the continuous line (Ycalc) correspond to the calculated spectrum, Yobs-Ycalc shown at the bottom is the difference between the measured and calculated intensities, and the vertical bars in the order of top to bottom indicate the peak positions of LSGM, NiO, $LaNiO_3$, $SrLaG_3O_7$, and $SrLaGaO_4$.(see Table 4.5).

Table 4.5 List of all the phases present and their cell parameters obtained from the XRD pattern in Figure 4.17 (from top to bottom)

Phase	Space group	Lattice parameters (Å)	Unit cell volume ($Å^3$)
LSGM	Pm-3m	a_o = 3.8860	58.6822
NiO	Fm-3m	a_o = 4.1741	72.7249
$LaNiO_3$	Pm-3m	a_o = 3.8561	57.3373
$SrLaGa_3O_7$	P-4 21m	a= b = 8.0361, c = 5.3047	342.5739
$SrLaGaO_4$	I 4/mmm	a = b =3.8428, c = 12.6544	186.8694

40

4.1.3.1.2 Sintering in various atmospheres

The XRD patterns of NiO-LSGM sintered at 1350°C for 2 h in air, argon or nitrogen atmospheres is shown in Figure 4.18. All the three samples show NiO and LSGM phases as they were the starting materials. It is evident from the XRD patterns that the samples sintered in nitrogen and argon show a high proportion of $SrLaGa_3O_7$ and La_2O_3 (LaOOH) and a small fraction of $SrLaGaO_4$. La_2O_3 phase with the JCPDF card number 22-0641, is found to match. The phase $LaNiO_3$ appears to be formed also in the samples sintered in argon and nitrogen atmospheres. These samples which are sintered in inert atmosphere show some metallic Ni. The metallic phase can also be seen under SEM.

From these observations it is evident that the sintering in inert atmosphere lead to the decomposition of LSGM into $SrLaGa_3O_7$, and La_2O_3. Later La_2O_3 reacted with moisture in the atmospheric air to form LaOOH.
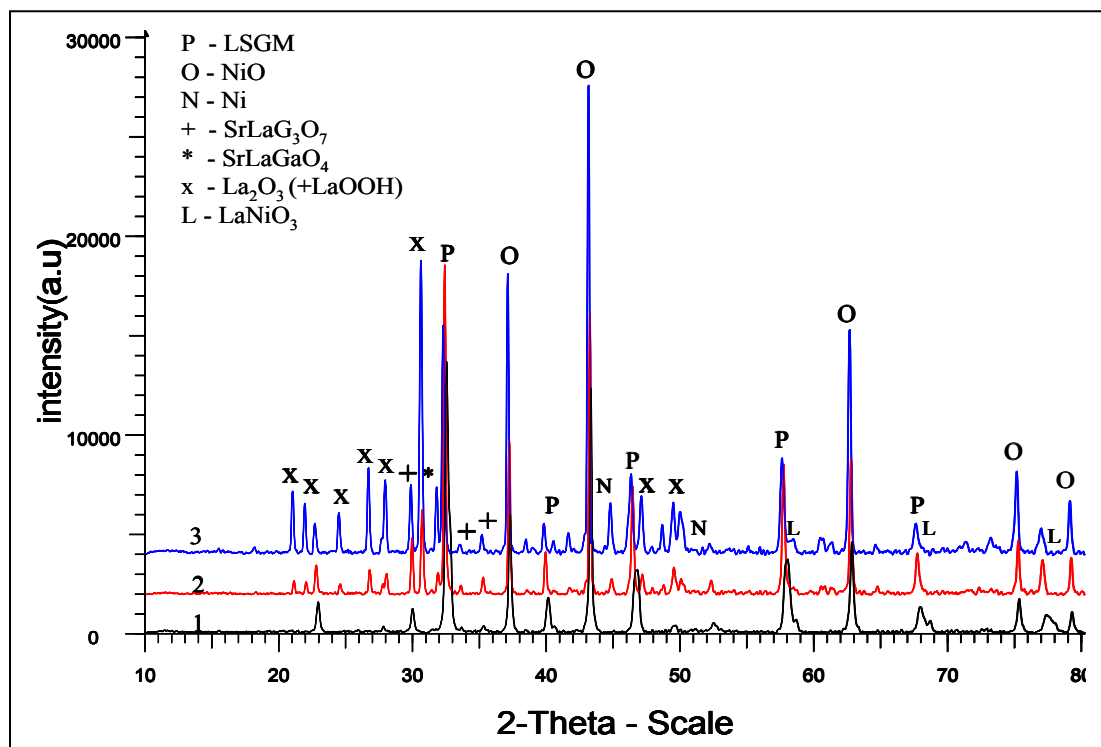
Figure 4.18 XRD patterns of NiO-LSGM sintered at 1350°C in air(1), argon(2) and nitrogen (3).

A comparison of the XRD patterns of the samples sintered in argon and nitrogen reveals that the samples sintered in nitrogen shows relatively high quantities of $SrLaGa_3O_7$ and La_2O_3

phases. This may be because the argon used was less pure than nitrogen and had relatively high oxygen content.

Sintering NiO-LSGM in air is leading to the formation of LaNiO$_3$-type phase as shown above. This observation motivated a detailed study of the NiO-LSGM interface using TEM.

4.1.3.1.3 NiO-LSGM interface

The STEM image of the interface between NiO and LSGM of the sample sintered in air at 1350°C is shown in the Figure 4.19. EDX spectra were recorded with a step of 10 nm along the line as shown in the Figure starting at point 1 in the NiO grain, across the interface to the point 12 in LSGM grain. The points of EDX measurement are marked in the Figure.

Intensities of all the cations (La, Sr, Ga, Mg, and Ni) as obtained from the EDX spectrum are plotted as a function of the distance d as shown in Figure 4.20. From literature it is known that NiO exhibits no solubility for Sr and La. Thus the intensities of all the elements were normalised with respect to the intensity of La starting from point 2 on the left side of the inclined interface into the LSGM(Ni) grain (Figure 4.19). The ratios I_{Ga}/I_{La}, I_{Sr}/I_{La}, I_{Mg}/I_{La} and I_{Ni}/I_{La}, are also plotted against the distance from the NiO–LSGM interface in order to understand the variation of intensities of Ga, Sr, Mg, and Ni (Figure 4.21a,b). It is clear that, starting from point 2 to point 12 all the elements La, Sr, Ga, Mg and Ni are present in various proportions. Also there is no point, where only the elements La, Ni, and O are present. I_{Sr}/I_{La} ratios remains almost constant, while I_{Ga}/I_{La} increases and I_{Ni}/I_{La} decrases from point 2 to point 12. I_{Mg}/I_{La} shows variation close to the interface but becomes horizontal with increasing distance.

From these observations it can be deduced that Ni, diffusing into LSGM, mainly replaces B-site atoms but not A-site atoms. Also the radii of different A-site and B-site cations (as shown in Table 4.6) [45] indicate that Ni can only replace Ga or Mg but not La or Sr.

Together with the observation that the Sr/La ratio remains almost constant, if it is assumed that there is no considerable amount of vacancy concentration on A-sites, it is possible to take the sum of site fractions, y, of Sr and La as 1.

Thus, in the perovskite LSGM(Ni)

$$y_{Sr} + y_{La} = 1 \qquad\qquad (4.1)$$

$$y_{Ga} + y_{Mg} + y_{Ni} = 1 \qquad\qquad (4.2)$$

where y_a is the site fraction of an element either on A or B-sites of the ABO_3 structure. Using the calculated k_{MgLa}, k_{SrLa}, and k_{GaLa} and the equations (4.1) and (4.2) it is possible to quantify the composition of LSGM(Ni).

By using the intensity data of Sr and La, the k_{SrLa}-factor and the Eq. (4.1), the concentration of Sr and La are calculated. Then concentration Ga and Mg are calculated by using their respective intensity values and k-factors with respect to La. Then the concentration of Ni is obtained by using the Eq. (4.2).

It is to be noted here that between point 2 and point 6 (Region B marked on Figure 4.19), due to the inclined interface, the EDX spectra recorded in region B originate from the phase mixture of NiO (with dissolved Ga and Mg) and LSGM (with dissolved Ni). So quantification of such EDX spectra by the above stated method would lead to the over-estimation of Ga and Mg and underestimation of the Ni content.

Keeping the problem of inclination of the interface with respect to the incident beam in mind, quantification of LSGM(Ni) using the above stated k-factors and perovskite structural conditions is done from point 6 to point 12. The quantified composition of LSGM(Ni) is shown in the Figure 4.22a. Figure 4.22b shows the Ni, Mg and Sr content within the LSGM(Ni) grain on an enlarged scale.
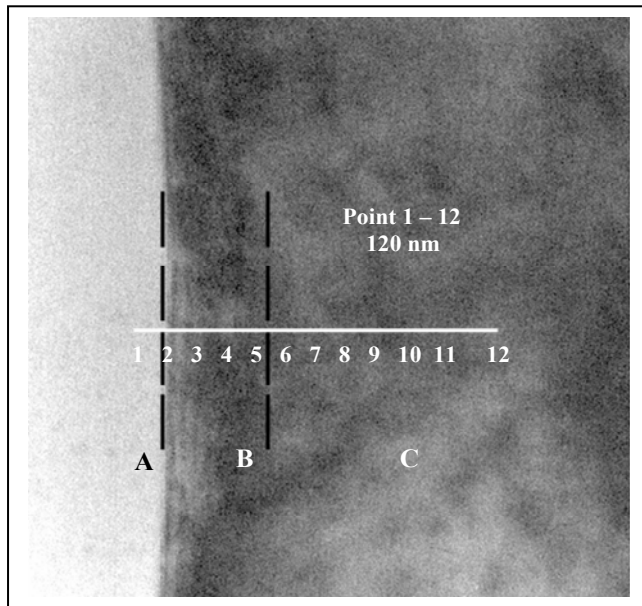
Figure 4.19 STEM bright-field image of NiO–LSGM interface. A:NiO grain, B: Projected area of inclined interface, C: LSGM grain. (Magnification 500000X)
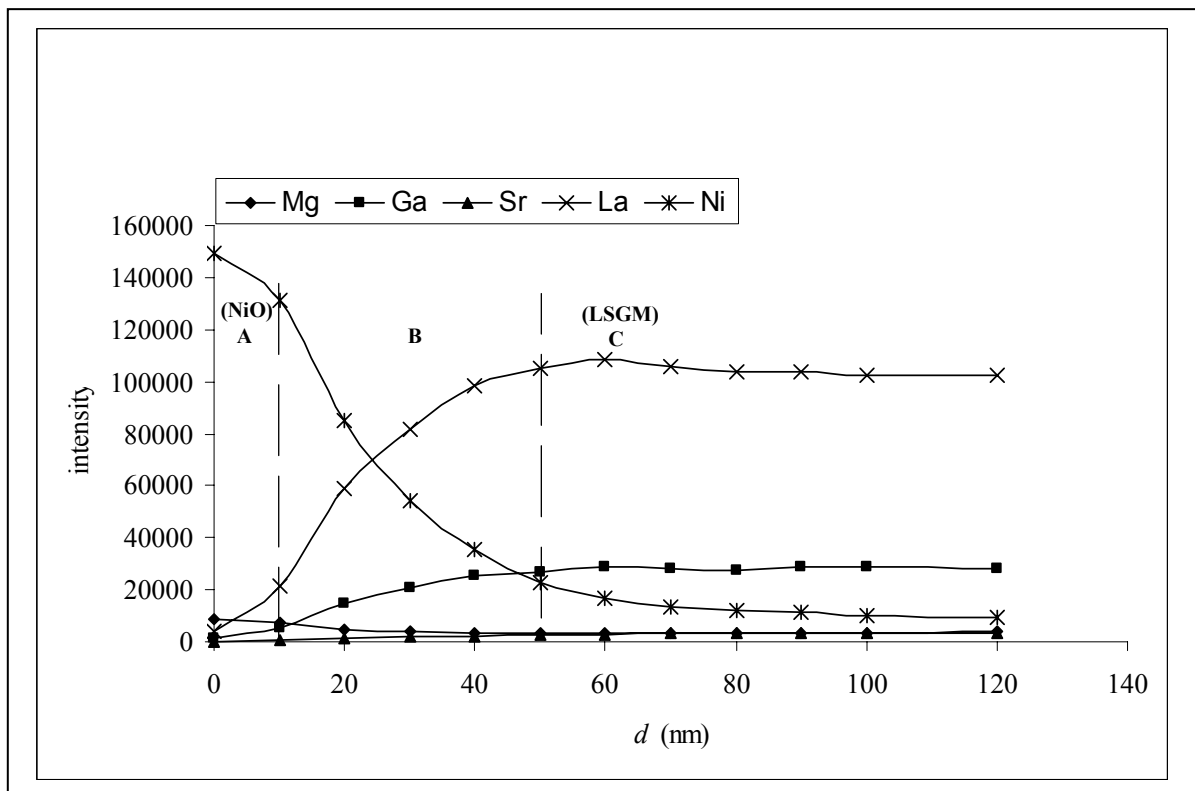
Figure 4.20 Intensity of various elements across the NiO-LSGM interface into LSGM (dashed lines depicting the NiO, NiO+LSGM, LSGM regions which correspond to A, B and C regions respectively in Figure 4.19)
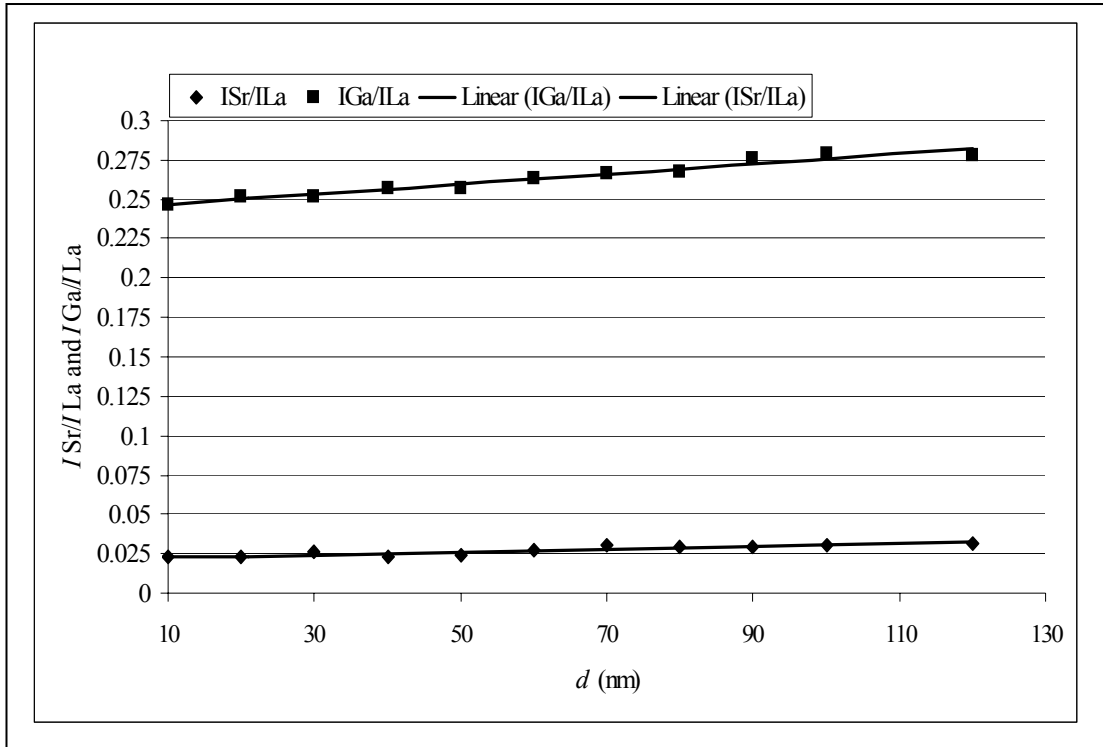
Figure 4.21a I_{Sr}/I_{La} and I_{Ga}/I_{La} plotted as a function of distance (nm) from the NiO–LSGM interface into LSGM (point 2 to point 12 as depicted on Figure 4.19)
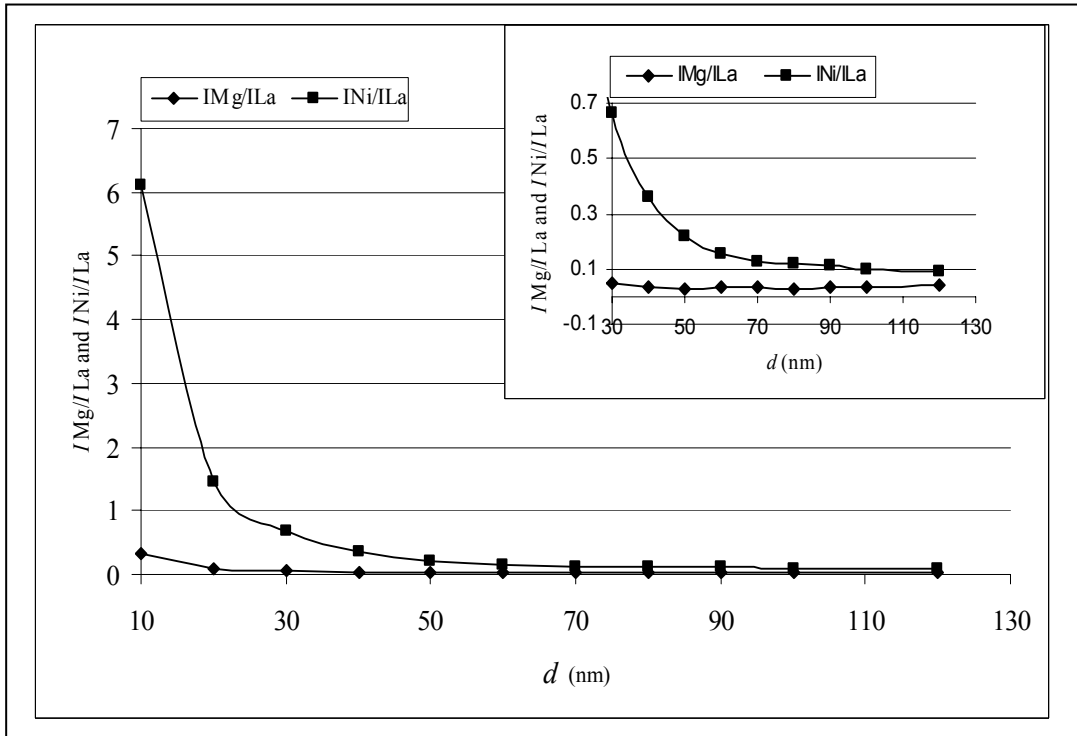
Figure 4.21b I_{Mg}/I_{La} and I_{Ni}/I_{La} plotted against the distance from the NiO–LSGM interface (point 2 to point 12 as depicted on Figure 4.19). Intensity ratios from d=30 nm to 120 nm are shown in the inset.
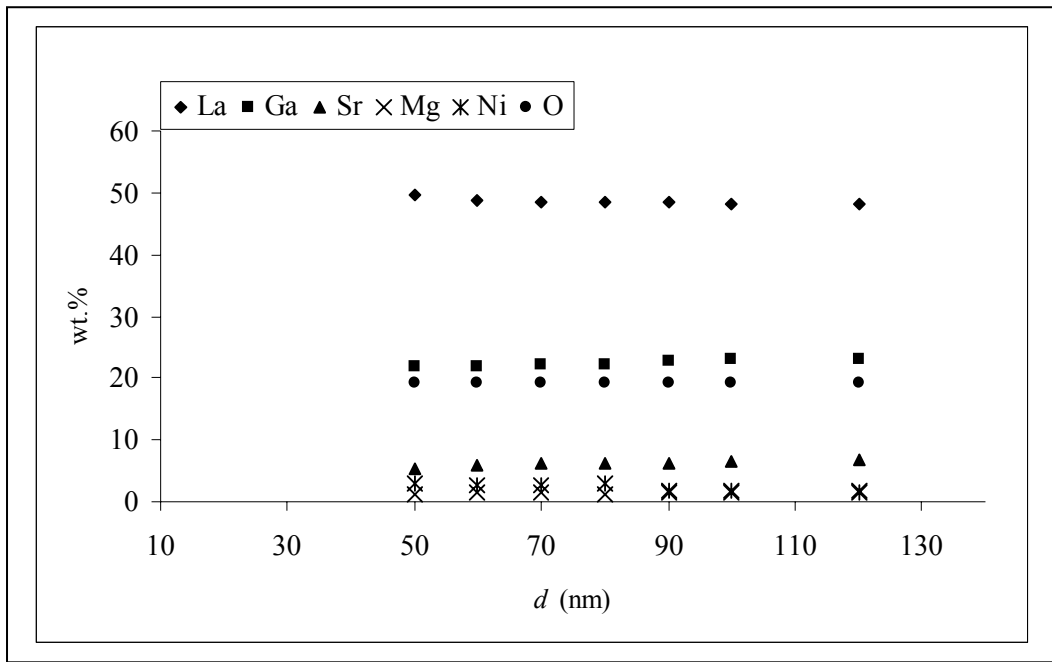
Figure 4.22a Composition inside the LSGM(Ni) grain (from point 6 to point 12 marked on Figure 4.19) as a function of distance from the NiO-LSGM interface. The relative errors in La, Sr, Ga, Mg, O and Ni quantities are 3%, 11%, 4%, 8%, 18% and 9% respectively.
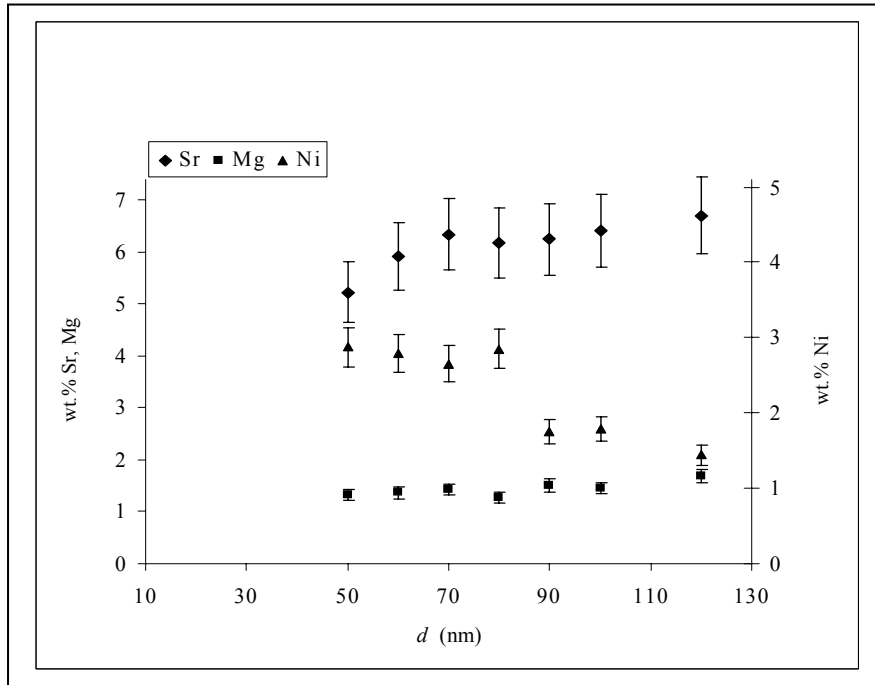
Figure 4.22b Variation of Ni, Mg and Sr content inside the LSGM(Ni) grain (from point 6 to point 12 marked on Figure 4.19) as a function of distance from the NiO-LSGM interface.

Table 4.6 : Effective ionic radii of different cations in LSGM(Ni) perovskite.

Cation (coordination number)	Ionic radius (Å)
La^{+3} (XII)	1.36
Sr^{+2} (XII)	1.44
Ga^{+3} (VI)	0.62
Mg^{+2} (VI)	0.72
Ni^{+3} (VI)	0.60
Ni^{+2} (VI)	0.69

4.1.3.2 Reduction of NiO-LSGM in H$_2$

The samples of NiO-LSGM which have been sintered at 1300°C were subsequently reduced in H$_2$ at two different temperatures 1000 and 750°C.
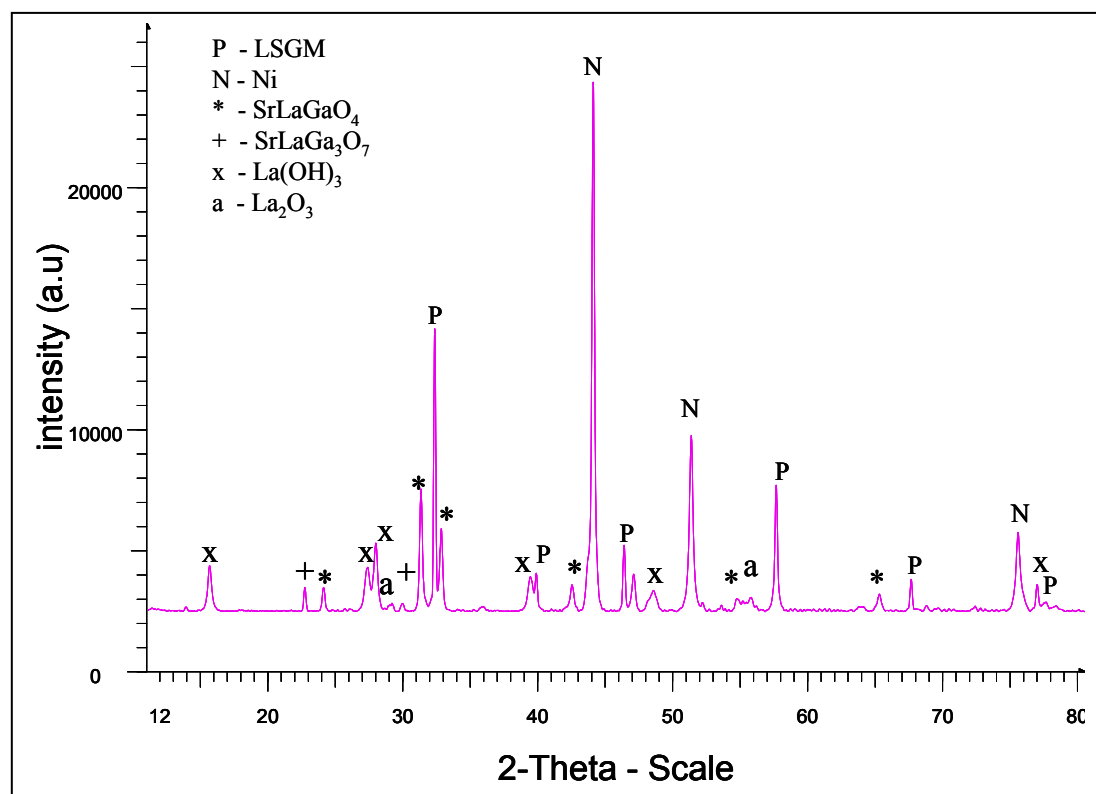
Figure 4.23 XRD pattern of Ni-LSGM cermet sintered at 1300°C in air for 2 h and then reduced at 1000°C in H$_2$ for 2 h.

Figure 4.23 shows the XRD of the NiO-LSGM which was sintered at 1300°C for 2 h and subsequently reduced at 1000°C for 2 h. The major phases LSGM and Ni can be seen from the diffraction pattern. Small fraction of SrLaGa$_3$O$_7$ is also present after sintering of the NiO-LSGM samples. From XRD, it appears that there is no increase in the fraction of this phase during reduction. However the SrLaGaO$_4$ appeared after reduction. Before reduction, the XRD of these sintered NiO-LSGM samples showed no SrLaGaO$_4$. It was only detected in the samples sintered at 1350°C and in XRD measurement performed at under extremely slow scanning conditions for determining lattice parameters (Figure 4.17). Either the content of phase was very low in quantity or not present at all after sintering at 1300°C. The XRD also clearly shows a considerable fraction of La(OH)$_3$ and a small fraction of La$_2$O$_3$. The presence of La(OH)$_3$ can be understood to be formed from the La$_2$O$_3$ phase. La$_2$O$_3$ formed during reduction is subsequently reacted with moisture in air when the sample is exposed to open

48

atmosphere, leading to the formation of La(OH)$_3$. So from the above observations it is clear that La$_2$O$_3$ and SrLaGaO$_4$ are mainly formed during the reduction of the NiO-LSGM sample at 1000°C for 2 h. The NiO-LSGM samples sintered in inert atmosphere(Ar and N$_2$) showed similar results (Figure 4.18).

So the above results lead to the understanding that some LSGM is decomposed under reducing condition to form Lanthanum oxide and SrLaGaO$_4$ phase. It is also evident from the results that the LaNiO$_3$-type phase formed during sintering at 1300°C can not be seen in the XRD of Ni-LSGM cermets after reduction. From TEM studies this LaNiO$_3$-type phase was found to be LSGM containing relatively high amounts of dissolved Ni.

NiO-LSGM reduced at 750°C for 4 h in H$_2$ also shows the same phases as above except for additional peaks, which can be associated with LaOOH phase.

The Figure 4.24a shows the SEM microstructure of the Ni-LSGM cermet obtained after reduction of NiO-LSGM at 1000°C for 2 h. The bright phase marked with "1" is LSGM and the dark phase marked with "2" is Ni. The exact composition of these phases as measured by EDX is shown in Table 4.7. It is evident that the Ni grains are not pure and contains ~8 at% dissolved Ga which comes from LSGM. LSGM is also showing some Ni which diffuses from the Ni phase. It is worth mentioning here that NiO grains before reduction showed no dissolved Ga. So it is clear that Ga diffused into Ni during reduction.

(a)   (b)
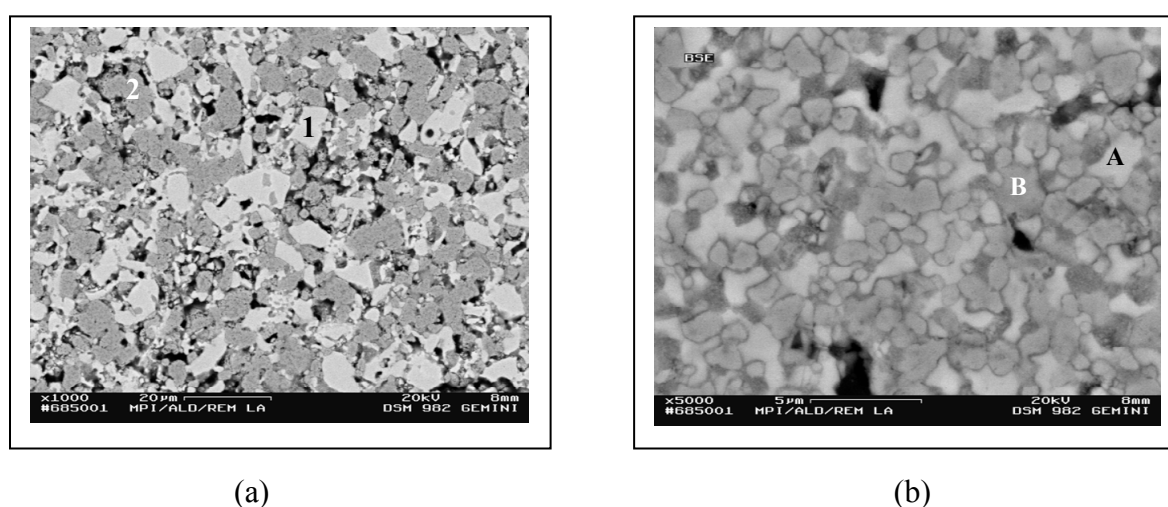
Figure 4.24 a,b NiO+LSGM(50 wt%), sintered at 1300°C for 2 h and then reduced in H$_2$ at 1000° C for 2 h (a) the microstructure represents the over-all microstructure of the sample (b) A location of microstructure with fine mixture of bright and dark phases.

Table 4.7 EDX results of the phases as shown in the Figure 4.24a

Bright phase (1)		Dark phase (2)	
Element	at %	Element	at %
O	53.12	O	6.89
Mg	3.51	Mg	2.82
Ni	2.08	Ni	81.61
Ga	19.73	Ga	8.33
Sr	4.09	Sr	0
La	17.47	La	0.45

Figure 4.24b shows fine mixture of dark and bright phases at a different location in the sample. The particles size in this location is very small (1-2 μm). Such areas of fine mixture of bright and dark phases were seen randomly at different locations in the sample. The EDX from the bright phase marked with "A" and the dark phase marked with "B" (in Figure 4.24b) can be seen in the Table 4.8. It is clear from the image that these particles are small in size and so it is likely that the EDX of the phases may contain elements from the adjacent phases or the phases beneath. However the analysis of the composition measured from these bright and dark areas give an interesting observation. The composition of the bright phase is mainly the perovskite LSGM phase with some dissolved Ni (and probably some Ni from the adjacent dark phase). The composition obtained from the point B on the dark phase can be understood as mainly from a mixture of La_2O_3 and Ni-Ga alloy. At 1000°C, which is the reducing temperature, from the Ni-Ga binary phase diagram, FCC Ni exhibits maximum a solubility of ~18 at% Ga. Together with the XRD data which show La_2O_3 phase after reduction, it can be confirmed that this composition is obtained from the mixture of Ni (with dissolved Ga) and La_2O_3 phases.

Table 4.8 EDX of the phases as shown in the figure 4.24b

Bright phase (A)		Dark phase (B)	
Element	at %	Element	at %
O	54.38	O	12.27
Mg	0.14	Mg	1.09
Ni	10.64	Ni	65.62
Ga	15.59	Ga	12.79
Sr	3.10	Sr	0.96
La	16.15	La	7.27

It can also be seen in the Figure 4.24a that the dark phase which is Ni, is not uniform in color. Figure 4.25 shows the microstructure of the NiO-LSGM sample sintered at 1300°C and reduced at 750°C for 4 h in H_2. It can be seen that the grain marked with "X" in the figure appears like a honeycomb structure.
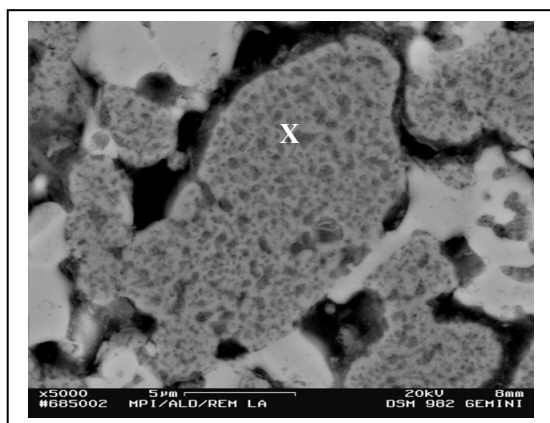
Figure 4.25 NiO+LSGM (50 wt%) sintered at 1300°C for 2 h and then reduced at 750°C for 4 h.

The overall composition of this grain obtained from EDX shows 85.74 at% Ni, 3.85 at% Ga, 2.53 at% Mg and 6.80 at % O. It is mainly nickel but, from this analysis it is not clear why the grains are appearing in such a way. One reason could be that the diffusion of Ga into Ni from the surrounding LSGM grains, is not uniform in the entire grain. As mentioned already such appearance of Ni grain can also be seen in the figure 4.24a. Later it will be seen that the Ni grain with this non-uniform distribution of Ga in it, reacts differently with H_2S.

4.1.3.3 Ni-LSGM cermets in H$_2$+H$_2$S (1 vol%)

After sintering at 1300°C for 2 h and subsequent reduction in H$_2$ at 1000°C for 2 h, Ni-LSGM cermets are studied in H$_2$+H$_2$S (1 vol%) gas. Figure 4.26 shows the XRD of the Ni-LSGM cermet after exposing to H$_2$+H$_2$S(1vol%) at 750°C for 3 h. The phase La$_2$O$_2$S can be seen in the XRD. It is also possible that GaS is present. Ni peaks can be seen in the XRD with a slight shift towards lower 2θ values. Pure Ni can not be stable at 750°C in H$_2$+H$_2$S(1 vol%) gas. It was shown in section 4.1.1 that nickel in Ni-YSZ cermet underwent melting and formed spheres of the eutectic composition of Ni and Ni$_3$S$_2$. LaGaO$_3$ (LSGM) and SrLaGaO$_4$ can also be seen while SrLaGa$_3$O$_7$ is hardly detectable by XRD. It is evident from the Figure 4.23 and Figure 4.26 that the La$_2$O$_3$ formed under reducing conditions due to the decomposition of LSGM, reacted with H$_2$S in the gas to form La$_2$O$_2$S.
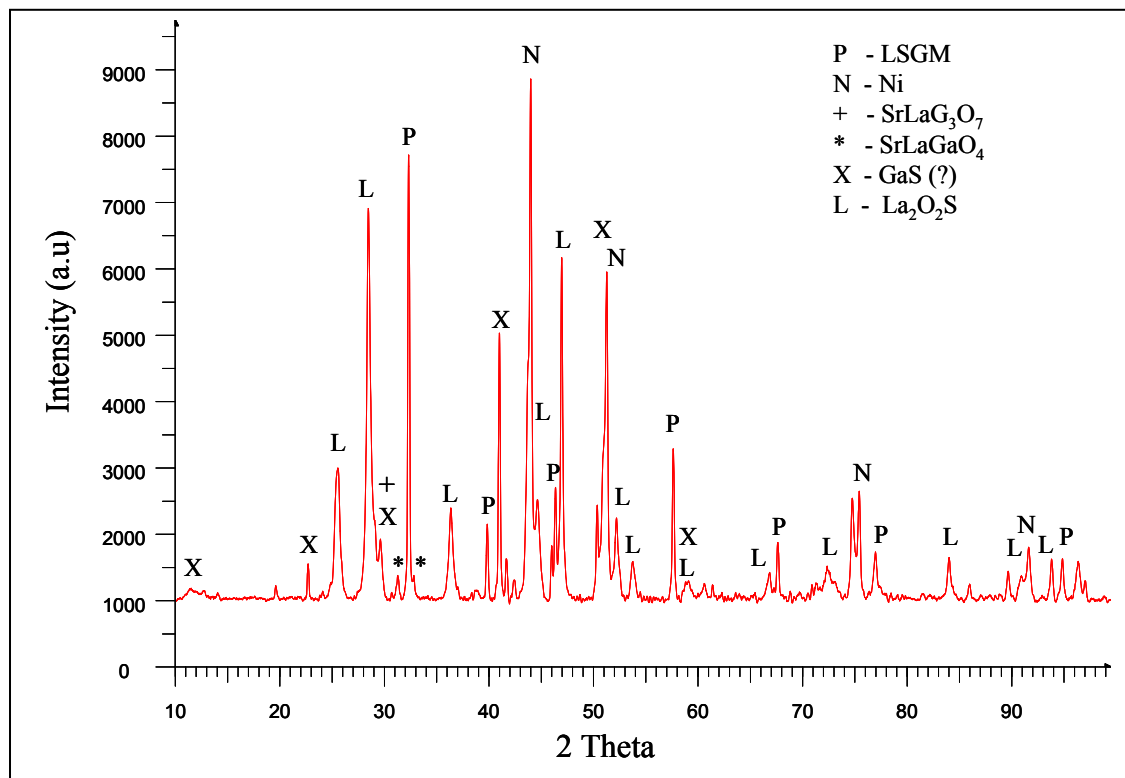
Figure 4.26 XRD of Ni-LSGM cermet after exposure to H$_2$+H$_2$S(1vol%) gas at 750°C for 3 h. The Ni-LSGM cermet was obtained from NiO-LSGM sintered at 1300°C in air for 2 h and subsequently reduced in H$_2$ at 1000°C for 2 h.
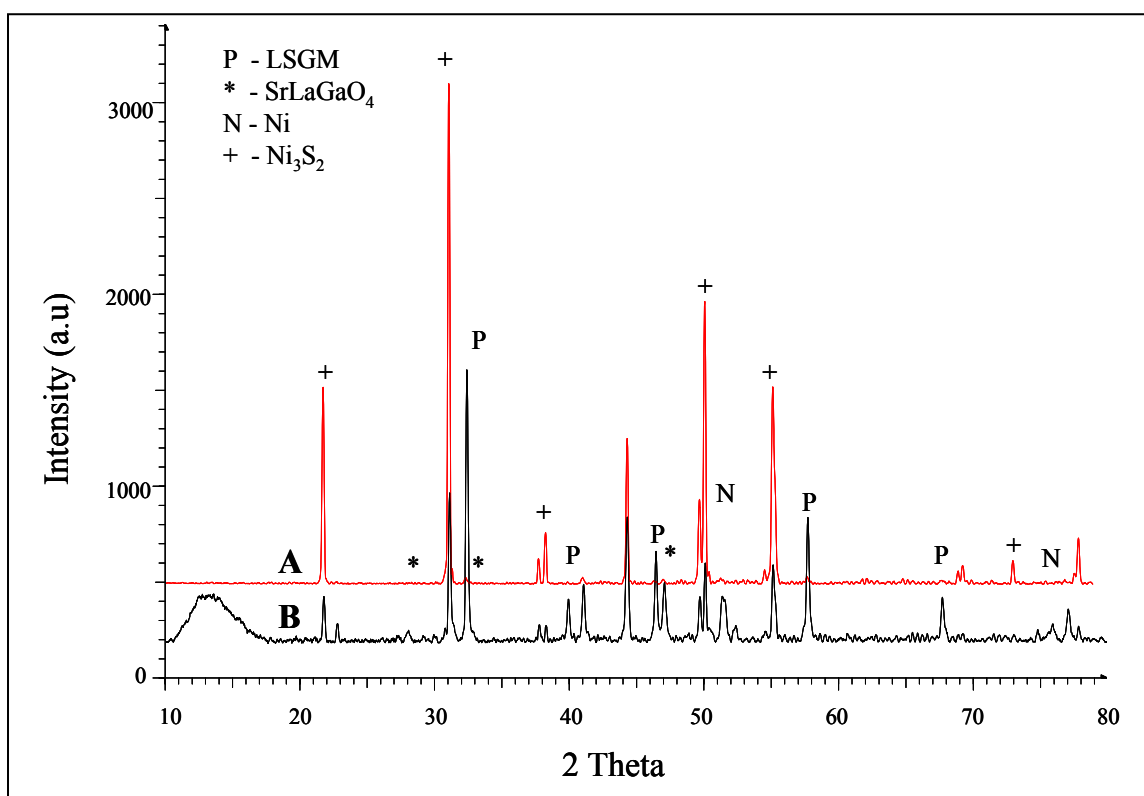
Figure 4.27 XRD pattern of Ni-LSGM cermet exposed to H_2+H_2S (1 vol%) gas at 500°C for 3 h. The Ni-LSGM cermet was obtained from NiO-LSGM sintered at 1300°C in air for 2 h and subsequently reduced in H_2 at 1000°C for 2 h. Pattern A-before removing the film formed over the surface, pattern B- after removing the film on the surface.

The XRD pattern of Ni-LSGM cermet after exposure to H_2+H_2S(1 vol%) gas at 500°C is shown in figure 4.27. A thin silvery film was formed on the surface of the cermet during the exposure. The film was very loosely bound to the sample. The pattern A is obtained when the sample was measured, as it is with the film, after the exposure. From the pattern A it is clear that the film consists of Ni_3S_2. When the thin Ni_3S_2 film was removed, the pattern B was recorded. Ni_3S_2 beside Ni, LSGM, and $SrLaGaO_4$ can be seen from the XRD pattern B. $SrLaGa_3O_7$ was not detected. It was shown that before exposure to H_2S, Ni in the Ni-LSGM cermet was containing some dissolved Ga. So a question arises if the nickel sulfide contains Ga or if there is a separate phase of gallium sulphide.

Figure 4.28 shows the SEM micrograph of the NiO-LSGM sintered at 1300°C for 2 h, reduced in H_2 at 1000°C for 2 h and exposed to H_2+H_2S (1 vol%) at 750°C for 2 h.
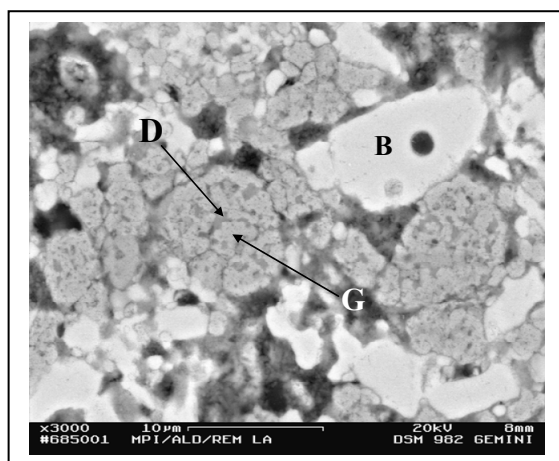
Figure 4.28 NiO-LSGM sintered at 1300°C for 2 h, reduced in H_2 at 1000°C for 2 h and exposed to H_2+H_2S (1 vol%) at 750°C for 2 h.

The bright, dark and grey phases are marked by B, D and G as shown in the figure 4.28. The composition of these phases as obtained from EDX is shown in the Table 4.9. The bright phase is LSGM with some dissolved Ni. The grey phase mainly shows Ni containing dissolved Ga. The dark regions in the grey phase mainly show nickel and sulphur. These dark regions appear to be nickel sulphide most probably Ni_3S_2. The EDX measured from different areas may contain elements from the surrounding phases. This problem is more pronounced for the grey and dark phases which are relatively small in area.

Table 4.9 EDX results of various phases as shown in the figure 4.28

Bright phase (marked by B)		Grey phase (marked by G)		Dark phase in grey phase (marked by D)	
Element	at %	Element	at %	Element	at %
O	50.22	O	8.17	O	4.56
Mg	2.55	S	2.84	Mg	0.33
S	0	Ni	73.60	S	17.35
Ni	2.23	Ga	10.33	Ni	73.14
Ga	23.03	Sr	1.16	Ga	4.00
Sr	4.08	La	3.90	Sr	0.34
La	17.93			La	0.29

An important observations from these EDX results is that those regions of Ni containing Ga (around 10 at%) seem to be not reacted with sulphur. The dark regions with mainly Ni and S and which are probably Ni_3S_2 do not contain Ga as much as in the grey phase. In any case it can be inferred that the Ni containing relatively high amounts of Ga (10 at%) doesn't contain S and the regions which appear to be nickel sulphide do not contain much Ga (<4 at%).

It can be seen in Figure 4.24b that, Ni-LSGM cermet showed few agglomerates of a fine mixture of phases in the microstructure. The EDX analysis of such areas after exposure to H_2+H_2S (1vol%) gas, led to an understanding that the bright phase in the agglomerate is either the perovskite phase or La_2O_2S, formed from the decomposition of LSGM and subsequent reaction of the La_2O_3 with H_2S in the gas. The grey phase in the agglomerate appears to be mainly nickel containing dissolved Ga (probably with ~10 at% Ga).

It was already found by XRD that Ni-LSGM cermet exposed to H_2+H_2S (1 vol%) at 500°C for 3 h shows a thin film of Ni_3S_2. SEM examination of the sample is carried out after removing the film. Figure 4.29a,b show the Ni-LSGM cermet after exposing to H_2+H_2S (1 vol%) at 500°C for 3 h.

(a)   (b)
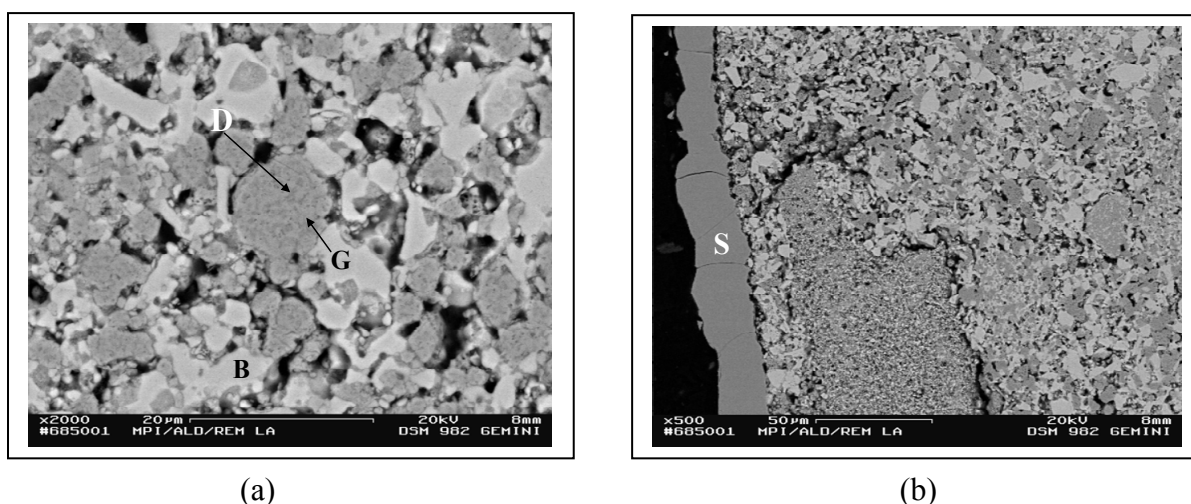
Figure 4.29 a,b SEM micrograph of the NiO-LSGM sintered at 1300°C for 2 h, reduced in H_2 at 1000°C for 2 h and exposed to H_2+H_2S (1 vol%) gas at 500°C for 3 h (in the figure (b) the thin layer of Ni_3S_2 can be seen)

The composition as obtained from the EDX of the bright(B), grey(G) and dark(D) phases in the Figure 4.29a is shown in the Table 4.10. The composition of the residual silvery film (skin) as shown in the Figure 4.29b is also given in the Table 4.10. It was shown in Figure 4.27 that the pattern A obtained from the film formed over the specimen, depicted only Ni_3S_2. Keeping the XRD data of this thin film and the composition of the skin from EDX together, it is possible to say that the film consists of Ni_3S_2 without any other elements.

Table 4.10 EDX results of the phases as shown in the Figure 4.29a,b

Bright phase (marked by B)		Grey phase (marked by G)		Dark phase in grey phase (marked by D)		Skin (marked by S)	
Element	at %	Element	at %	Element	at %	Element	at %
O	57.13	O	9.12	O	6.72	O	2.26
Mg	1.83	Mg	3.31	Mg	1.99	Mg	0
S	0.17	S	0.24	S	0.31	S	35.09
Ni	1.90	Ni	74.97	Ni	83.76	Ni	62.52
Ga	19.76	Ga	9.25	Ga	6.95	Ga	0.48
Sr	3.18	Sr	0.39	Sr	0.02	Sr	0
La	16.04	La	2.71	La	0.25	La	0

4.1.4 Ni-patterned LSGM

4.1.4.1 Ni-patterned LSGM in H_2

Figure 4.30 shows the Ni-patterned LSGM sample used for the Auger depth profile analysis. The analysis is carried from the surface of the nickel into LSGM across the interface. The Auger depth profile for the as prepared sample is shown in the Figure 4.31. The depth profile shows the clear interface of the as prepared sample. Broadening and extension of the Ni profile into LSGM is because of the surface roughness of LSGM (i.e the roughness at Ni-LSGM interface) and also because of the atomic mixing caused by the sputtering technique. Eventhough there are very less open pores, the open pores present on the surface of LSGM could also be a reason for the above. It can be seen that the La, Ga and O depth profiles are very steep on LSGM side close to the interface. The elements Mg and Sr are not detected in the spectrum because of their lower atomic percentages.
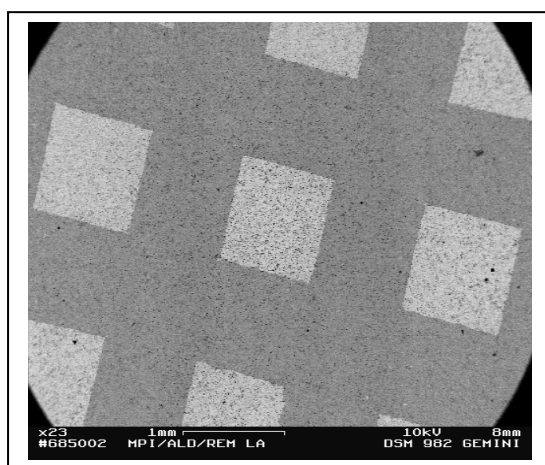
Figure 4.30 SEM micrograph of the Ni-patterned LSGM pellet (top view)
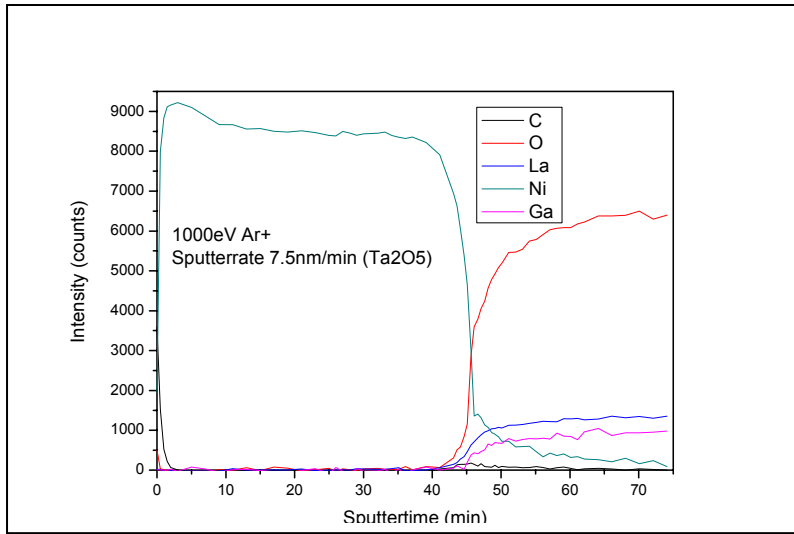
Figure 4.31 Auger depth profile of as prepared Ni-patterned LSGM

Figure 4.32 shows the Auger depth profile for the Ni-patterned LSGM which was annealed at 750°C for 24 h in hydrogen atmosphere. The depth profile shows diffusion of Ni into LSGM and Ga into Ni. Mg is not detected on either side of the interface. The sensitivity factors of the pure elements of Ni and Ga are used to quantify the composition on Ni-side.
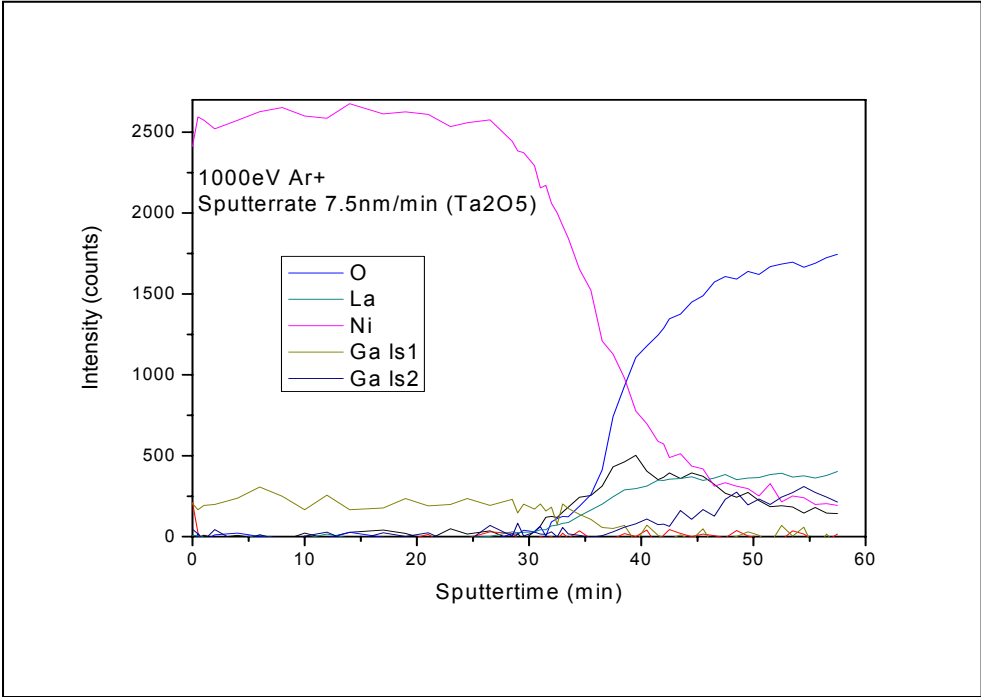
Figure 4.32 Auger depth profile of Ni-patterned LSGM treated at 750°C in H_2 for 24 h (Ga ls1 and Ga ls2 are Ga measured in Ni and Ga measured in LSGM respectively).

Figure 4.33 shows the depth profile of the Ni-patterned LSGM samples treated in H_2 at 650°C for 24 h. It is evident from the depth profile that, at 650°C there is no interdiffusion. The Auger depth profile of this Ni-patterned LSGM samples treated in H_2 at 650°C for 100 more hours also showed no interdiffusion. The depth profiles of the Ni-patterned LSGM samples treated at 600°C and 500°C in H_2 have also been recorded. From these results it is evident that there is no interdiffusion at and below 650°C. It would be interesting to investigate the Ni-patterned LSGM below this temperature to understand its performance as an SOFC electrode for oxidation of H_2.
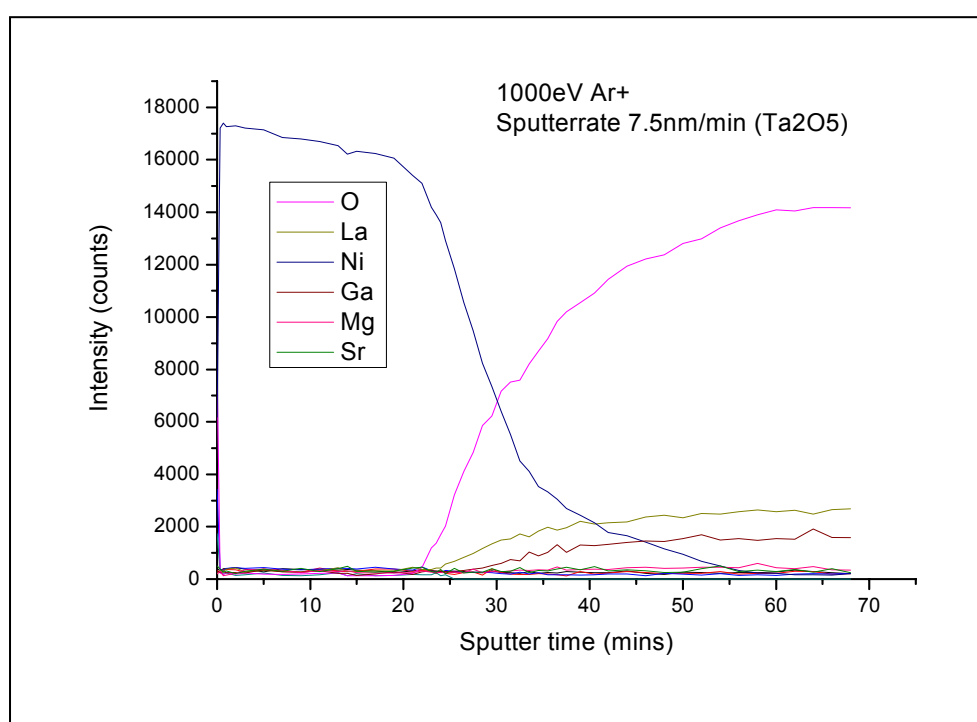
Figure 4.33 Auger depth profile of Ni-patterned LSGM treated at 650°C in H_2 for 24 h
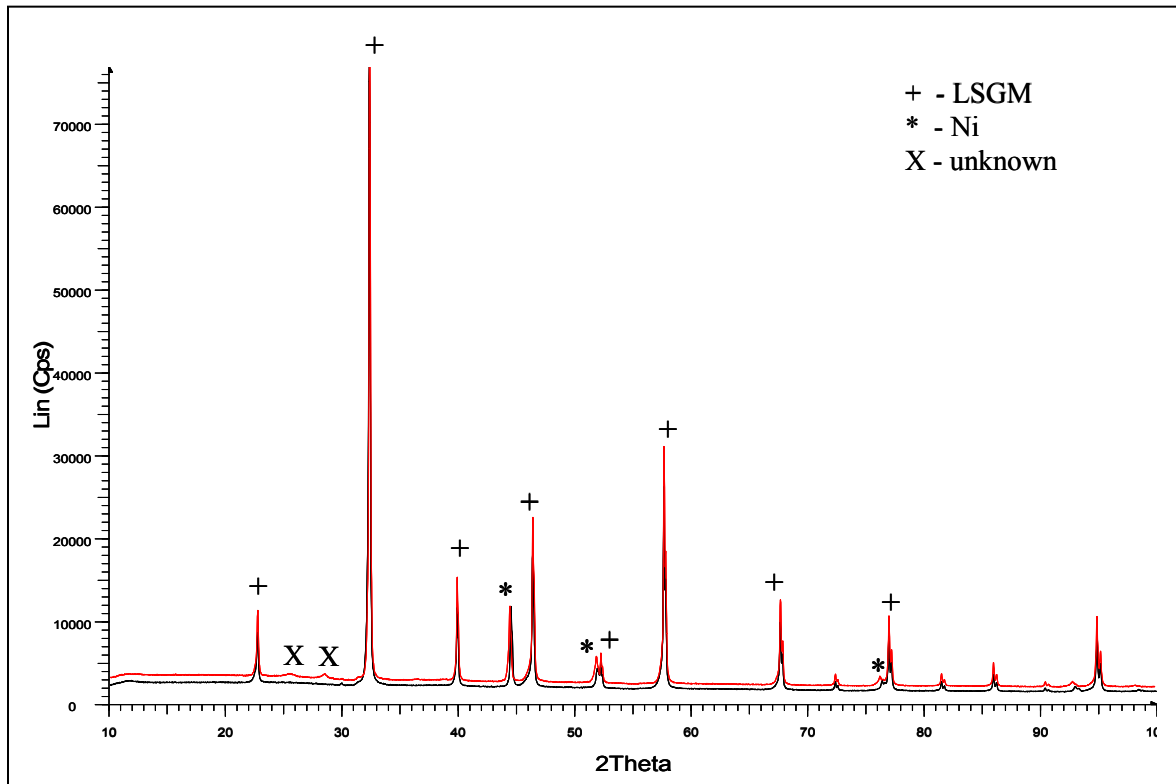
Figure 4.34a: XRD patterns of Ni-patterned LSGM before (bottom spectra) and after treatment at 750°C (top spectra) (+- LSGM, *- Ni, X-unknown)
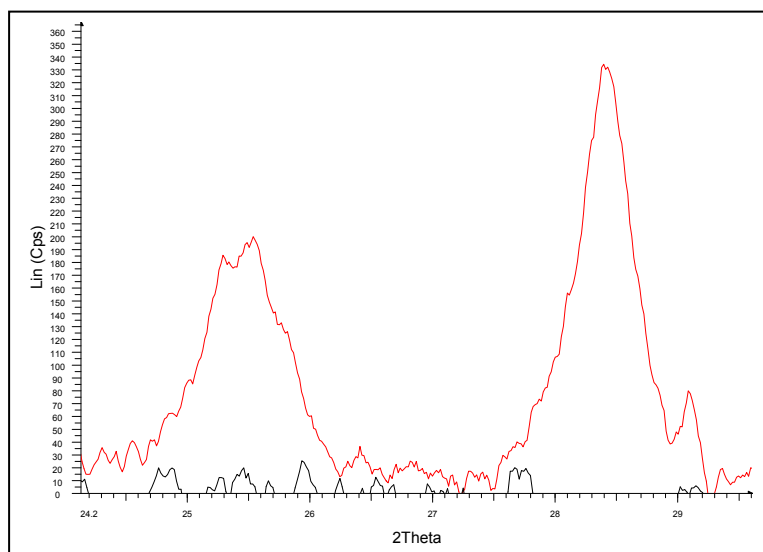
Figure 4.34b Magnified view of the new XRD peaks appeared in Ni-patterned LSGM treated in H_2 at 750°C for 24 h.

From the XRD of the untreated and treated Ni-patterned LSGM as shown in Figure 4.34a, it is clear that there is no formation of any further phase during the annealing treatment at 750°C, except the two very small unknown peaks at lower 2θ values (Figure 4.34b) There is no obvious reaction between Ni and LSGM. The Auger depth profile (Figure 4.32) shows Ga on Ni side and Ni on LSGM side. Thus from the XRD and Auger depth profile of the Ni-patterned LSGM, which was treated at 750°C in H_2 for 24 h, it is clear that Ni diffuses into perovskite LSGM and Ga diffuses out of LSGM into Ni. From the ionic radii of Ni^{+2}, Ni^{+3} and all the cations in LSGM as shown in Table 4.6, it is clear that Ni can only sit in B-sites of the LSGM replacing Ga and/or Mg. Since no Mg could be detected on either side, it is only possible to say from the depth profile that Ni replaces Ga in LSGM. Ga diffuses out of LSGM into Ni resulting in a formation of Ni-Ga alloy. It can also be seen from the depth profile that no La is found in Ni side. It is known from literature that there is no solubility for La in Ni. If it is assumed that the interdiffusion didn't lead to formation of vacancies on A-sites, then the sum of the site fractions of La and Sr on A-sites is 1. So, in general the situation in Ni-patterned LSGM after annealing in hydrogen at 750°C for 24 h is (Ni, Ga) | (La$_{0.8}$, Sr$_{0.2}$)(Ga^{+3},Mg^{+2} Ni^{+3}, Ni^{+2}) O$_{3-x}$.

The sensitivity factors of elemental Ni and Ga were used to quantify the composition of Ni side in the sample treated at 750°C in H_2. In Ni, around 10 at% Ga is found to be dissolved. Note that a more accurate calculation of the composition needs a standard which is similar to the sample under study. From the phase diagram of Ni and Ga, at 750°C the maximum solubility for Ga in Ni is 12 at%. It may be recalled here that in the previous section it was observed that the alloy of Ni containing ~10 at% dissolved Ga, is stable against H_2+H_2S(1vol%) gas at 750°C but reacts to form Ni$_3$S$_2$ at 750°C. So the Ni-patterned LSGM samples which are annealed in H_2 at 750°C for 24 h can be used to examine the stability Ni-Ga alloy patterns against H_2+H_2S (1 vol%) gas at 750°C and 500°C.
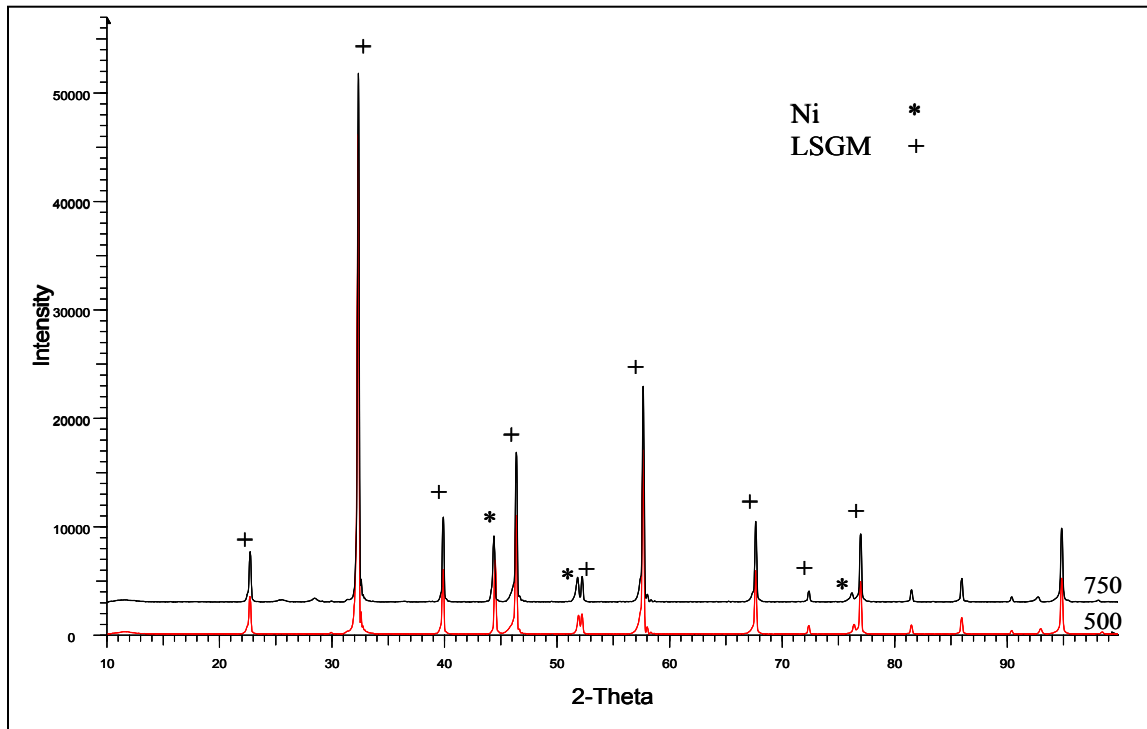
Figure 4.35 XRD patterns of Ni-patterned LSGM after treatment in H$_2$ at 500°C and 750°C

Figure 4.35 shows the XRD patterns of Ni-patterned LSGM treated in H$_2$ at 500°C and 750°C. As mentioned above except for the small unknown peaks observed in 750°C-treated sample, there are only Ni and LSGM phases. The XRD sample treated at 500°C is completely similar to the as prepared sample since there was no interdiffusion/reaction between Ni and LSGM during the treatment.

4.1.4.2 Ni-patterned LSGM in H$_2$+H$_2$S (1 vol%)

Ni-patterned LSGM after annealing in hydrogen atmosphere for 33 h was subsequently exposed to H$_2$+H$_2$S (1 vol%) at 750°C. As it was shown in the previous section, upon annealing the Ni-patterned LSGM in H$_2$ at 750°C, interdiffusion across the interface leads to the formation of Ni-Ga alloy. The stability of this Ni with dissolved Ga in H$_2$+H$_2$S (1 vol%) is of main interest in this section.

A Ni-YSZ cermet was also exposed along with the Ni-patterned LSGM (and LSGM coated completely with Ni sputtering). Figure 4.36 (photograph) shows the Ni-patterned LSGM sample and Ni-YSZ cermet after exposure at 750°C. Spherical particles of Ni+Ni$_3$S$_2$ eutectic

mixture can be seen on the Ni-YSZ cermet. However the nickel layer on LSGM can be still seen.
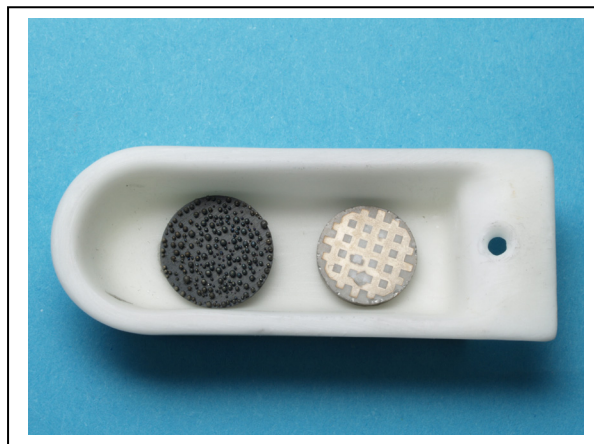
Figure 4.36 Photograph of the Ni-patterned LSGM (right) and Ni-YSZ cermet (left) after exposure to H_2+H_2S (1 vol%) gas at 750°C (The Ni-patterned LSGM was annealed in H_2 at 750°C for 33 h before exposure to H_2+H_2S).
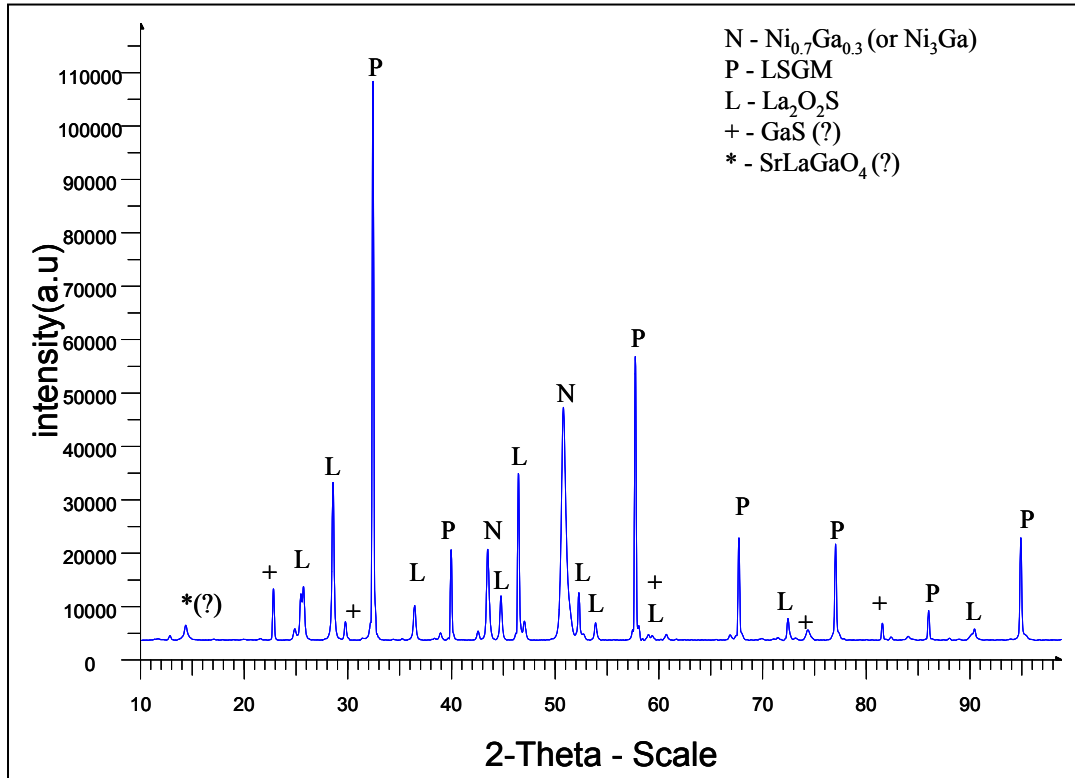
Figure 4.37 XRD of Ni-patterned LSGM after annealing in H_2 for 33 h followed by exposure to H_2+H_2S (1 vol%) gas at 750°C for 3 h

Figure 4.37 shows the XRD pattern of the Ni-patterned LSGM sample exposed to H_2+H_2S (1 vol%) gas at 750°C . The phase La_2O_2S can be seen from the XRD pattern after the exposure. The pattern XRD also shows $Ni_{0.7}Ga_{0.3}$ (or Ni_3Ga) and LSGM phases. The GaS phase is also most likely present. But not all the reflections corresponding to GaS are found while no nickel sulphide phase is present. The impurity phases $SrLaGaO_4$ and $SrLaGa_3O_7$ are not seen in the XRD.

Completely Ni coated LSGM samples were exposed to H_2+H_2S (1 vol%) at 500°C after the annealing in H_2 at 750°C. The XRD of these samples show mainly Ni_3S_2 and LSGM phases as well as $SrLaGaO_4$ impurity (Figure 4.38). This observation indicates that nickel (from the layer of Ni-Ga alloy) got converted into Ni_3S_2 during the exposure.
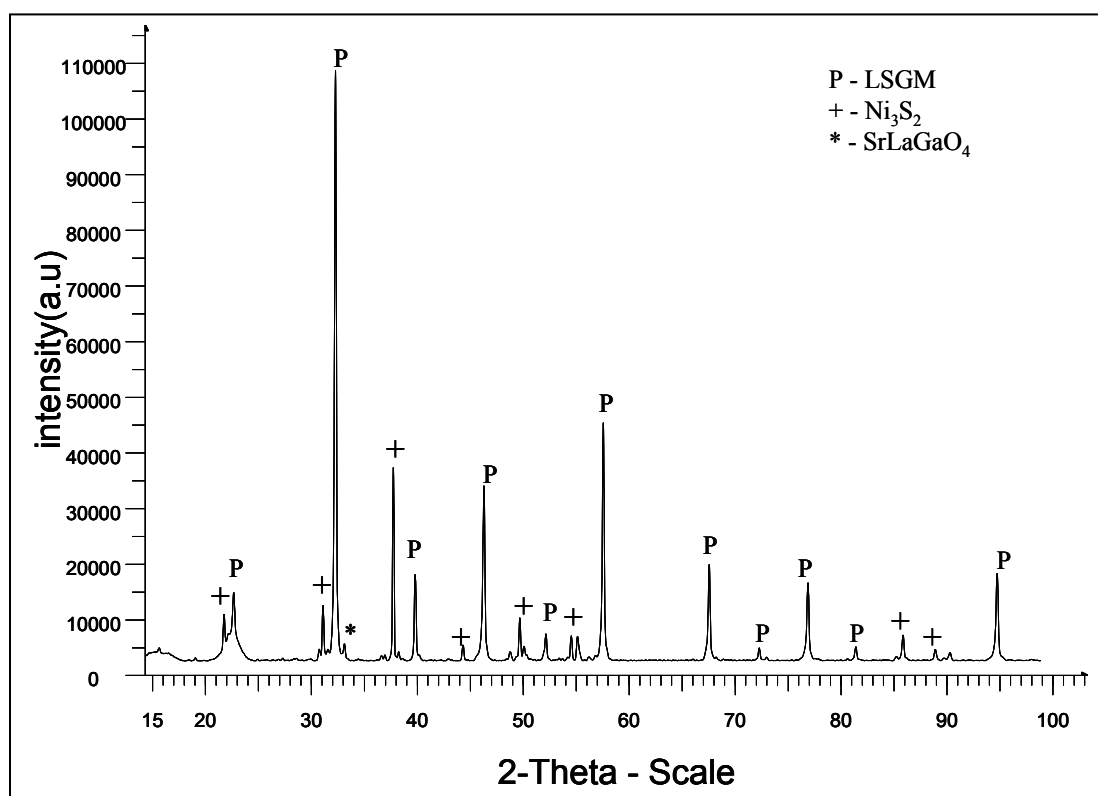
Figure 4.38 XRD of completely Ni coated LSGM after annealing in H_2 for 24 h and exposing to H_2+H_2S (1 vol%) gas at 500°C for 3 h

SEM examination of the Ni-patterned LSGM sample which was annealed in H_2 for 33 h and subsequently exposed to H_2+H_2S (1 vol%) gas at 750°C, was conducted. Figure 4.39 shows the SEM picture of the Ni-patterned LSGM annealed in H_2 and treated in H_2+H_2S (1 vol%) gas at 750°C for 3 h. Point A is marked over the surface of the electrolyte and point P is

marked over the Ni-pattern. Composition is obtained from the above Ni-pattern and from surface of the electrolyte.
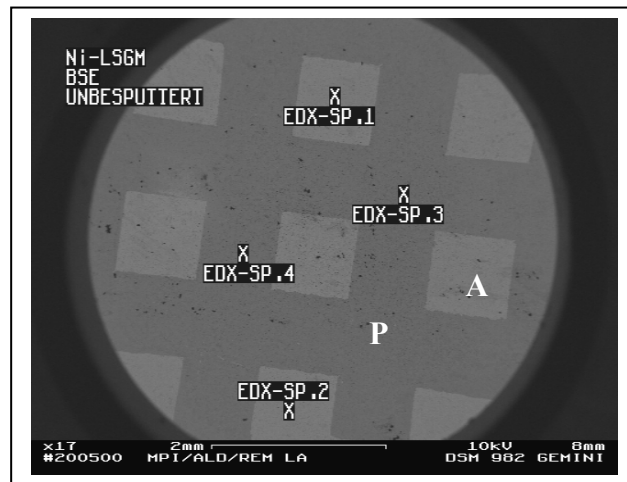
Figure 4.39 Ni-patterned LSGM after annealing in H_2 for 33 h and subsequently exposing it to H_2+H_2S (1 vol%) at 750°C.
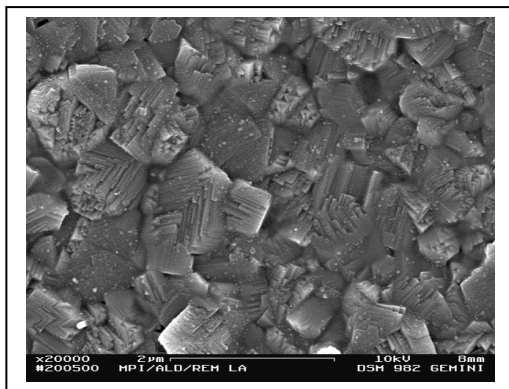
(a)   (b)

Figure 4.40 a,b Magnified views of the point P as shown in the Figure 4.39. The layered structure can be clearly seen in the image.
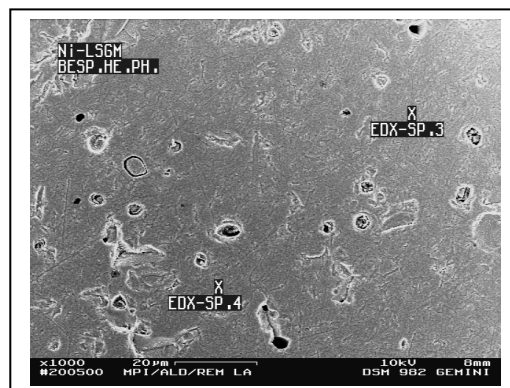
Figure 4.41 The surface of the electrolyte as marked by A in the Figure 4.39

The microstructure of the patterns can be seen in Figure 4.40a,b. In both cases, a layered structure can be seen. Figure 4.40b shows this feature at higher magnification. The compositions obtained by EDX from the layered structure and the surface of the electrolyte are given in Table 4.11. The composition measured from the layered structure show mainly Ni (~66 at%) and Ga (28 at%)

The composition obtained from the surface of the electrolyte shows a high percentage of sulphur (~25 at%) as given in Table 4.11. However as shown above, the XRD of this specimen indicates that the phases La_2O_2S, $Ni_{0.7}Ga_{0.3}$ and LSGM are present while the presence of GaS is most likely. So the composition measured over the surface of the electrolyte (point A) appears to be a mixture of phases.

Table 4.11 The EDX results of various phase as marked on the Figure 4.39 and Figure 4.41

Point A (on the electrolyte)		Point B(on pattern) spot 1 and spot 2	
Element	at %	Element	at %
O	26.33	1.64	3.28
Mg	4.53	0	0
S	24.18	0.89	1.62
Ni	1.46	69.20	65.93
Ga	3.29	28.51	27.41
Sr	12.41	0	1.26
La	27.80	0.63	1.30

4.2 Thermodynamic modelling of quaternary Ni-S-O-H system

4.2.1 Thermodynamic modelling of binary Ni-S system

4.2.1.1 Literature data

A considerable amount of thermodynamic data for the Ni-S binary has been published in literature. Chang et al [46] calculated the Ni-S binary phase diagram. This old modelling needs an update because the description of the phases by Chang et al is based on Wagner-Schottky model. More recent models based on the knowledge of crystallographic data improve the calculation of the diagram. Especially the non-stoichiometric phases Beta1, Beta2 and Delta should be described by compound energy formalism taking the recent crystallographic data. And also for pure elements the Gibbs energy descriptions used today are by Dinsdale [47]. So the diagram calculated by Chang et al needs an update. Recently Pelton et al published thermodynamic modelling of Ni-S binary phase diagram [48]. However, the non-stoichiometric phase Beta2 was not considered in their earlier publication while it is incorporated in their second publication [48-49]. In the experimental phase diagram reported earlier [43, 50] the Ni_9S_8 phase is not present on the phase diagram. So this phase is incorporated in the calculation of the binary phase diagram presented here.

Rosenquivst [51] reported the thermodynamics of Ni-S system in the temperature range of 400-1200 °C. Thermodynamic study of Ni-S system in a temperature range of 509-1287 K and in the composition range of 0.16 to 0.66 mole fraction of sulfur was reported by Miller et al [52]. Isothermal sublimation method was used to describe the temperature-composition region. The measured sulphur pressures over the entire temperature-compostion region were reported. Akira et al [53] also reported the thermodynamics of Ni-S system. The sulfur pressures in the composition range of 0.20 to 0.47 mole fraction of sulfur and in the temperature range of 801-1372 K were measured by the solid electrolyte galvanic cell technique.

Thermodynamics of Ni-S melts were also reported by many researchers. A study of thermodynamic properties of dilute solutions of sulfur in liquid nickel at 1540°C, was reported by Alcock et al [54]. Thermodynamic properties of dilute solutions of sulfur in liquid nickel upto 0.7 wt.% S in a temperature range of 1500-1575°C were investigated by Geiger et al [55] by measuring the equilibrium ratio of H_2S/H_2 gas mixture in equilibrium with the melt. Nagamori et al [56] studied the thermodynamic properties of Ni-S melts in a temperature range of 700°C to 1100°C. Partial pressures of sulphur determined from H_2S/H_2 ratio in

equilibrium with the liquid melts have been reported as a function of temperature and composition of the melt. Kellogg et al [57] also reported the equilibrium partial pressures of S_2 gas obtained from H_2S/H_2 gas mixture in equilibrium with the Ni-S melts in a temperature range of 1100°C to 1600°C and for melt compositions ranging from nickel saturation up to 27 wt% S. Kleppa et al [58] reported the high temperature calorimetry of liquid and solid phases of the Ni-S binary. The integral enthalpies of mixing of Ni and NiS to form liquid at 1100 K and enthalpies of formation of the solid phases were measured.

A lot of thermodynamic data of the solid phases on Ni-S binary phase diagram was reported in literature. Rau et al reported the sulphur pressures measured with H_2S/H_2 method in equilibrium with the high temperature $Ni_{1-x}S$ phase inside and adjacent to the homogeneity range [59]. They also reported the activity of sulphur as a function of composition and temperature for the other non-stoichiometric $Ni_{3\pm X}S_2$ phase, inside and at the boundaries of the homogeneity range [60]. Chang et al [61] determined the thermodynamic activity of sulphur in the β_1(Beta1)-Ni_3S_2 and β_2 (Beta2)-Ni_4S_3, γ-Ni_6S_5 and δ-NiS phases. The ratios of H_2S/H_2 in equilibrium with the metal sample or sulphide sample were measured and were used to calculate the activity of sulphur in solution relative to a standard state of S_2(gas) at 1 atm. Gronvol et al [62] reported thermodynamics of point defects in Nickel(II) sulphide with NiAs-type structure which has been modelled by statistical model based on the regular solution model.

Heat capacity of Haezelwoodite (Ni_3S_2) and high temperature, $Ni_{3\pm x}S_2$ phases have been measured by Gronvold et.al [63]. Heat capacity and thermodynamic properties of Nickel(II) sulphide in a temperature range of 298.15 to 1000 K has been reported by Stolen et al [64]. Two stable phases $Ni_{7\pm X}S_6$ and Ni_9S_8 phases have been reported in the composition range of 0.45 to 0.48 mole fraction of sulfur. The heat capacity and thermodynamic properties of the phases Ni_7S_6 and Ni_9S_8 from 5 K to 970K and 5 K to 673 K respectively, are reported [65].

The solubility limit of sulphur in solid nickel has been investigated by Kirkaldy et al [66-67]. They also reported the liquidus curve of Ni-S binary in the temperature range of 637-1453°C in a composition range of 0-0.334 mole fraction of sulfur. Kitkaze et al [68] studied the high temperature phase $Ni_{3\pm X}S_2$ by means of high temperature X-ray powder diffraction and differential thermal analysis. They found that this $Ni_{3\pm X}S_2$ phase field is divided into two phases namely Beta1 and Beta2 which are limited solid solutions with a miscibility gap

between them. Beta1 and Beta2 are reported to be face centred cubic and primitive cubic respectively. The XRD intensities of Beta1 and Beta2 phases at 600°C have been reported. The lattice parameter of these phases as a function of composition has been given.

4.2.1.2 Phases in the binary Ni-S phase diagram

Table 4.12 crystallographic data for the solid phases in the Ni-S binary system

Phase	Pearson symbol	Space group	Lattice parameter (pm)	Volume/atom (nm^3)
(Ni)	cF4	Fm3m	a=352.4	0.0109
$\beta^{\vert}$, Ni$_3$S$_2$(RT)	hR5	R32	a=573.8, c=712.6	0.0136
β_1, Ni$_3$S$_2$ (873K)	cF12 ?	Fm3m or F-43m (?)	a=521	0.0132
β_2, Ni$_4$S$_3$ (873K)	cP12?	Pm3m (?)	a=514	0.0138
γ or $\gamma^{\vert}$, Ni$_7$S$_6$	oC56	Cmcm	a=327.4, b=1135.9, c=1615.7	0.0143
Ni$_9$S$_8$	cF56	C222	a=933.59, b=1121.85, c=943	0.0145
δ, Ni$_{1-x}$S (HT)	hP4	P6$_3$/mmc	a=344, c=535	0.0137
ε, NiS (RT)	hR6	R3m	a = 959, c = 316	0.0140
ζ, Ni$_3$S$_4$	cF56	F4-3m	a = 949	0.0153
η, NiS$_2$	cP12	Pa-3	a = 568	0.0153
S	oF128	Fddd	a = 1044, b = 1285, c = 2437	0.0255

4.2.1.3 Thermodynamic Models of various phases

Liquid phase

Liquid phase has been modelled by associate solution model as it was done by Chang et al [46]. In the liquid phase a NiS associate is assumed to present along with atomic Ni and S.

Stoichiometric compounds

All the six solid phases, haezelwoodite (Ni$_3$S$_2$), Ni$_7$S$_6$, Ni$_9$S$_8$, millerite (NiS), Ni$_3$S$_4$ and NiS$_2$ on the phase diagram [43,50] are described as stoichiometric compounds.

Non-Stoichiometric compounds

Pyrrhotite Ni$_{1-x}$S (δ):

This phase has a NiAs-type structure which is a hexognal close packing of S-atoms (point symmetry 3m) with Ni and few vacancies in the octahedral voids (point symmetry 3m). This phase is modelled by a two-sublattice model, $(Ni,Va)_1S_1$ with Ni and vacancies (Va) present on the first sublattice and S on the second sublattice.

High temperature Haezelwoodite $Ni_{3\pm X}S_2$:

Earlier it was not clear whether this is a single phase field or a two phase field. A single phase was reported [51] with a compositional range from 0.36 to 0.443 atomic fraction of sulfur at 600 °C. It was also reported that a congruent transformation into low-temperature heazelwoodite (Ni_3S_2) occurs at 555±5 °C. In a much earlier publication by Line et al [69], the crystal structure of the high temperature Ni_3S_2 is reported to be face centred cubic with F4-3m space group. It was reported that the solid solution range extends from 37 to 43 atomic% S at 640 °C. However Rau et al [60] suggested wide homogeneity range for this high temperature $Ni_{3\pm X}S_2$ phase and also suggested that a second order phase transition takes place in the homogeneity range. However Lin et al proposed a division of the monophase field into two limited solid solutions of Beta1(Ni_3S_2) and Beta2 (Ni_4S_3) with two-phase field between them.

In a recent publication, Kitakaze et al. [68] confirmed the existence of Beta1 and Beta2 phases and reported that these phases have face centred cubic and primitive cubic cells, respectively. But the structure of these phases was not solved and the space groups are not known. However they reported the XRD powder data of these phases at 600 °C. It was also mentioned that the reflections (211) and (222) are only observed for the Beta2 phase.

If one assumes that the 4 S-atoms form cubic close packing like in the A1(Cu-) structure type, they have position (0 0 0) in space groups Fm3m or F-43m. Possible positions for Ni in these space groups are the octahedral voids (0.5 0.5 0.5) and/or the tetrahedral voids (0.25 0.25 0.25) + (0.75 0.75 0.75). The tetrahedral voids form a single 8-fold position in space group Fm3m, but two independent 4-fold positions in F4-3m.

Within the homogeneity range of Beta1 ($Xs=0.368$ to 0.412) there are 6.9 to 5.7 Ni-atoms per unit cell. If all the octahedral voids are occupied by Ni, the 8 tetrahedra voids contain 1.7 to 2.9 Ni atoms (site fraction .21 to 0.36). The corresponding model in the compound energy formalism is $Ni_4(Ni,Va)_8S_4$. If only tetrahedral voids are occupied by Ni then the formula is $(Ni,Va)_8S_4$. Both formulas are for space group Fm3m. If the 8 tetrahedral voids are split into 2 sets of each 4 positions (space group F-43m) more different formulas are possible. In literature in most recent publication Beta1 is modelled with two sub-lattice model $(Ni,Va)_2S_1$ assuming that nickel occupies exclusively tetrahedral voids in the FCC structure [49]. The

most general assumption, however, is that the octahedral and tetrahedral void are partially occupied: $(Ni,Va)_4$ $(Ni,Va)_8$ S_4.

An attempt has been made to understand the defect structure of these phases by calculating theoretical XRD patterns and comparing with the reported data. Winxpow software has been used to calculate the theoretical XRD pattern of Beta1 phase with two different space groups F4-3m and Fm3m and different site occupancies of Ni. Therefore X-ray intensities for Beta1 phase with the space groups Fm3m and F4-3m with various site occupancies have been calculated. Table 4.13 shows the experimental and calculated intensities for Beta1 with $(Ni,Va)_4(Ni,Va)_8S_4$ (space group Fm3m). The site occupancy on the first sublattice and on the second sublattice are 0.16 and 0.67 respectively. Even though there is no complete agreement between the calculated and experimental intensities, this calculated XRD spectrum is close to the experimental data. So the general model $(Ni,Va)_4$ $(Ni,Va)_8$ S_4 is assumed for the Beta1 phase.

Table 4.13 Calculated and experimental x-ray intensities (%) of the phase Beta1

h k l	Experimental XRD intensitites [68]	Calculated XRD intensities	
		For x_s=0.4	For x_s=0.406
111	11	7	4
200	-	3	0.3
211	-	-	-
220	100	100	100
311	5	2	1.26
222	-	-	0.06
400		13.0	
331		1.4	

Beta2 phase:

A primitive cubic cell was reported by Kitakaze et al [68]. But the defect structure is not known and Ni occupancies are not known. The dependence of lattice parameter on the mole fraction of S is very close to those of Beta1. Therefore most probably the two structures are very similar. In Beta2 the face centring is lost. Thus, the space group may change from Fm3m to Pm-3m or its subgroup P-43m. The 4 positions of S split into (0,0,0) and (0,1/2,1/2)+(1/2,0,1/2)+ (1/2,1/2,0) (Wyckoff position 1a and 3c respectively in Pm-3m or P-43m), and the positions of the octahedral voids into (1/2,1/2,1/2) and (1/2,0,0)+(0,0,1/2)+(0,1/2,0) (Wyckoff position 1b and 3d respectively in Pm-3m or P-43m). The positions of the tetrahedral voids change either to single 8-fold position (in Pm-3m) or two 4-fold positions. Thus in the case of Pm-3m group the general model is $(Ni,Va)_1$ $(Ni,Va)_3$

(Ni,Va)$_8$ S$_4$. However the theoretical X-ray intensities calculated assuming different occupancies of Ni for different space groups, to understand the actual structure, were not found to match with the experimental intensities. So the sublattice model assumed for this phase is (Ni,Va)$_3$ (Ni,Va)$_8$ S$_4$.

Gas Phase:

In the gas phase Ni(g) and the species of sulphur S$_1$(g), S$_2$(g), S$_3$(g), S$_4$(g), S$_5$(g), S$_6$(g), S$_7$(g), S$_8$(g) are considered.

4.2.1.4 Gibbs energies of hypothetical end-members of solution phases

Beta1:

The compositional range of Beta1 (and beta2) can be obtained with different combinations of end members Va$_4$Va$_8$S$_4$ and/or Ni$_4$Va$_8$S$_4$ + Ni$_8$Ni$_4$S$_4$ and/or Ni$_8$Va$_4$S$_4$. However the phase has been modelled to be made up of the end members Va$_4$Ni$_8$S$_4$ + Va$_4$Va$_8$S$_4$ and their interaction parameters. It means nickel occupancy in octrahedral voids is zero and it is only present in tetrahedral voids.

The initial values of the Gibbs energies of the end members for the optimisation are obtained as given below. Gibbs energy of FCC sulfur is taken for the end member Va$_8$Va$_4$S$_4$. So with G$_{Va4Va8S4}$ taken as 4GFCCS and G$_{Va4Ni6S4}$ as 2G$_{Ni3S2}$, the G$_{Va4Ni8S4}$ is obtained from the relation

$$0.75*G_{Va4Ni8S4} + 0.25*G_{Va4Va8S4} + RT(8 (0.75 \ln(0.75) + 0.25 \ln(0.25))) = G_{Va4Ni6S4} \quad (4.3)$$

Then these values are given as the initial values and optimisation is run to calculate the Gibbs energies of these end members and the interaction parameters.

The parameters for Beta2 were also obtained in the same way. For the phase Delta, the Gibbs energies of the two end-members Ni$_1$S$_1$ and Va$_1$S$_1$ are given by the Gibbs energy of NiS phase and FCC sulphur respectively as the initial values for optimisation. The actual model parameters are calculated from the experimental data during optimisation.

Calculations are performed with Thermo-Calc software. For pure elements, the standard Gibbs energy functions G_i^0 are taken from the SGTE unary database [47].

4.2.1.5 Calculated phase and property diagrams

Figure 4.42 shows the calculated Ni-S binary diagram. The newly incorporated Ni$_9$S$_8$ phase and the invariant reaction involving Ni$_7$S$_6$ and Ni$_{1-x}$S can be seen on the binary phase diagram.
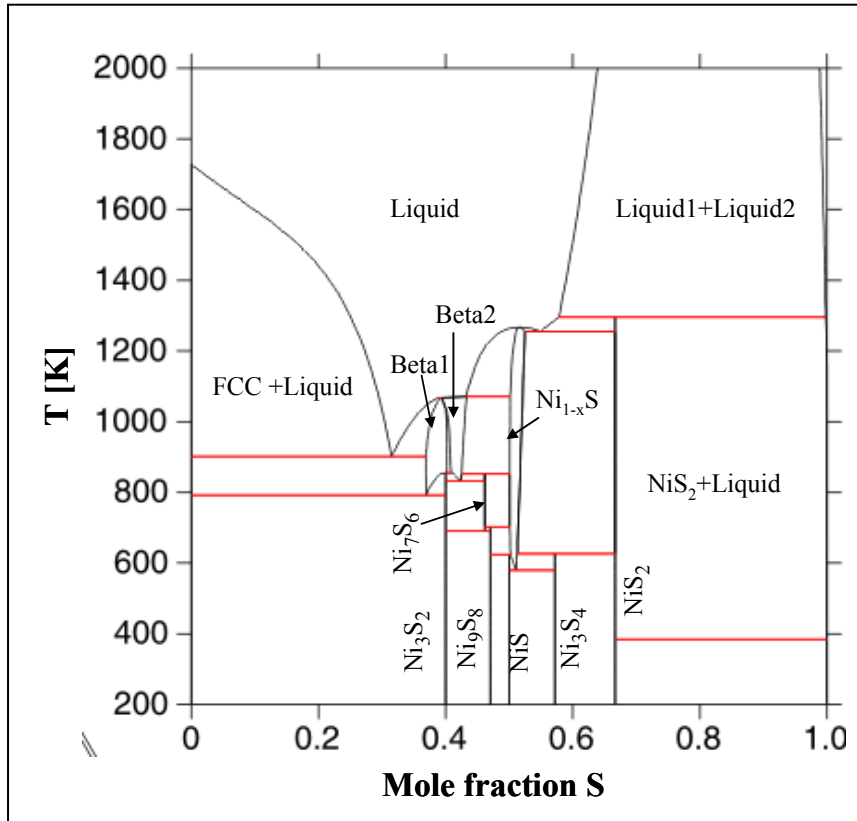
Figure 4.42 Calculated binary Ni-S phase diagram

The model parameters of the liquid modelled with the associated solution model is shown in the Table 4.14. The Gibbs energy data are expressed in terms of J/mol. The interaction parameters of the liquid phase modelled by Sharma et al [46] are converted to Redlich-Kister interaction parameters for the initial values in this optimisation of the liquid phase.

Table 4.14 Optimised model parameters of the liquid phase (GNILIQ, GSLIQ and GASS2 are the Gibbs energy descriptions of Ni (liquid), S (liquid) and S_2 (gas), respectively)

G(LIQUID,NI;0)	= +GNILIQ
G(LIQUID,S;0)	= +GSLIQ
G(LIQUID,NI1S1;0)	= -140804.191+159.4644*T- 13.513*T*LN(T) +0.5*GASS2+GNILIQ
G(LIQUID,NI,NI1S1;0) = -53619.8832+9.9716*T	
G(LIQUID,NI,NI1S1;1) = 38936.4207-9.6556*T	
G(LIQUID,NI1S1,S;0) = 60900-30.41*T	
G(LIQUID,NI1S1,S;1) = -4500-26.1*T	

The compounds Ni_3S_2 (Haezelwoodite), Ni_7S_6, Ni_9S_8, NiS(ε), Ni_3S_4 and NiS_2 are considered as stoichiometric compounds. Table 4.15 lists the optimised parameters of these

stoichiometric compounds. The Gibbs energies of formation of these compounds are calculated relative to Nickel (FCC) and S_2 (gas). The corresponding values reported by Sharma et al [46] and Chang et al [61] are taken as the initial values for optimisation.

Table 4.15 Optimised Gibbs energy of formation of stoichiometric compounds relative to FCC-Ni and S_2 (gas) (GHSERNI and GASS2 are the Gibbs energy descriptions of Ni (FCC), and S_2 (gas), respectively)

G(Ni_3S_2, NI:S;0) = -346585+170.625*T+3*GHSERNI+GASS2
G(Ni_7S_6, NI,S;0) = -937311.8+445.976*T+7*GHSERNI+3*GASS2
G(NiS, NI:S;0) = -152056+75.76*T+ GHSERNI+0.5*GASS2
G(Ni_9S_8, NI:S;0) = -1260130.03+ 623.45443*T+9*GHSERNI+4*GASS2
G(NiS_2, NI:S;0) = -268157.6372+176.1+GHSERNI+GASS2
G(Ni_3S_4, NI:S;0) = -572961.42+ 328.11875*T+3*GHSERNI+2*GASS2

The optimised model parameters of the non-stoichiometric phases Beta1, Beta2 and Delta are shown in the Table 4.16a, b, and c.

Table 4.16a Beta1- $(Ni,Va)_4$ $(Ni,Va)_8$ S_4 (GHSERS is the Gibbs energy description of S (Orthorhombic))

G(BETA1,VA:NI:S;0) = -489000+2300.87*T-400*T*ln(T)
G(BETA1,VA:VA:S;0) = 23600+1.0*T+4*GHSERS
G(BETA1,NI:NI:S;0) = 8.37E-04 + 8.31047629E-03*T
G(BETA1,NI:VA:S;0) = 1.10E-02 + 2.47E-02*T
G(BETA1,VA:NI,VA:S;0) = -575000+135*T
G(BETA1,VA:NI,VA:S;1) =3.557919+1.67665*T

Table 4.16b Beta 2- $(Ni,Va)_3$ $(Ni,Va)_8$ S_4 (GHSERS is the Gibbs energy description of S (Orthorhombic))

G(BETA2,VA:NI:S;0) = -445630+2261.3*T-400*T*ln(T)
G(BETA2,VA:VA:S;0) = 29776.4706-5.8823+4*GHSERS
G(BETA2,NI:NI:S;0) = 1.50 + 1.16*T
G(BETA2,NI:VA:S;0) = 9.62E-01 + 1.12*T
G(BETA2,VA:NI,VA:S;0) = -743789.141+290.86*T
G(BETA2,VA:NI,VA:S;1) = 2.9565+0.47687*T

Table 4.16c Delta - $(Ni,Va)_1S_1$ (GHSERNI, GASS2 and GHSERS are the Gibbs energy descriptions of Ni (FCC), S_2 (Gas) and S (Orthorhombic), respectively)

G(DELTA,NI:S;0)	=-147799.5769-69.4+GHSERNI+0.5*GASS2
G(DELTA,VA:S;0)	=79.36*T+GHSERS
G(DELTA,NI,VA:S;0)	=-51930.2-46.4*T

Comparison with experimental data

Figure 4.43 shows the calculated Ni-S binary phase diagram with experimental data points plotted on it, to show the agreement between both.
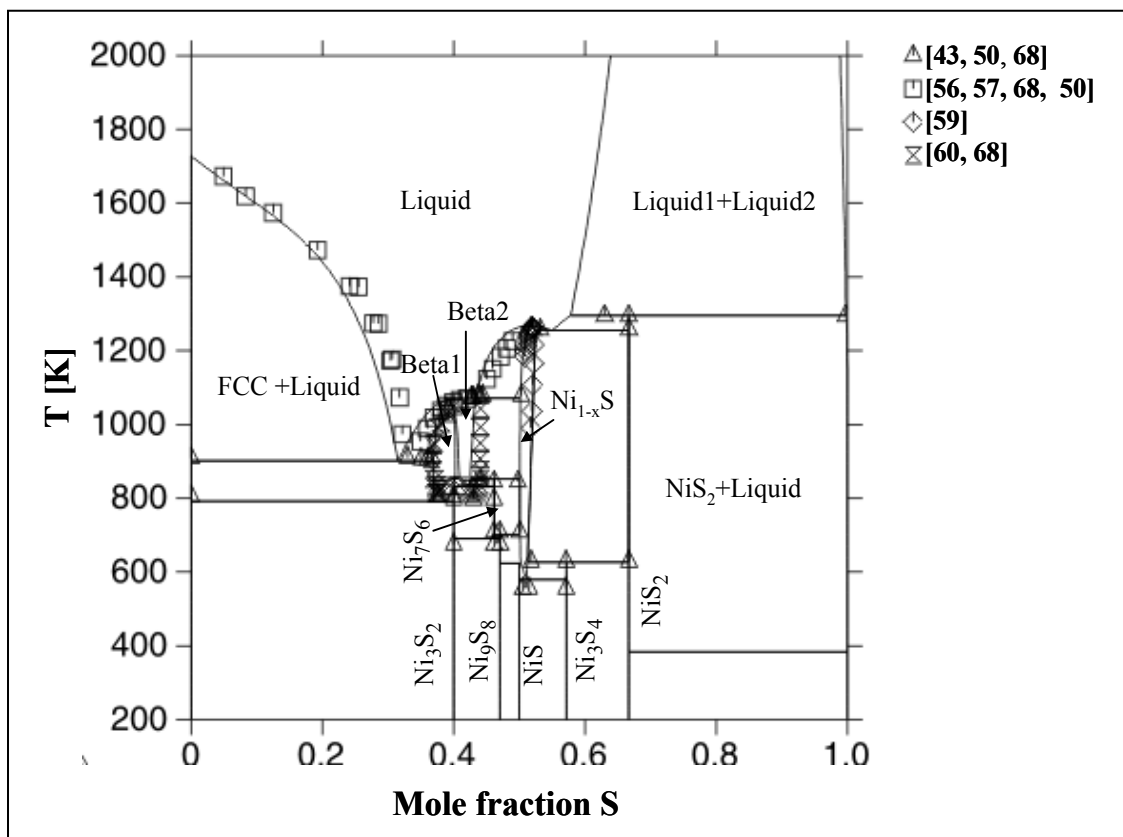
Figure 4.43 Calculated binary Ni-S phase diagram with experimental data points

The calculated and experimental temperatures of various invariant reactions and the composition of the phases involved the invariant reactions, are shown in the Table 4.17. There is a good agreement between the calculated and experimental values with in the limits of uncertainty set during the optimisation.

Table 4.17 the calculated and experimental temperatures of the invaraint equilibria and the composition of the involved phases

Reaction	Composition, at% S			Temperature(°C)	Reference
Liquid = Ni(FCC)	0	0	0	1455	[43,50]
				1455	Calculated
Liquid = Ni + β_1	33	0	36.7	637	[43,50]
	31.5	0	36.9	628.8	Calculated
Liquid = δ + η	53.2	52.1	66.7	985	[43,50]
	54.99	52.5	66.7	981.6	Calculated
Liquid + δ = β_2	43.7	50.3	44.4	805	[43,50]
	43.22	50.2	43.3	798.1	Calculated
Liquid + β_2 = β_1	42.7	44.1	42.75	800	[43,50]
	38.9	39.44	39.6	794.2	Calculated
β_1 = Ni + β'	37.5	0	40	533	[43,50]
	37	0	40	519.5	Calculated
β_1 = β' + β_2	40.5	40	41.5	564	[43,50]
	40.2	40	40.9	581.5	Calculated
β_2 = γ + β'	43	46.15	40	524	[43,50]
	42.3	46.15	40	559.5	Calculated
Ni$_9$S$_8$ = γ + δ	47.05	46.15		436	[43,50]
	47.05	46.15	0.5008	429.6	Calculated
δ = ϵ + ζ	51.5	50.5	57.14	282	[43,50]
	51.1	50.0	57.14	306.0	Calculated
β_2 + δ = γ	44.1	49.8	46.15	573	[43,50]
	42.6	50.05	46.15	578.4	Calculated
δ + η = ζ	51.8	66.7	57.14	356	[43,50]
	51.3	66.7	57.14	353.1	Calculated
Liquid = δ		51.7		995	[43,50]
		51.7		994.3	Calculated
β_1 = β'		40		565	[43,50]
		40		581.7	Calculated
Liquid = S(orthorho.)		100		115.2	[43,50]
		100		112	Calculated
Liquid1+Liquid	63	99.7	66.67	1022	[43,50]

75

$2 = \eta$	57.81	99.8	66.67	1022	Calculated

Figure 4.44 shows the calculated and experimental partial pressure of S_2(gas) in equilibrium with the Ni-S melt as a function of the composition of the melt at different temperatures. A good agreement between the calculated and experimental values can be seen.
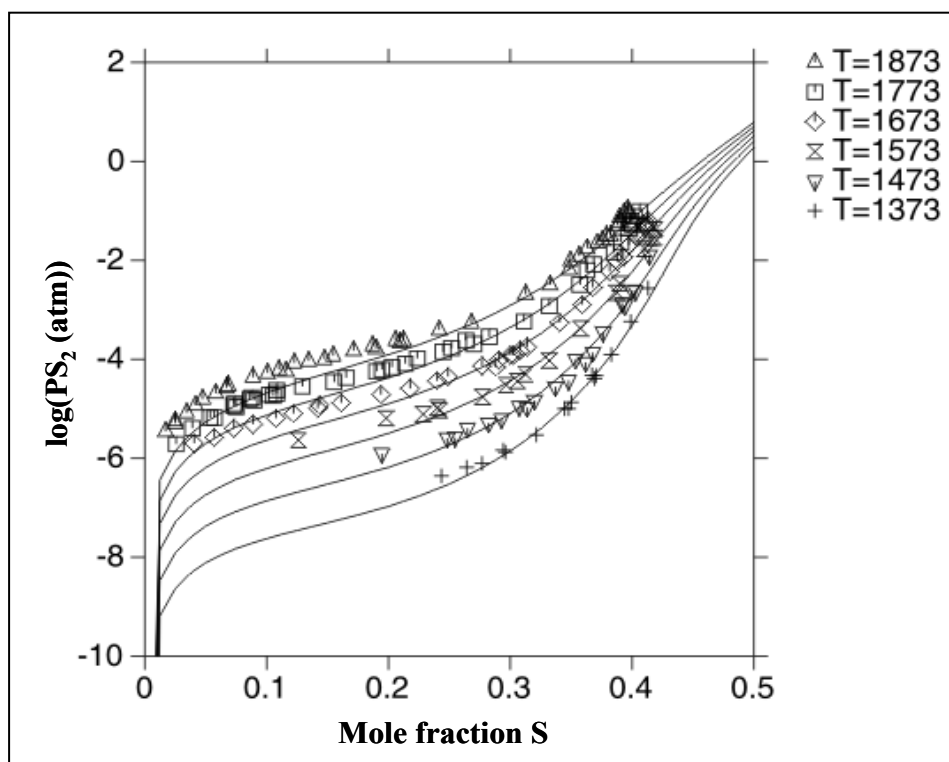
Figure 4.44 Partial pressure of S_2(gas) in equilibrium with the liquid phase as a function of composition.

The enthapies of mixing of liquid Ni and liquid NiS to form the Ni-S melt of various compositions at 1100 K are shown in the Table 4.18. The calculated and experimental values show a good agreement.

Table 4.18 Enthalpy of mixing of Ni(liquid) and NiS(liquid) at 1100 K

Mole fraction NiS	ΔH_{mix} (J/mole) calculated	ΔH_{mix} (J/mole) [49]	ΔH_{mix} (J/mole), Experimental [58]
0.576	-16916	-15367	-13700±1000
0.603	-17231	-15663	-15300±1000
0.667	-17537	-15878	-15900±1000
0.754	-16656	-14694	-12900±1000

A comparison of the calculated and experimental partial pressures of S_2 (gas) (activity of sulphur in solution relative to a standard state of S_2 (gas) at 1 atm pressure) in equilibrium with the solution phases Beta1, Beta2 and Delta are shown in the figure 4.45a,b,c, respectively. A good agreement of calculated values is obtained with the experimental values published in literature [61,59].
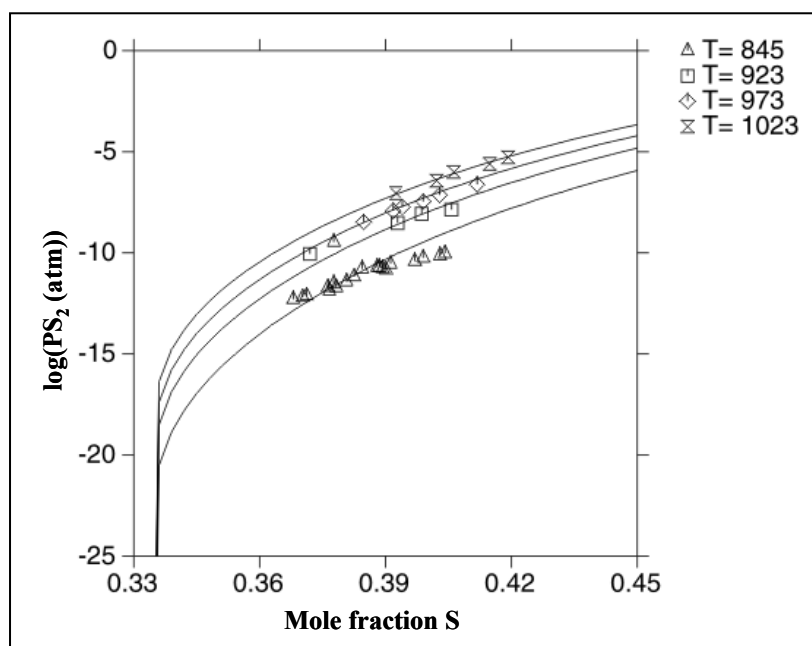
Figure 4.45a
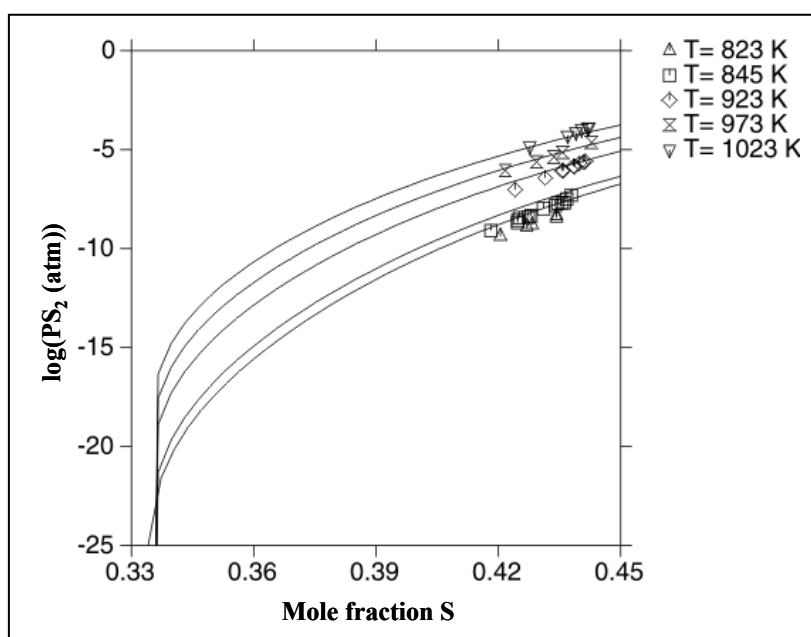
Figure 4.45 b
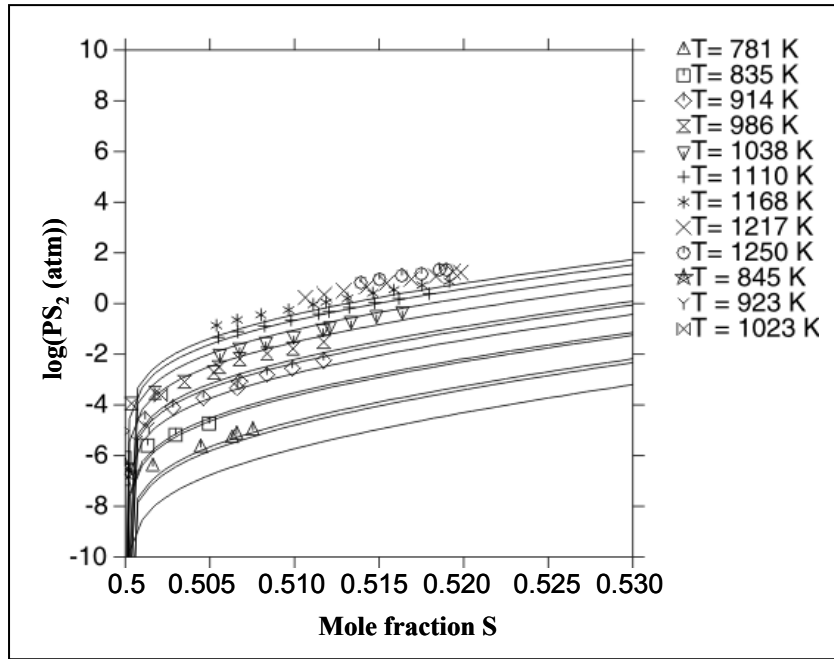
Figure 4.45 c

Figure 4.45 a,b,c Partial pressure of S_2(gas) in equilibrium with the Beta1 (a) , Beta2 (b) and Delta (c) phase as a function of composition.

Figure 4.46 shows the calculated log (PS_2) − 10000/T diagram with the experimental data points plotted over the diagram. A good agreement between the calculated and experimental data can be seen.
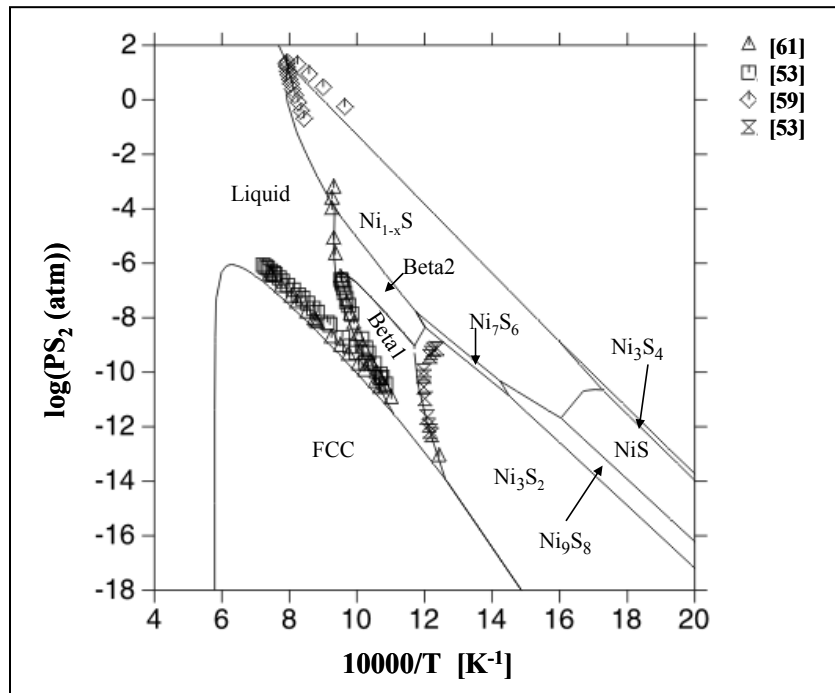
Figure 4.46 Calculated log (PS_2) vs 1/T diagram

4.2.2 Thermodynamic modelling of ternary Ni-O-S system

4.2.2.1 Literature data

Kellogg [70] reported a review of high-temperature equilibrium measurements and other thermochemical data available for sulfation reactions of the type $MSO_4 = MO + SO_3$.

Ingraham [71] studied the thermodynamics and thermal decomposition of the $NiSO_4$ in the temperature range of 1000-1500 K. The predominance volume diagrams for the Ni-S-O system were calculated by combining the measured equilibrium pressures of SO_3, SO_2, O_2 with the earlier published data on the oxide and sulphide systems. Thermodynamic properties of the chemical reactions of the type $MSO_4(s) = MO(s) + SO_3$ (g), measured by a solid concentration cell were reported by Gauthier et al [72]. Jacinto et al [73] reported an updated predominance area diagrams for the Ni-S-O system with included stability zones for all the known nickel sulphides. The construction of these diagrams was performed in the temperature range where all the phases are in solid state. Lalauze et al [74] studied the interaction between gaseous sulfur dioxide and nickel oxide by means of the Temperature-programmed desorption (TPD) and microcalorimetric techniques. The difference in calorimetric data of SO_2-NiO interactions depending on the different kinds of chemisorbed oxygen species on the solid has been discussed.

Lenz et al [75] investigated the nickel rich corner of the Ni-O-S system in the temperature range of 850-1600°C. The saturation boundaries of NiO(S) as a function of sulfur level in the matte for temperature ranges from 1200°C to 1600°C in 100°C intervals were reported. Oxygen and sulphur contents of liquid in equilibrium with both Ni(s) and NiO(s) and partial pressures of SO_2 as functions of temperature were reported.

Saito et al [76] reported the standard free energy change of the dissociation reaction of $NiSO_4$ to NiO and SO_3, calculated from the measured dissociation pressure from an emf measurement of the SO_2-O_2-SO_3 concentration cell with NASICON solid electrolyte.

Chang et al [77] studied the different two phase equilibria in Ni-S-O ternary system and measured the oxygen potentials of the two phase equilibria.

Sarrazin et al [78] proposed a method to describe the multicomponent atmosphere generated by SO_2 or SO_2-O_2 mixtures by taking SO_3, SO_2, SO species into account. Then the model was applied to explain the thermodynamic behaviour of Ni in an atmosphere of SO_2 or SO_2-O_2 mixtures.

Activity coefficients of oxygen in nickel-sulfur melts determined at 1423 K were reported by Yao et al [79]. Redox equilibria containing two of the solid nickel sulfides, Ni_3S_2, Ni_4S_3, NiS and NiO(s) or SO_2(g) have been studied in the temperature range of 850-1000 K to understand the phase relationships in the Ni-S-O system [80]. Shariat et al calculated the predominance area diagrams in Ni-O-S system [81].

Table 4.19 shows crystallographic data for the solid phases in Ni-O-S ternary system. The solid phases of the Ni-S binary are shown in Table 4.12.

Table 4.19 Crystallographic data for the solid phases in the Ni-O-S ternary system

Phase/ temperature range	Pearson symbol space group /proto type	Lattice parameter
NiO	Fm3m	a_o = 417.71
NiSO4	C M C M	a=516.6,b=784.6, c=636.2,

4.2.2.2 Thermodynamic modelling of phases

The thermodynamic description of Ni-O binary system is taken from literature [82]. The Ni-S binary is modelled in this work. The thermodynamic data of the phases in O-S binary system are taken from the SGTE database [83].

Liquid Phase

The liquid phase in the Ni-O binary system is modelled by an associated solution model. NiO associate is assumed to exist along with Ni and O in the liquid phase. The liquid phase in the Ni-S binary system is also modelled by the associated solution model. NiS associate is assumed in this liquid phase along with Ni and S. The liquid phase in the ternary system is modelled with an associated solution model assuming the NiS and NiO associates exist along with atomic Ni, O, and S.

Ternary compound

$NiSO_4$ is treated as stoichiometric compound. Its Gibbs energy of formation relative to Ni(S), O_2(gas), and S_2(gas), is obtained from the literature [73]. This value is further examined using the recent data of partial pressures of $P(O_2)$ and $P(S_2)$ for univariant equilibria in Ni-S-O system involving $NiSO_4$ phase [78,84].

4.2.2.3 Calculated potential phase diagrams

Figures 4.47 and 4.48 show the calculated predominance area diagram of the Ni-O-S system in $P(S_2)$-$P(O_2)$ and $P(SO_2)$-$P(O_2)$ coordinates at 900 K. The experimental data points [78,73] of the univariant equilibria are shown on the diagrams. It has to be mentioned here that in the experimental diagrams the high temperature phase $Ni_{3\pm x}S_2$ (Beta1) is treated as a single phase region i.e, Beta1 and Beta2 regions as a single phase region.
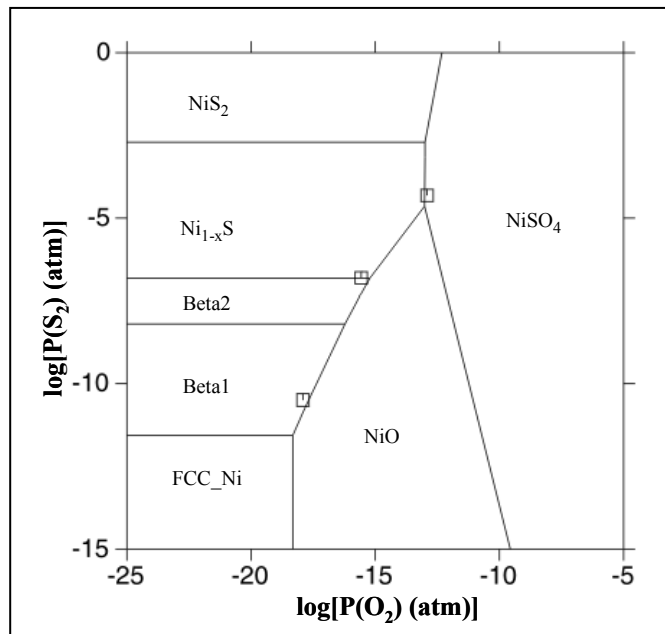
Figure 4.47 Predominance area diagram of Ni-O-S system in $P(S_2)$-$P(O_2)$ coordinates at 900 K (the experimental data points of three-phase equilibria [78] can be seen on the diagram).
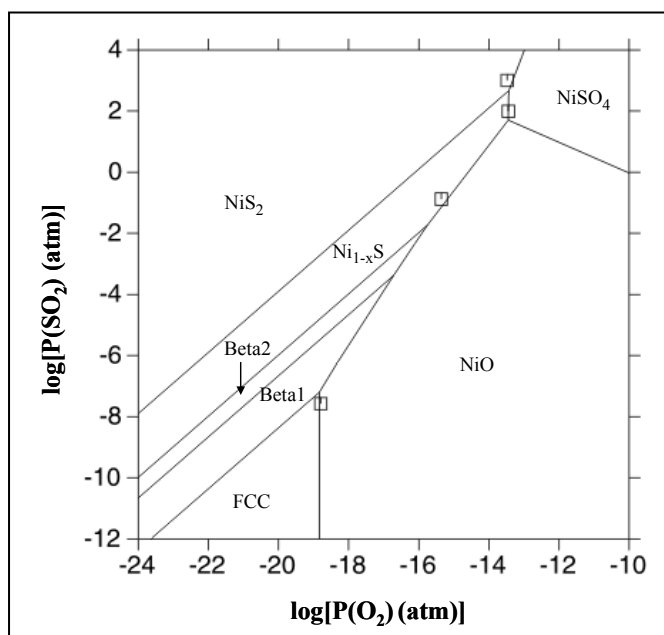
Figure 4.48 Predominance area diagram of Ni-O-S system in $P(SO_2)$–$P(O_2)$ coordinates at 883 K (the experimental data points of three-phase equilibria [73] can be seen on the diagram)

The stability diagram of in $P(O_2)$ - T, coordinates at a constant sulphur chemical potential is shown in Figure 4.49
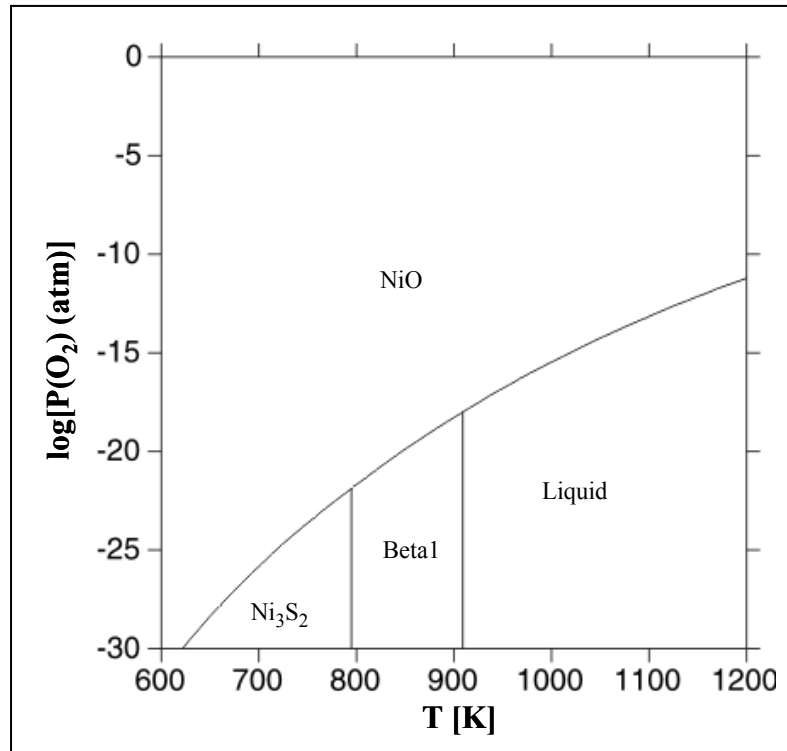
Figure 4.49 Stability diagram of Ni-O-S system in $P(O_2)$ - T coordinates at a constant chemical potential of sulfur ($\mu_s = 10^{-5}$).

A plot of log $P(SO_2)$ at the univariant equilibrium, S (in matte) + 2 NiO(s) = 2 Ni(s) + SO_2(g), as a function of temperature is shown in the Figure 4.50. A comparison of the calculated and experimental values can be seen. It has to be mentioned here that, for the liquid phase only the extrapolated binary-interaction parameters are used and the ternary interaction parameters are kept to zero.
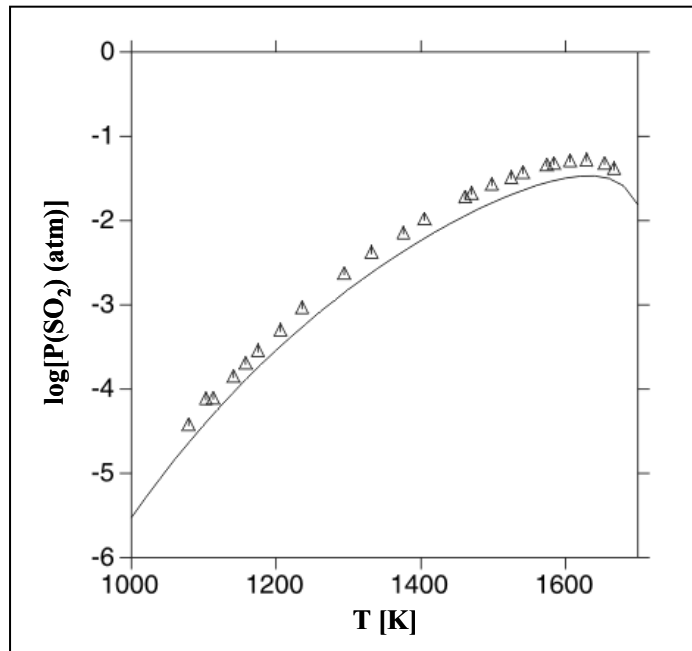
Figure 4.50 log[P(SO$_2$)] as a function of temperature for the equilibrium S (in matte) + 2 NiO(s) = 2 Ni(s) + SO$_2$(g) with the liquid phase(The experimental data points [75] can be seen on the plot).

It is evident from the figure 4.50 that the there is a good agreement between the calculated and experimental data of P(SO$_2$) for the univariant equilibrium of NiO(s) and Ni(S) in equilibrium with the liquid phase in the temperature range of 830°C to 1420°C. So the liquid phase in the Ni-O-S ternary is well modelled with the extrapolated parameters from the lower order binaries, Ni-O and Ni-S.

The optimised Gibbs energy of description of NiSO$_4$ is given below in Table 4.20.

Table 4.20 Gibbs energy description of NiSO$_4$

Parameter	function
G(NiSO4,NI:S:O;0)	-936967-15.37*T*ln(T)+552.02*T +0.5*GASS2+4*GHSEROO+GHSERNI

This modelled Ni-O-S ternary can now be used for the calculation of Ni-S-O-H quaternary.

83

4.2.3 Thermodynamic modelling of ternary Ni-O-H system

4.2.3.1 Literature data

There are two ternary compounds reported in the ternary system, $Ni(OH)_2$ and $NiOOH$ (Table 4.21). Structurally nickel oxyhydroxides has two forms, β-NiOOH and γ-NiOOH. β-NiOOH crystallizes in the hexagonal system with the brucite structure [85-86]. The structure γ-NiOOH is of C19 or $CdCl_2$-type. $Ni(OH)_2$ is designated by β-$Ni(OH)_2$ and α-$Ni(OH)_2$. β-$Ni(OH)_2$ is well crystallized $Ni(OH)_2$, isomorphous with brucite, while α-$Ni(OH)_2$ is used for a large set of disordered Ni(II) hydroxides and doesn't represent a well defined polymorph of $Ni(OH)_2$.

β-$Ni(OH)_2$ decomposes to NiO at 325°C [87]. Fang et al [88] found that γ-NiOOH has higher thermal decomposition temperature and better thermal stability than β-NiOOH. NiOOH decomposes to NiO according to the reaction

$$NiOOH = 2NiO + H_2O + 1/2\ O_2 \qquad (4.4)$$
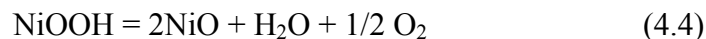
The β-NiOOH decomposes at 229.1°C whereas γ-NiOOH at 294.5°C. Komath et al [89] reported a decomposition temperature of ~230°C for γ-NiOOH.

Table 4.21 Crystallographic data for solid phases in the Ni-O-H ternary system

Phase/ temperature range	Pearson symbol space group /proto type	Lattice parameter(pm)
β- $Ni(OH)_2$	P3-M1	a = 312.6, c = 460.5
γ- NiOOH	CdCl2 type	a = 282, c = 2065

4.2.3.2 Thermodynamic modelling of phases

Ni-H binary is taken from the optimization of Zeng et al [90]. Ni-O binary is obtained from literature [82]. H-O binary data are obtained from the SGTE database. The liquid phase is assumed to contain Ni, O, and H along with the species Ni_1O_1, H_2O_2, and H_2O_1. The ternary compounds $Ni(OH)_2$ and NiOOH are treated as stoichiometric line compounds.

Their Gibbs energy data are obtained from SGTE database [83].

4.2.3.3 Calculated phase diagrams

It is known from the literature [87,89] that the ternary compound Ni(OH)$_2$ is not stable above 598 K and NiOOH is not stable above 567.5 K. So in the temperature range of interest (for intermediate temperature SOFC) these ternary compounds are not stable.

The Gibbs energies of these compounds obtained from SGTE substance database are adjusted according to the decomposition temperatures. Isothermal ternary phase diagrams are calculated at three different temperatures 400 K, 570 K and 600 K.

The isothermal section at 400 K shows the phase relations with both the ternary compounds stable at the temperature as shown in the Figure 4.51. At 570 K NiOOH is not stable as it can be seen in the Figure 4.52. Figure 4.53 shows the isothermal section at 600 K with no ternary compounds stable at that temperature.
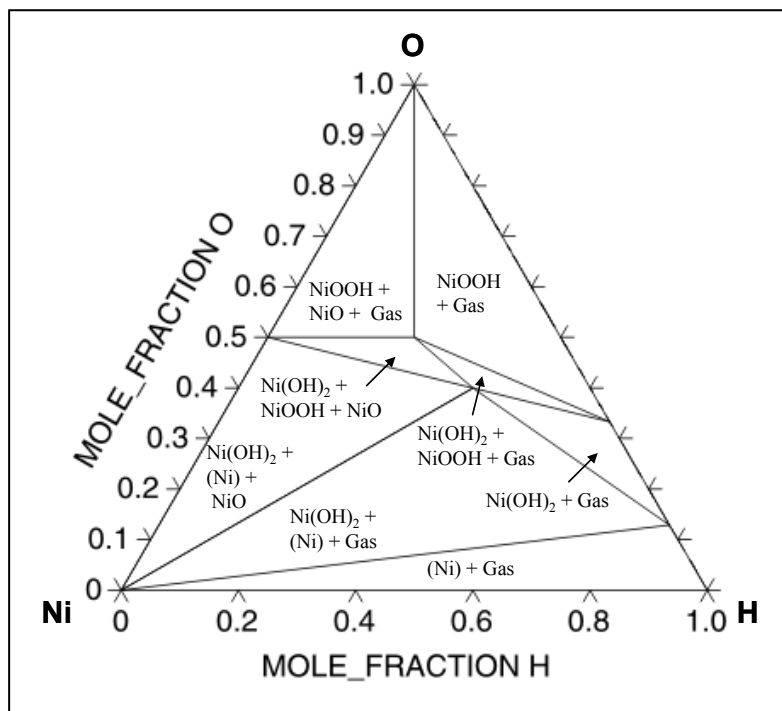
Figure 4.51 Ternary Ni-O-H isothermal section at 400 K
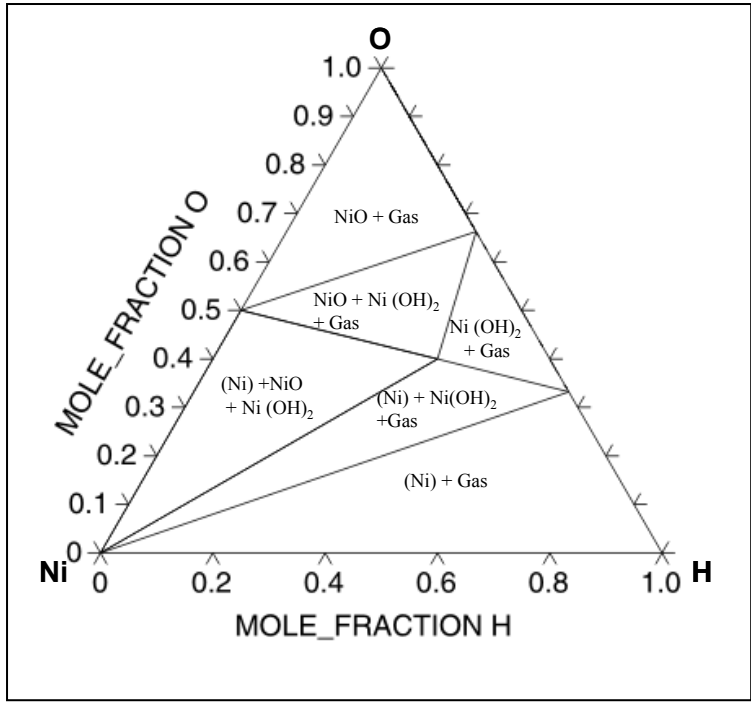
Figure 4.52 Ternary Ni-O-H isothermal section at 570 K
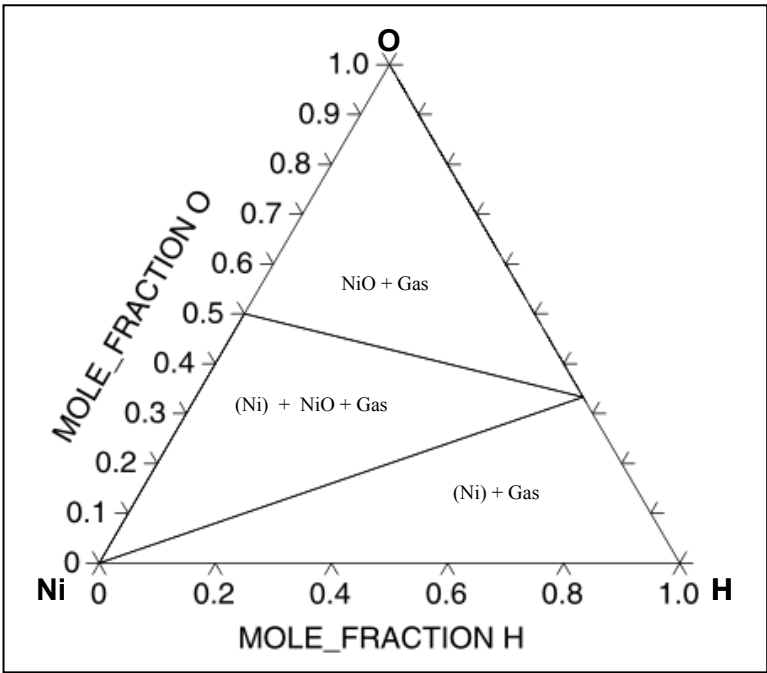
Figure 4.53 Ternary Ni-O-H isothermal section at 600 K

The optimised Gibbs energy models for the Ni(OH)$_2$ and NiOOH phases are given in Table 4.22.

Table 4.22 The optimised Gibbs energy model parameters

Parameter	Function
G(NiOOH,NI:O:H;0)	-628609.861+742.053243*T-73.45766*T*LN(T) -.01379017*T**2-1.50846617E-10*T**3+519168*T**(-1)
G(Ni(OH)2,NI:O:H;0)	-601758.851+ 553.961061*T-92.94439*T*LN(T) -.006690875*T**2-1.4826055E-10*T**3+663786*T**(-1)

This optimised Ni-O-H ternary is used for the calculation Ni-S-O-H quaternary.

4.2.4 Quaternary Ni-S-O-H system

The quaternary system is extrapolated from the four ternary systems (Ni-O-H, Ni-O-S, Ni-S-H and S-O-H).

The hydrates like $Ni(SO_4)(H_2O)_6$ belonging to the quaternary are not incorporated into the calculations. The solid phases from the lower order systems as shown in the previous chapters are incorporated into the quaternary system.

The gas phase is assumed to contain H, NiH, NiOH, HO, HO_2, H_2, NiH_2O_2, H_2O, H_2O_2, Ni, NiO, O, O_2, O_3, S, S_2, S_3, S_4, S_5, S_6, S_7, S_8, SO, SO_2, S_2O, O_3S, HSO, HS, H_2SO, HSOH, $H_2S O_4$, H_2S, and H_2S_2.

The liquid phase is modelled with Ni, S, NiS, NiO, H, H_2O, H_2O_2, $H_{10}O_8S$, $H_{15}O_{10.5}S$, $H_2S O_4$, H_4O_5S, H_6O_6S and H_8O_7S. It has to be noted that in the composition and the temperature range of our interest, the species H_2O, H_2O_2, $H_{10}O_8S$, $H_{15}O_{10.5}S$, $H_2S O_4$, H_4O_5S, H_6O_6S and H_8O_7S are not considered in the liquid phase.

Figures 4.54 and 4.55 show the stability of Ni as a function of $\log[P(H_2S)/P(H_2)]$ and $\log[P(H_2O)/P(H_2)]$ at 823 K and 1023 K respectively. The stability diagrams are calculated at $\ln(a_{H2})$ = -0.03045 which corresponds to P_{H2} of 0.97 atm in the $H_2+H_2O+H_2S$ gas mixture. Similarly, the stability diagrams can be calculated at the temperature of interest.
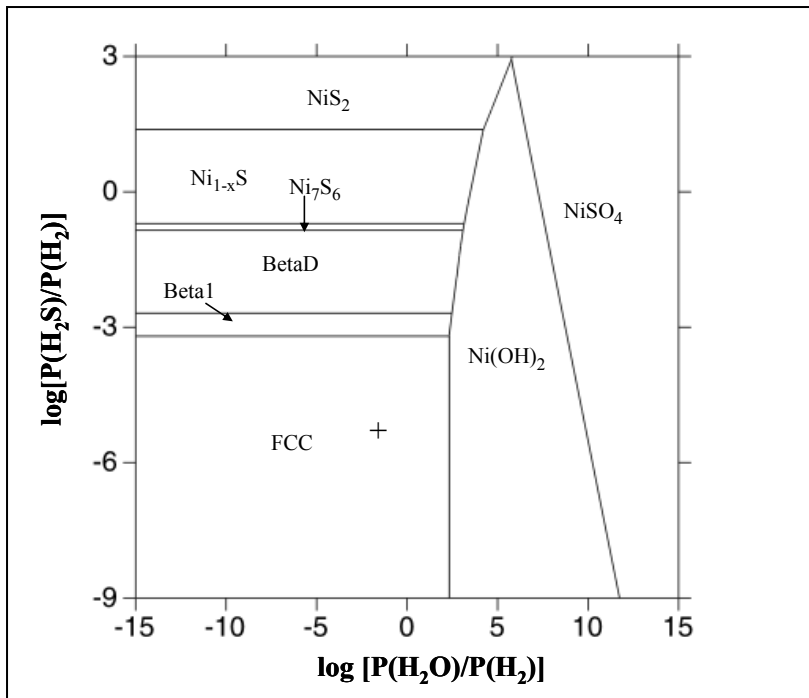
Figure 4.54 Predominance area diagram of Ni-S-O-H system at 823 K and $\ln(a_{H2}) = -0.03045$, in $\log[P(H_2S)/P(H_2)]$-$\log[P(H_2O)/P(H_2)]$ coordinates (a mark '+' is shown for 5ppm of H_2S in ~97 vol% H_2 and ~3 vol% H_2O gas).
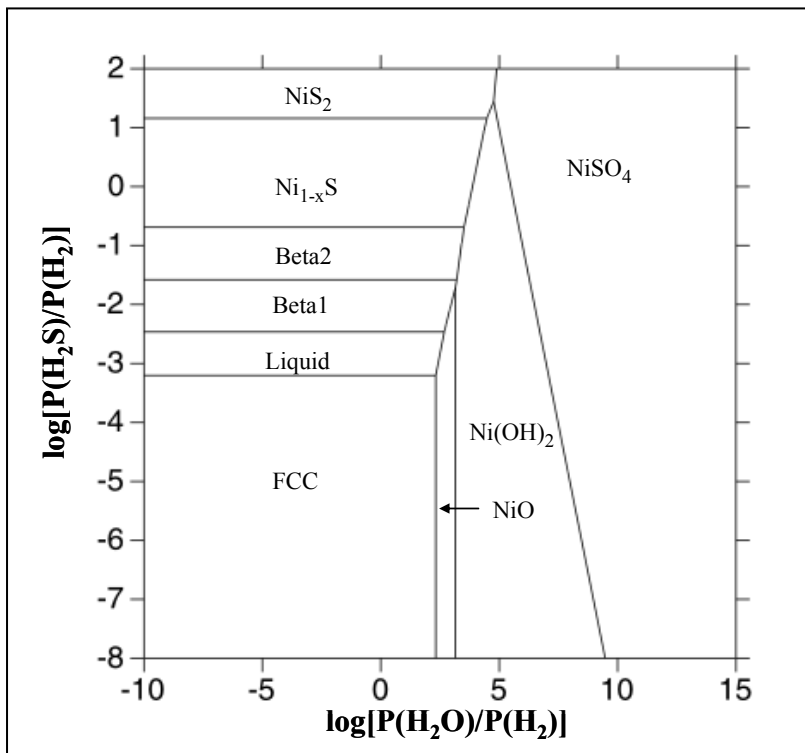
Figure 4.55 Predominance area diagram of Ni-S-O-H system at 1023 K $\ln(a_{H2}) = -0.03045$, in $\log[P(H_2S)/P(H_2)]$-$\log[P(H_2O)/P(H_2)]$ coordinates.

It can be seen from the figures (4.54 and 4.55) that at 1023 K there is an intermediate phase region of NiO between FCC_Ni and $Ni(OH)_2$ but not at 823 K. The drawback of Ni in the Ni-YSZ cermet anodes to form Ni(OH)2 at higher partial pressures of water in the fuel gas, is known [24]. So the calculated predominance area diagrams can be very useful to know the tolerance limits of Ni to partial pressures of H_2O and H_2S in the $H_2+H_2O+H_2S$ gas mixture at different temperatures.

4.3 Electrochemistry of Ni-patterned electrodes in H_2 + H_2O (+H_2S) atmospheres

4.3.1 Ni-patterned YSZ single crystals in H_2+H_2O

Figure 4.56 shows the Nyquist plot of the symmetrical cell of Ni-patterned YSZ single crystal with <111> orientation. It is clear from the plot that a perfect semicircle is recorded at higher frequencies. But at lower frequencies (<30 mHz) the same arc becomes slightly non-ideal. In the immediate next measurements the shoulder (deflection) disappeared. So it is either a single arc or two extremely overlapping arcs. In the case of two extremely overlapping arcs, both yield almost the same capacitance and resistance values. The situation of two extremely overlapping arcs may occur because of the possible change of the activation energy of the same activated process from high frequency end to low frequency end. Such a change in activation energy could occur because of the change in the surface chemistry of the electrode and/or electrolyte at lower frequencies. However it has been shown in literature by finite element studies that non-ideal impedance arcs may result from the frequency-dependent current lines and can not be understood in terms serial equivalent circuit models [91]. Keeping the perfect ideal nature of the semicircle in most of the frequency range and appearance of the deviation only at lower frequency, it can be considered that this is a single impedance arc.
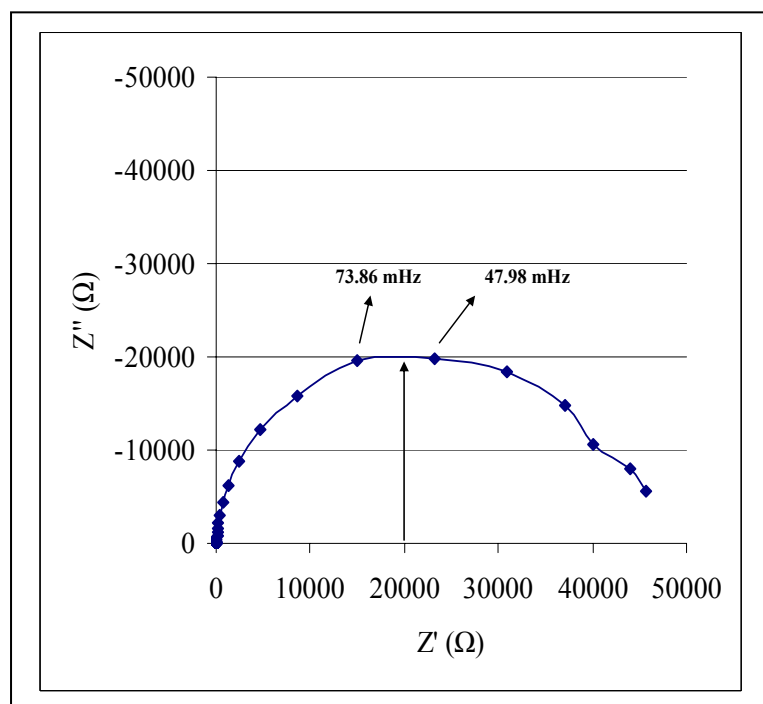
Figure 4.56 Impedance plot of Ni-patterned YSZ<111> single crystal at 823K in H_2 (99 vol%) + H_2O (1vol%)

Figure 4.57a shows the Nyquist plots of the Ni-patterned-YSZ single crystals with three different orientations measured at 823 K (for the experimental conditions see the Table 3.1). A single arc was measured in all the cases and the arcs are almost close to ideal semicircle. The exponent (n) of the constant phase element (CPE) obtained from the equivalent circuit fitting $(R_e(R_pQ_p))$ (the equivalent circuit is shown in the figure 3.8) is very close to one. The results of the equivalent circuit fit are shown in Table 4.23. The geometrical interfacial area of Ni-YSZ is 0.5204 cm^2 (according to the size and design of the pattern) was used to calculate the capacitance per unit interfacial area. It can be seen from the Table 4.23 that the exponent n is almost close to one. The exponent "n" becomes unity for ideal capacitance. So the CPE measured with the single crystals of different orientations is close to ideal capacitance. The capacitance values are obtained at summit frequency.

The absolute impedance |Z| as a function of frequency and phase angle as a function of frequency on Bode representation are shown in Figures 4.57b and 4.57c. The plot of log|Z| vs log(ω) of Ni-patterned YSZ<111> cell shows a slope of -0.94. The plot of phase angle (Φ) vs log(ω) is nearly a symmetrical bell curve but it doesn't reach 90°.
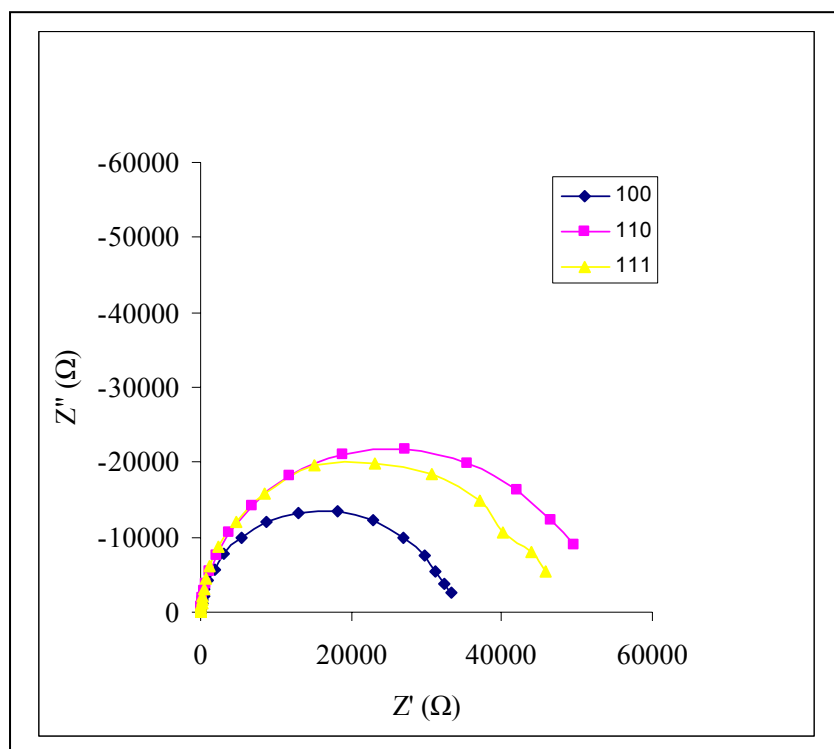
Figure 4.57a Nyquist plots of Ni-patterned-YSZ single crystals with three different orientations at 823 K in H$_2$ (99 vol%) + H$_2$O (1 vol%) .
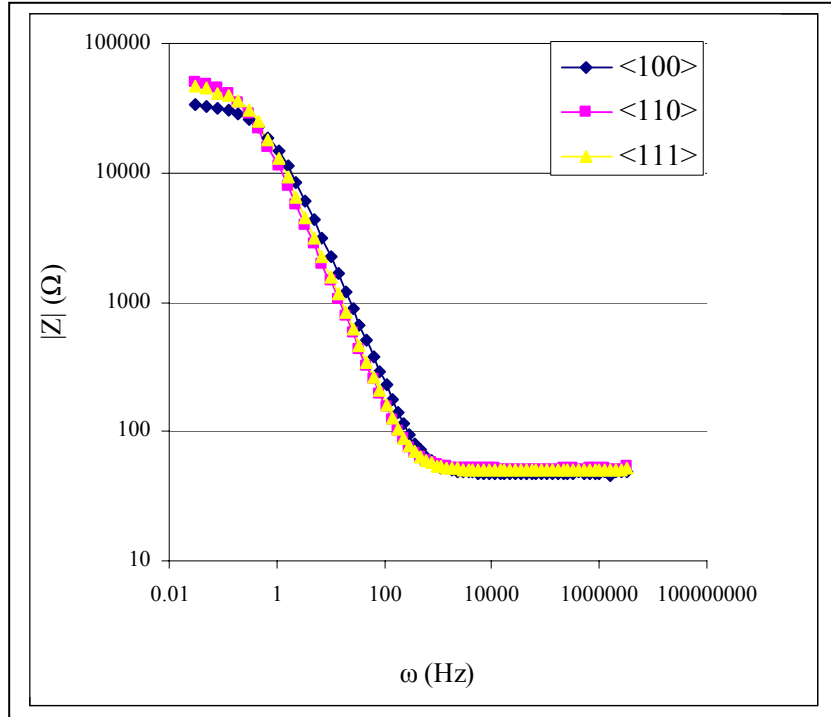
Figure 4.57b Bode plots of Ni-patterned-YSZ single crystals with three different orientations at 823 K in H_2 (99 vol%) + H_2O (1 vol%).
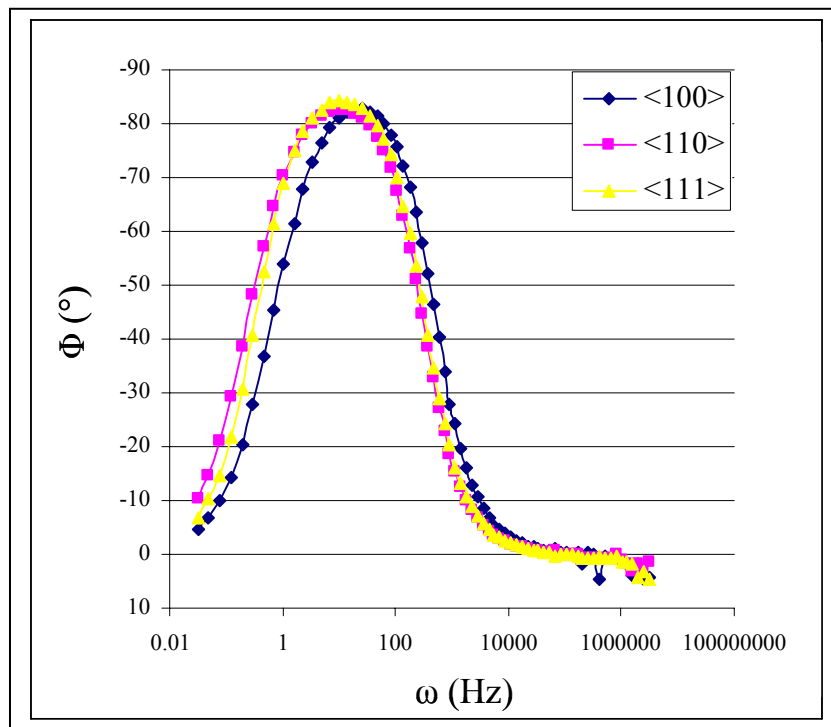
Figure 4.57c Bode plots of Ni-patterned-YSZ single crystals with three different orientations at 823 K in H_2(99 vol%) + H_2O (1 vol %).

Table 4.23 Equivalent circuit fit results of Ni-patterned YSZ single crystals of different orientations measured at 823 K

Orientation of YSZ in Ni-YSZ-Ni	R_e Ω	R_p, $k\Omega$	Peak frequency(f*) Hz	Capacitance from CPE (Q_p) $\mu F/cm^2$	Exponent of CPE n
<100>	47.01	30.09	0.074	100.92	0.961
<110>	50.93	48.11	0.031	167.62	0.952
<111>	50.38	42.78	0.048	135.31	0.975

Figures 4.58a and 4.58b show the high frequency intercepts of the YSZ single crystals at 823 K and 773 K. The values of the high frequency intercepts of the Nyquist plots of Ni-patterned YSZ single crystals for three different orientations are listed in Table 4.24. It can be seen from the table that the obtained capacitance from CPE is different depending on the face of the YSZ single crystals. It is evident that $C_{<100>} < C_{<111>} < C_{<110>}$.
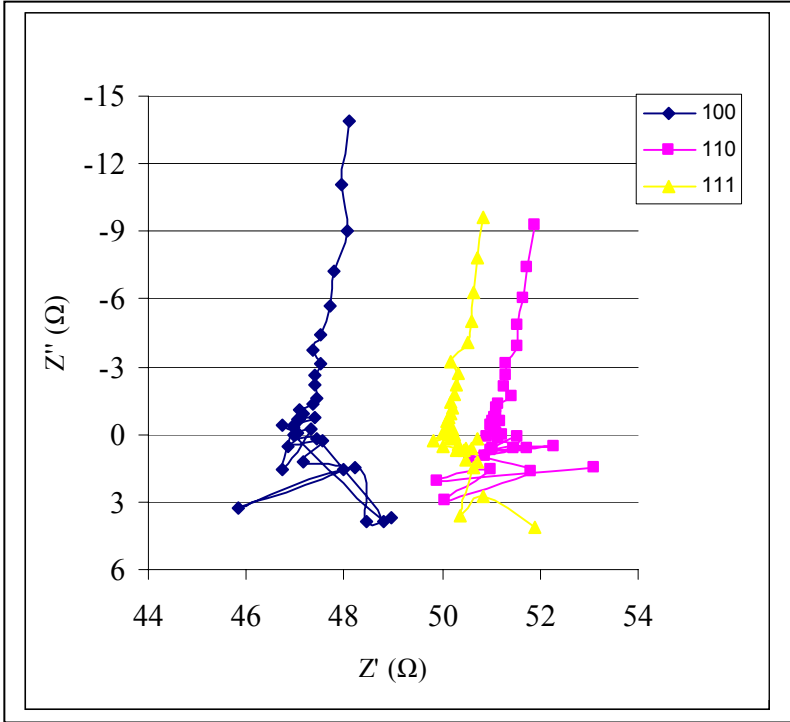
Figure 4.58a High frequency intercepts of the Nyquist plots of Ni-patterned-YSZ single crystals with three different orientations measured at 823 K in $H_2 + H_2O$ (1 vol %).
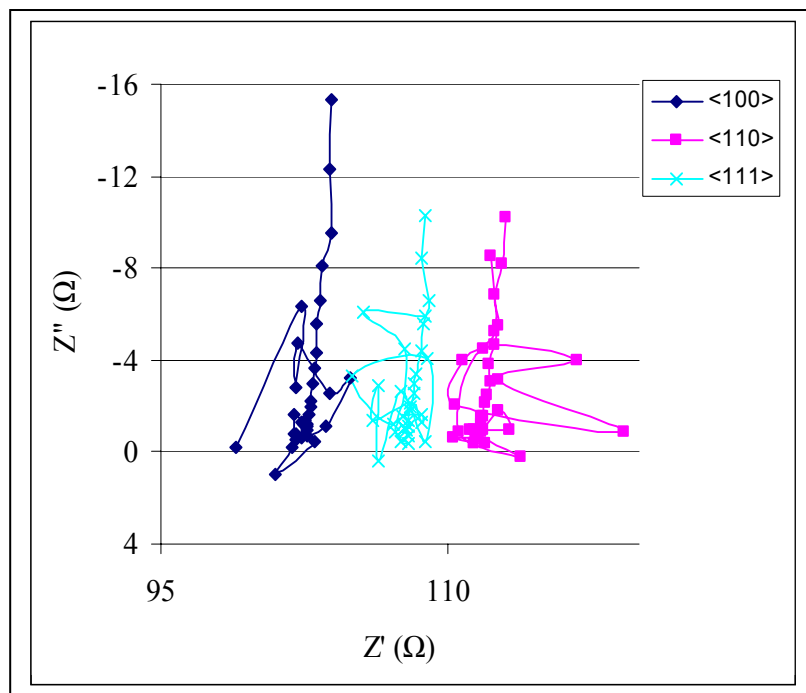
Figure 4.58b High frequency intercepts of the Nyquist plots of the Ni-patterned-YSZ single crystals with three different orientations measured at 773 K in $H_2 + H_2O$ (1 vol %).

Table 4.24 The high frequency intercepts (R_e) from the Nyquist plots of Ni-patterned YSZ single-crystal symmetrical cells at two different temperatures 823 K and 773 K (from Figures 4.58a and 4.58b).

Orientation	Re (Ω) at 823 K	Re (Ω) at 773 K
<100>	47.3	102
<110>	51.1	111
<111>	50.2	108

Measurements were conducted twice to check the reproducibility of the various results in the single crystal measurements. A comparison of the two sets of experiments lead to some interesting observations. The results of the equivalent circuit fit of the impedance data of the second set of measurements under similar conditions are shown in Table 4.25. From the second set of measurements with the three different orientations it was found that the measured polarisation resistance (R_p) of all the three cells is less than their respective values in the first set of measurements (Table 4.23). And also the trend of the obtained Rp depending on the orientation is not same as the first set of measurements. However it can be seen that the capacitance from CPE and the exponent 'n' are similar to the first set of measurements and are well reproduced. The capacitance values obtained for different orientations of YSZ are

94

related as $C_{<100>} < C_{<111>} < C_{<110>}$. The exponent 'n' is also found to vary depending on the face of the YSZ single crystal.

The difference in high frequency intercept depending on the orientation especially between the <100> and <110>, <111> orientations, was found to be reproducible, although it is known that the cubic crystals are isotropic in conductivity. Table 4.26 lists the values of the high frequency intercepts of the Nyquist plots measured at 823 K and 773 K from the second set of measurements.

Table 4.25. Equivalent-circuit fit results of Ni-patterned YSZ single crystals measured at 823 K (second set)

Orientation of YSZ in Ni-YSZ-Ni	R_e Ω	R_p k Ω	Peak frequency(f^*) Hz	Capacitance from CPE(Q_p) $\mu F/cm^2$	Exponent of CPE n
<100>	48.96	18.22	0.1462	92.91	0.961
<110>	52.17	18.68	0.09537	153.67	0.957
<111>	52.87	22.18	0.09537	130.82	0.974

Table 4.26 The high frequency intercepts (R_e) from the Nyquist plots of Ni-patterned YSZ single-crystal symmetrical cells at two different temperatures 773 K and 823 K (second set).

Orientation	R_e (Ω) at 823 K	R_e (Ω) at 773 K
<100>	47.3	102
<110>	51.1	111
<111>	50.2	108

Table 4.27 shows the the capacitance obtained from CPE (Q_p) of Ni-patterned YSZ single crystal cells of different orientations. It can be seen from the Table that the capacitance is almost independent of temperature.

Table 4.27 Capacitance obtained from CPE of symmetrical cells of Ni-patterned YSZ single crystals of three different orientations as a function of temperature

Temperature	C<100> $\mu F/cm2$	C<110> $\mu F/cm2$	C<111> $\mu F/cm2$
823 K	92.91	153.67	130.82
773 K	90.05	140.72	131.51
723 K	80.84	131.86	125.86

4.3.2 Ni-patterned YSZ polycrystalline samples

4.3.2.1 In H_2+H_2O

Figure 4.59 shows the Nyquist plots of the Ni-patterned YSZ symmetrical cell at 823K at different partial pressures of water in H_2 gas. A single arc was observed in the whole range of experimental conditions (Table 3.1). It appears that a single electrode process is responsible for the arc. A relaxation frequency, ω^* of 1.474 Hz was obtained from the Nyquist plot, at which the imaginary impedance of the arc reaches its maximum value.
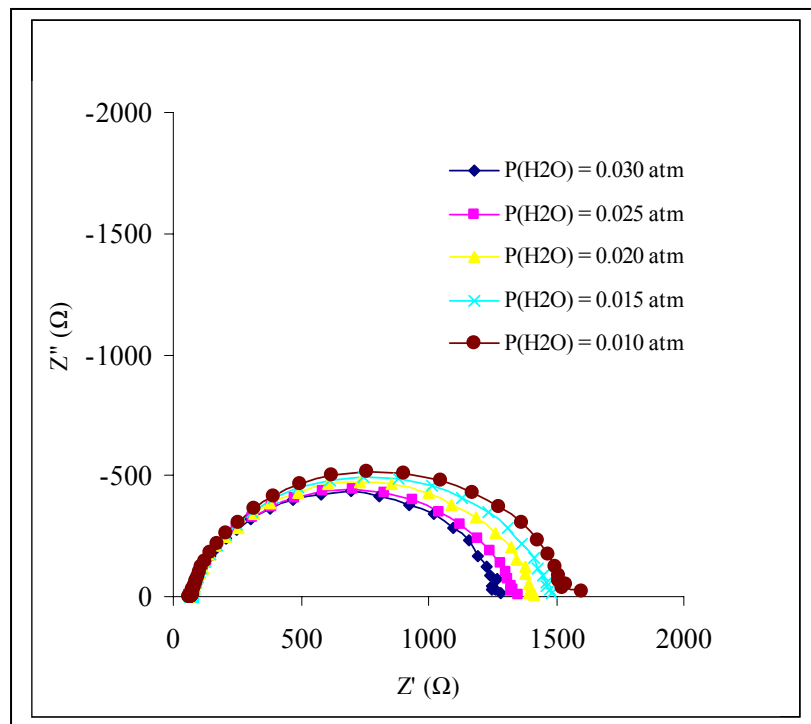
Figure 4.59 Nyquist plots of the Ni-patterned YSZ polycrystalline symmetrical cells at 823 K as a function of $P(H_2O)$ in H_2+H_2O gas.

A single arc was reported by Mizusaki et al [28] and Gauckler et al [30] for their Ni-patterned YSZ single crystals measured under similar conditions. Gauckler et al also measured the impedance spectra with different applied anodic overpotentials and with different lengths of triple phase boundaries [92,30]. However for the Ni-YSZ cermets Mogensen et al reported two or three distinct arcs from the measurements conducted in the temperature range of 850-1000°C in H_2+H_2O atmosphere [24].

Even though this apparently single arc can be fitted with two or more number of electrode processes, but a single rate limiting step is assumed because of the following reason.

Almost a perfect single semicircle was measured for the Ni-patterned YSZ single crystals as shown in the previous chapter. The frequency exponent of CPE of the Ni-patterned YSZ single crystals is close to 1. However in the case of Ni-patterned YSZ polycrystalline samples the measured arc is relatively depressed and its frequency exponent of the CPE is around 0.8. Relatively low value of the exponent in the case of polycrystalline YSZ may be probably because of the distributed reaction rates of the same rate limiting process. So in the case of Ni-patterned polycrystalline samples it can be assumed that a single electrode process is responsible for the observed impedance arc.

The impedance spectra of these Ni-patterned YSZ polycrystalline symmetrical cells were fitted with an equivalent circuit $(R_e(R_pQ_p))$ (Figure 3.8).

Table 4.28. Equivalent circuit fit results of the imepdance of Ni-patterned YSZ polycrystalline samples

Capacitance from CPE($\mu F/cm^2$)	R_e (Ω)	R_p (kΩ)	n	Peak frequency, f* (Hz)	T(K)
116.03	71.33	1.681	0.819	1.474	823
112.53	154.7	3.372	0.811	0.717	773
113.91	383.6	7.241	0.793	0.332	723
114.83	1100	16.77	0.775	0.146	673

Table 4.28 shows the obtained values of capacitance of CPE, Re and Rp. The capacitance values were calculated at peak frequency. It can be seen that the obtained capacitance values are independent of temperature. These capacitance values fall in between the values exhibited by single crystals of different orientations. The capacitance per unit area was calculated from the geometrical interfacial area of Ni-YSZ interface.

Table 4.29 shows the capacitance obtained from the impedance arc at 823K as a function of $P(H_2O)$. It can be seen that the capacitance slightly increases with increasing partial pressure of water in the gas.

Table 4.29 Capacitance of CPE, obtained from the equivalent circuit fit, as a function of $P(H_2O)$ at 823 K.

$P(H_2O)$ (atm)	Peak frequency (Hz)	Capacitance of CPE ($\mu F/cm^2$)	Exponent of CPE (n)
0.03	2.077	116.29	0.807
0.025	2.077	113.89	0.810
0.02	2.077	110.65	0.813
0.015	2.077	108.97	0.815
0.01	2.077	106.51	0.821
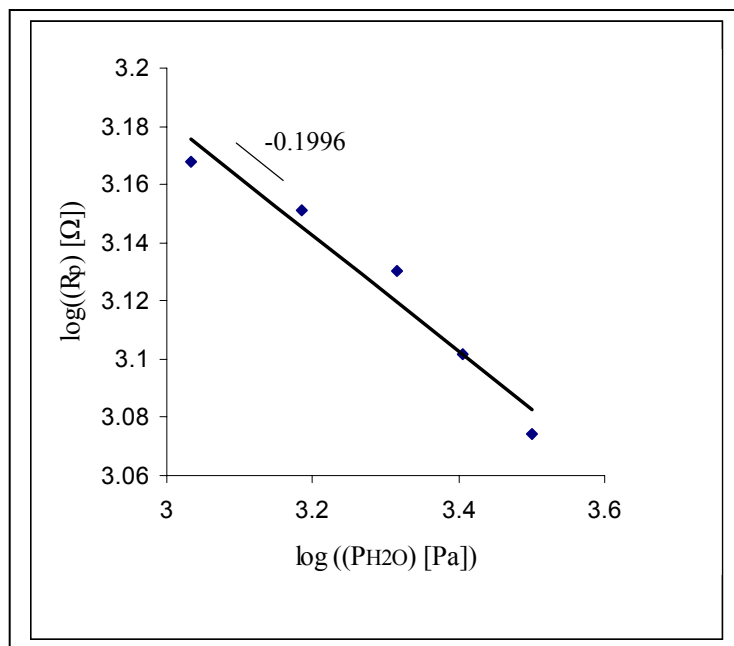
Figure 4.60 Dependence of the electrode resistance of Ni-patterned YSZ polycrystalline samples on $P(H_2O)$ in the gas mixture H_2+H_2O at 823 K.

Figure 4.60 shows the variation of electrode polarisation resistance as a function of partial pressure of water vapour in the gas mixture. The slope of the logarithmic plot is -0.1996. It can be seen that the dependence is not very steep. In literature a stronger dependence with a slope of -0.67 is reported [30] from the measurements in a gas mixture of $H_2+N_2+H_2O$. As it can be seen the total polarisation resistance decreases with increasing partial pressure of water in the gas mixture H_2+H_2O.

The temperature dependence of the electrolyte conductivity determined from the high frequency intercept of the Nyquist plot can be seen in the figure 4.61. Activation energy of 0.87 eV is obtained from the plot. Similar activation energy of 0.84-0.86 eV is reported in literature but measured in the high temperature regime, 600-1000°C [29,93].
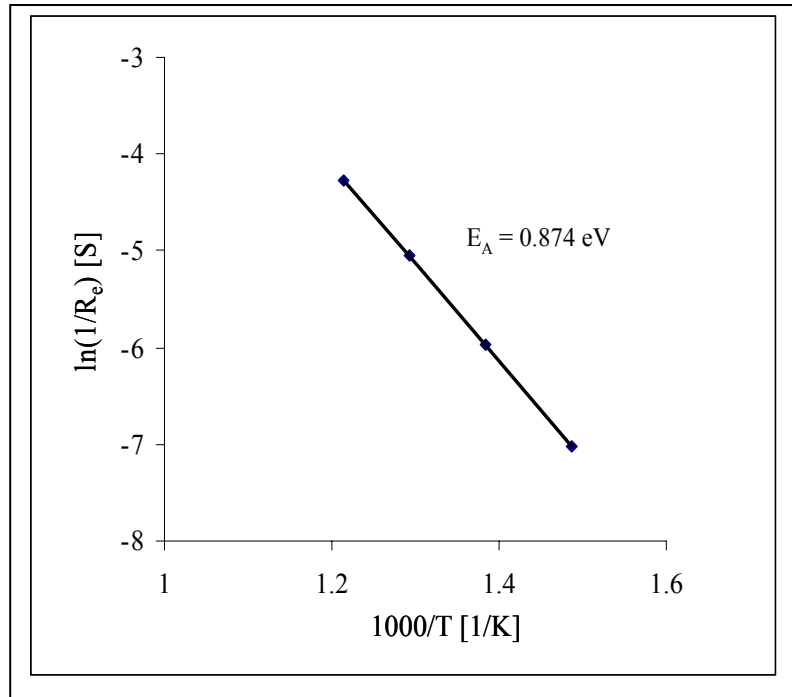
Figure 4.61 Arrhenius plot of the conductivity of the electrolyte measured in H_2 + H_2O (3 vol%)

Figure 4.62 Arrhenius plot of the electrode conductivity of Ni-patterned YSZ (polycrystalline) cells measured in H_2 + H_2O (3vol%) gaseous atmosphere.

Temperature dependence of the electrode conductivity measured in H_2+H_2O (3 vol%) is shown in the figure 4.62. Activation energy of 0.74±0.03 eV was determined from the plot. In

literature in the similar measurements with Ni-patterned electrodes Gauckler et al [30] and Boer et al [29] reported an activation energy of 0.88 ± 0.04 eV and 1.606 eV, repectively.

4.3.2.2 Effect of 5 ppm of H_2S in $H_2 + H_2O$

The impedance spectra recorded as a function of time in H_2+H_2O (3 vol%)+H_2S (5 ppm) gaseous atmosphere at 823 K are shown in Figure 4.63a. The first impedance spectrum shown in the figure is the spectrum measured with no H_2S in the gas mixture H_2+H_2O (6 vol%). The release of H_2S means, as mentioned already, the H_2+H_2O (6 vol%) gas mixture and H_2+H_2S (10 ppm) gas from the gas bottle are fed (mixed) into a chamber in the required ratios, before feeding into the impedance cell. The moment H_2S was released, the measurement was started. From then onwards the impedance spectra are continuously recorded as a function of time in the H_2+H_2O (3 vol%)+H_2S (5ppm) gaseous atmosphere. It can be seen in the figure that the impedance spectrum measured immediately after the release of the H_2S shows an initial drop in the electrode impedance and then increases afterwards (Figure 4.63b).
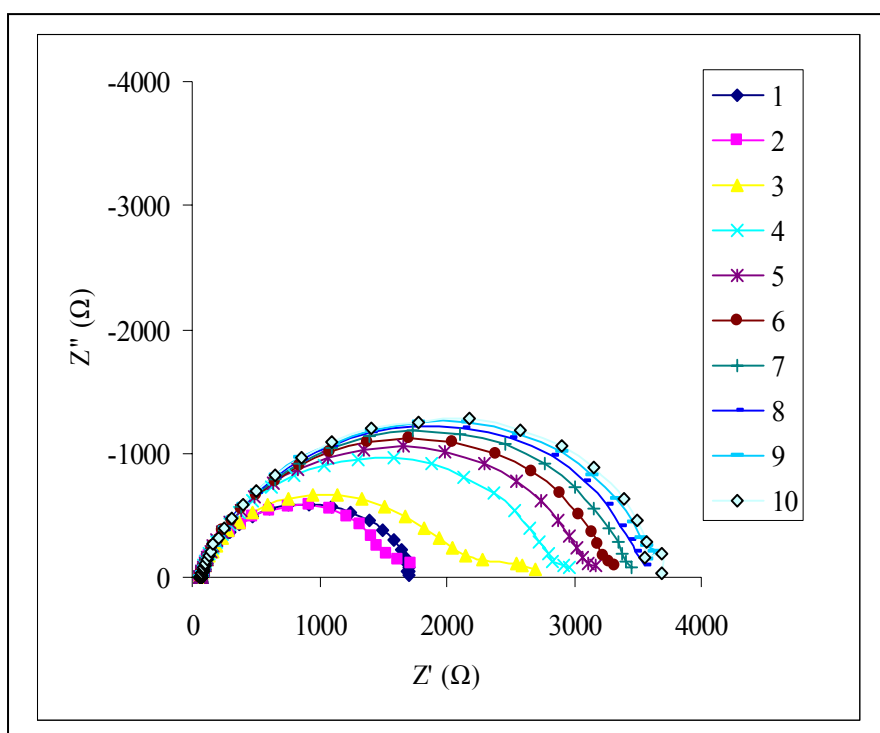
Figure 4.63a The electrochemical impedance spectra of Ni-patterned YSZ with 5 ppm H_2S in H_2+H_2O (3 vol%) gas as a function of time at 823K. (1- no H_2S, 2-immediatly after release of H_2S, 3-after 51 min , 4- after 91 min,5- after 133 min, 6- after 173 min, 7-after 223 min, 8-after 264 min, 9- after 314 min, 10-after 357 min)
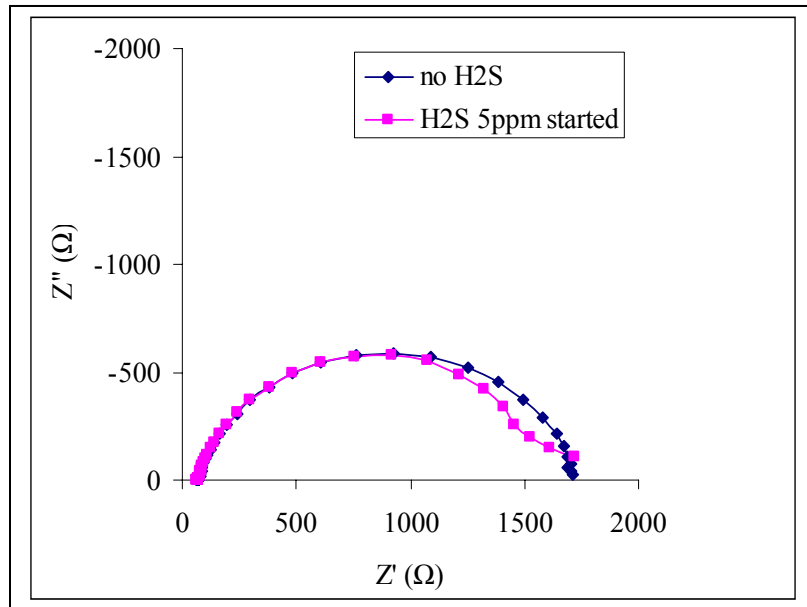
Figure 4.63b Initial drop in the impedance spectrum immediately after the release of 5 ppm of H_2S into the gaseous atmosphere H_2+H_2O (3 vol%) (also seen in the Figure 4.63a)
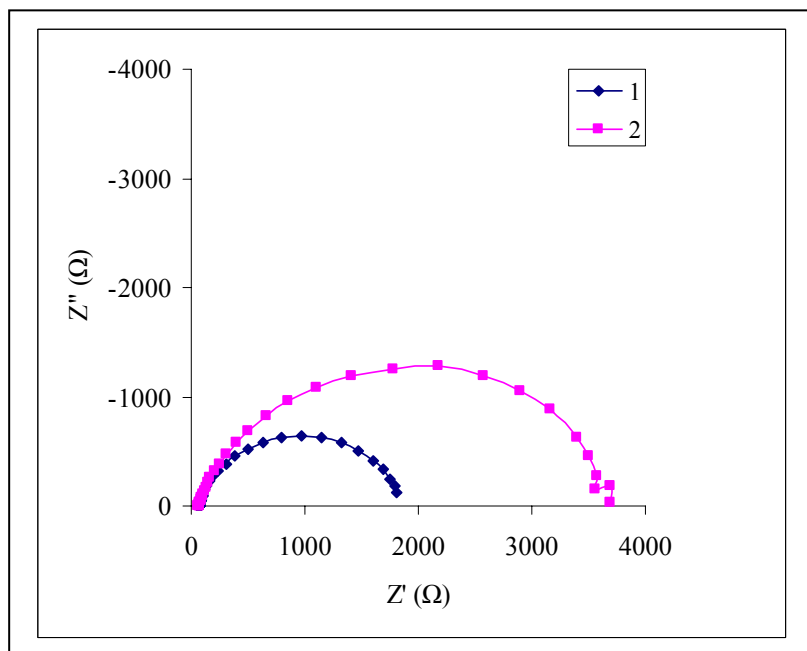
Figure 4.63c Impedance spectra of Ni-patterned YSZ polycrystalline cells in H_2+H_2O (3 vol%) gas with and without 5 ppm of H_2S at 823 K(1- in H_2+H_2O (3 vol%),2- H_2+H_2O (3 vol%)+5 ppm H_2S)

After 6 hours, the impedance spectrum of the symmetrical cell reached saturation in the gaseous atmosphere containing 5 ppm H_2S. Figure 4.63c compares the impedance plots measured in H_2+H_2O (3 vol%) gas with and without 5 ppm of H_2S. An increase in R_p (the low

frequency intercept on the Nyquist plot) by 100% because of 5 ppm of H_2S can be seen from the figure. When the spectrum becomes stable, H_2S supply was stopped and reversibility of the impedance spectrum was recorded as a function of time. Figure 4.64 shows the reversal of the impedance spectrum starting from immediately after the withdrawal of 5 ppm of H_2S from the gaseous atmosphere. The reversal of the spectrum is measured in the gaseous atmosphere of H_2+H_2O (6 vol%) for totally 40 hours. It can be seen that the spectrum didn't reverse completely to the initial one even after 40 hours.
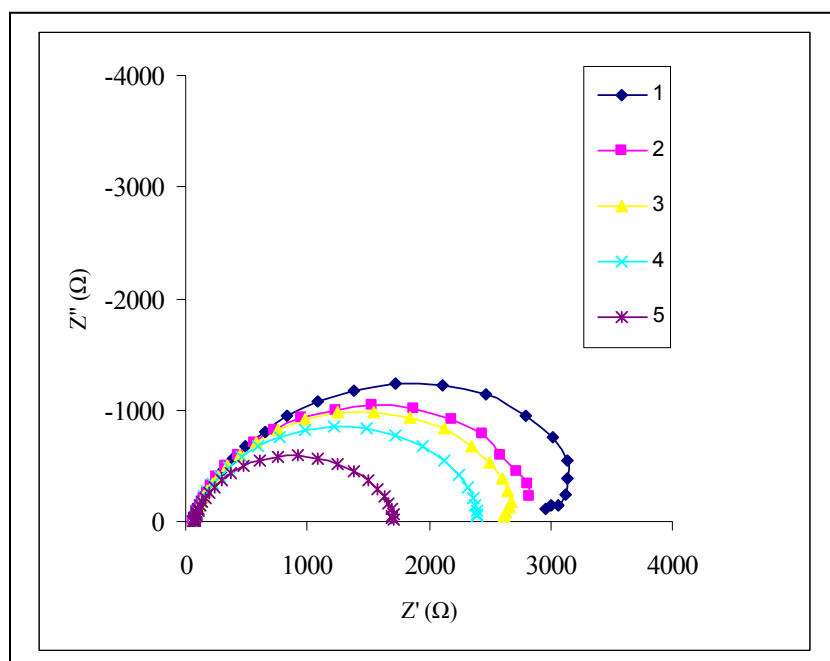
Figure 4.64 Impedance spectra as a function of time after removal of 5 ppm of H_2S from the H_2+H_2O gas at 823 K. (1- H_2S is withdrawn, 2- after 192 min,3- after 673 min, 4- after 2437 min, 5- before H_2S poisoning)

Impedance of the Ni-patterned polycrystalline YSZ cells in H_2+H_2O (3 vol%)+H_2S (5 ppm) gas was also measured as a function of temperature. The Arrhenius plot of the electrode conductivity with 5 ppm H_2S in H_2+H_2O (3 vol%) gas mixture is shown in Figure 4.65. It can be seen that the activation energy obtained from the slope of the plot is close to the activation energy determined without 5ppm of H_2S in H_2+H_2O (3 vol%) gas (Figure 4.62).
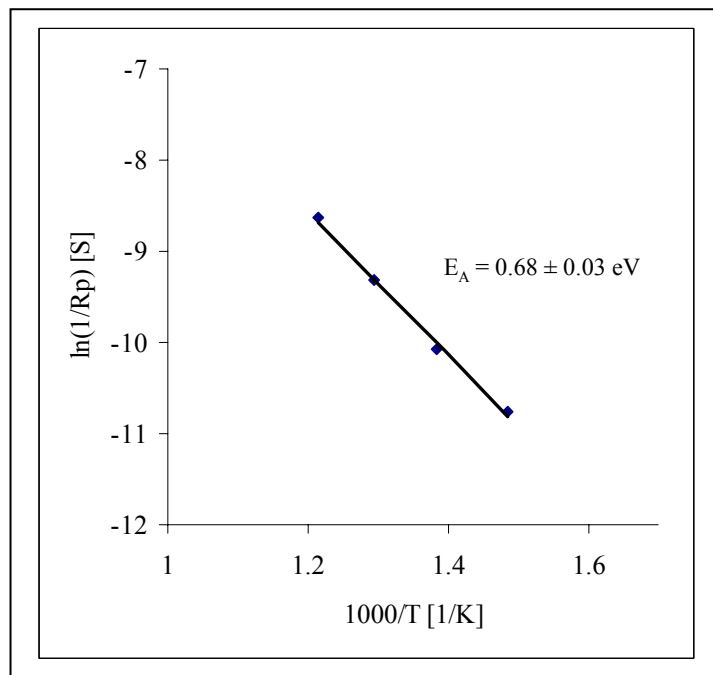
Figure 4.65 Arrhenius plot of the electrode conductivity of Ni-patterned YSZ in H_2+H_2O (3 vol%) + H_2S (5 ppm).

4.3.3 Ni-patterned LSGM

4.3.3.1 In H_2+H_2O

Nyquist plots of Ni-patterned LSGM symmetrical cells measured in H_2+H_2O gas at 823 K as a function of partial pressure of H_2O is shown in the figure 4.66.
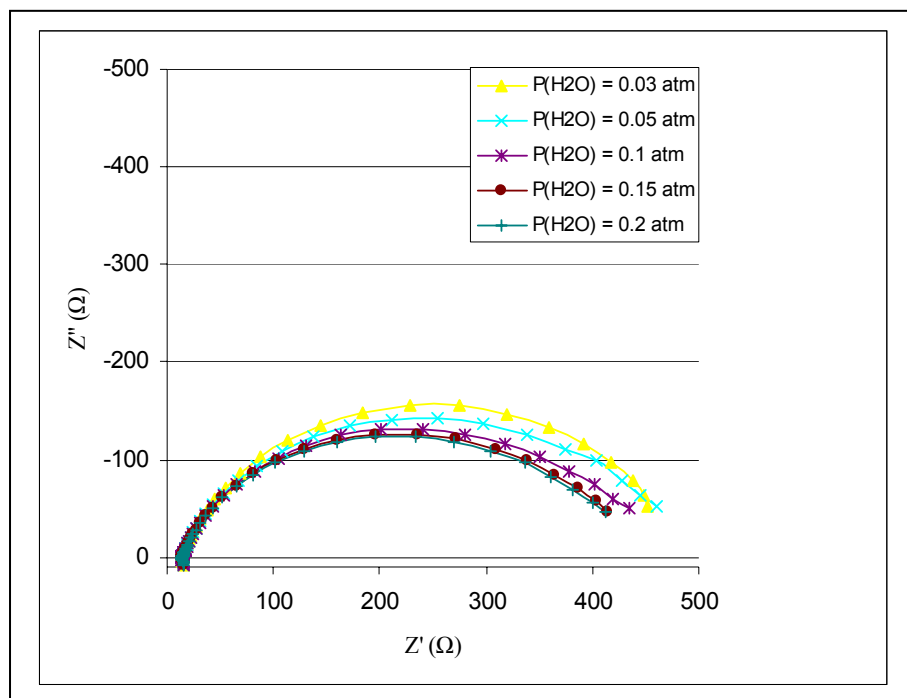
Figure 4.66 Nyquist plots of Ni-patterned LSGM cells at 823 K as a function of partial pressure of H_2O in H_2+H_2O gas.

As in the case Ni-patterned YSZ single crystals and Ni-patterned YSZ polycrystalline samples, a single arc is observed in the whole range of experimental conditions.

The equivalent circuit $R_e(R_1Q_1)$ (Figure 3.8) is used to analyse the data. The values of R_e, R_1 and Q_1 obtained from the equivalent circuit fit are shown in the Table 4.30.

Table 4.30 Results of Equivalent circuit fit of Ni-patterned LSGM polycrystalline samples in H_2+H_2O (3 vol%) gas

Capacitance from CPE ($\mu F/cm^2$)	R_e (Ω)	R_p (Ω)	Exponent of CPE (n)	Peak frequency(f*) (Hz)	T (K)
958.5	13.99	408.2	0.764	0.799	823
1193.1	24.39	948.2	0.746	0.236	773
1554.8	55.91	1776	0.708	0.0983	723
3111.1	159.9	3876	0.653	0.0159	673

It is evident from Table 4.30, that the capacitance values are dependent on temperature unlike Ni-patterned YSZ polycrystalline sample.

Figure 4.67 shows the electrolyte resistance R_e, obtained from the high frequency intercept of the Nyquist plot as a function of temperature. The conductivity of LSGM obtained at 823 K is 0.0106 S/cm which is in good agreement with the conductivity data (0.026 S/cm at 868 K) reported by Goodenough et al for LSGM of similar composition. They measured the conductivity of LSGM with various concentration of Sr- and Mg- dopants by using platinum electrodes [3]. The activation energy obtained from the slope of the Arrhenius plot is 0.763 eV.
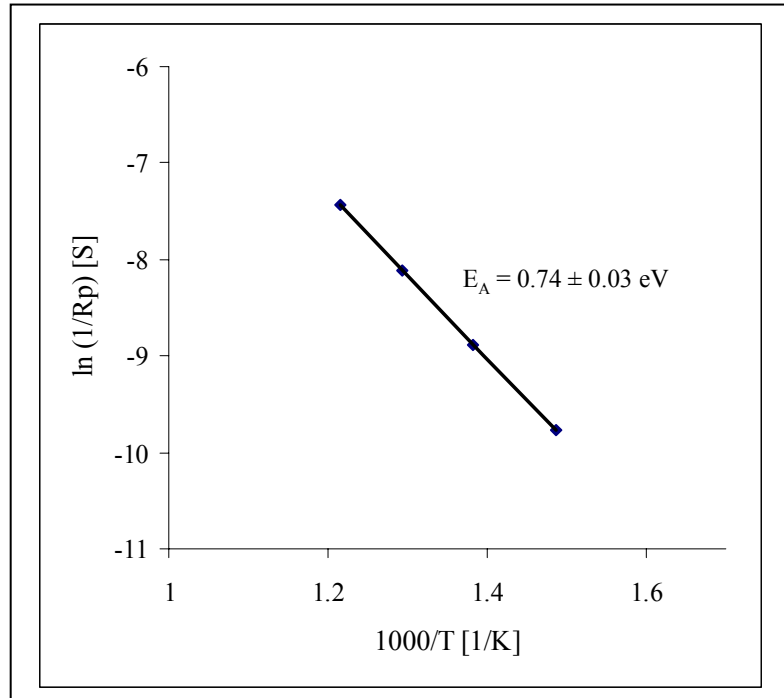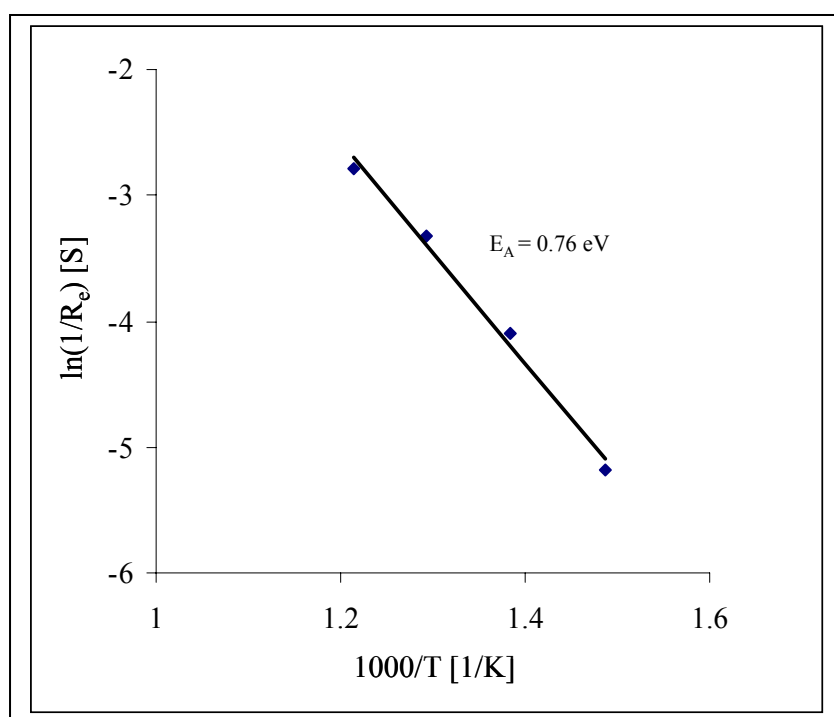

Figure 4.67 Arrhenius plot of the electrolyte conductivity of Ni-patterned LSGM cells measured in $H_2 + H_2O$ (3 vol%) gas.

The electrode conductivity σ_p (=1/R_p) is plotted as a function of temperature as shown in Figure 4.68. The activation energy obtained from the plot is 0.71 ± 0.03 eV. Studies with Ni-LSGM electrode system without having any reactivity problem are not reported in literature. So a direct comparison can not be made.
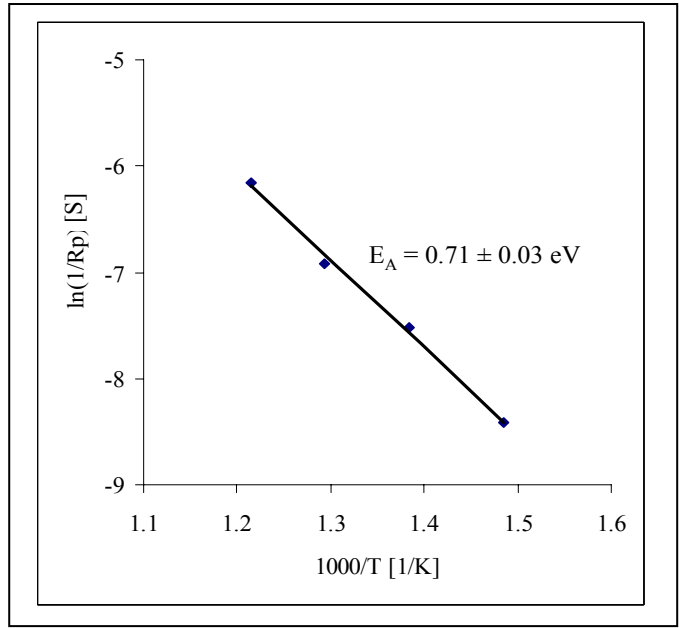
Figure 4.68 Temperature dependence of the electrode conductivity of Ni-patterned LSGM symmetrical cell measured in H_2+H_2O (3 vol%) gas

Figure 4.69 depicts the dependence of polarisation resistance on partial pressure of H_2O in the fuel gas phase. The partial pressure of water in H_2+H_2O gas mixture was varied from 0.01 atm to 0.2 atm. It can be seen that there is very little influence of partial pressure of water on R_p. However the R_p slightly decreases with the increasing partial pressure of H_2O (can also be seen from the nyquist plots in Figure 4.66). The slope the log R_p vs log$P(H_2O)$ plot is -0.0485. The similar effect $P(H_2O)$ on R_p at lower temperatures has been found.
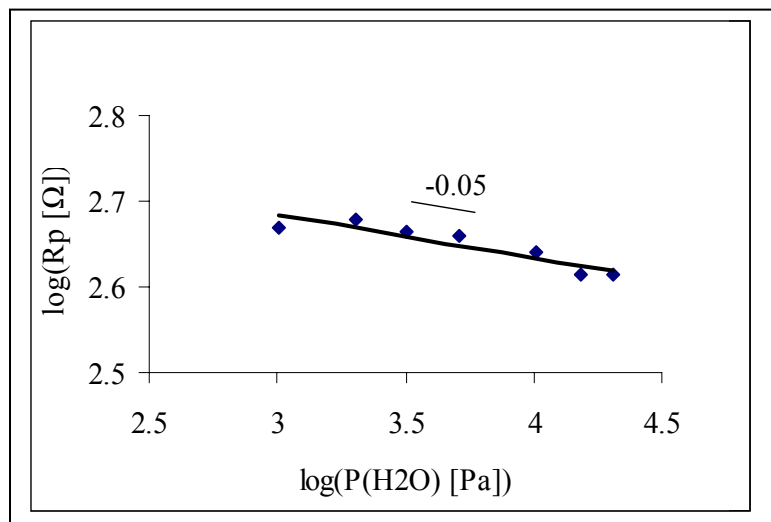
Figure 4.69 Effect of $P(H_2O)$ on the polarisation resistance (R_p) of Ni-patterned electrodes on LSGM electrolyte, at T=823 K

4.3.3.2 Effect of 5 ppm of H₂S in H₂+H₂O

The effect of 5 ppm of H_2S to the H_2+H_2O fuel gas on the complex impedance spectrum is shown in the figure 4.70a. The impedance spectra are numbered from 1-8 as shown in the figure. Spectrum 1 is measured in H_2S free H_2+H_2O (40 vol%) gas, before the addition of 5 ppm of H_2S. Immediately after the addition of H_2S the impedance measurements are started and continuously performed until the spectra showed no change with time. The spectrum 2 was recorded immediately after the addition. The spectrum measured immediately after the addition of H_2S showed an initial drop in the impedance values before increasing to higher impedance values. It is worth mentioning here that the measurements of impedance spectra run from the high frequency limit to the low frequency limit. Figure 4.70b depicts the initial drop in the impedance measured immediately after the introduction of 5 ppm of H_2S. The spectra 3-8 were measured continuously one after the other. The electrode resistance R_p increased with time and became stable after 3 ½ h. The spectrum has reached a saturation value after 223 min and remained stable.
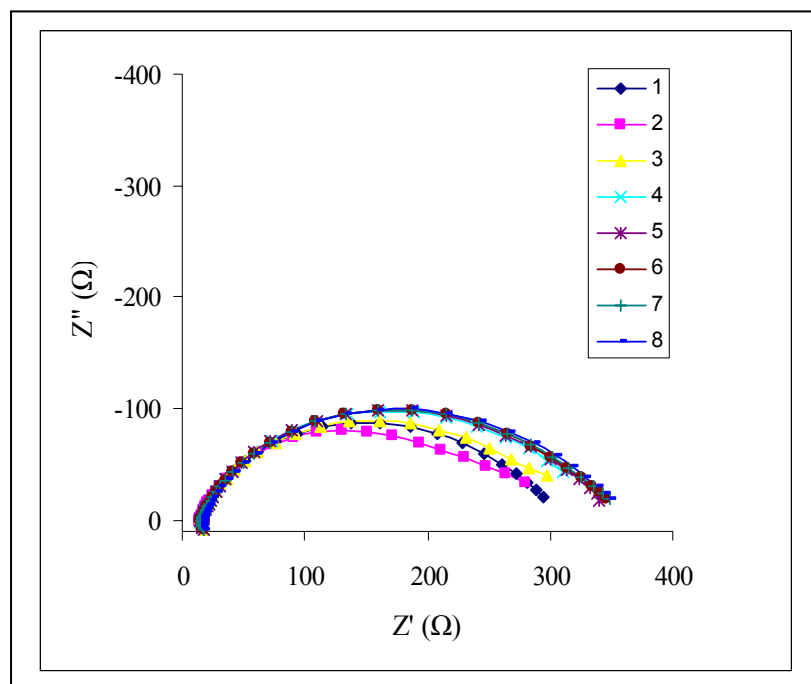
Figure 4.70a The effect of 5 ppm of H_2S in H_2 + 20 vol% H_2O on the impedance spectra of Ni-patterned LSGM symmetrical cells at 823 K (1- no H_2S, 2- 5 ppm of H_2S released, 3- after 24 min, 4-after 37 min, 5-after 79 min, 6-after 130 min, 7-after 178 min, 8-after 223 min)
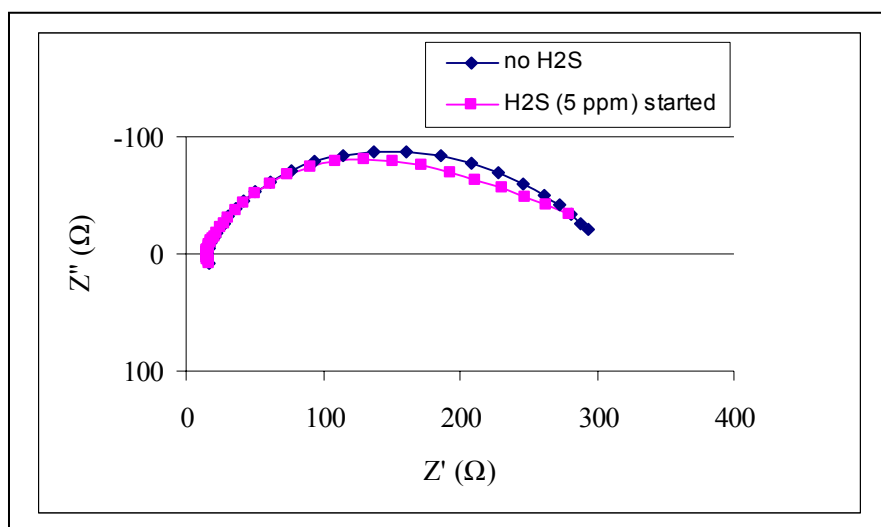
Figure 4.70b Initial drop in the impedance spectrum immediately after the release of 5ppm of H_2S into H_2+20 vol% H_2O at 823 K.

Results show that with addition of 5 ppm of H_2S the cell performance is degraded. But the degradation is preceded by a short increase in the electrode current i.e a short enhancement in the cell performance. It is worth mentioning here that the initial drop has been reproduced several times. It was shown in the previous section that the same effect was also observed with the Ni-patterned YSZ cells.

After the impedance spectrum has reached its maximum and has become stable, H_2S was withdrawn from the gas mixture to check the reversibility of the spectrum. The complex impedance measurements were continuously performed as function of time in the H_2+H_2O (40 vol%) gas. Figure 4.71 depicts the reversibitliy of the impedance spectra after withdrawing 5 ppm H_2S from the H_2+H_2O gas mixture. The impedance spectra are numbered from 1-5 (not all measurements which were done while checking for the reversibility are shown). The spectrum 5 is the measurement done before the addition of 5 ppm of H_2S. It can be seen that spectra 4 and 5 completely match with each other showing the complete reversal of impedance with the removal of H_2S from the gas. The time taken for complete reversal i.e., from the spectrum 1 to 5 is 4 h 18 min.
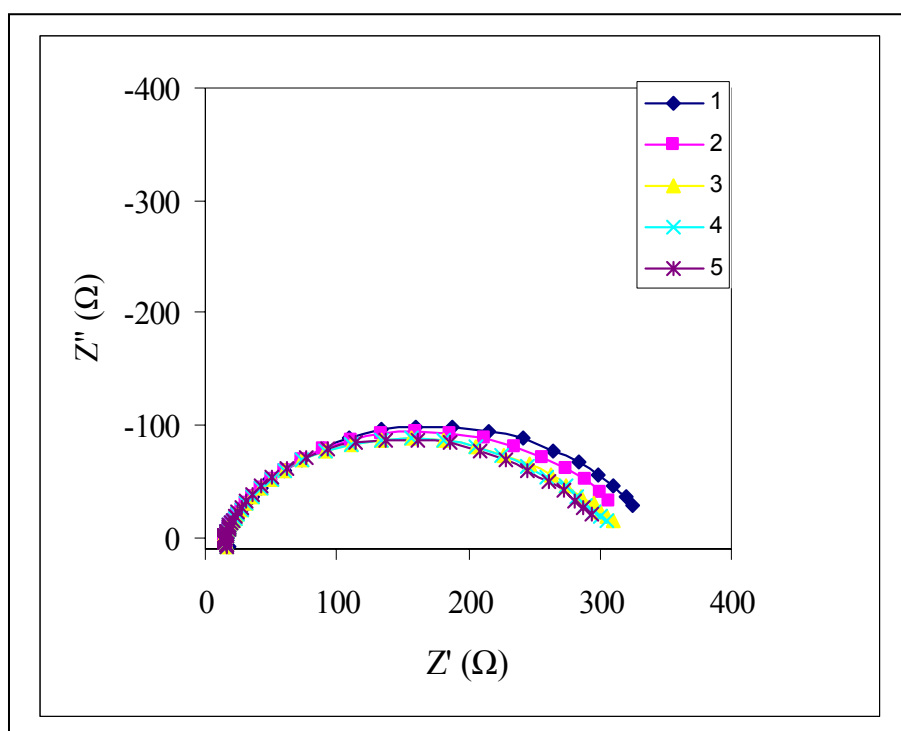
Figure 4.71 Reversibility of the impedance of Ni-patterned LSGM symmetrical cells in H_2+H_2O (40 vol%) at 823 K after the withdrawal of 5 ppm of H_2S (1- H_2S withdrawn, 2- after 50 min, 3-after 192 min, 4-after 258 min, 5-before H_2S poisoning-initial).

Figure 4.72a shows the complex impedance spectra measured in the gaseous atmosphere of H_2+H_2O (3 vol%) + 5 ppm of H_2S at 823 K. The spectra are numbered from 1 to 6. Spectrum 1 was measured in H_2S free atmosphere of H_2+H_2O (6 vol%). Spectrum 2 was measured immediately after the addition of H_2S to the gas composition in the frequency range of 2.5 Hz to 10 mHz. The spectrum 2 was started from the frequency, 2.5 Hz because it was seen above in figure 4.70b that the spectrum starts showing the drop at around 2 Hz frequency during the measurement performed immediately after the addition of 5 ppm of H_2S. It can be clearly seen again from the spectrum 2 that the impedance drops initially as if the addition of 5 ppm of H_2S would improve the performance (with respect to H_2S free gas), before showing the increase in impedance. After 5 h 46 min the impedance arc became stable and showed no further increase.
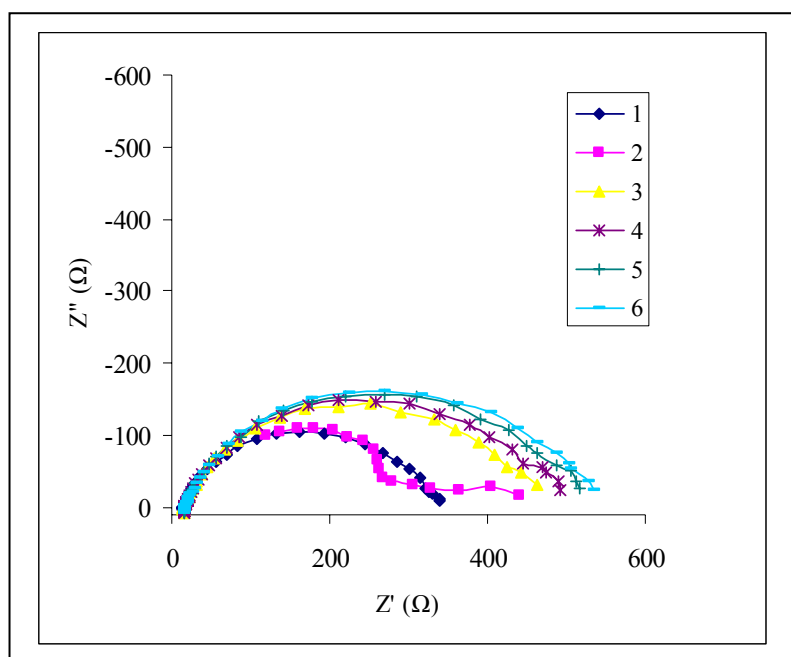
Figure 4.72a Electrochemical impedance spectra of Ni-patterned LSGM symmetrical cells at 823 K in H_2+H_2O (3vol%)+5ppm of H_2S as a function of time starting from the introduction of H_2S into impedance cell (1-in H_2+H_2O (6 vol%) with no H_2S, 2-immediately after addition 5ppm of H_2S,3-after 61 min , 4- 143 min, 5-after 254 min, 6-after 346 min)
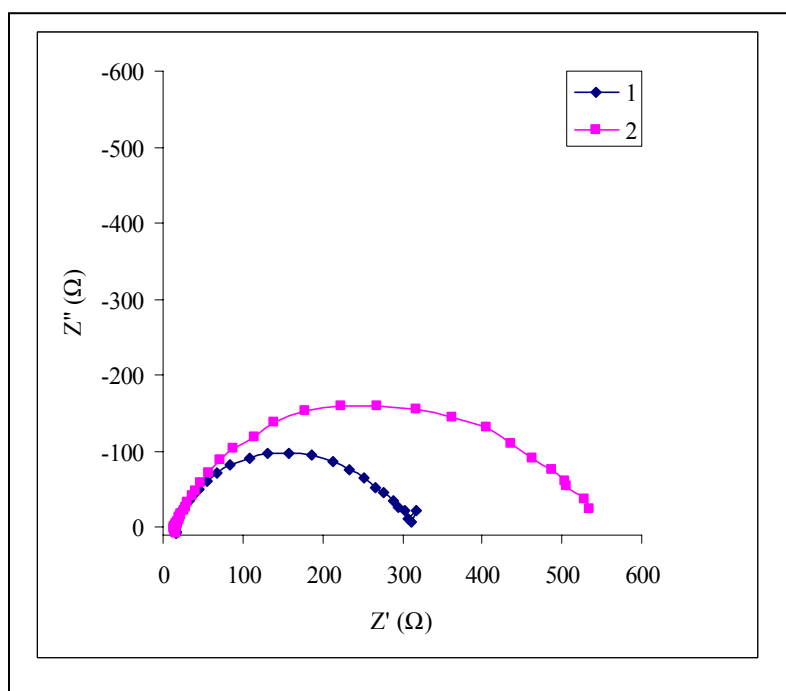
Figure 4.72b Imedance spectra of Ni-patterned LSGM cells in H_2+H_2O (3 vol%) gas with and without 5 ppm of H_2S at 823 K (1-in H_2+H_2O (3 vol%), 2- in H_2+H_2O (3 vol%)+5 ppm of H_2S).

An increase in R_p by 70% due to the presence of 5 ppm of H_2S in H_2+H_2O (3 vol%) gas at 823 K can be seen from figure 4.72b

4.3.4 Comparison of the Ni-patterned YSZ and Ni-patterned LSGM

Figure 4.73 shows the complex impedance plots of the of the Ni-patterned YSZ and Ni-patterned LSGM symmetrical cells at 823 K in H_2+H_2O (3 vol%). It may be recalled here that similar Ni-patterns are used for both YSZ and LSGM. So the length of triple phase boundary (TPB), the width of the Ni-stripes and the total area over which the Ni-patterns are made, are all same for YSZ and LSGM.

It can be clearly seen from the Figure that the polarisation resistance R_p determined from the low frequency intercept of the Nyquist plot is different for YSZ and LSGM. In other words the electrode conductivity (σ_P) of the Ni-patterned LSGM is 3.65 times the electrode conductivity of Ni-patterned YSZ. The calculated σ_P of Ni-patterned LSGM is 2.19×10^{-3} Ω^{-1} Cm^{-2} and of Ni-patterned YSZ is 6.01×10^{-3} Ω^{-1} Cm^{-2} .
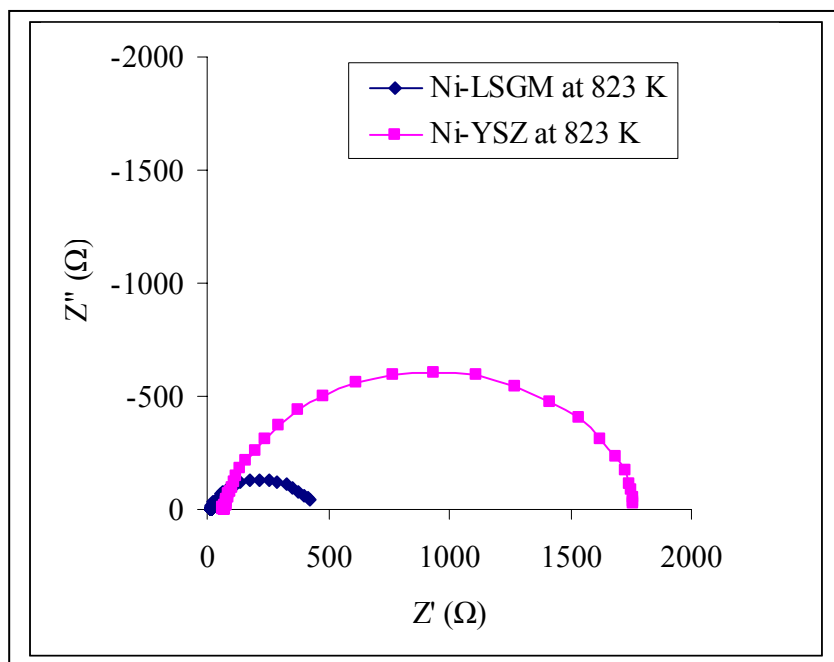
Figure 4.73 Nyquist plots of Ni-patterned YSZ and Ni-patterned LSGM symmetrical cells at 823 K in H_2+H_2O (3 vol%) for the same length of triple phase boundary.
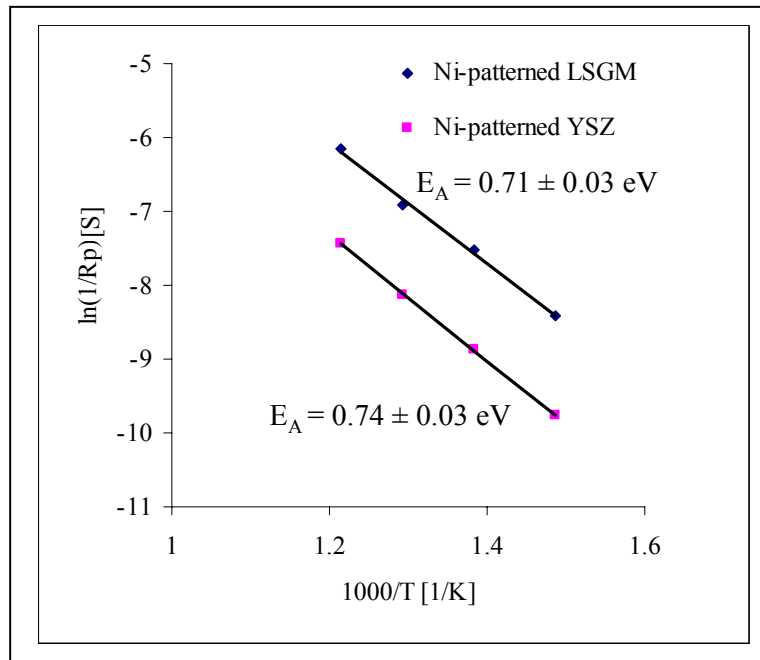
Figure 4.74 Arrhenius plots of the electrode conductivities of Ni-patterned YSZ and LSGM cells in H_2+H_2O (3 vol%) gas at 823 K.

The activation energy of the electrode conductivity of Ni-patterned YSZ and Ni-patterned LSGM derived from the slope of the Arrhenius plot are compared in figure 4.74. It can be seen from the plot that the activation energies are very similar.

Figures 4.60 and 4.69 show the dependence of polarisation resistance of Ni-patterned YSZ and Ni-patterned LSGM on the partial pressure of H_2O in the fuel gas. Ni-patterned LSGM shows very little dependence of R_p on the partial pressure while the Ni-patterned YSZ shows a relatively steep dependence.

From the equivalent circuit fit it is clear that the capacitance obtained from the CPE of Ni-patterned YSZ symmetrical cell is independent of temperature. But the capacitance of Ni-patterned LSGM symmetrical cell is dependent on temperature.

By comparing figures 4.63c and 4.72b which show the poisoning effect of 5 ppm of H_2S in H_2+H_2O (3 vol%) fuel gas, it is evident that the presence of 5 ppm of H_2S in H_2+H_2O (3 vol%) gas caused an increase of electrode resistance in the case of Ni-patterned LSGM by around 70% while it is doubled (increase of 100%) in the case of Ni-patterned YSZ.

It is worth to note that 5 ppm of H_2S in H_2+H_2O (20 vol%) led to an increase of electrode resistance by only ~20 % for Ni-patterned electrodes on LSGM (Figure 4.70a).

The poisonous effect of 5 ppm of H_2S is found to be reversible. The reversibility of Ni-patterned LSGM cells in 40 vol% of H_2O in fuel is found to be faster and complete in 4 h (figure 4.71). At the same time with 6 vol% H_2O Ni-patterned LSGM cells didn't show complete reversibility in the measured duration of time. However ~50 % reversal was observed in 30 min. The reversibility of poisonous effect of 5ppm of H_2S on the Ni-patterned YSZ cells with 6 vol% H_2O was very slow. It took 11 h for Ni-patterned YSZ for the reversal of 50 % of the increased electrode resistance (figure 4.64).

5.0 Discussion

5.1 Stability and performance of Ni-cermet anodes in H_2+H_2S

5.1.1 Ni-YSZ cermets in H_2+H_2S (1 vol%)

Ni is highly reactive to sulphur in the gas. Even at 500°C in H_2+H_2S (1 vol%) gas, nickel forms nickel sulphide (Ni_3S_2). At 750°C nickel undergoes eutectic melting upon its reaction with H_2S in the gas. The eutectic melt which comes out of the sample can be seen as small tiny spheres sticking to the surface of the sample. So it is possible to say from the Ni-S phase diagram, that at temperatures above 901 K (as given in Table 4.17) nickel in the cermet melts eutectically by reacting with H_2S in the H_2+H_2S (1 vol%) gas. In order to understand the stability of Ni in gaseous atmosphere containing various species like H_2, H_2S, SO_2, H_2O etc., it is necessary to consider the quaternary Ni-S-O-H system.

From XRD and SEM, YSZ is found to be stable against the gas in the temperature range of investigation.

5.1.2 Ni-CGO cermets in H_2+H_2S (1 vol%)

It is evident from the results that both Ni and CGO in the cermet are reactive to H_2S in H_2+H_2S (1 vol%) gas at 750°C. However CGO is found to be resistant to the gas at 500°C while Ni is poisoned.

The reactivity of CGO with H_2S in the gas at 750°C leads to the formation of Ce_2O_2S-based compound. This compound was found to contain some dissolved Gd. When CGO alone is exposed, the reactivity of CGO at 750°C leads to the formation of Ce_2O_2S-based compound with some dissolved Gd. The possible reaction is:

$$2 \, (Ce,Gd)O_{2-x} + H_2S + H_2 = (Ce,Gd)_2O_2S + 2 \, H_2O. \qquad (5.1)$$
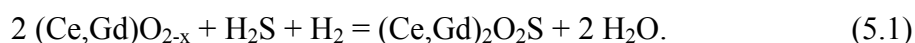
The cracks seen on the spheres (Figure 4.12a) are probably formed because of the evolution of water vapour during the reaction. And also the reaction product, i.e the sulphur is found by EDX on the surface but not in the core of the sample. The tolerance limit of CGO for H_2S in the gas as a function of temperature is not known. So this stability aspects need to be further investigated in order to understand the applicability of CGO as electrolyte material with fuels containing H_2S.

5.1.3 Ni-LSGM cermets

5.1.3.1 Reactivity of NiO-LSGM during sintering

It is seen from the results that the NiO-LSGM reactivity during sintering at high temperatures leads to the formation of $LaNiO_3$-type phase. This has been also reported in literature [5,9]. It

has also been mentioned that this LaNiO$_3$-type phase might contain other elements. Sintering at temperatures below 1200°C didn't show LaNiO$_3$-type phase. However this temperature is not sufficient to get a good sintered pellet.

An attempt has been made if the problem of reactivity can be avoided by sintering in inert atmosphere i.e., in argon and nitrogen. But sintering in inert atmosphere at high temperatures causes the decomposition of LSGM mainly into SrLaGa$_3$O$_7$ and La$_2$O$_3$, as seen in the results. From the point of view of microstructural stability, the NiO-LSGM sintered in air is much better than the samples sintered in inert atmosphere. Thus sintering in inert atmosphere is not useful in achieving sintered NiO-LSGM without any reactivity.

In the case of NiO-LSGM samples sintered in air NiO-LSGM interfacial reactivity leads to the formation of LaNiO$_3$-type phase. Pure LaNiO$_3$ has rhombohedral (R-3C) structure. Its stability as a function of temperature and oxygen partial pressure is known from the literature [94]. Pure LaNiO$_3$ is not stable above 1100 °C under atmospheric air conditions. However, the LaNiO$_3$-type phase, which was formed during sintering at 1350 °C in this study is found to be cubic with the space group Pm–3m and is not therefore pure LaNiO$_3$. Furthermore, the crystal structures of both LaNiO$_3$-type phase and LSGM (with some dissolved Ni) phases are found to be the same with unit cell volumes of 57.3373 and 58.6822 (Å)^3, respectively. Substitution of B-site cations (Ga^{+3} or Mg^{+2}) by Ni^{+3} or Ni^{+2}, respectively, leads to the shrinkage of the unit cell volume. The ionic radii of six-fold coordinated Ni^{+3} and Ni^{+2} are 0.6 Å and 0.69 Å, respectively, whereas the ionic radii of Ga^{+3} and Mg^{+2} cations are 0.62 Å and 0.72 Å respectively. It is also worth mentioning that no cubic perovskites are reported to form in La–Ga–Ni–O or La–Sr–Ni–O systems. In La(Ga,Ni)O$_3$ perovskites, only rhombohedral and orthorhombic structures are possible [94], while in (La,Sr)NiO$_3$ perovskites, within the known Sr solubility–limit, only rhombohedral structure is reported [95-96]. Thus it is very likely that the cubic LaNiO$_3$-type phase could be (La,Sr)(Ga,Mg,Ni)O$_{3-x}$ perovskite with relatively high amounts of Ni.

The STEM/EDX analysis also showed that there is no pure LaNiO$_3$ at the interface of NiO-LSGM after sintering at 1350 °C for 2 h. The almost a constant value of I_{Sr}/I_{La} right from the point on the interface into LSGM(Ni) shows that the perovskite phase is present without any interlayer of impurity phases like SrLaGaO$_4$ or SrLaGa$_3$O$_7$. Interdiffusion across the interface led to the migration of Mg and Ga into NiO and Ni into LSGM. So the interface can now be represented as Ni(Mg,Ga)O – (La,Sr)(Ga,Mg,Ni)O$_{3-x}$.

5.1.3.2 Reactivity of sintered NiO-LSGM in H$_2$

It was shown that reactivity of NiO and LSGM during sintering leads to the formation of LaNiO$_3$-type phase. Beside the formation of this phase, SrLaGa$_3$O$_7$ impurity phase is also found. This impurity phase, in very small amounts (<5 vol%) is also present in the as prepared LSGM. However after reduction, from the XRD and SEM analysis of the produced Ni-LSGM cermets, it is clear that La$_2$O$_3$ and SrLaGaO$_4$ are mainly formed during the reduction of the NiO-LSGM sample at 1000°C for 2 h, while the LaNiO$_3$-type phase which was identified after the sintering of NiO-LSGM, is not seen after the reduction. In TEM study of the NiO-LSGM interface, it was identified that this LaNiO$_3$-type phase is not pure LaNiO$_3$ and most likely it is the cubic LSGM containing high amounts of dissolved Ni. So this leads to the understanding that some LSGM especially LSGM containing dissolved Ni decomposed under reducing condition to form La$_2$O$_3$ and SrLaGaO$_4$ phase. It is also likely that the latter phase may contain some dissolved Ni in it. Thus the LaNiO$_3$-type phase which is LSGM(Ni) with high amounts of Ni can not be seen after the reduction. Now from the mass balance point of view a question arises about excess amount of "Ga". From SEM/EDX analysis of the Ni-LSGM cermets, it was shown that Ni contains some dissolved Ga (~9 at%). It was also shown from the SEM /EDX analysis of the sintered NiO-LSGM samples that NiO had no dissolved Ga. Thus it is evident that during reduction Ga from LSGM diffused into Ni. This is accompanied by the decomposition of the LSGM(Ni) phase into La$_2$O$_3$ and SrLaGaO$_4$.

In literature [5] it was reported that the sintering of NiO-LSGM at 1400°C led to the formation of LaNiO$_3$ which doesn't conduct oxide ions under anodic conditions (in reducing atmosphere). Further it is mentioned that the formation of lanthanum-nickel oxide under anodic condition could occur when a high current is passing through the LSGM/anode interface even at lower temperatures since an oxidation reaction occurs at the anode-electrolyte interface [5]. But as it was seen from the results, this LaNiO$_3$-type phase is not stable in reducing conditions and most likely decomposed to La$_2$O$_3$ and SrLaGaO$_4$ accompanied by diffusion of Ga into Ni. So it is evident that the poor anode performance due to the reactivity of NiO/Ni-LSGM can be attributed to the decomposition of LSGM(Ni) accompanied by the Ga diffusion out of LSGM(Ni) into Ni. The Auger studies of Ni-LSGM interface at 750°C also showed the interdiffusion across the interface which can be seen in the section 4.1.4.1.

5.1.3.3 Reactivity of Ni-LSGM cermets in H_2+H_2S (1 vol%)

Ni-LSGM cermet which was produced from sintering of NiO-LSGM at 1300°C for 2 h and its subsequent reduction in H_2 at 1000°C for 2 h, was exposed to H_2+H_2S (1 vol%) gas for 3 h. It is interesting to see from the XRD results of the exposed specimen that Ni is still present even after exposure to H_2+H_2S (1 vol%) gas at 750°C for 3 h. From SEM/EDX analysis of composition of the Ni grains it is evident that Ni is not pure but it is the FCC solid solution with around 10 at% Ga. So this Ni-Ga alloy is found to be stable in H_2+H_2S (1 vol%) gas at 750°C even after for 3 h of exposure. La_2O_3 and $La(OH)_3$ (formed from La_2O_3) which were found in the cermet before exposure to H_2+H_2S (1 vol%) are converted to La_2O_2S. Further diffusion of Ga into Ni and decomposition of nickel containing LSGM is also likely to occur during the exposure at 750°C to H_2+H_2S (1 vol%) gas. This point of increased Ga diffusion from LSGM(Ni) across the interface into Ni at 750 °C in H_2+H_2S (1 vol%) gas is discussed with Ni-patterned LSGM samples.

However, the Ni-LSGM cermet which was exposed to H_2+H_2S (1 vol%) gas at 500°C for 3 h showed a film of Ni_3S_2 phase formed over the surface of the specimen as detected by XRD. The SEM anaylsis of the film (shown as the skin) showed only Ni and S. But it was clear that before exposure Ni had some dissolved Ga. In SEM/EDX examination, no compounds of Ga and S were detected, while from XRD it was not clear if there was any formation of gallium sulphides. Probably only Ni from Ni-Ga alloy reacts with H_2S in the gas at 500°C leading to Ni_3S_2 and Ga enrichment in the remaining Ni-Ga alloy. The SEM analysis after removing the surface film, showed mainly Ni-Ga alloy and LSGM. From XRD and SEM it is evident that the Ni-Ga alloy is not stable against H_2+H_2S (1 vol%) gas at 500°C. The remaining phases are present, as obtained after reduction and before the exposure.

5.1.3.4 Reactivity of Ni-patterned LSGM in H_2

The Auger depth profile analysis of Ni-LSGM interface of the Ni-patterned LSGM revealed that there is no interaction between Ni and LSGM below 650°C in hydrogen atmosphere. So if the reaction between NiO and LSGM can be avoided during fabrication of the electrode, Ni-LSGM cermet can be used as an anode in the lower regime of the intermediate temperature range. However in this work, for the study of the electrochemical performance, the Ni-

patterned LSGM cells were made by photolithography and were investigated in the safe temperature regime as identified by the Auger study.

The Auger and XRD investigation of Ni-patterned LSGM also revealed that at 750°C interdiffusion occurred across the Ni-LSGM interface. The reactivity didn't cause formation of any new phase, but Ga diffused out of LSGM while Ni diffused in. It is not clear about the oxidation state of Ni in LSGM, i.e. if it is Ni^{+2} and/or Ni^{+3}. So now the interface can be written as $(Ni, Ga) \mid (La_{0.8}, Sr_{0.2})(Ga^{+3}, Mg^{+2} Ni^{+3}, Ni^{+2}) O_{3-x}$.

5.1.3.5 Reactivity of Ni-patterned LSGM and completely Ni-coated LSGM in H_2+H_2S (1 vol%)

From Auger spectroscopic study of Ni-patterned LSGM samples, it was found that interdiffusion across the Ni-LSGM interface during annealing at 750°C in hydrogen gas leads to the situation of $(Ni,Ga)-(La,Sr)(Ga,Mg,Ni)O_{3-x}$ (i.e. leads to the formation of Ni-Ga alloy). The composition of the Ni-Ga alloy patterns was calculated to be Ni-10 at%Ga. From the studies of Ni-LSGM cermets it was found that the Ni-Ga alloy formed in the course of preparation of the cermet is stable against H_2+H_2S (1 vol%) gas at 750°C but not at 500°C.

So keeping the above two observations in mind the stability of the patterns of Ni-Ga alloy obtained on LSGM substrate after annealing in H_2 at 750°C for 24 h, was studied in H_2+H_2S (1 vol%) gas at two different temperatures 750°C and 500°C. The samples were exposed to H_2+H_2S (1 vol%) gas for 3 h.

The characterisation of the samples (Ni-patterned LSGM and completely Ni-coated LSGM) exposed at 750°C, by XRD and SEM/EDX showed three important features.
1. The Ni-Ga alloy (the pattern) is not reactive to H_2S in the gas.
2. A sheet-like microstructure of the Ni-Ga alloy patterns is observed (shown in the SEM) and,
3. The Ni-patterns (the sheet like structure) contain 27-29 at% Ga.

There are two points to be discussed further. Firstly the patterns of Ni-Ga alloy have not reacted with H_2S in the gas to form any sulphides. Secondly the composition of these patterns before and after exposure to H_2+H_2S (1 vol%) gas indicates that further interdiffusion (diffusion of Ga into Ni) took place during the exposure at 750°C leading to a supersaturated

solid solution of Ni-Ga. If the layered structure is because of the formation of Ni_3Ga, then it can be interpreted as the precipitation of this compound (Ni_3Ga) from the supersaturated solution of FCC Ni with dissolved Ga [97]. So irrespective of the fact that whether the patterns are a supersaturated solid solution of Ni with 30 at% Ga or Ni_3Ga compound, it can be clearly stated that the solid solution of FCC Ni with 10 at% Ga obtained after annealing the Ni-patterned LSGM in H_2 at 750°C, remained resistant to H_2+H_2S(1 vol%) gas. In contrast, in the case of Ni-YSZ cermets treated along side with the Ni-patterned LSGM samples showed eutectic melting and formation of the tiny spheres of eutectic mixture.

However the Ni-patterned LSGM samples after annealing (in H_2 at 750°C for 24 h) and exposure (in H_2+H_2S (1 vol%) at 500°C for 3 h showed Ni_3S_2 in XRD. It is not clear if this sulfide contains some dissolved Ga. But it is clear that the Ni layer which becomes Ni-Ga alloy after annealing in H_2 is not stable against the H_2+H_2S (1 vol%) gas at 500°C. The exact composition of the sulphide formed is not known while the XRD indicates it to be Ni_3S_2. It is worth mentioning here that the Ni-LSGM cermets exposed to H_2+H_2S (1 vol%) gas at 750°C and 500°C showed a similar behaviour. The Ni-Ga alloy is found to be stable in H_2+H_2S (1 vol%) gas at 750°C but forms Ni_3S_2 at 500°C.

Hence from the observations of the stability of the alloy of Ni and Ga at two different temperatures it will be interesting to calculate the stability diagrams of Ni-Ga alloy in H_2+H_2S gaseous atmosphere. Ultimately the interest would be to understand the stability of Ni-Ga alloy under the working conditions of the fuel cell with the fuel gas containing H_2S impurity beside H_2 and H_2O.

5.1.3.6 Stability of Ni in oxygen, hydrogen and sulphur-containing atmospheres

The stability diagrams of Ni in $H_2+H_2O+H_2S$ atmosphere show that the thermodynamic tolerance limit of partial pressure of H_2S in the gas mixture is not influenced by the partial pressure of H_2O in the gas. The tolerance limit of Ni for sulphur from the point of view of thermodynamic stability expressed as $logP(S_2)$ is -9.7516 at T=1023 K and -14.50719 at T=773 K. By considering $H_2 + 1/2\ S_2 \rightarrow H_2S$, the corresponding $P(H_2S)\ /P(H_2)$ is 1.507×10^{-3} at T=1023 K and 1.9503×10^{-4} at T=773 K. Note that in the further discussion the values of $P(S_2)$ are converted into corresponding values of "$P(H_2S)/P(H_2)$" according to the afore mentioned equilibrium reaction.

The ratio of partial pressure of H_2S to that of H_2, in the $H_2 + H_2S$ (1 vol%) gas mixture, is $\sim10^{-2}$. At this partial pressure of sulphur and at a temperature of 750°C, Ni in the Ni-CGO and Ni-YSZ cermets electrode had undergone melting by reacting with H_2S to form a melt of eutectic composition. However, at 500°C Ni in the cermets reacts with H_2S to form Ni_3S_2 (Haezelwoodite) phase according to the reaction

$$3 \text{ Ni} + 2 \text{ S} = Ni_3S_2 \qquad (5.2)$$
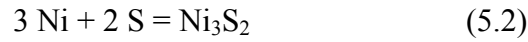
This can also be seen from the stability diagram of Ni calculated as a function of partial pressure of sulphur and temperature as shown in the Figure 5.1. The points marked on the diagram at 500°C and 750°C show Ni_3S_2 and liquid respectively.
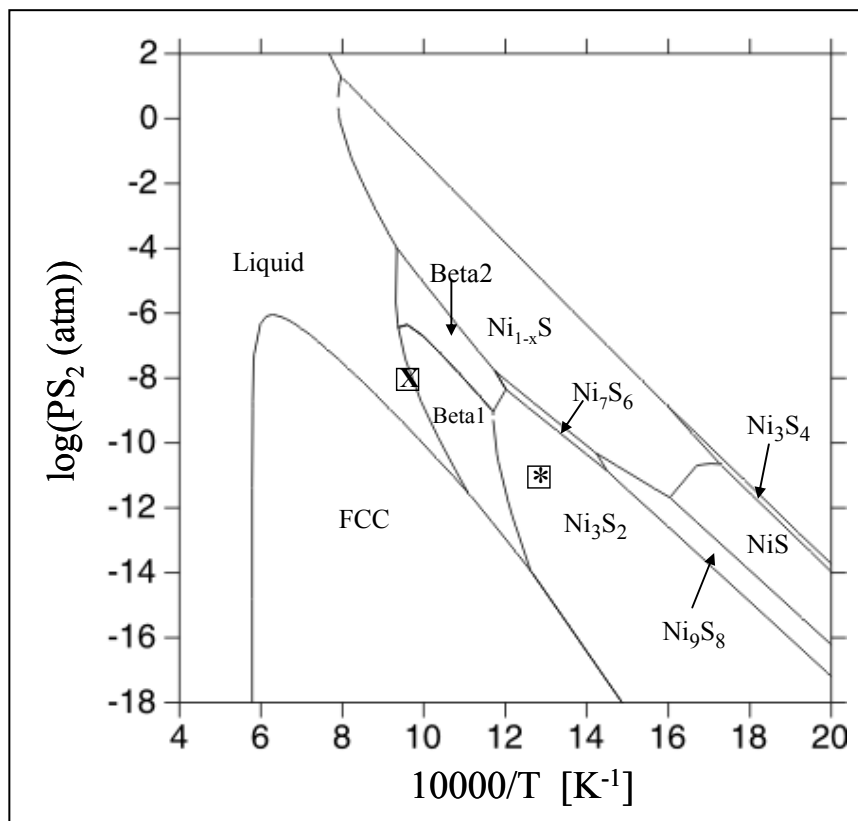
Figure 5.1 Calculated $logP(S_2)$- 10000/T diagram of Ni-S binary (*- correspond to 773 K and H_2+H_2S (1 vol%) gas composition and X – corresponds to the 1023 K and H_2+H_2S (1 vol%) gas composition

As it has already been discussed, the interaction of Ni and LSGM at various stages of preparation of Ni-LSGM cermet has finally led to a solid solution of FCC Ni with ~10 at% Ga and this Ni-Ga alloy was found to be stable in the H_2+H_2S (1 vol%) gas mixture at 750°C. This caused interest to calculate Ni-Ga-S ternary diagram to understand the tolerance limit of FCC Ni-Ga alloy to H_2S in the gas. So, the Ni-Ga-S ternary phase diagram was calculated

from the Ni-S binary modelled in this work, optimised Ni-Ga binary taken from literature [98] and Ga-S binary data taken from SGTE database [83]. The calculated predominance area diagram is shown in the figure 5.2. Stability of various phases in the Ni-Ga-S ternary at 1023 K as a function of partial pressure of sulphur and activity of Ga is shown.
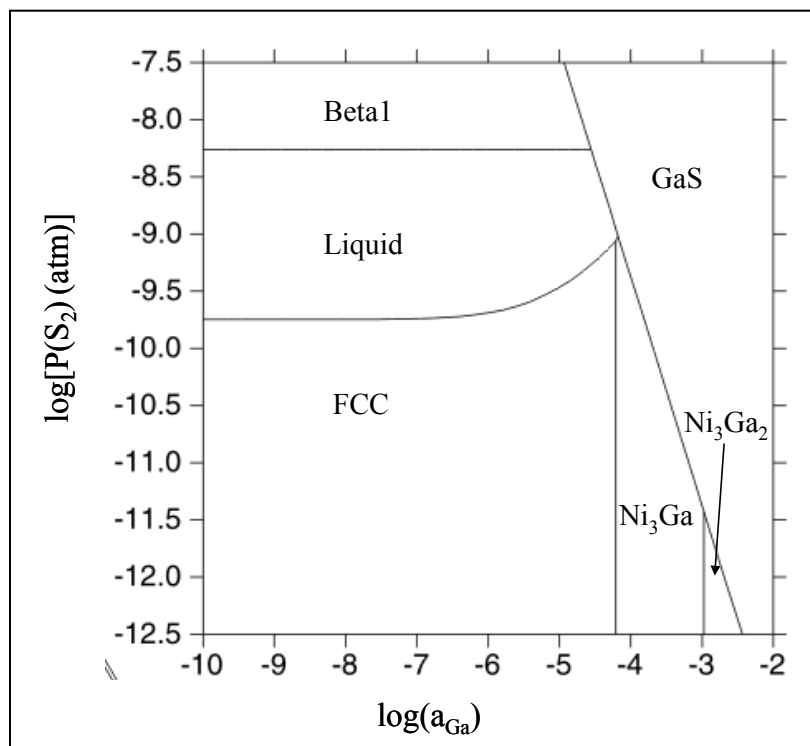
Figure 5.2 Predominance area diagram in Ni-Ga-S ternary at 1023 K in coordinates of partial pressure of sulphur and activity of Ga (the reference states are FCC for Ni and Ga, and gas for sulphur)

It can be seen from the Figure 5.2 that with increasing activity of Ga in the FCC solid solution of Ni, the FCC – liquid equilibrium moves towards higher partial pressure of sulphur. In other words, the stability region of FCC solid solution of Ni and Ga moves towards higher values of partial pressures of sulphur. The higher tolerance limit of FCC solid solution of Ni-Ga alloy at 1023 K can be better appreciated by comparing figure 5.2 with figure 5.3. Figure 5.3 shows the stability of various phases in the ternary system Ni-Ga-S at 773 K. It is clear from the figure that at 773 K the sulphur tolerance limit of the FCC phase has come down. The partial pressure for the "FCC – Ni_3S_2" equilibrium is relatively low when compared with the partial pressure for the "FCC - liquid" equilibrium. And also the "FCC – Ni_3S_2" equilibrium shifts only very little towards higher partial pressures of sulphur with increasing activity of Ga. Thus it is evident from the figures 5.2 and 5.3 that the FCC phase exhibits relatively high

sulphur tolerance at 1023 K. However it has to be mentioned that the ternary Ni-Ga-S system is not optimised. Only the thermodynamic models of the binary systems Ni-S, Ga-S and Ni-Ga are used in the calculation. Thermodynamic optimisation of the ternary compound $NiGa_2S_4$ and especially the thermodynamic optimisation of the ternary liquid is important to precisely understand the limits of tolerance of FCC solid solution of Ni as a function of dissolved Ga. Calculation based on the existing database shows that at 1023 K, the FCC phase (of Ni-Ga alloy) can show a tolerance limit of 8.72×10^{-10} of partial pressure of S_2 i.e. 0.334 vol% of H_2S in H_2+H_2S gas mixture. But, from the experiments the Ni-Ga (~10 at%) alloy is found to be resistant against H_2+H_2S (1 vol%) gas, at 1023 K. The difference in experimental and calculated values of tolerance limits of $P(S_2)$ could be due to the fact that the optimised thermodynamic description of ternary liquid on the Ni-Ga-S system is not available.
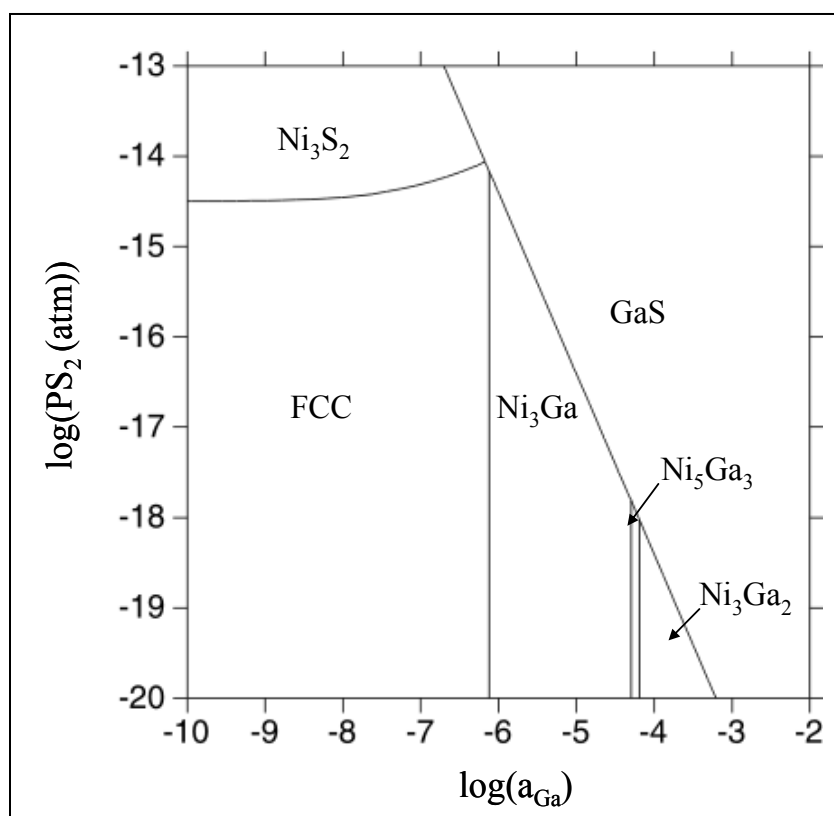
Figure 5.3 Predominance area diagram in Ni-Ga-S ternary at 773 K in coordinates of partial pressure of sulphur and activity of Ga (the reference states are FCC for Ni and Ga, and gas for sulphur)

Using the calculations of the systems Ni-O-S-H and Ni-Ga-S, make one to understand the thermodynamic stability of the Ni (and higher sulfur-tolerance of FCC Ni-Ga alloy) as a

function of partial pressures of sulphur, hydrogen and oxygen at the required operating temperature of SOFCs. The thermodynamic tolerance limit of FCC Ni for poisonous sulphur can be calculated from the above diagrams.

The 5 ppm of H_2S in ~97 vol% H_2 and 3 vol% H_2O corresponds to the point marked by '+' on figure 4.54, log[$P(H_2O)/P(H_2)$] vs log[$P(H_2S)/P(H_2)$] at 823 K. It can be seen from the figure that FCC Ni is stable under these conditions. However chemisorption of sulphur on Ni under these conditions affects the electrochemical performance of Ni in Ni-cermets and Ni-patterned model electrodes. So the effect of 5 ppm of H_2S on the electrochemical performance of Ni-patterned electrodes is studied.

5.2 H₂-Oxidation reaction mechanism at Ni-patterned electrodes on YSZ and LSGM

5.2.1. Ni-Patterned single crystal YSZ symmetrical cells in H₂+H₂O

Studies to understand the reaction kinetics of Ni-patterned YSZ single crystal electrodes in H_2+H_2O are reported earlier in literature [30, 92]. But the effect of the surface structure (i.e the face of the YSZ crystal) of the YSZ electrolyte on reaction kinetics has not been investigated so far. It is noteworthy to mention here that the dimensions of all the three YSZ single crystals, design of the Ni-patterns, and length of triple phase boundary are the same in all three cases. Only the crystallographic orientation of the YSZ single crystal is different from each other.

In the whole range of temperatures and partial pressures of H_2O in the gas mixture H_2+H_2O, a single arc is observed. As shown in figure 4.56 the Nyquist plot is a perfect semi circle except for the appearance of a shoulder at the lower frequencies. The Nyquist plots of all the single crystal measurements are very close to a perfect semicircle. The exponents of the constant phase elements obtained from the equivalent circuit fit using a single "RQ" element, are close to unity. Hence it is possible to say that a single elementary process is responsible for the impedance arc (the rate limiting step).

The slight non-ideality (n > 0.95) in arcs and the behaviour of constant phase element, may be, because of distributed reaction rates of the same elementary reaction process.

The electrolyte resistances R_e obtained from the high frequency intercepts of the Nyquist plots are found to be different depending on the orientation and the difference in R_e is found to vary with temperature. The difference can be seen mainly between <100> orientation and the other two orientations. There is almost no difference in R_e obtained from the <110> and <111> measurements. This has been found to be reproducible as shown in the results and appears as if the conductivity measured is different depending the orientation of the single crystal. But YSZ (ZrO_2-9.5 mol% Y_2O_3) single crystals with 9.5 mol% Y_2O_3 are cubic in structure (Fm3m). It is known that the cubic crystals are isotropic and the conductivity is same in all the crystallographic directions. R_e is almost same for the <110> and <111> orientations but comes less for the <100> orientation. It is probably because of the slight angular mismatch between the orientation of Ni-patterns on the two opposite faces of the YSZ crystals of the <100> orientation, as shown in the Figure 5.4. It has to be mentioned here that during the preparation of symmetrical cells of the YSZ single crystals, a perfect match of Ni-patterns on the two faces of the YSZ single crystals was obtained for the crystals with <110> and <111>

orientations. In other words in the case of YSZ crystals with <110> and <111> orientations, the structured Ni-pattern on one side is exactly the mirror reflection of the Ni-pattern on the opposite face. However, a mismatch of 5°(maximum) between the Ni-patterns made on the opposite faces, is possible in the case of YSZ crystals of <100> orientation. This could be the reason for the variation in the high frequency intercept of the Nyquist plots (R_e) depending on the orientation of YSZ single crystals.
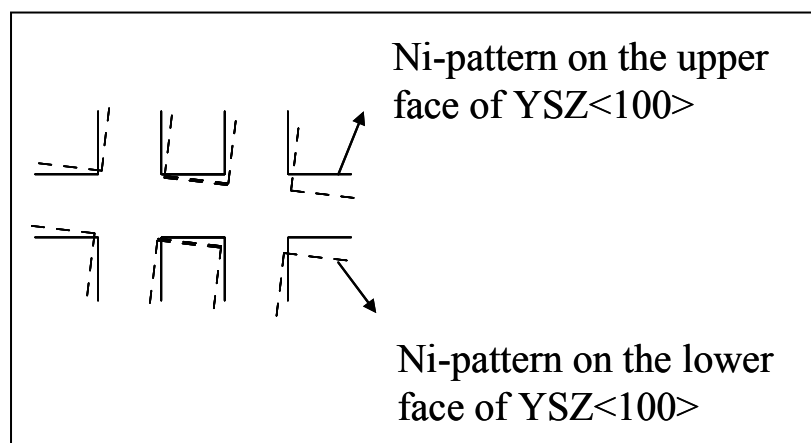
Figure 5.4 mismatch of the Ni-pattern electrodes on the opposite faces of the YSZ<100> electrolyte.

The capacitance obtained from the Ni-patterned YSZ single crystal cells is independent of temperature. At the same time as shown in the results, the obtained capacitance values are found to depend on the orientation. These values are found in the order of $C_{<100>} < C_{<111>} < C_{<110>}$. These capacitance values are very well reproduced with the same relationship. The double layer capacitance of 30 $\mu F/cm^2$ is predicted from the models [99], so that the capacitance values of 100-300 $\mu F/cm^2$ can not be attributed purely to a double layer. Mogensen et al [100] reported similar value (~100 $\mu F/cm^2$) of capacitance for Ni-YSZ in H_2 atmosphere. The high capacitance values which can not be exclusively due to double layer capacitance was thought to be due to the formation of an adsorbed O^{-2} ions and also to some extent OH^- ions. Capacitance values of 40-200 $\mu F/cm^2$ were reported by Neophydites et al [101] from their AC impedance study of Ni-YSZ cermet anodes in methane fuelled fuel cells. They speculated that the observed capacitance could be a double layer capacitance and/or pseudo capacitance associated with the adsorption of species on Ni-YSZ cermet accompanied by charge transfer.

So the obtained capacitance values from the single crystal measurements with different orientations can not be exclusively due to a double layer. But the obtained values could be due to capacitance associated with the adsorption process accompanied by charge transfer reaction.

The R_p (total polarisation resistance) obtained from the low frequency intercept also appears to be different depending on the face of the YSZ crystal. But solely from the above measurements (figure 4.57a and Table 4.25) it is not possible to unambiguously interpret the variation of R_p and its dependence on the face of the YSZ crystal.

A possibility of a difference in polarisation resistance (the low frequency intercept of the impedance arc) could occur, if the rate determining step responsible for the impedance arc is assumed as an elementary charge-transfer reaction

$$H_{Ni} + O^{-2}_{(electrolyte)} \quad <==> OH^{-}_{(Ni)} + e \qquad (5.3)$$
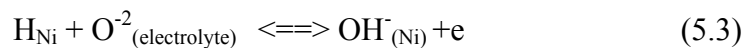
Then the rate of the above reaction can be different for different orientations of the sample because

1. The O^{-2} concentration on the surface of the electrolyte is different or the width of the triple phase boundary i.e. the width of the region where the above reaction can occur is different for different orientations.

2. The binding energy of O^{-2} on the surface and the heat of the reaction as well as the intrinsic barrier of the reaction are different in different orientations. The activation energy of the reaction is related to the heat of the reaction as given by equation (5.4) [102]

$$E_a = E_a^{\circ} + \gamma_p \Delta H_r \qquad (5.4)$$

E_a --- activation energy of the reaction

ΔH_r --- heat of the reaction

E_a° --- intrinsic barrier to the reaction

γ_p --- transfer coefficient

So the activation energy and the rate of the reaction can be different depending on the face of the YSZ crystal. In equation (5.4), ΔH_r may also include electrostatic contributions due to surface charges. Further experiments are necessary in order to understand the dependence of R_p and its relationship with the orientation of YSZ.

5.2.2 Ni-patterned polycrystalline YSZ symmetrical cells

5.2.2.1 In H_2+H_2O

A single arc is observed in the whole range of experimental conditions. Understanding of the reaction mechanism and the rate determining step has to be derived from the impedance arc and its response to the various experimental variables. Often the impedance arcs (the Nyquist plots) measured in solid state ionics are not perfect semicircles and they are slightly depressed. In order to describe such an impedance arc in terms of equivalent circuit elements, a constant phase element (CPE) is used. There are many possible reasons for the occurrence of behaviour like CPE, for example distributed relaxation frequencies, distributed rates of the same elementary process etc. Also the equivalence circuit fit of such depressed arcs is not a trivial task. A depressed arc may be fitted with a single "RQ" element or more than one. The important point here is to know how many processes are responsible for the observed impedance arc. As mentioned already a depressed arc may be due to distributed rates of the same elementary process or may be due to two or more elementary processes with very close relaxation frequencies.

In experiments with Ni-patterned electrodes a single arc has been measured in the whole range of experimental conditions. Now the question is how many elementary processes are responsible for the observed impedance arc.

It has been shown in the single crystal measurements that a single arc is very close to a perfect semi circle (with the exponent of CPE (n) $\geq$0.95). The equivalent circuit used to describe the data was Re(RpQp). Using the same circuit for the Ni-patterned polycrystalline samples gives the capacitance values similar to the values obtained from the single crystal measurements. Furthermore when the capacitance obtained from Ni-patterned polycrystalline YSZ cells is compared with capacitance obtained from Ni-patterned YSZ sinlge crystals of different orientations, it appears that the capacitance of the former is an average of the capacitances of different orientations. As it can be seen in Tables 4.23 and 4.28, the capacitance of the polycrystalline YSZ cells is ~115 μF/cm^2 where as for YSZ<100>, YSZ<111>, and YSZ<110> single crystal cells, the capacitance is ~100, ~135 and ~167 μF/cm^2 respectively. The exponent of CPE obtained for polycrystalline samples is ~0.82. The relatively less value of 'n' of polycrystalline samples, may be understood as the distributed rates of the same process (occurring on different orientations of grains of YSZ).

In similar studies in literature [30], a single arc was reported with the Ni-patterned electrodes on YSZ<100>. The reported arc was much depressed with the exponent n=0.49 and it was assumed that a single process was responsible for the arc.

So from the above discussion, it may be taken that a single process represented by RpQp is responsible for the impedance arc in Ni-patterned YSZ polycrystalline samples (as in the case of Ni-patterned YSZ single crystals).

The capacitance exhibited by the Ni-patterned polycrystalline YSZ cells is independent of temperature. It is worth mentioning here that the capacitance values are calculated at summit frequency but not at an arbitrary frequency of 1000 Hz. It has to be kept in mind that it is important to clearly understand if the obtained capacitance is due to two phase boundary (double layer) or if it is due to the elementary process occurring at three phase boundary (TPB). Figure 5.5 shows the equivalent circuit elements for the two phase and three phase boundaries of the Ni-patterned YSZ cell. If the double layer capacitance is dominating, the capacitance associated with the elementary process at TPB may not be visible. The temperature-independent capacitance (Table 4.28) as in the case of Ni-patterned YSZ single crystals, points towards double layer capacitance. And as mentioned already the capacitance obtained from Ni-patterned YSZ polycrystalline cells appears to be average of the capacitances of Ni-patterned YSZ single crystals with different orientations. Thus as discussed in the case of Ni-patterned YSZ single crystal cells the observed capacitance of polycrystalline YSZ cells can not be exclusively due to a double layer capacitance, but could be associated with adsorption of species accompanied by charge transfer reaction.

1 – Capacitance of two phase boundary (double layer)
2 – Electrode process at three phase boundary (TPB)
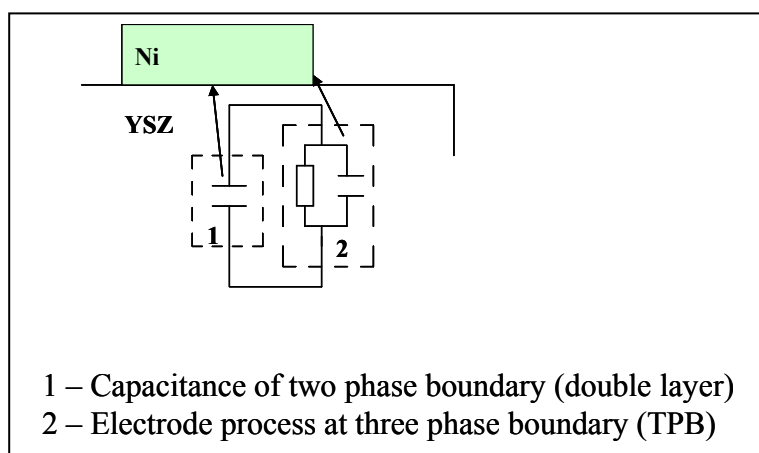
Figure 5.5 Equivalent circuit for the Ni-patterned electrode YSZ (showing the capacitance of double layer and the capacitance associated with an activated process at TPB).

Partial pressure of water $P(H_2O)$ is found to have catalytic effect on the reaction rate of the electrode process responsible for the impedance arc. With increasing $P(H_2O)$, the polarisation resistance is found to decrease. A slope of -0.1996 is obtained in this work from the logarithmic plot of electrode resistance as a function of partial pressure of water (shown in Figure 4.60). The catalytic effect of water on the reaction rate was also reported in the earlier studies with the Ni-patterned electrodes [29,30,92]. However a much stronger dependence of electrode resistance on the partial pressure of water with a slope of -0.67, was reported in literature by Gauckler et al [30]. Mizusaki et al [92] have also reported a stronger dependence of R_p on PH_2O.

The activation energy obtained from the main impedance arc (i.e the activation energy obtained from the Arrhenius plot of the electrode conducitivty) of the Ni-patterned YSZ polycrystalline samples, is 0.73 eV. This is the activation energy of the electrode process responsible for the arc.

In earlier studies with Ni-patterned electrodes, Gauckler et al [30] reported 0.88 eV as the activation for their main impedance arc. From the obtained activation energy of the impedance arc and its dependence on the partial pressure of water in the gas, they interpreted the electrode process as either adsorption/desorption of hydrogen or the removal of O^{-2} from the electrolyte. Mizusaki et al [92] in their studies with the Ni-patterned electrodes reported a much larger dependence of the electrode conductivity on partial pressure of H_2 and H_2O and considered a reaction of the first order to be the rate-determining step. They interpreted the dissociative adsorption of reactants on the surface of the Ni near the TPB or the surface diffusion of adsorbed species as the rate determining step.

From the above observations, the following mechanism is assumed (for Ni-patterned YSZ samples) and it is further evaluated by attempting to explain the effect of 5 ppm of H_2S on the impedance arc. The reaction mechanism is shown in figure 5.6. Hydrogen is dissociatively adsorbed onto Ni. Hydroxyls are formed on Ni. O^{-2} ions may also be present on the surface of Ni due to spillover effect from the YSZ. The surface of the YSZ is thought to have O^{-2} and OH^- groups [100,103]

Dissociative adsorption of H_2 on nickel

$$H_2 \leftrightarrow 2H_{Ni} \qquad\qquad (5.5)$$

Formation of hydroxyl on Ni

$$H_{Ni} + O^{-2}_{YSZ} \leftrightarrow OH^{-}_{Ni} + e \qquad\qquad (5.6)$$

Formation of H_2O on Ni

$$H_{Ni} + OH^{-}_{Ni} \leftrightarrow H_2O_{Ni} + e \qquad\qquad (5.7)$$

$$H_2O_{Ni} \leftrightarrow H_2O(gas) \qquad\qquad (5.8)$$
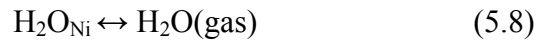
The major adsorbed species on Ni are OH^{-}, H_{ad} and H_2O_{ad}. O^{-2} ions may also present on the surface of Ni due to spillover effect from the YSZ. The assumed reaction mechanism also leads to the understanding of the effect of 5 ppm of H_2S on the impedance spectra of symmetrical cells of Ni-patterned YSZ.

From the above discussion of T-independence of capacitance obtained from the impedance arc and the above reaction mechanism it can be assumed that the rate limiting step which is responsible for the impedance arc is the reaction 5.6 (i.e., the formation/dissociation of OH^{-} on Ni). As already seen with the cells of YSZ single crystals the dependence of total polarisation resistance (R_p) which is inversely related to the rate of the elementary process responsible for the impedance arc, on the face of the YSZ single crystals also support this assumption. The process of formation and adsorption of OH^{-} on Ni from the reaction between O^{-2}_{YSZ} and H_{Ni} at Ni-YSZ interface (two phase boundary) may be thought to be responsible for the observed capacitance. At the two phase boundary it is thought to be a capacitive process, but not to be a DC process.
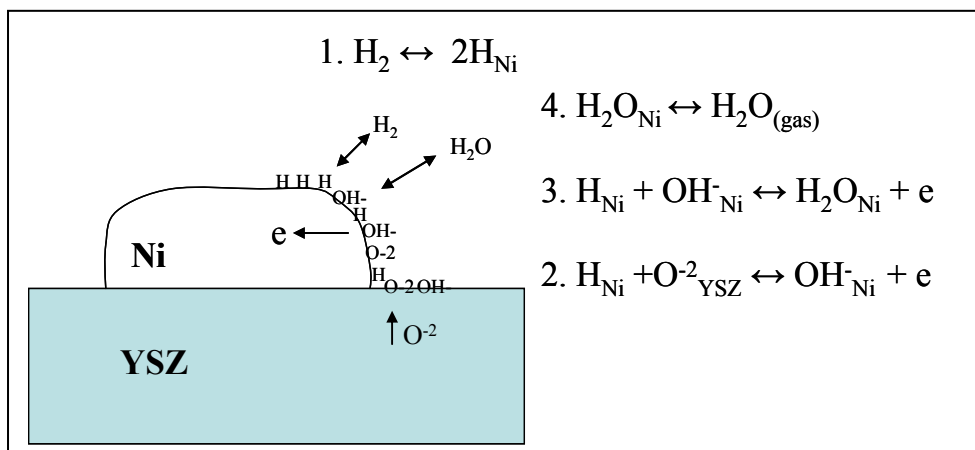
Figure 5.6 the reaction mechanism at Ni-patterned electrodes on YSZ

5.2.2.2 Effect of 5 ppm of H_2S in H_2+H_2O

Now the effect of H_2S on the reaction mechanism has to be understood. With 5 ppm of H_2S the polarisation resistance was found to increase by a factor of 2. Sulphur is known to be poisonous to Ni in Ni-cermet anodes [31]. Even 2 ppm of H_2S is known to increase the total polarisation resistance of the electrode. But an interesting observation of the effect of H_2S in the initial stages of its interaction with the Ni-patterned YSZ, has been identified as shown in the results (figure 4.63a,b). The initial drop in the impedance values (i.e., momentary increase in the current) precedes the poisoning effect. Therefore the reason must be combined with the interaction of H_2S with Ni and YSZ.

H_2S is known to dissociate at Ni surfaces where sulphur is adsorbed while H_2 gas is released [104-105]. The interaction of few ppms of H_2S with the surface of YSZ and its influence on the surface chemistry is not well known, although YSZ electrolyte is used in H_2S gas sensors. At such a low concentrations of H_2S its interaction with YSZ can be thought to be quickly reversible upon the withdrawal of H_2S impurity from gaseous atmosphere. But it was shown in the results that the reversibility of the electrode conductivity was very slow and it was not complete even after 40 h. So the poisonous effect of 5 ppm of H_2S can be understood to be due to the chemisorption of S on the surface of Ni.

With adsorbed S on the surface of Ni, the uptake of H decreases. The adsorption sites for H are blocked by adsorbed S [106]. The ratio of surface chemisorbed S to chemisorbed H is dependent on the temperature [107-108]. The quantity of S uptake or quantity of S chemisorbed onto Ni is also dependent on the substrate [105].

In literature very little information is available on the interaction of H_2S with Ni at high temperatures in H_2+H_2O atmospheres.

Ruan et al [109] studied the reaction of H_2S with adsorbed O_{ad} on Ni(110). The (2x1)O_{ad} reconstructed Ni(110) surface was exposed to H_2S at 300K leading to S_{ad} and H_2O according to the reaction

$$H_2S = H_2S_{ad} \qquad\qquad (5.9)$$

$$H_2S_{ad} + O_{ad} = S_{ad} + H_2O\uparrow \qquad\qquad (5.10)$$
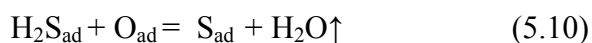
They have studied the progression of transition of (2x1)O_{ad} structure to (4x1)S_{ad} structure and recorded a series of Scanning Tunnelling Microscopy (STM) images showing the various stages of H_2S adsorption on oxygen-covered Ni(110) surface. From the data it was stated that "the catalytic substrate is not necessarily a static substrate to which the adsorbate bind. When adsorbed reactant or intermediates are involved in reconstructions, the mesoscopic topography of the surface may change, which in turn influence the structure sensitive chemical reactions" [109].

So the effect of 5 ppm of H_2S on impedance spectrum as a function of time may be understood as explained as follows

1. With no H_2S in the gas phase the possible reaction mechanism is given above (Reactions 5.5-5.8 and figure 5.6). The OH^- groups are formed and present on the surface of Ni. The presence of O-2 because of spillover of O^{-2} from YSZ was mentioned in the reaction mechanism. Now when 5 ppm H_2S is introduced into the gas mixture, H_2S reacts with the surface of Ni according to

$$H_2S = H_2S_{Ni} \qquad\qquad (5.11)$$

$$H_2S_{Ni} + 2OH^-_{Ni} = S_{Ni} + 2 H_2O\uparrow + 2e \qquad\qquad (5.12)$$
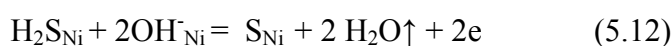
Initially as the above reaction proceeds the surface coverage of OH^- and O^{-2} decreases. The reaction 5.12 might be occurring simultaneously along with the reaction 5.6 and 5.7 though the rate of the latter two reactions is decreasing. So the net rate of the above three reactions at

the beginning results in a slightly higher current leading to the drop in the impedance spectrum. As the adsorption of S progresses according to the reaction 5.12 the surface coverage of OH^- (and O^{-2}) keeps decreasing. And when the adsorption of S approaches saturation the reaction 5.12 stops while only reactions 5.6 and 5.7 proceed at decreased rates. This causes the impedance of the electrode to increase with time. Once the sulphur adsorption reaches the saturation level the impedance spectrum becomes stable and shows no further increase.

2. Alternatively, if it is assumed that the dissociative adsorption of H_2S on Ni proceeds according to the reactions 5.13 and 5.14, then the formation of intermediate H_{Ni}, on the surface of Ni may cause the increase in reaction rates of 5.6 and 5.7. Initially when not much S is adsorbed the availability of this excess H_{Ni} causes an increase of the current which is seen as the drop in the impedance.

$$H_2S = H_2S_{Ni} \hspace{3cm} (5.13)$$

$$H_2S = 2H_{Ni} + S_{Ni} = H_2 + S_{Ni} \hspace{2cm} (5.14)$$

But with progressive adsorption of sulphur the surface concentration of various adsorbed species come down and so the impedance increases.

It is also possible that both of the above two mechanisms are operative leading to the initial drop in the impedance spectrum.

The activation energy of the impedance arc with 5 ppm H_2S in the gas is found to be same as the activation energy obtained in the H_2 + 3 vol% H_2O. There was no change in the shape of the impedance arc and a single arc was recorded also with the 5 ppm H_2S impurity. So based on the activation energies of the impedance arc with and without 5 ppm H_2S, it appears that the reaction mechanism remains unchanged with the same rate limiting step. But the reaction rate is decreased with the presence of H_2S impurity in the fuel gas.

5.2.2.3 Reversibility of the poisonous effect of H_2S

The performance of the electrode is reversible upon the withdrawal of 5 ppm of H_2S from the gas mixture at 823 K. The poisoning effect of 2-15 ppm of H_2S on Ni-YSZ cermets is shown to be completely reversible at 1273 K [31] after removing the H_2S impurity from the gas phase. In this work as shown in the results (figure 4.64), the reversibility was checked for 40 h. The spectrum was reversing but very slowly. Only 65% of the increased polarisation

resistance is reversed in 40 h. It is evident that the reversal of the poisoning effect, i.e., desorption of the adsorbed S is extremely slow in comparison to the time taken for the increase due to the poisoning effect of H_2S.

5.2.3 Ni-patterned LSGM symmetrical cells

5.2.3.1 In H_2+H_2O

In literature impedance analysis of Ni-patterned LSGM samples has not been reported so far. Also the electrode performance in the low temperature regime where Ni-LSGM does not show reactivity has not been studied. This may be because of the NiO-LSGM reactivity during sintering at high temperatures. In the earlier investigations with Ni-LSGM cermets [5,7] a poor performance of the cells was reported due to the reactivity of Ni and LSGM.

In this study, Ni-patterned LSGM cells prepared by photolithography were investigated in the temperature region where the Ni-LSGM interface is stable without any interdiffusion.

The electrolyte conductivity obtained from these Ni-patterned LSGM cells are in agreement to the values reported by Goodenough et al [3] measured with platinum electrodes. Note that R_e in figure 4.67, is the high frequency intercept of the impedance plot which also includes the resistance of the leads. The lead resistance is subtracted from R_e for the resistance of the electrolyte (LSGM).

A single arc is observed for Ni-patterned LSGM samples also. A single electrode process is assumed to be responsible for the observed impedance arc as in the case of Ni-patterned YSZ. The activation energy obtained from the impedance arc is also similar to the activation energy obtained from the impedance arc of the Ni-patterned YSZ cells. But the capacitance values obtained from the equivalent circuit fit, at peak frequency, are dependent on the temperature unlike Ni-patterned YSZ cells. The high capacitance obtained and its temperature dependence indicate that it can not be double layer capacitance at the Ni/LSGM interface. So it is not possible to directly assume the same reaction mechanism for Ni-patterned electrodes on LSGM as Ni- patterned YSZ.

Understanding the possible rate limiting step only based upon the activation energy obtained from the impedance arc is not possible. Many elementary reactions fall in a close range of activation energy.

The high value of capacitance obtained and its decrease with increasing temperature points towards additional processes at the TPB (capacitance shown in box 2 in figure 5.5), contributing to capacitance, such as adsorption processes on Ni or LSGM. Very little dependence of the electrode resistance on the partial pressure of water, though it slightly decreases with increasing $P(H_2O)$, indicates that the rate determining electrode process can not be adsorption/desorption reaction of H_2O either on Ni or on LSGM.

For the same design of Ni-patterns and TPB length, the electrode conductivity of Ni-patterned LSGM is 3.65 times the electrode conductivity of Ni-patterned YSZ cells. It indicates a possibility that either O^{-2} is directly involved in the rate determining step or it influences the concentration of intermediate species taking part in the rate determining step. However the exact reaction path is not clear.

To summarize, with the Ni-patterned electrodes on LSGM the rate determining step responsible for the impedance arc is not clearly understood. However an adsorption (on Ni or LSGM) reaction involving O^{-2} ions could be the rate determining step. It is important to know the various surface species in the vicinity of TPB of Ni-patterned electrodes on LSGM for a clear understanding of the mechanism. And also a detailed further study of reaction kinetics of Ni-patterned electrodes with LSGM electrolyte, is necessary.

5.2.3.2 Effect of 5 ppm of H_2S in H_2+H_2O

As observed with the Ni-patterned YSZ, Ni-patterned LSGM symmetrical cells also showed an initial drop in the impedance measured immediately after the introduction of 5 ppm of H_2S. As already mentioned this effect may be due to the reaction involving the dissociative adsorption of H_2S with the charged species on the surface of the Ni as given in reaction 5.12. The surface coverage of the charged species decreases to a lower value and that occurs via the reaction 5.12 which initially increases the net current in comparison to the charge transfer reaction(s) under equilibrium conditions with no H_2S.

The increase in the polarisation resistance because of 5 ppm of H_2S is dependent on the partial pressure of H_2O in the gas mixture. An increase of 70% in R_p is noticed due to the presence of 5 ppm of H_2S in H_2+H_2O (3 vol%) gas with respect to the spectrum measured in H_2+H_2O (3 vol%). When the $P(H_2O)$ is 20 vol% the increase in R_p due to the presence of 5 ppm of H_2S is less than 20%.

The activation energies of the impedance arc measured with and without 5 ppm of H_2S are found to be the same. The same observation was made also with the Ni-patterned YSZ. It appears that the reaction mechanism remains unaltered because of the introduction of 5ppm of H_2S. In other words introduction of 5 ppm of H_2S into H_2+H_2O gas mixture doesn't seem to change the electrode reaction mechanism, but only affects the rate of the rate-determining electrode process.

5.2.3.3 Reversibility of the poisonous effect of H_2S

When 5 ppm of H_2S is withdrawn from the gaseous atmosphere the impedance spectrum reverses relatively quickly in comparison to the Ni-Patterned YSZ cells. The partial pressure of water found to influence also the time taken for the reversibility of the impedance spectrum i.e., the time taken for the impedance spectrum to reach the initial state before H_2S poisoning.

The reversibility of R_p as a function of time at different partial pressures of H_2O shows that at lower $P(H_2O)$ it takes longer time for the reversal. R_p reversed to initial state in 4 h 18 min in H_2+H_2O (40 vol%) while it didn't reverse completely in H_2+H_2O (6 vol%) even after 14 h. The exact reason for this behaviour is not known. It may be possible that at lower partial pressures of H_2O the samples may exhibit a relatively high uptake of S. It could be a reason for a slow reversal at lower partial pressures of H_2O. Another possible reason could be the effect of $P(H_2O)$ on the kinetics of S desorption. However, it has to be noted here that the reversibility at 6 vol% H_2O was very slow and after showing about 50% reversibility, the impedance started to increase again. More experiments are necessary to understand the reversibility of the poisonous effects in H_2 gas with low partial pressures of H_2O.

5.2.4 Comparison of the Ni-patterned YSZ and Ni-patterned LSGM cells

One important observation which can be derived from the comparison of Ni-patterned YSZ and Ni-patterned LSGM cells in H_2+H_2O atmosphere is that the electrode conductivity (σ_p) of Ni-patterned LSGM cells is 3.65 times the electrode conductivity of Ni-patterned YSZ cells for the same TPB length and design of Ni-patterns. It shows the role of the electrolyte in the reaction mechanism.

The activation energy of σ_p for both the electrodes with and without 5 ppm of H_2S is found to be the same (±0.03 eV). But the rate determining step responsible for the impedance arc is may be different for Ni-patterned YSZ from Ni-patterned LSGM. The former electrode

appears to be limited by the adsorption process accompanied by charge transfer while the latter seems to be limited by an adsorption process which is not known.

Both the electrodes exhibit a momentary initial drop in the impedance values before increasing due to the poisonous effect of H_2S. H_2S dissociatively adsorbs on Ni surface simultaneously reducing the surface coverage of charged species on Ni.

Because of the introduction of 5 ppm of H_2S into H_2+H_2O (3 vol%) gas the R_p increase by 100% in the case of Ni-patterned electrodes on YSZ cells and by 70% in the case of Ni-patterned electrodes on LSGM.

The reversibility of the poisonous effect of S on the impedance spectrum is different for Ni-patterned YSZ from Ni-patterned LSGM. Time taken for 50% reversal of increase in Rp in H_2+H_2O (6 vol%) gas is 30 min for Ni-patterned LSGM while it takes 673 min for Ni-patterned YSZ. However in both the cases the complete reversal appears to take a very long time. This needs further experiments for longer duration of time. The kinetics of S desorption from unsupported and Al_2O_3-supported Ni is known to be different [105]. The support is known to have its effect on the desorption kinetics. To clearly understand the effect of substrate on adsorption/desorption of S, the knowledge of substrate induced structural modifications of Ni close to the interface, the binding and concentration of the adsorbant (S) on Ni at the Ni-substrate interface and triple phase boundary, and interaction of the H_2S with the substrate itself, is required.

6.0 Conclusions

6.1 Microstructural stability of Ni-YSZ, Ni-LSGM and Ni-CGO cermets

The stability of Ni-YSZ, Ni-LSGM and Ni-CGO cermets in H_2+H_2S (1 vol%) gas in the temperature range of 500-750°C was studied. It is confirmed that S is highly poisonous to Ni.

Ni-YSZ cermets

S in the gas is highly reactive to Ni in the cermets even at 500°C. It forms Ni_3S_2 at 500°C and undergoes eutectic melting at 750°C. However from the XRD and SEM investigations, YSZ is found to be stable in H_2+H_2S (1 vol%) gas in the temperature range of investigation.

Ni-CGO cermets

The microstructure of the Ni-CGO cermet is stable with no reactivity between Ni and CGO in hydrogen atmosphere. In H_2+H_2S (1vol%) gaseous atmosphere CGO in the cermet is stable at 500°C but forms oxysulphide $((Ce,Gd)_2O_2S)$ at 750°C.

Ni-LSGM cermets

NiO-LSGM reactivity during sintering in air at high temperatures (1200-1350°C) was investigated. NiO reacts with LSGM during sintering in air at high temperatures (>1200°C) forming a cubic $LaNiO_3$-type phase. XRD and TEM investigation of the NiO-LSGM reactivity revealed that interdiffusion across the interface leads to diffusion of Ni into LSGM. Ni sits in the B-sites of the perovskite replacing Ga and Mg. It is very likely that the $LaNiO_3$-type phase is similar to the cubic LSGM phase with a relatively high amount of Ni. The possible crystal chemistry of this phase is $(La,Sr)(Ga,Mg,Ni) O_{3-x}$.

NiO-LSGM reactivity was found to be a problem in preparation of NiO-LSGM sintered compacts. Sintering NiO-LSGM in inert atmosphere (in Argon or Nitrogen) was also not helpful to produce NiO-LSGM sintered compacts without any reactivity or decomposition of LSGM.

NiO/Ni and LSGM are also reactive in hydrogen atmosphere even at temperatures as low as 750°C. The reduction of NiO-LSGM to produce Ni-LSGM cermets led to the decomposition of $LaNiO_3$-type phase (i.e $LSGM(Ni)$) into La_2O_3 and $SrLaGaO_4$ accompanied by diffusion of excess amount Ga into FCC_Nickel. After reduction Ni in the cermet contained about 9 at% of dissolved Ga.

Interestingly the FCC solid solution of Ni-Ga alloy was found to be stable in H_2+H_2S (1 vol%) gas at 750°C. If this alloy can also be a good electrocatalyst with its relatively high

tolerance limit of H_2S in comparison to pure Ni, it will be a potential candidate for anode material to work with sulphur containing fuels.

Ni-LSGM cermets without any reactivity, for their investigation as a SOFC anode could not be made. Ni-patterned LSGM symmetrical cells were made by photolithography for electrochemical impedance studies.

Auger investigation of the Ni-LSGM interface of these Ni-patterned LSGM cells was carried out to understand the threshold temperature below which the interface is stable. It was found that at temperatures below 650°C the interface is stable without any reactivity and/or interdiffusion. However at 750°C interdiffusion across the interface leads to the incorporation of Ni into LSGM with simultaneous diffusion of Ga from LSGM into Ni.

The Ni patterns made on LSGM, single crystal YSZ and polycrystalline YSZ samples are found to be mechanically stable only below 550°C. At higher temperatures (>550°C) the Ni patterns showed disintegration. So the EIS investigation of the symmetrical cells could be carried out only below 550°C.

6.2 Thermodynamic modelling Ni-S-O-H quaternary

A consistent set of thermodynamic data of the quaternary system Ni-S-O-H was performed by using the CALPHAD methodology. For this the binary system Ni-S was newly assessed in this work. The solid solution phases were modelled by using sublattice models and the liquid phase was modelled by associated solution model.

The binary systems Ni-O and Ni-H were taken from the literature. The ternary systems Ni-O-H and Ni-O-S were calculated by extrapolation technique as employed in CALPHAD methodology and the quaternary system Ni-S-O-H was calculated from the lower order systems.

The predominance area diagrams with different potentials (variables) as axes were calculated. Using the Ni-S-O-H database the stability diagrams of the FCC Ni phase can be calculated at required temperature with required independent variables as partial pressures of gaseous species ($P(H_2S)/P(H_2)$, $P(H_2O)/P(H_2)$ etc.,).

The system Ni-Ga-S ternary was calculated to understand the stability of Ni-Ga alloy in H_2+H_2S (1 vol%) gas. The calculations revealed that FCC solid solution of Ni-Ga alloy shows

a relatively higher tolerance for S than pure Ni at 750°C. However the stability of this Ni-Ga alloy is almost the same as pure Ni at 500°C.

6.3 Effect of H2S on electrochemistry of Ni-patterned electrodes

6.3.1 Ni-patterned YSZ
6.3.1.1 single crystal cells

A single impedance arc very close to a perfect semicircle was measured for the symmetrical cells of Ni-patterned YSZ single crystals. The exponent of CPE obtained from the equivalent circuit fit results is very close to 1.

EIS analysis of the symmetrical cells of Ni-patterned YSZ single crystals of different orientations revealed that the capacitance calculated from impedance arc is dependent on the orientation of the YSZ single crystal. The capacitance values are found in the order of $C_{<100>} < C_{<111>} < C_{<110>}$. The capacitance values are found to be temperature-independent but can not be purely due to the double layer. However, no clear conclusion could be drawn regarding the dependence of Rp (total polarisation resistance of the cell) on the face of the YSZ crystal.

6.3.1.2 polycrystalline cells

The impedance analysis of Ni-patterned YSZ symmetrical cells also revealed that a single process is responsible for the impedance arc. The capacitance obtained from equivalent circuit fit of the impedance data is found to be independent of temperature. The obtained capacitance values can not be *exclusively* due to the double layer capacitance. However the capacitance values of polycrystalline samples appears to be average of the capacitance measured with single crystal cells of different orientations. The observed capacitance could be double layer capacitance and/or pseudo-capacitance associated with adsorption of species accompanied by partial charge transfer.

A possible reaction mechanism for H_2 oxidation at Ni patterned electrodes on YSZ electrolyte was given. Formation of OH⁻ from the reaction between adsorbed H and O^{-2} could be the rate limiting step responsible for the impedance arc. The oxidation of H_2 at Ni-patterned electrodes close to equilibrium conditions appears to be limited by the elementary process $H_{Ni} + O_{YSZ}^{-2} \Leftrightarrow OH_{Ni}^{-}$.

Even 5 ppm of H2S in H_2+H_2O gas is found to be poisonous to the Ni-electrodes on YSZ. The H2S is found to double the total polarisation resistance of symmetrical cell. An interesting

observation of an initial drop in the impedance spectrum immediately after the release of H_2S may be due to the reaction between OH^- intermediates and the H_2S during the initial stages of dissociative adsorption of H_2S on Ni surface. The poisonous effect of H_2S is reversible upon its withdrawal from H_2+H_2O gaseous atmosphere. But at 823 K the reversibility is very slow.

It appears that addition of 5 ppm of H_2S does not lead to change of the rate limiting step. However the addition leads to a decrease in the rate of the reaction. The same activation energy obtained from the impedance arc with and without 5 ppm of H_2S supports this assumption.

6.3.2 Ni-patterned LSGM

Ni-patterned LSGM symmetrical cells (Ni-LSGM-Ni) are studied for the first time in the temperature range where there is no Ni-LSGM interfacial reactivity. The measured conductivity of LSGM is in good agreement with the conductivity data in literature, measured with Pt electrodes. If Ni-LSGM reactivity can be avoided Ni-LSGM will be a better candidate for anode material for intermediate temperature SOFCs

Single impedance arc was measured in a wide range of experimental conditions and thus a single electrode process was assumed. The equivalent circuit fit results revealed that the capacitance is dependent on temperature unlike Ni-patterned YSZ cells. The rate determining step responsible for the impedance arc is not clearly understood. However an adsorption (on Ni or LSGM) reaction involving O^{-2} ions could be responsible for it.

The presence of even 5 ppm of H_2S in H_2+H_2O gas is found to decrease the electrode conductivity. However the decrease in the electrode conductivity is dependent on the partial pressure of water in the gas. In dry gas the effect of 5 ppm of H_2S is much more poisonous.

The initial drop in the impedance spectrum immediately after the release of H_2S was also observed with Ni-Patterned LSGM cells. The initial enhancement in the reaction rate is may be due to the reaction of H_2S with the charged intermediates on Ni surface during initial stages of its dissociated adsorption.

From the same activation energy obtained from the impedance arc with and without 5 ppm of H_2S it seems that the rate determining process was same in both atmospheres. But with 5ppm of H_2S the rate of the reaction was decreased.

The poisonous effect of 5 ppm of H_2S is reversible. The time taken for complete reversibility is dependent on the partial pressure of water in the H_2+H_2O gas. At lower partial pressures of water longer periods are required.

7.0 Zusammenfassung

Eine wichtige Anforderung an Hochtemperaturbrennstoffzellen (SOFC) bei der Stromerzeugung ist die Verwendung einer möglichst breiten Auswahl von Brennstoffen. Unter den Ni-Cermets ist Ni-YSZ das Standardmaterial für die SOFC- Anode (Brenngaselektrode). Allerdings sind Schwefelverunreinigungen, die in verschiedenen Brenngasen (z.B. Biogas) vorkommen, abhängig von ihrer Konzentration abträglich für die Stabilität und die elektrochemische Leistungsfähigkeit des Ni-Katalysators in den Cermet-Anoden. In der vorliegenden Arbeit wird deshalb die mikrostrukturelle Stabilität von Ni-YSZ, Ni-CGO und Ni-LSGM-Cermets in H_2S-haltigem Wasserstoffgas im mittleren Temperaturbereich des SOFC Betriebs untersucht. Eine thermodynamische Modellierung des quaternären Ni-S-O-H Systems wurde durchgeführt, um die thermodynamische Stabilität sowie die Schwefeltoleranzgrenze von Ni in einer aus H, O und S aufgebauten Gasatmosphäre zu berechnen. Die Auswirkung von H_2S im Brenngas, in Konzentrationen unterhalb der thermodynamischen Toleranzgrenze, auf die elektrochemische Leistungsfähigkeit der Anoden wurde untersucht durch die Anwendung Ni-strukturierter Elektroden auf YSZ und LSGM.

7.1 Mikrostrukturelle Stabilität von Ni-YSZ und Ni-CGO Cermets in H_2+H_2S

Ni-YSZ und Ni-CGO Cermets wurden in einer H_2+H_2S (1 Vol.%) Gasatmosphäre im mittleren Temperaturbereich (500-750°C) untersucht, um ihre mikrostrukturelle Stabilität in H_2S-haltigen Gasen zu verstehen. H_2S in der Gasatmosphäre ist für das Ni in den Cermets hochgradig giftig. Bei Temperaturen über 901 K (berechnete eutektische Temperatur) bildet Ni aufgrund seiner Reaktion mit Schwefel eine eutektische Schmelze und gemäß dem binären Ni-S Phasendiagramm entsteht bei 773 K Ni_2S_3. Das YSZ im Cermet ist dagegen stabil gegenüber der H_2+H_2S (1 Vol.%) Gasatmosphäre im untersuchten Temperaturbereich. Jedoch zeigt CGO eine Reaktion mit H_2S in Abhängigkeit von der Temperatur. Es reagiert zu $(Ce,Gd)_2O_2S$ bei 750°C, während es bei 500°C noch stabil bleibt.

7.2 Mikrostrukturelle Stabilität von Ni-LSGM-Cermets in H_2 und H_2+H_2S

7.2.1 Ni-LSGM als eine neuartige Cermet Anode für H_2-Oxidation

Ni-LSGM-Cermets wurden als neuartiges Anodenmaterial für Hochtemperaturbrennstoffzellen untersucht. Aus der Literatur ist bekannt, dass NiO und LSGM während der Herstellung der Brennstoffzelle miteinander reagieren. In dieser Arbeit

wurde versucht, NiO-LSGM-Proben zu versintern, ohne dass es zu einer Reaktion zwischen NiO und LSGM kommt. Eine durch Sinterprozesse an Luft entstehende LaNiO$_3$-artige Phase bildet sich auch während des Sinterprozesses in Inertgasatmospähre. In der Literatur wird die verminderte Leitfähigkeit bei der Messung mit einer Ni-LSGM-Cermet-Anode mit einer solchen isolierenden LaNiO$_3$-artigen Phase in Verbindung gebracht. Allerdings waren genauere Kenntnisse über deren Struktur und die Zusammensetzung dieser Zwischenschicht nicht vorhanden. Da es wichtig ist, die Struktur und Zusammensetzung der durch den Sinterprozess gebildeten Zwischenschicht zu verstehen, wurde eine detaillierte TEM-Untersuchung der NiO-LSGM-Grenzfläche durchgeführt.

Die TEM-Untersuchung der NiO-LSGM-Grenzfläche nach dem Sintern an Luft bei 1350°C ergab, dass die gebildete LaNiO$_3$-artige Phase eine Ähnlichkeit mit der kubischen LSGM-Phase mit einem relativ hohen Ni-Gehalt aufweist. Die Kristallchemie entspricht (La,Sr)(Ga,Mg,Ni)O$_{3-x}$. Während des Sinterns führt eine Interdiffusion durch NiO-LSGM zu einer Diffusion von Ni in die LSGM-Phase. Ni sitzt auf den B-Plätzen derPerowskitstruktur. Die Analyse der Zusammensetzung über die NiO-LSGM-Grenzfläche ergibt die Phasen Ni(Mg,Ga)O – (La,Sr)(Ga,Mg,Ni)O$_{3-x}$.

Eine weitere Reaktion von NiO/Ni mit LSGM wurde während der Reduktion der gesinterten NiO-LSGM-Proben in H$_2$ zur Herstellung der Ni-LSGM-Cermets beobachtet. Die LaNiO$_3$-artige Phase (z.B. LSGM(Ni)) zerfällt in La$_2$O$_3$ und SrLaGaO$_4$, begleitet von einer Diffusion von überschüssigem Ga in kubisch flächenzentriertes Nickel. So zeigten sich etwa 9 at% gelöstes Ga im Ni. Ni-LSGM-Cermets ohne chemische Reaktionen ließen sich zur Betrachtung als SOFC-Anodenmaterial nicht herstellen.

7.2.2 Ni-LSGM-Cermets in H$_2$+H$_2$S

Die Ni-LSGM-Cermets wurden auf ihre Stabilität in H$_2$+H$_2$S (1 Vol.%)-Atmosphäre untersucht. Interessanterweise ist die FCC Festphasenmischung Ni-Ga stabil gegenüber der H$_2$+H$_2$S-Atmosphäre bei 750°C, obwohl bekannt ist, dass reines Ni die eutektische Mischung Ni+Ni$_2$S$_3$ bildet. Der Anstieg der Schwefeltoleranzgrenze dieser Ni-Ga-Legierung bei 750°C wird darüber hinaus gestützt durch Phasendiagrammberechnungen des ternären Systems Ni-Ga-S. Die relativ höhere Toleranz der Ni-Ga-Legierung gegenüber H$_2$S erweckt das Interesse, die elektrokatalytischen Eigenschaften des Materials zu untersuchen.

7.3 Ni-strukturiertes LSGM in H_2 und H_2+H_2S

Da Ni-LSGM-Cermets nicht erfolgreich hergestellt werden konnten, wurden zur Untersuchung der elektrochemischen Leistungsfähigkeit Ni-strukturierte LSGM-Zellen mittels Fotolithografie hergestellt. Ni-strukturierte Elektroden sind Modellelektroden zum besseren Verständnis der Elektrodenreaktionsmechanismen. Ein Hochtemperatur-Sinterschritt wurde ebenfalls vermieden. Die Grenzflächenstabilität dieser Ni-strukturierten LSGM-Zellen in gasförmiger Wasserstoffatmosphäre wurde im mittleren Temperaturbereich untersucht. Die Auger-Tiefenprofilanalyse an diesen Zellen zeigt, dass bei Temperaturen unter 650°C die Grenzfläche stabil ist, ohne Reaktionen oder Interdiffusion aufzuweisen. Allerdings erfolgt bei 750°C die Interdiffusion über die Grenzfläche, die zu einer Diffusion von Ni in die LSGM-Phase mit einer gleichzeitigen Diffusion von Ga in die Ni-Phase führt. Aus diesem Grund wurden die Untersuchungen zur elektrochemischen Leistungsfähigkeit der symmetrischen, Ni-strukturierten LSGM-Zellen im Temperaturbereich unter 650°C durchgeführt, in dem keine Reaktionen zwischen Ni und LSGM auftreten.

7.4 Thermodynamische Modellierung des quarternären System Ni-S-O-H

Thermodynamische Modellierung des quaternären Systems Ni-S-O-H mit Hilfe der CALPHAD-Methode wurde durchgeführt, um die Stabilität von Ni in einer Atmosphäre, die S_2O und H enthält, zu verstehen. Zur Modellierung des binären Phasendiagramms Ni-S wurden Untergittermodelle für die nicht-stöchiometrischen Phasen verwendet. Optimierte Diagramme für Ni-O und Ni-H wurden der Literatur entnommen. Die ternären Diagramme für Ni-O-S und Ni-O-H wurde durch Extrapolation aus den entsprechenden binären Diagrammen gewonnen. Im System Ni-O-S ist $NiSO_4$ die einzige vorliegende ternäre Verbindung. Die ternären Verbindungen $Ni(OH)_2$ und $NiOOH$ im System Ni-O-H wurden als stöchiometrische Verbindungen betrachtet. Die Modelparameter der ternären Verbindungen wurden unter Verwendung der experimentellen Daten optimiert. Das quaternäre System Ni-S-O-H wurde mittels der Extrapolationsmethode, wie sie in CALPHAD angewandt wird, berechnet.

Phasendiagramme mit verschiedenen Potential-Variablen als Achsen wurden berechnet (predominance area diagrams). Die Stabilität von Ni in H_2S, H_2O and H_2S Atmosphäre kann aus den berechneten Stabilitätsdiagrammen mit den benötigten unabhängigen Variablen ($P(H_2S)/P(H_2)$ gegenüber $P(H_2O)/P(H_2)$) als Achsen vorhergesagt werden. Ähnliche

Potenialdiagramme für die Stabilität von Ni in gasförmigen Atmosphären der Spezies S, O und H können aus dem quaternären System Ni-S-O-H berechnet werden.

Das Phasendiagramm des ternären Systems Ni-Ga-S wurde berechnet, um die relativ höhere H_2S-Toleranz von Ni – Ga FCC Mischkristallen im Vergleich mit reinem Ni zu erklären. Die mittels dieses ternären Systems bei 750 °C berechneten Diagramme unterstützen den mit steigender Ga-Aktvität ansteigende Schwefel-Toleranz in der FCC Ni-Ga Legierung. Allerdings zeigten die bei 500 °C berechneten Potentialdiagramme, dass die Schwefeltoleranz der Ni-Ga Legierung nicht stark mit dem Ga-Gehalt ansteigt und fast gleich bleibt wie die von reinem Ni. Das ist in vollständiger Übereinstimmung mit dem experimentellen Befund für die Stabilität der Ni-GA Legierung in H_2 + H_2S (1vol%) Atmosphäre.

7.5 Einfluss von H_2S auf den Reaktionsmechanismus der H_2-Oxidation an Ni-strukturierten Elektroden

Die Untersuchung des Einflusses von H_2S auf den elektrochemischen Reaktionsmechanismus der H_2-Oxidation an den Anoden von SOFCs beinhaltete zwei wichtige Schritte. Erstens das Verständnis des Reaktionsmechanismus der Wasserstoff-Oxidation an der Anode und zweitens die Untersuchung des Einflusses von H_2S auf die Elektrochemie des anodischen Prozesses. Der Reaktionsmechanismus der H_2 Oxidation an Ni-YSZ Cermet-Anoden wurde in der Literatur ausführlich unersucht. Es wurde auch versucht, an Ni-Strukturen, die als Modell-Elektroden komplexe Mikrostrukturen vermeiden, die Reaktionswege und verschiedenen elementaren Reaktionsschritte zu verstehen. Bislang wurde allerdings kein klares Verständnis der Elektrochemie der H_2-Oxidation an der Anode erzielt. Verschiedene Autoren schlagen verschiedene Reaktionsmechanismen und ratenbegrenzende Schritte vor.

7.5.1 Elektrochemie von Ni-strukturierten YSZ Zellen in H_2+H_2O mit bzw. ohne 5ppm H_2S

Symmetrische Zellen aus Ni-strukturierten YSZ Einkristallen mit verschiedenen kristallografischen Orientierungen wurden in H_2+H_2O Atmosphäre in einem mittleren Temperaturbereich unersucht ,mit dem Ziel, den H_2-Oxidationsmechnismus und die Rolle, die der Elektrolyt dabei spielt, zu verstehen. Elektrochemische Impedanzspektroskopie (EIS) wurde angewandt, um die Prozesse and den Elektroden zu verstehen.

Im Messbereich der experimentellen Bedingungen wurde gefunden, dass Ni-struktrierte YSZ-Zellen begrenzt sind durch einen einzigen Prozess an der Elektrode. Ein einzelner Impedanzbogen, sehr nahe an einem perfekten Halbkreis, wurde gefunden. Der CPE-Exponent, der sich aus der entsprechenden Anpassung ergab, ist sehr nahe 1.

Die Widerstand der Gesamtpolarisation (total polarization resistance Rp), der eine inverse Relation zur Rate der elementaren Prozesse hat, die den Impedanzhalbkreis bestimmen, scheint von der Oberflächenorientierung der YSZ-Kristalle abzuhängen. Hinsichtlich dieser Abhängigkeit konnte jedoch keine klare Schlussfolgerung gezogen werden. Es sind weitere Experimente notwendig, um die Abhängigkeit von Rp und seine Beziehung zur Oberflächenstruktur des YSZ zu verstehen.

Die Impedanzanalyse von symmetrischen, Ni-struktrierten YZ-Einkristallen unterschiedlicher Orientierung ergab weiterhin, dass die aus dem Impedanzbogen berechnete Kapazität von der Oberflächenorientierung der YSZ-Einkristalle abhängt. Eine Relation der Kapazitätswerte von $C_{<100>} < C_{<111>} < C_{<110>}$ wurde festgestellt. Die gefundenen Kapazitätswerte sind unabhängig von der Temperatur, aber nicht einzig durch eine Doppelschicht bestimmt.

Im Falle von Ni-strukturieretn polykristallinen YSZ-Zellen wurde ebenfalls gefunden, dass ein einiger Prozess den Impedanzbogen bestimmt. Die von diesen polykristallinen Proben gezeigten Kapazitätswerte sind ähnlich denen der einkristallinen Zellen und liegen im Bereich des Mittelwerts, der an einkristallinen Zellen unterschiedlicher Orientierung gemessen wurde. Ebenso wie im Falle einkristalliner Zellen war die Kapazität temperaturunabhängig. Daher können die Kapazitätswerte nicht *ausschließlich* von der Doppelschicht-Kapazität herrühren. Die beobachtet Kapazität kann eine Doppelschicht-Kapazität und/oder eine Pseudokapazität sein, die verbunden ist mit der Adsorption von Spezies, begleitet von partiellem Ladungsaustausch.

Es wurde festgestellt, dass Wasser einen katalytischen Effekt bei der H_2-Oxidation zeigt. Jedoch wurde, abweichend von Literaturdaten, nur eine sehr geringe Abhängigkeit der Elektrodenleitfähigkeit vom Wasser-Partialdruck gefunden.

Folgender Reaktionsmechanismus an den Ni-strukturierten ein- und polykristallinen Zellen wird vorgeschlagen:

Dissoziative Adsorption von H_2 an Ni

$$H_2 \leftrightarrow H_{Ni} \qquad\qquad (7.1)$$

Bildung von Hydroxil an Ni

$$H_{Ni} + O^{-2}_{YSZ} \leftrightarrow OH^-_{Ni} + e \qquad (7.2)$$

Bildung von H_2O an Ni

$$H_{Ni} + OH^-_{Ni} \leftrightarrow H_2O_{Ni} + e \qquad (7.3)$$

$$H_2O_{Ni} \leftrightarrow H_2O(gas) \qquad (7.4)$$
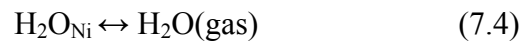
Die elementare Reaktion "$H_{Ni} + O^{-2}_{YSZ} \leftrightarrow OH^-_{Ni} + e$" wird als der ratenbestimmende Schritt betrachtet, der für den Impedanzhalbkreises verantwortlich ist. Die Bildung und Adsorption von OH^- an Ni aus der Reaktion zwischen O^{-2}_{YSZ} und H_{Ni} an der Ni-YSZ Grenzfläche (Zwei-Phasen-Grenzfläche) kann als der für die beobachtete Kapazität verantwortliche Prozess betrachtet werden. Es wird angenommen, dass dies ein kapazitiver Prozess ist, und kein DC-Prozess.

Der Einfluss von 5 ppm H_2S auf die H_2-Oxidationskinetik an Ni-strukturierten Elektroden wurde untersucht. Es wurde festgestellt, dass sogar eine solch geinge Konzentration von H_2S in $H_2 + H_2O$-Gas schädlich für die Ni-Elektroden ist. Das Hinzufügen von 5 ppm H_2S verdoppelte den Widerstand der Gesamtpolarisation symmetrischer Zellen. Es ergab sich jedoch keine Änderung der Form des Impedanzhalbkreises und es wurde ein einzelner Halbkreis gemessen. Die daraus bestimme Aktivierungsenergie war dieselbe unter den Bedingungen mit bzw. ohne 5 ppm H_2. Daraus kann gefolgert werden, dass das Hinzufügen von 5 ppm H_2 nicht zu einer Änderung des ratenbegrenzenden Schrittes führt, sonder zu einer Verringerung der Reaktionsrate.

Interessanteweise wurde ein Abfallen des Impedanzspektrums unmittelbar nach Hinzufügen des H_2S beobachtet. Dies kann von folgender Reaktion zwischen OH^- und H_2S zu Beginn der dissoziativen Adsorption von H_2S an der Ni-Oberfläche herrühren,

$$H_2S_{Ni} + 2OH^-_{Ni} = S_{Ni} + 2\,H_2O\uparrow + 2e \qquad (7.5)$$
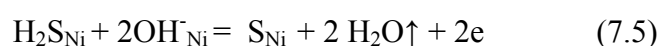
Der schädliche Einfluss von H_2S ist reversibel, jedoch ist die Reversibilität bei 823 K sehr langsam.

7.5.2 *Elektrochemie von Ni-strukturierten LSGM-Zellen in H_2+H_2O mit bzw. ohne 5ppm H_2S*

Die Elektrochemie von Ni-strukturiertem LSGM wird erstmals untersucht in einem Temperaturbereich, in dem keine Ni-LGSM Grenzflächenreaktivität existiert. Die Ergebnisse sind sehr ermutigend und wenn Ni-LSGM Cermets hergestellt werden können, welche keinerlei Reaktivität zeigen, dann sind das bessere Anodenmaterialien zum Betrieb in einem als sicher bestimmten Temperaturbereich. Die gemessene Leitfähigkeit des LSGM der symmetrischen Zellen ist in guter Übereinstimmung mit Literaturdaten (welche allerdings mit Pt-Elektroden gemessen wurden).

Der Reaktionsmechanismus und ratenbestimmende Schritt bei der H_2-Oxidation an Ni-strukturierten Elektroden auf LSGM ist nicht notwendigerweise derselbe wie an Ni-strukturiertem YSZ. Bei LSGM wurde auch ein einzelner Bogen gemessen, über den gesamten Bereich der experimentellen Bedingungen und ein Einzelelektrodenprozess konnte als Ursache für den Bogen angenommen werden. Die entsprechenden Anpassungen zeigten, dass die Kapazität, anders als bei YSZ, temperaturabhängig ist. Der ratenbestimmende Schritt ist noch nicht vollständig verstanden. Die Wert der gemessenen Kapazität und seine Temperaturabhängigkeit deuten jedoch darauf hin, dass eine Adsorptionsreaktion (an Ni oder LSGM, die O^{-2}-Ionen einschließt, den Impedanzhalbkreis bestimmen.

Die Beimischung von 5ppm H_2S zum H_s+H_2O Gasgemisch reduzierte, wie im Fall von YSZ, die Leitfähigkeit der Elektrode. Dies hängt ab vom Wasser-Partialdruck im Gas. In trockenem Gas ist der Effekt sehr viel schädlicher. Für dieselbe Gasmischung und unter denselben experimentellen Bedingungen ist der Effekt bei YSZ-Zellen stärker ausgeprägt als bei LSGM-Zellen.

Auch das anfängliche Absinken im Impedanzspektrum unmittelbar nach dem Einleiten von H_2S wurde bei LSGM-Zellen beobachtet. Dieselben Prozesse wie für YSZ-Zellen diskutiert, können als Ursache für das anfängliche Ansteigen der Reaktionsrate angenommen werden.

Auch im Falle der LSGM-Zellen bleibt der Reaktionsmechanismus bei Zumischung von 5 ppm H_2S unverändert, während die Reaktionsrate, die den Impedanzbogen bestimmt, sich verlangsamt. Diese Annahme wird unterstützt durch die Tatsache, dass die Aktivierungs-energie von der Präsenz von H_2S unbeeinflusst ist.

Der schädliche Effekt der H_2S-Verunreinigung ist ebenfalls reversibel. Im Falle der LSGM-Zellen geht der Effekt von H_2S schneller zurück als bei YSZ-Zellen, bei gleicher Gas-Zusammensetzung und gleicher Temperatur. Weiterhin wurde festgestellt, dass mit höherem Wasser-Partialdruck der schädliche Einfluss von H_2S schneller zurückgeht.

References

[1] S.C. Singhal , "Advances in solid oxide fuel cell technology", Solid State Ionics ,135 (2000) 305–313.

[2] T. Ishihara, H. Matsuda, Y. Takita, "Doped $LaGaO_3$ Perovskite Type Oxide as a New Oxide Ionic Conductor", J. Am. Ceram. Soc. 116 (1994) 3801-3803.

[3] K. Huang, R. Tichy, J.B. Goodenough, "Superior Perovskite Oxide-Ion Conductor; Strontium- & Magnesium-Doped $LaGaO_3$: I, Phase Relationships and Electrical Properties" J. Am. Ceram. Soc. 81 (1998) 2565-2575.

[4] K. Huang, R. Tichy, J.B. Goodenough, "Superior Perovskite Oxide-Ion Conductor; Strontium- & Magnesium-Doped $LaGaO_3$: II, ac Impedance Spectroscopy", J. Am. Ceram. Soc. 81 (1998) 2576-2580.

[5] K. Huang, R. Tichy, J.B. Goodenough, "Superior Perovskite Oxide-Ion Conductor; Strontium- & Magnesium-Doped $LaGaO_3$: III, Performance Tests of Single Ceramic Fuel Cells", J. Am. Ceram. Soc. 81 (1998) 2581-2585.

[6] X. Zhang, S. Ohara, R. Maric, K. Mukai, T. Fukui, H.Yoshida, M. Nishimura, T. Inagaki, K. Miura,"Ni-SDC cermet anode for medium-temperature solid oxide fuel cell with lanthanum gallate electrolyte", J. Power Sources. 83 (1999) 170-177.

[7] X. Zhang, S. Ohara, R. Maric, H. Okawa, T. Fukui, H. Yoshida, T.Inagaki, K. Miura, "Interface reactions in the NiO-SDC-LSGM system", Solid State Ionics. 133 (2000) 153-160.

[8] K. Huang, J. wan, J.B. Goodenough, "Increasing power density of LSGM-based solid oxide fuel cells using new anode materials", J. Electrochem. Soc. 148 (2001) A788-A794.

[9] X. Zhang, S. Ohara, H. Okawa, R. Maric, T. Fukui, "Interactions of a $La_{0.9}Sr_{0.1}Ga_{0.8}Mg_{0.2}O_{3-delta}$ electrolyte with Fe_2O_3, Co_2O_3 and NiO anode materials." Solid State Ionics 139 (2001) 145-152.

[10] P. Huang, A. Horky, A. Petric, "Interfacial Reaction between Nickel Oxide and Lanthanum Gallate during Sintering and its Effect on Conductivity." J. Am. Ceram. Soc. 82(1999) 2402-2406.

[11] M. V. Rao, M. Zinkevich, F. Aldinger, "Ni-based cermet anodes for IT-SOFC: Stability and performance with sulfur-containing gaseous fuels."Proceedings, Sixth European Solid Oxide Fuel Cell Forum, Lucerne, Switzerland, Vol. 3, (2004) 1505-1513.

[12] A.Atkinson, S.Barnett et al, "Advances anodes for high-temperature fuel cells", Nature Materials, vol3, Jan 2004, 17-27.

[13] J. P. P. Huijsmans, F. P. F. van Berkel and G. M. Christie, "Intermediate temperature SOFC – a promise for the 21st century", J. Power Sources, 71 (1998) 107-110.

[14] Takehisa Fukui, Satoshi Ohara, Kenji. Murata, Hiroyuki Yoshida, Kazuhiro Miura, Toru Inagaki, "Performance of intermediate temperature solid oxide fuel cells with $La(Sr)Ga(Mg)O_3$ electrolyte film", J. Power Sources, 106 (2002) 142-145.

[15] S. Wang , T. Kato , S. Nagata .T. Kaneko N. Iwashita ,T. Honda , M. Dokiya, "Electrodes and performance analysis of a ceria electrolyte SOFC", Solid State Ionics, 152-153 (2002) 477-484.

[16] V. Brichzin, J. Fleig , H.-U. Habermeier, G. Cristiani, J. Maier, "The geometry dependence of the polarization resistance of Sr-doped LaMnO3 microelectrodes on yttria-stabilized zirconia", Solid State Ionics 152– 153 (2002) 499– 507

[17] R.A. De Souza, J.A. Kilner, "Oxygen transport in $La_{1-x}Sr_xMn_{1-y}Co_yO_{3-\delta}$ perovskites : Part I. Oxygen tracer diffusion", Solid State Ionics 106 (1998) 175–187.

[18] Akira Endo, Manabu Ihara, Hiroshi Komiyama, Koichi Yamada,"Cathodic reaction mechanism for dense Sr-doped lanthanum manganite electrodes", Solid State Ionics 86-88 (1996) 1191-1195.

[19] Jürgen Fleig, "SOLID OXIDE FUEL CELL CATHODES: Polarization Mechanisms and Modeling of the Electrochemical Performance", Annual Review of Materials Research Vol. 33 (2003) 361-382

[20] M. J. L. Ostergard, C. Clausen, C. Bagger and M. Mogensen, "Manganite-Zirconia composite cathodes for SOFC: Influence of structure and composition", Electrochimica Acta. Vol. 40 (12) (1995) 1971-1981.

[21] Mette Juhl, Seren Primdahl, Carrie Manon, Mogens Mogensen, "Performance/structure correlation for composite SOFC cathodes", Journal of Power Sources 61 (1996) 173-181.

[22] Olga A. Marina , Carsten Bagger, Søren Primdahl, Mogens Mogensen, "A solid oxide fuel cell with a gadolinia-doped ceria anode: preparation and performance", Solid State Ionics 123 (1999) 199–208

[23] G. Pudmich , B.A. Boukamp , M. Gonzalez-Cuenca , W. Jungen , W. Zipprich , F. Tietz "Chromite/ titanate based perovskites for application as anodes in solid oxide fuel cells", Solid State Ionics 135 (2000) 433–438

[24] S.Primdahl, PhD thesis, "Nickel/Yttria stabilised zirconia cermet anodes for solid oxide fuel cells" University of Twente, The Netherlands.

[25] P.Holtappels, I.C.Vinke, L.G.J de Haart and U.Stimming, "Reaction of hydrogen/water mixtures of Nickel-Zirconia cermet electrodes - II. AC Polarization characteristics", J. Electrochemical Society 146(8) (1999) 2976-2982.

[26] P.Holtappels, L.G.J de Haart and U.Stimming, "Reaction of hydrogen/water mixtures of Nickel-Zirconia cermet electrodes - I. DC Polarization characteristics", J. Electrochemical Society 146(5) (1999) 1620-1625.

[27] S.P.Jiang and S.P.S Badwal, "Hydrogen oxidation at the nickel and platinum electrodes on yttria-tetragonal zirconia electrolyte", J. Electrochemical Society 144 (11) (1997) 3777-3784.

[28] Junichiro Mizusaki, Hiroaki Tagawa, Takatoshi Saito, Tamaki Yamamura, et al "Kinetic studies of the reaction at the nickel pattern electrode on YSZ in H2-H20 atmospheres", Solid State Ionics 70/71 (1994) 52-58.

[29] Baukje de Boer, Phd thesis, "SOFC Anodes : Hydrogen oxidation at porous nickel and nickel/yttria-stabilised zirconia cermet electrodes" University of Twente, The Netherlands.

[30] A.Bieberle, L.P. Meier, and L.J.Gauckler, "The electrochemistry of Ni-pattern anodes used as a solid oxide fuel cell model electrodes", J. Electrochemical Society, 148 (6) (2001) A646-A656

[31] Yoshio Matsuzaki , Isamu Yasuda, "The poisoning effect of sulfur-containing impurity gas on a SOFC anode: Part I. Dependence on temperature, time, and impurity concentration", Solid State Ionics 132 (2000) 261–269

[32] Hans J. Seifert, Fritz Aldinger, "Applied phase studies" Z. Metallkunde, 87(11) (1996) 841-853.

[33] David R.Gaskell, "Introduction to metallurgical thermodynamics", McGrahill

[34] N.Saunders and A.P.Miodowink, "CALPHAD, calculation of phase diagrams- A comprehensive guide" Pergamon (1998).

[35] Ursula R.Kattner, "The Thermodynamic Modeling of Multicomponent Phase Equilibria", JOM, 49 (12) (1997) 14-19.

[36] H. L. Lukas and S. G. Fries, "Demonstration of the Use of BINGSS with the Mg–Zn System as Example," J. Phase Equilib., 13 [5] (1992) 532–41.

[37] J.O. Andersson, T.Helander,, L.Höglund, P.Shi, B. Sundman, Calphad, 26 (2002) 273-312.

[37] Patrice E.A. Turchi, Igor A. Abrikosov, Benjamin Burton, Suzana G. Fries, Göran Grimvall, Larry Kaufman, Pavel Korzhavyi, V. Rao Manga, Munekazu Ohno, Alexander Pisch *et al,* "Interface between quantum-mechanical-based approaches, experiments and CALPHAD methodology", CALPHAD, (In press)

[38] Kequin Huang, Man Feng, and John B.Goodenough, "Synthesis and electrical properties of dense $Ce_{0.9}Gd_{0.1}O_{1.95}$ cermaics, J.Am. Ceram. Soc., 81(2) (1998) 357-362.

[39] J. Rodriguez-Casvajal: FULLPROF: A program for Reitveld Refinement and pattern Matching Analysis; XV congress of the IUCr, Toulouse; France, (1990) 127.

[40] Z. Horita, T. Sano, M. Nemoto, "An extrapolation method for the determination of Cliff-Lorimer k_{AB} factors at zero foil thickness", J. Microscopy 143 (1986) 215.

[41] J.R. Macdonald, "Impedance Spectroscopy", JohnWiley&Sons, Inc., NewYork, NY, USA (1987).

[42] Carl Hamann, Andrew Hamnett, Wolf Vielstich, "Electrochemistry", Wiley-VCH, 1998.

[43] M.Singelton, P.Nash, K.J.Lee, Phase Diagrams of binary nickel alloys, ASM, 1991, 277

[44] Michael Rozumek, PhD thesis, "Kristallchemische eigenschaften ausgewählter funktions-keramiken im quasi-quaternären system Ga2O3-La2O3-MgO-SrO", University of Stuttgart, Germany.

[45] R.D. Shannon, "Revised Effective Ionic radii and systematic studies of interatomic distance in halides and chalcogenides" Acta Cryst. A32 (1976) 751.

[46]1. Sharma R.C., Chang. Y. A. "Thermodynamics and Phase Relationships of Transition Metal-Sulfur Systems: IV. Thermodynamic Properties of the Ni-S Liquid Phase and the Calculation of the Ni-S Phase Diagram." Metallurgical Transactions B 11B (1980) 139-146.

[47] Dinsdale A T, SGTE data for pure elements, CALPHAD, Vol.15, No.4, 317-425.

[48] Peter W, "Thermodynamic analysis of high-temperature heazelwoodite", Z. Metallkd., 97, (2006), No.1, 17-21

[49] Peter W, Pelton A D, "Thermodynamic modelling of the Ni-S system", Z. Metallkd., 95, (2004), No.8, 672-681 .

[50] Massalski .T .B, "Binary alloy phase diagrams", ASM international, 2nd Ed., 1990, Vol.3, 2850.

[51] Rosenquist T, "A thermodynamic study of the iron, cobalt, and nickel sulphides", Journal of the iron and steel institute, Jan (1954), 37-57.

[52] Schiffman R.A., Miller.R. A. "Knudsen Effusion of an Incongruent Subliming System: Thermodynamics of Nickel-Sulfur." High Temperature Science 10 (1978) 17-26.

[53] Akira E, Tadashi N, Toshio O et al, "A thermodynamic study of the systems Ni-S and Co-S by CaF$_2$ solid electrolyte galvanic cell technique", Transactions of the Japan institute of metals, Vol. 27, No.11 (1986), 890-897

[54] Alcock C B, Cheng L L, " A thermodynamic study of dilute solutions of sulphur in liquid iron, cobalt, and nickel and binary alloys between these metals", Journal of the iron and steel institute, Jun 1960, 169-173.

[55] Venal W.V., Gordon. H. G. "The Thermodynamic Behavior of Sulfur in Molten Nickel and Nickel-Base Alloys." Metallurgical Transactions 4 (1973) 2567-2573.

[56] Nagamori M., Ingraham. T. R. "Thermodynamic Properties of Ni-S Melts Between 700°C and 1100°C." Metallurgical Transactions 1(1970) 1821-1825.

[57] Meyer G.A., Warner. J. S., Rao Y.K., Kellogg H.H. "Thermodynamic Properties of Molten Sulfides: Part I. The System Ni-S." Metallurgical Transactions B 6B (1975) 229-235.

[58] Cemic L., Kleppa. O. J. "High temperature calorimetry of sulfide systems. I. Thermochemistry of liquid and solid phases of Ni+S." Geochimica et Cosmochimica Acta 50 (1986) 1633-1641.

[59] Rau.H. "Range of homogeneity and defect interaction in high temperature nickel sulfide $Ni_{1-x}S$." J. Phs. Chem. Solids 36 (11-D) (1975) 1199-1204.

[60] Rau.H. "Homogeneity range of high temperature $Ni_{3+x}S_2$." J. Phs. Chem. Solids 37(10-C) (1976) 929-930.

[61] Lin R.Y., Hu. D. C., Chang Y.A.. "Thermodynamics and Phase Relationships of Transition Metal-Sulfur Systems: II. The Nickel-Sulfur System." Metallurgical Transactions B 9B (1978) 531-538.

[62] Stolen S., G. F. "Thermodynamics of point defects in monochalcogenides of iron, cobalt and nickel with NiAs-type structure." J. Phs. Chem. Solids 48(12) (1987) 1213-1225.

[63] Stolen S., G. F., Westrum E.F., Jr., Kolonin G.R.. "Heat capacity and thermodynamic properties of synthetic heazlewoodite, Ni_3S_2, and of the high-temperature phase $Ni_{3+x}S_2$." J. Chem. Thermodynamics 23 (1991) 77-93.

[64] Gronvold F., S. S.. "Heat capacity and thermodynamic properties of millerite from 298.15 to 660K and NiAs-type nickel(II) sulfide from 260 to 1000K. Thermodynamics of the NiAs-type to millerite transition." Thermochimica Acta 266 (1995) 213-229.

[65] Stolen S., F. H., Gronvold F., Seim H., Westrum E.F., Jr.. "Phase stability and structural properties of $Ni_{7\pm delta}S_6$ and Ni_9S_8.Heat capacity and thermodynamic properties of Ni_7S_6 at temperatures from 5K to 970K and of Ni_9S_8 from 5K to 673K." J. Chem. Thermodynamics 26 (1994) 987-1000.

[66] Brigham R.J., N. H., Kirkaldy J.S. "Solubility limit for sulphur in nickel between 637°C and 1400°C.", Canadian Metallurgical Quarterly 9(4) (1970) 525-529.

[67] Kirkaldy. J.S. "Comments on "Grain boundary segregation and the grain size dependence of strength of nickel-sulfur alloys"." Metallurgica 3 (1969) 947-948.

[68] Kitakaze A, Sugaki A, Sendai, "Study of the $Ni_{3+x}S_2$ phase in the Ni-S system with emphasis on the phase of high-form Ni_3S_2 (β_1)and Ni_4S_3(β_2)", N.Jb.Miner.Mh, Jan 2001, 41-48.

[69] Line G.Huber M, "Etude radiocristallographique a haute temperature de la phase non stoechiometrique Ni3+x S2, Comptes Rendus Hebdomadaires des Seances de l'Academie des Sciences (1963) 256, 3118-3120.

[70] Kellogg, H. H. "A critical review of sulfation equilibria." Transactions of the metallurgical society of AIME 230 (1964) 1622-1634.

[71] Ingraham, T. R.. "Thermodynamics of the thermal decomposition of Nickel(II) Sulfate: the Ni-S-O system from 1000 to 1150K." Transactions of the metallurgical society of AIME 236 (1966) 1064-1071.

[72] M. Gauthier, C. W. B. (1983). "Oxide-Sulfate equilibria in the Mg, Ni and Mn systems measured by a solid K_2SO_4 concentration cell." Metallurgical Transactions B 14B: 117-124.

[73] J. Jacinto, M. N., H.Y. Sohn "Predominance area diagrams of the system Ni-S-O." Transactions of the institution of mining and metallurgy, Section C: Mineral processing 92, Dec (1983). 225-228.

[74] R. Lalauze, J.-C. L. T., C. Pijolat, M. Soustelle. "Temperature-programmed desorption and microcalorimetric studies of the SO_2-O_2-NiO system." J. Phys. Chem, 87 (1983) 3405-3407.

[75] Lenz J G, Conard B R, "The nickel rich corner of the nickel-oxygen-sulphur system at 850°C- 600°C", Nickel Metall. Symp. Proc., 25th Annu. Conf. Metall., Vol.1 (1986) 203-221.

[76] Y. Saito, T. M., Y. Yano. "Dissociation pressures of metal sulfates by electromotive force measurement on SO_2-O_2-SO_3 concentration cells with nasicon solid electrolyte." Canadian Metallurgical Quarterly 25(1) (1986) 51-57.

[77] Ker-Chang Hsieh, Y. A. C.. "A solid-state emf study of ternary Ni-S-O, Fe-S-O and quaternary Fe-Ni-S-O." Metallurgical Transactions B 17B (1986) 133-146.

[78] P. Sarrazin, A. S.. "Corrosion of metals in multicomponent gas atmospheres: generalization of the use of phase-stability diagrams." Oxidation of Metals 30(1/2) (1988) 107-124.

[79] S. Yao, A. A., M. Taguchi, Z. Kozuka. "The activity coefficients of oxygen in Ni-S and Co-S Melts." Metallurgical Transactions B, 21B (1990) 529-536.

[80] E. Osadchii, E. R., B. Saitton. "Equilibrium studies of the system Ni-S-O using the solid electrolyte galvanic cell technique." Acta Chemica Scandinavica 44 (1990) 476-480.

[81] Shariat M H, Behgozin S A, "A new look at nickel-oxygen-sulfur diagrams", CALPHAD, Vol.20, No.1 (1996) 47-67.

[82] Kowalski.M, Spencer. P.J., "Thermodynamic revaluation of the Cr-O, Fe-O and Ni-O systems:Remodelling of the liquid, BCC and FCC phases" CALPHAD 19(3) (1995) 229-243.

[83] SGTE database 2004

[84] P.Kofstad, Akesson G, "High-temperature corrosion of nickel in SO_2" Oxidation of Metals, 12, (1978) 503.

[85] McEwen, R. S. "Crystallographic studies on nickel hydroxide and the higher nickel oxides." J. Phys. Chem. 75(12) (1971) 1782-1789.

[86] P. Oliva, J. L., J.F. Laurent, C.Delmas, J.J.Braconnier, M.Figlarz, F.Fievet A.de Guibert "Review of the structure and the electrochemistry of nickel hydroxides and oxy-hydroxides." Journal of Power Sources 8 (1982) 229-255.

[87] R. Acharya, T. S., S. Anand, R.P. Das "Preparation, characterization and electrolytic behavior of beta-nickel hydroxide." Journal of Power Sources 109 (2002) 494-499.

[88] Wu Fang-Fang, Wang J-M, Chen H, Zhang J-Q," Synthesis and physicochemical properties of NiOOH with different phase structures", 28(11) (2004) 700-703.

[89] M. komath, S. T., K.A. Cherian, A. Ray "Preparation of gamma-nickel oxyhydroxide through high temperature reaction of nickel with anhydrous sodium hydroxide." Mater. Chem. & Phys. 36 (1993) 190-193.

[90] Zeng K, Klassen T, Oelerich W, Bormann R," Thermodynamics of the Ni-H system", Journal alloys and compounds, 283 (1999) 151-161.

[91] J. Fleig, "Impedance Spectroscopy on Solids: The Limits of Serial Equivalent Circuit Models", Journal of Electroceramics, 13, 637–644, 2004.

[92] Junichiro Mizusaki, Hiraoki Tagawa et al, "Preparation of nickel pattern electrodes on YSZ and their electrochemical properties in H2-H2O atmospheres" J. electrochem. Soc Vol. 141(8) (1994) 2129.

[93] Geyer J, H.Kohlmüller, H.Landes, R.Stübner, , "Investigations into the kinetics of the Ni-YSZ-cermet-anode of a solid oxide fuel cell" Proceedings of the fifth international symposium on solid oxide fuel cells (SOFC-V), Ed., Stimming U, Singhal SC, Tagawa H, Lehnert W, Electrochem. Soc. (1997) 585-594.

[94] N. Solak, M. Zinkevich, F. Aldinger, private communications.

[95] H. Obayashi, T. Kudo, "Some crystallographic, electrical and thermochemical properties of the perovskite-type $La_{1-x}M_xNiO_3$ (M: Ca, Sr and Ba)." Japanese J. App. Phys. 14 (1975) 330-335.

[96] J.A. Alonso, M.J. Martinez-Lope, M.A. Hidalgo, " Hole and electron doping of $RNiO_3$ (R = La,Nd)", J. Sol. State. Chem. 116 (1995) 146-156.

[97] Dongman Kim and Alan J. Ardell, "Coarsening Behavior of Ni3Ga Precipitates in Ni-Ga Alloys: Dependence of Microstructure and Kinetics on Volume Fraction", Metallurgical and Materials Transactions A, Vol 35A (2004), 3063

[98] Gröbner. J, Wenzel. R, Fischer.G.G and Scmid-Fetzer. R, "Thermodynamic calculation of the biunarysystems M-GA and investigations of ternary M-Ga-N phase equilibria (M=Ni, Co, Pd, Cr)", J. Ph. Equilib. 20(6) (1999) 615-625.

[99] N.L. Robertson, J.N.Michaels, "Double layer capacitance of porous platinum electrodes in zirconia electrochemical cells", J. Electrochem. Soc., 138 (1991) 1494

[100] Kek D, Mogensen M, Pejovnik S," A study of metal(Ni, Pt, Au)/Yttria-Stabilised zirconia interface in hydrogen atmosphere at elevated temperatures, J. Electrochem. Soc., 148(8) (2001) A878-A886.

[101] S.Bebilis, S.Neophytides, "AC impedance study of Ni-YSZ cermet anodes in methane-fuelled internal reforming YSZ fuel cells", Solid state ionics, 152-153 (2002) 447-453.

[102] Richard I. Masel, " Principles of adsorption and reaction on solid surfaces", Wiley series in chemical engineering

[103] Neophytides S. G. and Vayenas C. G., "TPD and Cyclic Voltammetric Investigation of the Origin of Electrochemical Promotion in Catalysis", J. Phys. Chem. 99(47) (1995) 17063

[104] Rostrup-Nielsen J R, "Chemsiroption of hydrogen sulfide on a supported nickel catalyst", J. Catalysis, 11 (1968) 220-227.

[105] J.L. Oliphant, R. W. F., R.B. Pannell, C.H. Bartholomew "Chemisorption of hydrogen sulfide on nickel and ruthenium catalysts. I. Desorption Isotherms." J. Catalysis, 51 (1978) 229-242.

[106] D.W. Goodman, M. K, "Chemisorption and reactivity studies of H_2 and CO on sulfided Ni(100)." Surface Science 105 (1981) L265-L270.

[107] R.B. Pannell, K. S. C., C.H. Bartholomew. "The stoichiometry and poisoning by sulfur of hydrogen, oxygen and carbon monoxide chemisorption on unsupported nickel." J. Catalysis 46 (1977) 340-347.

[108] C.H. Bartholomen, R. B. P.. "Sulfur poisoning of hydrogen and carbon monoxide adsorption on supported nickel." Applied Catalysis, 2 (1982) 39-49.

[109] Bruce C.Gates, Helmut Knözinger, "Impact of surface science on catalyis", Academic press (2000).

Curriculum Vitae (Lebenslauf)

Personal

Name: Manga Venkateswara Rao
Date of Birth: 18-06-1974
Sex: Male
Nationality: Indian
Marital status: Unmarried

Career summary

Schooling   1979 – 1991
Visakhapatnam

D.Met.E (Diploma in Metallurgical Engineering)   Jan'1992 – Dec'1996
Govt. Polytechnic College, Visakhapatnam

AMIIM (Associate Member of IIM)   Jan'1997 – Dec'1998
Indian Institute of Metals, Calcutta

M.Tech (Materials technology)   Jun'1999 – Dec'2000
Indian Institute of Technology, Madras

Ph.D Student   Apr'2002 – Dec'2006
Max-Planck-Institut für Metallforschung, PML,
Stuttgart, Germany